The Properties of AGN in the context of X-ray Binaries

MIDDLETON, MATTHEW,JAMES

The Properties of AGN in the context of X-ray Binaries

by Matthew J. Middleton

A thesis submitted to the University of Durham
in accordance with the regulations for
admittance to the Degree of Doctor of Philosophy.

Department of Physics
University of Durham
September 2009

Preface

“ Some men see things the way they are and ask, “Why?”, I dream things that never were and ask, “Why not?” ”. - George Bernard Shaw

Black holes are undoubtedly the most fascinating and exciting objects in the Universe, capturing the imagination of scientists and film writers alike. It has been a long standing objective of the scientific community to understand how these objects work and whether the black holes seen in the centers of galaxies, including our own, show analogous physics to those seen in stellar mass binary systems in other parts of the galaxy.

In this body of work I aim to introduce the reader to the many broad facets of the subject to which the first 4 chapters are dedicated. These explain the mechanisms allowing black holes to be seen, i.e. luminous accretion and reprocessing of radiation, the environments black holes are found in and the effect this can have on observations.

The 5 chapters following the introduction are the papers that I have published from my studies in this field as I try to address the outstanding problems which present obstacles to our understanding of unified black hole accretion.

I hope that you, the reader will find this work compelling in nature and an enjoyable insight into one of the greatest mysteries of the Universe.

Contents

List of Figures

Declaration

The work described in this thesis was undertaken between 2005 and 2009 while the author was a research student under the supwervision of Prof. Chris Done in the Department of Physics at the University of Durham. This work has not been submitted for any other degree at the University of Durham or any other University.

Portions of this work have appeared in the following papers:

- Middleton M., Done C., Gierliński M., 2007, MNRAS, 381, 1426
- Middleton M., Done C., Schurch N., 2008, MNRAS, 383, 1501
- Gierliński M., Middleton M., Ward M., Done C., 2008, Nature, 455, 369
- Middleton M., Done C., Ward M., Gierliński M., Schurch N., 2009, MNRAS, 394, 250
- Middleton M., Done C., 2009, in press

Acknowledgements

I would firstly like to thank my supervisor, Professor Chris Done, who has been a great support over the past 5 years, has given me a great start into the industry and without whom this thesis would not have been so exhaustive. Likewise I would like to thank Marek Gierliński who, together with Nick Schurch, taught me more about statistics and programming in Perl than I could ever have imagined needing (I was wrong).

I think its fair to say that, without the support of my family and friends, I wouldn't have made it through the last 4 years at University with my sanity intact. Importantly I'd like to recognise how much of a friend Hugh Dickinson has been to me and thank him for useful Physics chat and for introducing me to rowing (something that Chris is forever thankful for). I would also like to thank Nic Ross who kept me going in my early University career and inspired me to get into the strange world that is Astronomy, cheers Niccy P.

I would also like to thank all of my rowing colleagues and specifically head coach Wade Hall-Craggs for showing me that pain is but an inconvenience on the path to success (something I have come to understand only too well when writing this body of work).

And finally and most importantly I owe a great deal to my mother, Janet, who has supported me on every level throughout my life but especially at University when it was most necessary and most appreciated.

Chapter 1

Introduction to: Black hole radiative processes

Black holes are formed during the cataclysmic death of massive stars, when the star has effectively run out of fuel and can no-longer support its own gravitational contraction. If the mass of the progenitor is great enough, the star will experience a super-nova and collapse to form a neutron star, where the neutron degeneracy pressure is enough to prevent further collapse. If the progenitor is more massive still, then this mechanism cannot save the star and it collapses down to a singularity or stellar mass 'black hole'.

At the other end of the mass spectrum are the supermassive black holes that reside at the centre of galaxies and have masses in the range 10^5 - $10^9 M_\odot$. If these are 'feeding' then the result is an active galactic nucleus (AGN). Stellar mass black holes in X-ray binaries are discussed in detail in chapter 2 and AGN in chapters 3 and 4.

Although black holes exist as a solution of Einstein's field equations of general relativity (GR) they are not directly observable. They can, however, be detected by their effect upon the local universe, by which we mean the effect of a black hole's gravitational potential well upon matter and photons travelling within its sphere of influence.

Far out from the black hole the matter follows paths that are well described by Newtonian physics. This material accretes towards the black hole by dissipating angular momentum. GR effects mean that the material can only maintain a circular

orbit down to a last stable orbit (LSO), the position of which is dependant upon the mass and 'spin' of the black hole. The latter is the residual angular momentum of the singularity following its 'birth' and may be increased or decreased by absorbing angular momentum from matter or radiation entering the black hole and is described by the dimensionless parameter: $a{=}Jc/GM^2$. For the case where the black hole has zero spin (a=0) the object is referred to as a Schwarzchild black hole with matter and radiation following paths as determined by the Schwarzchild metric of GR and the LSO at $3R_s$ where $R_s{=}2GM/c^2$. However if the black hole is spinning in the direction of the disc (a>0) then the LSO is dragged inwards and the path of matter and radiation is determined by the Kerr metric.

Thus, whilst we cannot 'see' black holes, we can expect to detect them by radiation produced by accretion (see the following section) or their effect on other stellar bodies. For example, if nearby stars fall within the black hole's sphere of influence they will enter a roughly Keplerian orbit. Such observations have allowed the most accurate measurements of black hole mass (e.g. Sgr A* - Schodel et al. 2002).

1.1 Accretion

In the simplest terms, matter travelling within the gravitational potential well of the black hole will form an accretion disc and through angular momentum transport will in-fall towards and eventually past the LSO.

The total energy released by this accretion is given by:

$$L = \eta \dot{M} c^2 \tag{1.1}$$

where η is the efficiency of accretion, $\dot{M}$ is the mass accretion rate and c is the speed of light in a vacuum.

The balance of gravitational force and radiation force provides a theoretical Ed-

dington limit to this luminosity, given by:

$$L_{Edd} = 1.26{\times}10^{38}\frac{M}{M_{\odot}}ergs^{-1} \tag{1.2}$$

This is, however, only valid in the case of spherical systems and disc accretion may not necessarily obey this limit.

During the process of accretion each annulus in the disc emits thermal radiation due to the loss of gravitational potential energy into rotational kinetic energy and through friction between adjacent annuli of matter. This emission is approximated by a black body.

The luminosity of a given annulus of width dR is given by:

$$dL = A\sigma T^4 = 2{\times}2\pi RdR\sigma T^4 \tag{1.3}$$

where A is the emitting area of an annulus in the disc (multiplied by a factor of two for the two sides), T is the temperature of the black body emission and σ is the Stefan-Boltzmann constant.

If half of the potential energy is liberated as radiation (virial) everywhere then we also have:

$$dL = \frac{GM\dot{M}}{2R^2}dR \tag{1.4}$$

where M is the central mass which implies:

$$\Longrightarrow T^4 = \frac{GM\dot{M}}{8\pi R^3\sigma} \tag{1.5}$$

From the above equations it is clear that T $\propto$ $R^{-3/4}$ and so the inner radii are obviously much hotter and will emit thermal radiation at subsequently shorter wavelengths. From the superposition of blackbodies across a range of annuli in the disc we get a 'multi-colour disc blackbody' as depicted in figure 1.1.

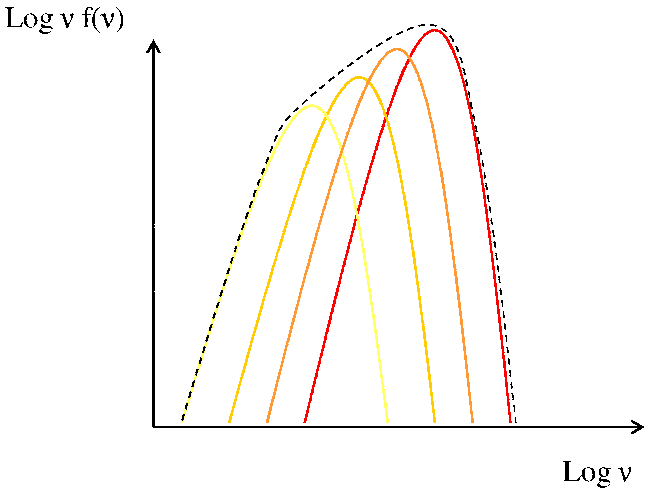

Figure 1.1: The multi-colour disc blackbody, formed from the black-body emission of many annuli with the hottest being those closer to the compact object.

This rather simple derivation only conserves energy whereas simultaneously conserving angular momentum gives:

$$T^4 = \frac{3GM\dot{M}}{8\pi R^3\sigma}(1-\sqrt{R_{in}/R}) \tag{1.6}$$

where R_{in} is the inner radius of the disc.

The real picture is more complex than this, and given that we are observing material in strong gravity, general relativistic effects are important although the approach produces very similar results (Norikov & Thorne 1973). In addition the peak of the disc emission is determined by the position of the LSO (thusly spin) with distorting effects on the observed spectrum due to strong gravity (Cunningham 1975; Zhang et al. 1997).

This emitted spectrum is independent of the viscosity prescription that we apply

to remove angular momentum from the disc and precipitate accretion. The most prevalent of these is the 'alpha' prescription of Shakura & Sunyaev (1973) where the disc forms a geometrically thin, optically thick disc with viscous stress proportional to the sum of radiation ($\propto T^4$) and gas pressure ($\propto T$). This is a simple *ad hoc* description used throughout much of accretion physics although it is believed that the magneto-rotational instability (MRI) of Balbus & Hawley (1998) provides the true underlying physical mechanism of angular momentum transport.

1.2 Comptonisation

As photons leave the disc they interact with high energy electrons possibly in some sort of corona (e.g. Wilms et al. 1999) resulting in scattering. The effect of this depends upon several factors including the temperature and optical depth, τ, which is related to the number of scatterings the photon takes to escape from the plasma. This can be best described by an incident radiation field of intensity I upon a medium of density ρ with an absorption coefficient κ being scattered over a distance ds. The change in intensity is then dI = -$\kappa\rho$Ids. By integrating we arrive at $\mathrm{I/I_0} = \mathrm{e}^{-\kappa\rho s}$. Defining τ=$\kappa\rho$ds this becomes $\mathrm{I/I_0} = \mathrm{e}^{-\tau}$. Therefore the intensity drops by a factor of 1/e whenever the optical depth is unity. Note that τ may also be defined as [the number density (of electrons, n)] $\times$ [the distance travelled] $\times$ [the absorption cross section (σ)].

Single scattering

For low photon energies, $h\nu = \epsilon \ll \mathrm{m_e c^2}$ the scattering of radiation from free charges reduces to classical Thompson scattering. However, this must also take into account quantum effects of the kinematics of the scattering process (as the photon possesses momentum as well as energy) and associated cross-sections. Taking the

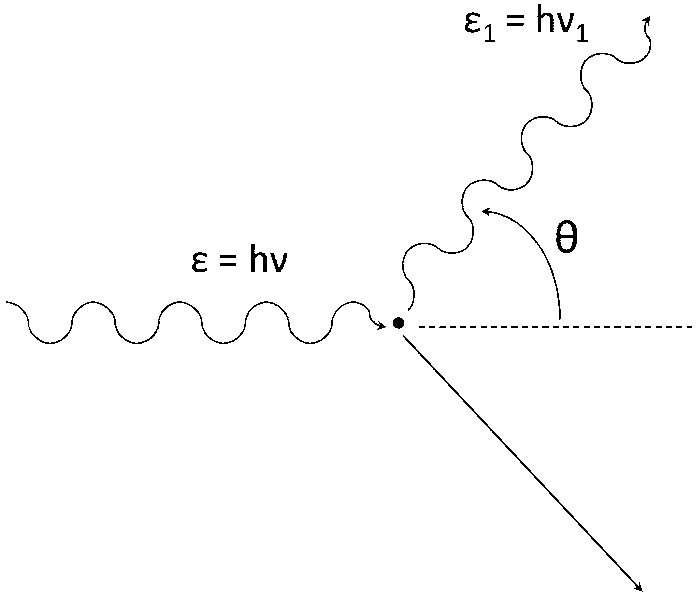

Figure 1.2: A single Compton scattering off a stationary electron by a photon.

most simple case of a single scattering from an electron at rest (fig 1.2), conservation of momentum and energy lead to the formula:

$$\epsilon_1 = \frac{\epsilon}{1 + \frac{\epsilon}{mc^2}(1 - cos\theta)} \tag{1.7}$$

In this case of Compton down-scattering, energy is transferred from the photon to the electron as the electron recoils.

If we now consider the electron to be moving, then energy may be transferred from the electron to the photon assuming the electron has sufficient kinetic energy relative to the photon. This process is known as inverse Compton scattering. If we consider ourselves to be in the rest frame of the electron and account for the Doppler effect between the observer's frame and electron rest frame (figure 1.3) we obtain:

$$\epsilon^{'} = \epsilon\gamma(1-\frac{v}{c}cos\theta) \tag{1.8}$$

$$\epsilon_1 = \epsilon_1^{'}\gamma(1+\frac{v}{c}cos\theta_1^{'}) \tag{1.9}$$

where $\gamma \equiv \sqrt{1-(\frac{v}{c})^2}$.

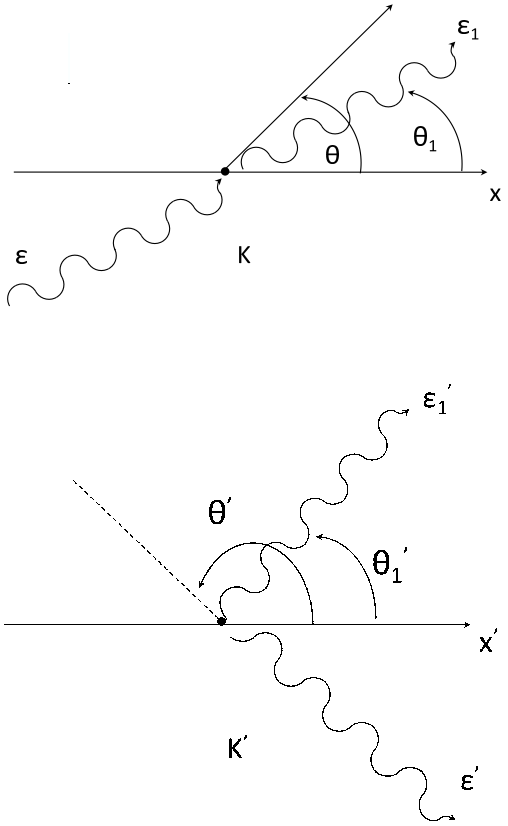

Figure 1.3: Scatterings in the observer's frame, K and the electron rest frame K'. The analysis in differing frames leads to equations 1.8 and 1.9.

From equation 1.7 we can see that, if the scattering has $\epsilon_1^{'} \approx \epsilon^{'}$ (i.e. $\epsilon^{'}/mc^2 \ll 1 \longrightarrow \gamma\epsilon \ll mc^2$ which is the Thompson limit) then:

$$\epsilon_1^{'} \approx \epsilon^{'}[1 - \frac{\epsilon^{'}}{mc^2}(1 - cos\Theta^{'})] \tag{1.10}$$

where

$$cos\Theta^{'} = cos\theta_1^{'}cos\theta^{'} + sin\theta^{'}sin\theta_1^{'}cos(\phi^{'} - \phi_1^{'}) \tag{1.11}$$

and $\phi^{'}$ and $\phi_1^{'}$ are the respective azimuthal angles of the scattered photon and incident photon in the rest frame.

For an isotropic distribution of photons and electrons then $\theta_1^{'}$ and $\theta \sim \pi/2$ (Rybicki & Lightman 1986). Then the ratio of the photon energy before, in the rest frame of the electron and post scattering is: $1{:}\gamma{:}\gamma^2$.

As a direct result of this it is easy to see that a low-energy photon may gain a huge increase in energy by a factor γ^2 via this process.

Multiple scatterings - Thermal distribution

The previous description only holds for a single scattering of a photon and electron whereas we want a description of multiple scatterings and the effect this has upon the total energy of the photon distribution given a particular distribution of electrons. To do this we must determine the conditions under which the scattering process significantly affects the total photon energy, limiting this consideration to situations where the Thompson limit applies in the electron rest-frame ($\gamma\epsilon \ll$mc^2).

In a finite medium we can define a Compton y-parameter as the [energy gain per scattering] $\times$ [the number of scatterings].

In order to work out the first element of this parameter, the Compton scattering is firstly averaged over all angles (as described in Blumenthal and Gould 1970)

assuming a thermal distribution of electrons. The fractional energy change in the photon distribution in the electron rest frame is:

$$\frac{\Delta\epsilon^{'}}{\epsilon^{'}} \equiv \frac{\epsilon_1^{'} - \epsilon^{'}}{\epsilon^{'}} = -\frac{\epsilon^{'}}{mc^2} \tag{1.12}$$

Moving to the lab frame this becomes:

$$\frac{\Delta\epsilon}{\epsilon} = -\frac{\epsilon}{mc^2} + \frac{\alpha}{mc^2} = \frac{\alpha - \epsilon}{mc^2} \tag{1.13}$$

where α=4kT for the non-relativistic and $16(\mathrm{kT})^2$ for relativistic case respectively.

We now have the first term for the y-parameter in each case for a thermal electron distribution. The second term of the Compton y-parameter, the number of scatterings that occur, is determined by the optical depth. This can be seen as the term, $(\tau+\tau^2)$, such that in a medium of low optical depth the second term drops out, whereas in media of high optical depth the second term dominates. Combining the two elements gives the Compton y-parameter for a thermal distribution of electrons in both non-relativistic (NR) and relativistic (R) cases. To simplify we include the dimensionless temperature normalised with respect to the electron rest energy:

$$\Theta = \frac{kT}{mc^2} \tag{1.14}$$

$$\longrightarrow y_{NR} = 4\Theta(\tau + \tau^2) \tag{1.15}$$

$$\longrightarrow y_R = 16\Theta^2(\tau + \tau^2) \tag{1.16}$$

The full description of the effect upon the shape of the energy spectrum with a Comptonising medium of finite optical depth is described in detail in a number of sources (specifically the seminal work of Sunyaev & Titarchuk 1980 and the review of Pozdnyakoz, Sobel & Sunyaev 1976).

I will now discuss the specific effects of differing y-parameters upon a thermal distribution of electrons. In the case where the electrons are relativistic, the amount the energy will be amplified by is $\Delta\epsilon/\epsilon \approx 16\Theta^2 = A$.

Clearly, in the case where the optical depth is small, the energy exchange is $\sim y$ and if $y \ll 1$ the spectrum is not altered by Compton scattering as very little energy is exchanged between the electron and photon populations. However, in the case where $y \geq 1$, inverse Compton scattering is important and a power-law spectrum results (see the Monte Carlo simulations of Pozdnyakoz, Sobel & Sunyaev 1976):

Given an initial intensity $I(\epsilon_i)$ at a mean photon energy ϵ_i (where $\gamma\epsilon_i \ll mc^2$) then, following k scatterings:

$$\epsilon_k = \epsilon_i(1 + A)^k \tag{1.17}$$

Each scattering intercepts a fraction, τ, of the previous spectrum and boosts this in energy by a factor [1+A], hence the intensity after k scatterings is:

$$I(\epsilon_k) \sim I(\epsilon_i)(\frac{\epsilon_k}{\epsilon_i})^{-\alpha} \tag{1.18}$$

where

$$\alpha \equiv \frac{-ln\tau}{lnA} \tag{1.19}$$

This Comptonised spectrum is shown in figure 1.4 and starts from the top of the soft-photon distribution and ends at $\sim 3\Theta$. Above this energy, the spectrum falls off exponentially in accordance with the high-energy tail of the Maxwellian distribution. The sum total (i.e. after k scatterings) between these energies appears as a power-law unless $\Theta \gg 1$ in which case the energy shift is so large that individual scatterings may be resolved.

A power-law, Compton spectrum is also produced if $y \sim 1$ and we are instead scattering in an optically thick plasma ($\tau \gg 1$) where Θ is small (Shapiro, Lightman

Figure 1.4: An approximation to the Compton spectrum resulting from repeated scatterings from a thermal population of relativistic electrons. This is well described by a power law of index $-\alpha$ and is formed when the seed distribution is scattered to a lower intensity by a factor τ and is shifted in energy each scattering by (1+A) Note that at E$\sim$3Θ the fall off in energy reflects the shape of the Maxwellian tail of the input thermal distribution.

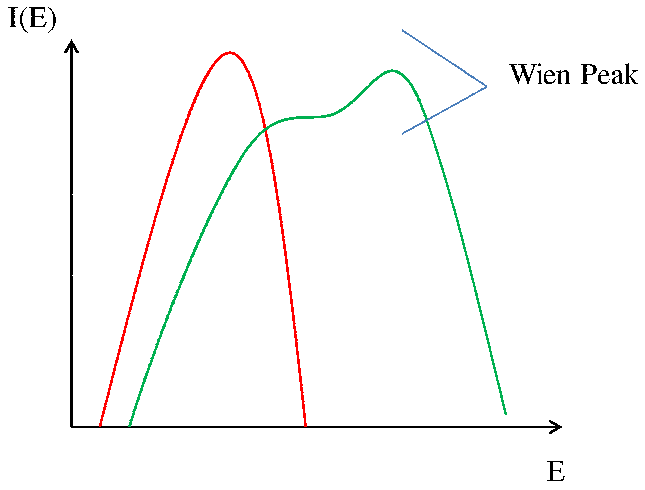

Figure 1.5: An approximation to the Compton spectrum created when y≫1 such that a Wien peak is formed.

& Eardley 1976; Pozdnyakov, Sobel & Sunyaev 1976; Sunyaev & Titarchuk 1980). However, if y≫1 a Wein peak forms in the spectrum (figure 1.5) as all the photons pile up at the electron temperature.

The full output Compton spectrum for multiple scatterings in the non-relativistic limit require solutions to the Kompaneets (Fokker-Planck) equation (Kompaneets 1957) which describes the evolution of the photon distribution in this regime.

Multiple scatterings - Non-thermal distribution

In the above section the assumption was that the electrons had a purely thermal (Maxwellian) distribution. However, the origin of the Comptonising region is unclear and it is possible that the electrons instead have a non-thermal distribution, i.e that of a power-law of the form $N(\gamma) \propto \gamma^{-p}$. The rate at which energy is lost from this

distribution of particles of energy γ is:

$$f(\epsilon)d\epsilon = \dot{\gamma}N(\gamma)d\gamma \tag{1.20}$$

Where $\dot{\gamma}$ is the rate of loss of energy from electrons of Lorentz factor γ and is the maximum rate at which the photons gain energy. As $\epsilon_f \sim \gamma^2\epsilon_i$ this becomes:

$$f(\epsilon) \propto \gamma^2\gamma^{-p}\frac{d\gamma}{d\epsilon} \propto \epsilon^{-(p-1)/2} \tag{1.21}$$

Therefore, the first order, relativistic Compton spectrum is a power law of index α=(p-1)/2. The details of this spectrum are given by Zdziarski (1986a) but can be approximated in the same way as the thermal case with a fraction τ_{tot} of the input spectrum scattering up to $\gamma^2_{max}\epsilon_0$, where τ_{tot} is found from integrating the electron distribution, $\tau(\gamma) = \tau(1)\gamma^{-p}$.

Following this initial scattering, the input distribution is no longer mono-energetic as there is the initial distribution and the first order scattering. As a result, the second order Compton spectrum has intrinsic curvature and extends from ϵ_0 to $\sim \epsilon_0\gamma^4_{max}$ (fig 1.6). These multiple scatterings continue until the energy gained is close to the energy of the electrons, i.e. $(\gamma^2)^n\epsilon_0 \sim \gamma_{max}mc^2$.

An initially non-thermal electron distribution can thermalise or partially thermalise by interactions between electrons. This can lead to a hybrid (thermal at low energies, non-thermal at high energies) electron distribution. However, in the studies hereafter I use models for only thermal or non-thermal Comptonisation and refrain from analysis of hybrid plasmas.

1.3 Secondary effects

The high-energy, Compton scattered photons can be seen directly as a continuum but can also be absorbed and/or reflected and reprocessed themselves by the disc if

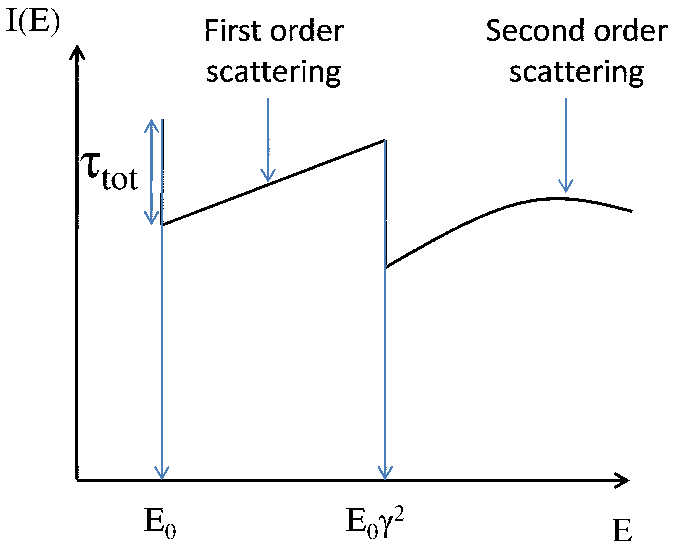

Figure 1.6: An approximation to the first and second order Compton spectra resulting from scatterings from a non-thermal population of electrons. In a similar way to the thermal Compton spectrum, each scattering results in a drop in τ_{tot} with an energy shift of γ^2. Curvature is introduced following the initial scattering due to the incident spectrum now being more complex.

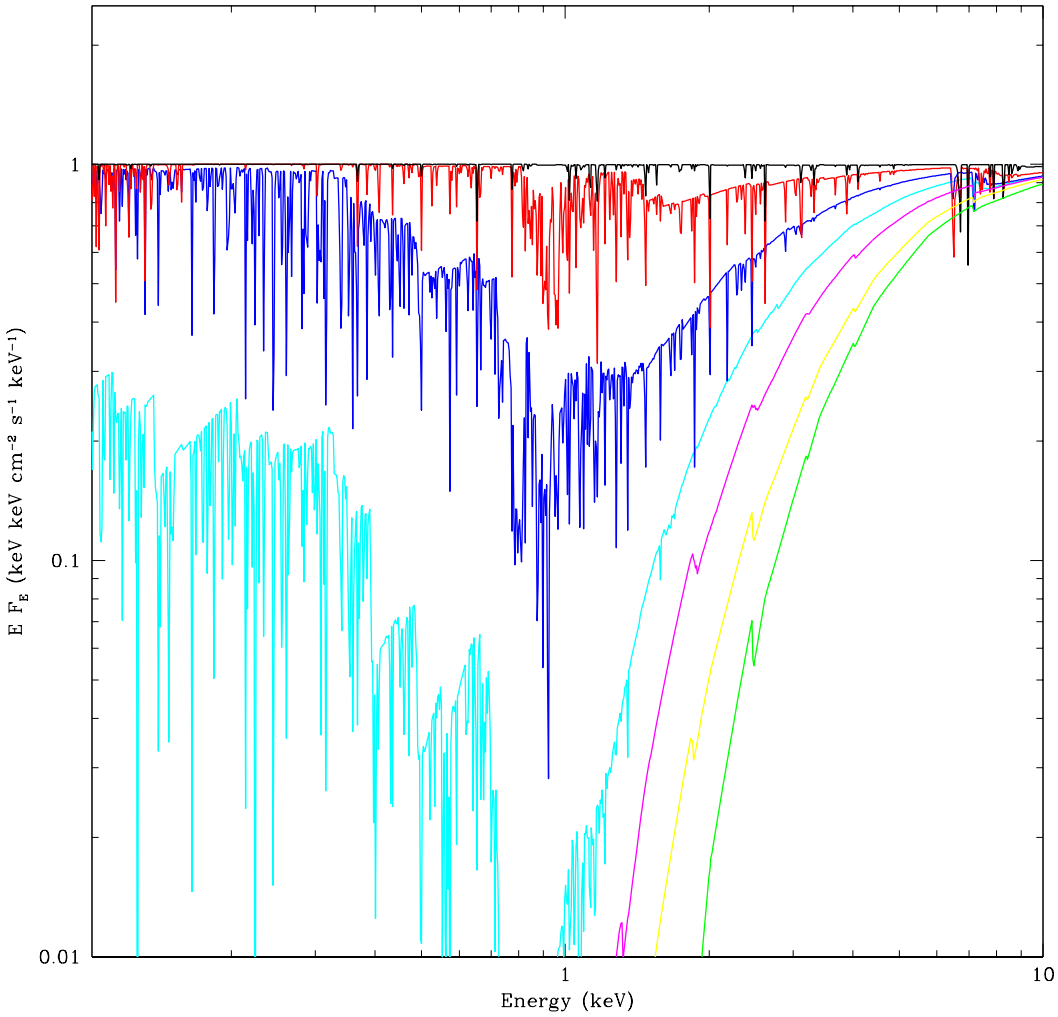

Figure 1.7: Absorption from a flat ($\Gamma = 2$) power-law, illuminating a column (5×10^{22}cm^{-2}) of warm, optically thin gas of varying ionisation parameter (logξ= -2-green -1-yellow 0-magenta 1-cyan, 2-blue, 3-red, 4-black).

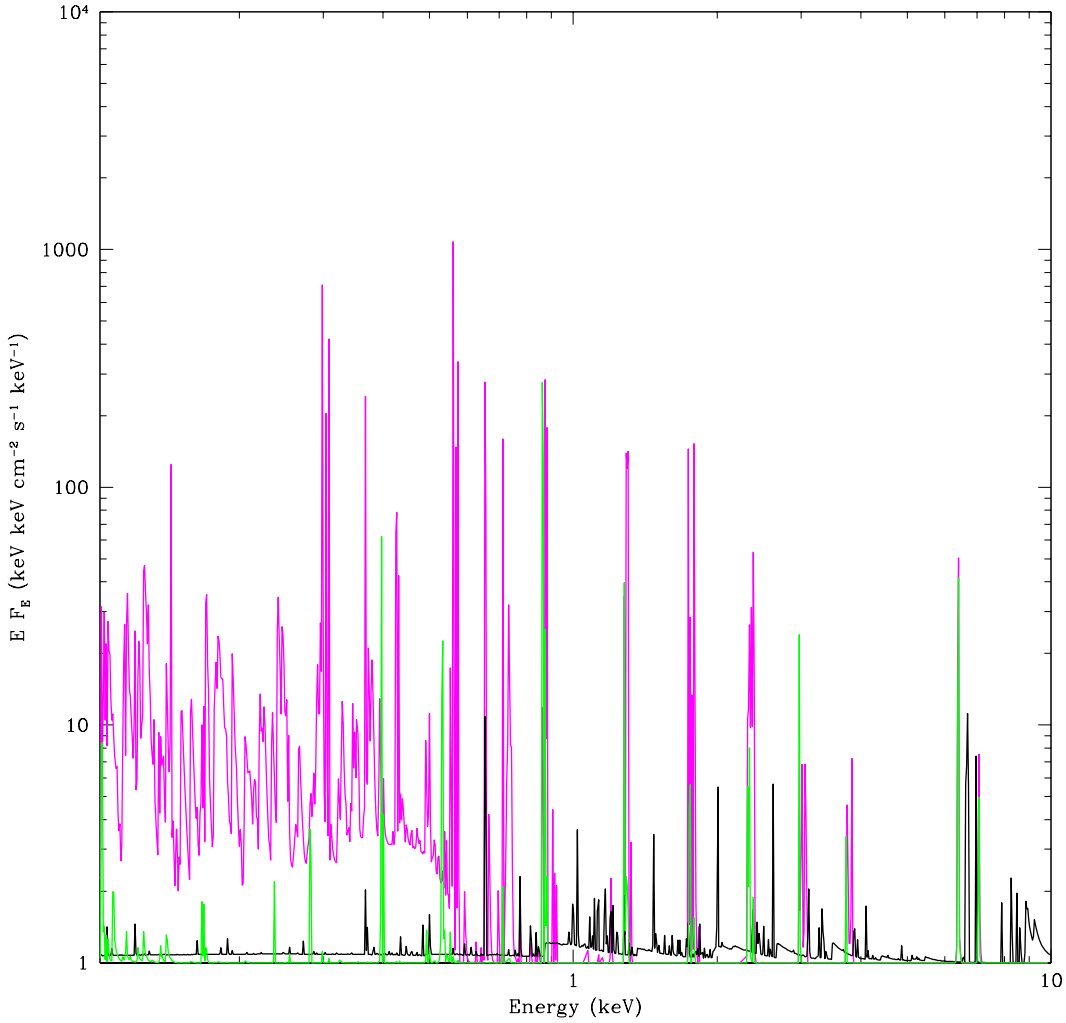

Figure 1.8: Emission from a flat ($\Gamma = 2$) power-law, illuminating a column (5×10^{22}cm^{-2}) of warm, optically thin gas of varying ionisation parameter (logξ= -2-green 0-magenta 4-black).

down-scattered. These processes are described below.

1.3.1 Absorption

Photo-electric absorption is highly dependent upon the ionisation structure of the Compton-thin plasma, parameterised by:

$$\xi = \frac{L}{nr^2} \tag{1.22}$$

where L is the ionising luminosity, n is the proton density and r is the distance to the central source (Tarter et al. 1969).

The effect of absorption on a Γ=2 power-law continuum for a range of ionisation parameters is shown in figure 1.7 and the equivalent emission in figure 1.8.

A full treatment of these features is given in the review of Turner & Miller (2009) where it is clear that the relative dominance of the various emission and absorption features depends on the selected geometry of the ionised material and so conversely the measurement of absorption features can constrain the geometry if components can be adequately separated in observational data. FeKα is the strongest of these, in neutral material being formed of a doublet at 6.404 and 6.391 keV (which is indistinguishable by current X-ray spectrometers) and in photo-ionised gas is dominated by a complex of permitted and forbidden transitions in the 6.5-6.95 keV range (Bianchi et al. 2005 and references therein).

The above features assumed that the interacting medium was static, however we know that these systems must be dynamic in nature and as such must apply suitable modifications to the spectra. These effects are thermal, kinematic and relativistic in origin.

Thermal broadening creates a Doppler spread in energy where, for a gas of temperature T, containing ions of mass m_{ion}:

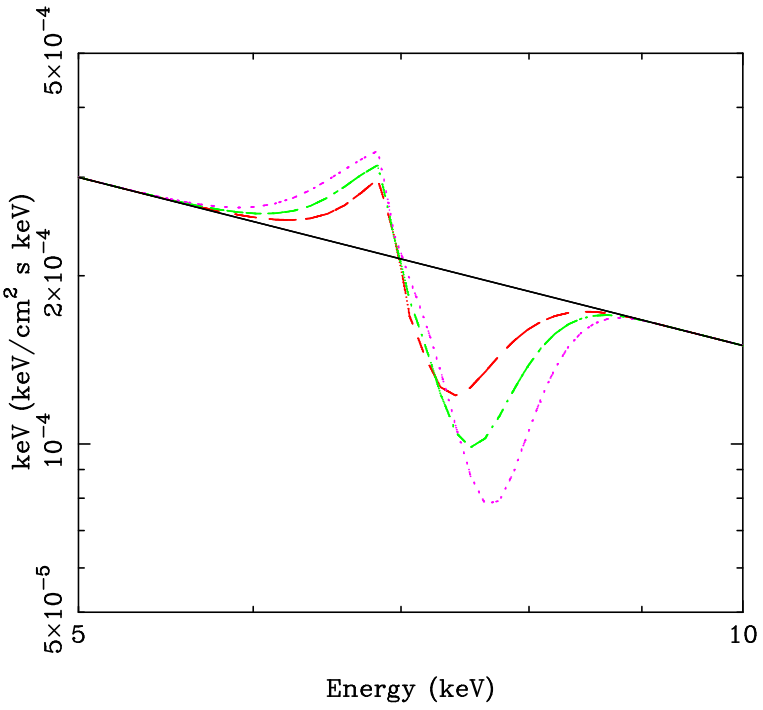

Figure 1.9: The P Cygni profile of a H-like Iron resonance line for varying optical depth of gas (Done et al. 2007).

$$\frac{\Delta E}{E} \sim \sqrt{\frac{2kT_e}{m_{ion}c^2}} \tag{1.23}$$

The most obvious kinematic distortions come from the velocity of the absorber leading to standard Doppler effects which broaden and distort the spectrum. A special case of this is the P Cygni profile, seen in the emission from a sphere of outflowing gas such that the absorption component of the line is blue shifted relative to the emission component (fig 1.9) with geometrical effects determining the relative sizes of emission and absorption. In the case of a symmetric sphere, the orientation of the observer to the material determines the amount of distortion applied to the feature (see Sim et al. 2008).

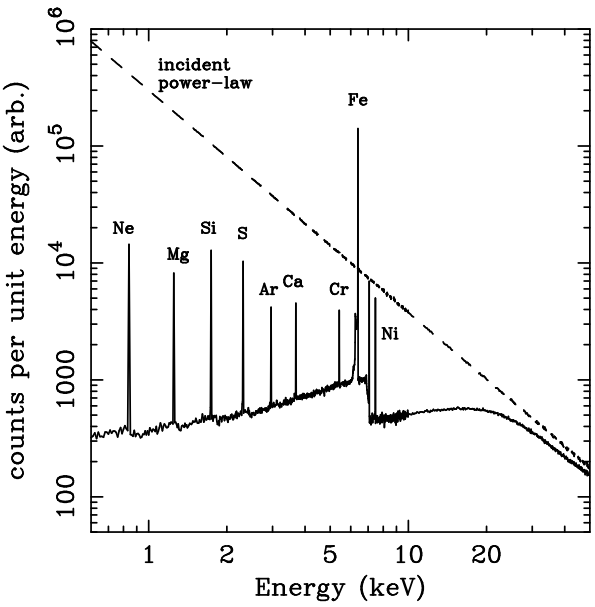

Figure 1.10: Monte Carlo simulations showing the reflection features from an illuminating power-law continuum (from Reynolds 1996).

1.3.2 Reflection

A proportion of the Comptonised emission is likely to be down-scattered and intercept the cold, optically thick disc material with the resulting interaction imprinting atomic features onto the continuum. The review of Fabian et al. (2000) explains this process in great detail. In the simplest case we consider a semi-infinite slab of cold gas such that the metal population is neutral but H and He are mostly ionised. Hard X-ray photons entering the slab may undergo further Compton scattering and may leave the slab, may be destroyed by Auger de-excitation or be re-processed into a fluorescent line photon. The summation of these processes is a reflection spectrum which is super-imposed onto the power-law continuum and contains a pronounced 'hump' from Compton scattering of hard X-rays (Guilbert & Rees 1988; Ferland & Rees 1988; George & Fabian 1991; Reynolds & Fabian 1997; Matt et al. 1991) and

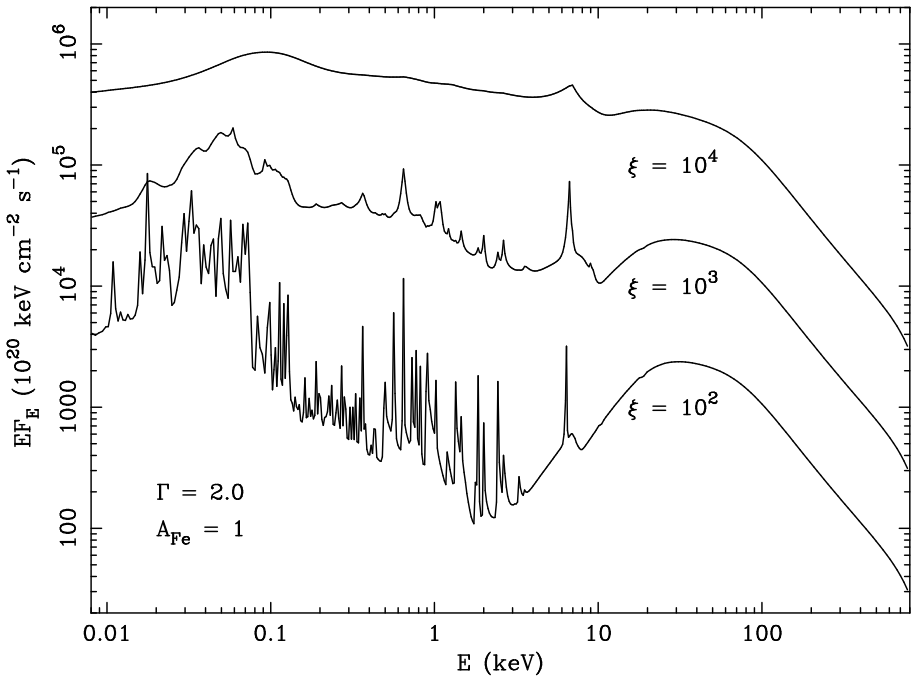

Figure 1.11: Reflection of an illuminating Γ=2 power-law from material of solar abundance for three differing ionisation parameters.

photo-electric features. The emission line spectrum contains primarily fluorescent Kα lines of the most abundant metals with the Iron feature being the strongest. The signature features of reflection therefore, are the Iron Kα line and spectral flattening as the Compton hump emerges at $\sim$ 10 keV. Figure 1.10 shows Monte Carlo simulations of these processes between 0.6 and 50 keV (Reynolds 1996).

The relative strength of reflected to incident spectrum is heavily dependent upon the viewing and illuminating angles (Ghisellini et al. 1994; George & Fabian 1991; Matt et al. 1997) with the shape of the spectrum being determined by the ionisation structure and elemental abundance of the upper layers of the disc (see Ross & Fabian 1993 for a quantitative description). This dependence upon ionisation state is shown in fig 1.11 (Ross & Fabian 2005).

As with absorption, the reflection features can suffer distortion by kinematic and

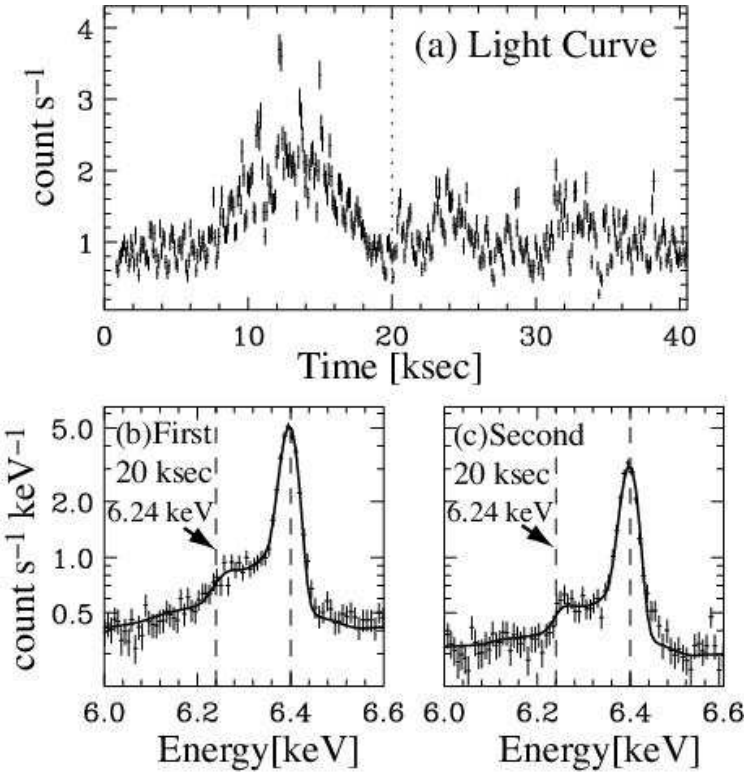

Figure 1.12: The Iron line profiles visible in the lightcurve of GX301-2 where the 'Compton shoulder' has been clearly resolved (from Watanabe et al. 2003).

radiative effects. In particular, further Compton down scattering of the emission can shift the photon energy by ∼80eV which is comparable to the instrumental resolution and can lead to the development of a 'Compton shoulder' at energies below the central line energy (fig 1.12).

As shown in fig 1.13, if the reflecting gas has relativistic velocities then the red peak of spectral lines are suppressed by relativistic aberration and conversely the blue peak is boosted. If this material is in close proximity to the black hole then gravitational red-shifting and time dilation redistributes line photons to lower energies dependent upon the radial location of the gas, together with a Doppler shift of comparable magnitude. Where the emission is from a disc, gravitational

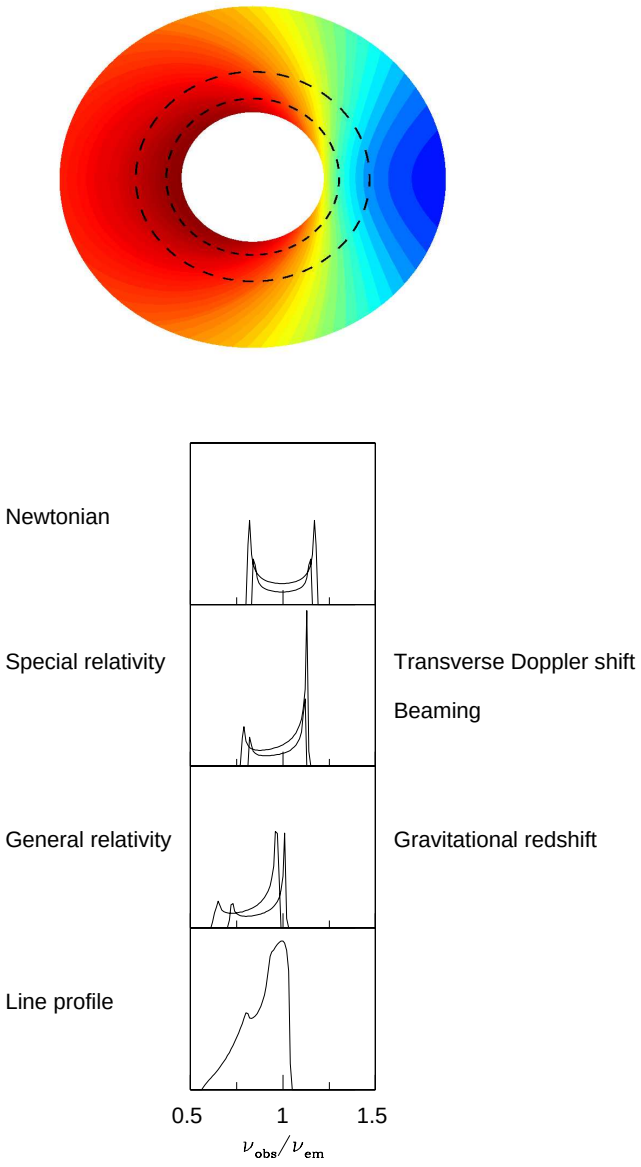

Figure 1.13: The possible distorting effects on an emission line profile from a disc in several regimes. The 'double-horned' profile (Newtonian) can be seen with increasing distortion as Doppler effects are applied (from Fabian et al. 2000).

light bending can also have a huge distorting effect if viewed at large inclination angles.

Chapter 2

Introduction to: Black hole X-ray Binaries

In this section I will describe the smaller of the two black-hole systems, the black-hole X-ray binaries (BHXRBs).

Given that up to 50% of stars are members of binary systems it is likely that, in certain instances, these systems will remain gravitationally bound following one of the stars undergoing supernova. In this case the system comprises a stellar mass black hole and a visible star and, if it emits radiation in the X-rays due to accretion, is termed an X-ray binary.

The general classification of these systems is dependent only upon the secondary, with the compact object being either a black hole or neutron star. A low-mass X-ray binary (LMXB) has a low mass secondary star. The only way this can transfer matter to the compact object is through the inner Lagrange point (semi-detached). This can occur through angular momentum loss in the final stages of evolution to the compact object or via expansion of the secondary as it evolves from the main sequence to giant branch.

Where the secondary is an O or B type, a Be type or supergiant star, the system is a high mass X-ray binary (HMXB). In these systems a proportion of the stellar wind from the massive star contributes to the accreting matter and X-ray production.

The manner in which we observe these systems has been revolutionised by the advent of the new generation of X-ray satellites which have provided far improved spectral and timing resolution together with optical and high-energy detectors and

on-board spectrometers.

In the following chapter I will review the energetics and introduce physical concepts that have a direct effect upon the way we view and analyse these exciting systems.

2.1 The disc revisited

The description of the accretion disc in section 1.1 provided a global solution, i.e. it made the *ad hoc* assumption that the mass accretion rate through the disc was constant with radius. This is not generally true and, as a result, the disc is no longer in a steady state (see e.g. the reviews of Done, Gierliński & Kubota 2007 and Lasota 2001).

The Hydrogen Ionisation instability

Discs may be thermally and/or viscously unstable. The former occurs when a small increase in temperature leads to a further rise in temperature with the overall perturbation growing on timescales $t_{ther} \sim \alpha^{-1} t_{dyn}$. The latter occurs when an increase in mass accretion rate leads to a larger increase so that the disc is eaten away at that given radius, occurring on timescales $t_{visc} \sim \alpha^{-1}(H/R)^{-2} t_{dyn}$ where H is the vertical scale of the disc at radius R and the dynamical (orbital) timescale for a Schwarzchild black hole of mass m is:

$$t_{dyn} = 4.5(\frac{m}{10})(\frac{r}{6})^{3/2} ms \tag{2.1}$$

At low mass accretion rates, a Shakura-Sunyaev alpha disc is both thermally and viscously unstable at temperatures around the ionisation of Hydrogen (10^{4-5}K). Below this temperature, the material is mostly neutral. A small increase in temperature however means that the highest energy photons at the end of the Wien distribution

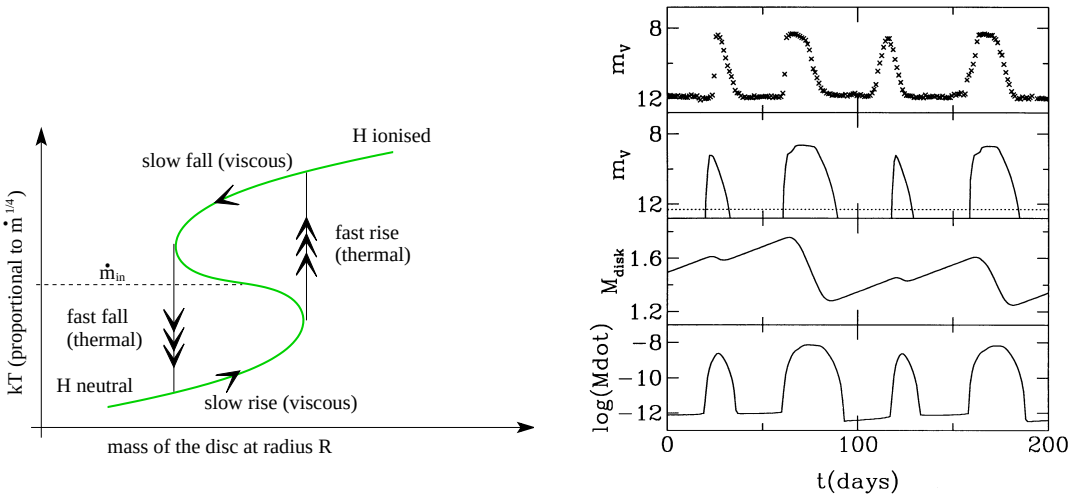

Figure 2.1: Left: The heating track for the Hydrogen ionisation instability showing how the viscous and thermal instabilities in a standard Shakura-Sunyaev disc can cause the disc to empty and refill on the viscous timescale. Right: The theoretical result for the instability which is a good match to the observed lightcurves of dwarf novae. From Cannizzo (1993).

may begin to ionise some of the Hydrogen. As these photons are absorbed, the disc temperature increases which in turn increases the fraction of photons that can ionise Hydrogen. This creates a runaway process until all the Hydrogen is almost completely ionised (Frank, King & Raine 2002; Kato, Fukue & Mineshige 1998).

In the Shakura-Sunyaev alpha disc scenario, the viscous stresses that remove angular momentum are proportional to the pressure and thus depend on the temperature. As such, the increase in temperature from the thermal instability drives an increase in mass-accretion rate through the disc at this point, so the disc is eaten away at that radius. However, this leads to a drop in pressure so the heating drops accordingly until the ionised Hydrogen recombines. This triggers the thermal instability but with runaway cooling until the Hydrogen is mostly neutral. The low temperature results in a lower mass accretion rate so the disc builds up again (Frank,

King & Raine 2002; Kato, Fukue & Mineshige 1998). This instability is shown in figure 2.1a (from Done, Gierliński & Kubota 2007) where the disc temperature and hence mass accretion rate jump discontinuously at a given radius.

This local instability will affect the rest of the disc structure if the mass accretion rate changes between annuli are large enough. The global effect is a limit-cycle between the Shakura-Sunyaev disc with larger mass accretion rate ($\dot{M}$) than mass transfer from the companion ($\dot{M}_{trans}$) such that the whole disc is eaten away on the viscous timescale, to a quiescent disc where Hydrogen is mostly neutral everywhere (fig 2.1b from Cannizzo 1993). This quiescent disc does not have a constant mass accretion rate at all radii and, as such, is unlike that described by the Shakura-Sunyaev equations. Instead, it has a more or less constant temperature and decreasing mass accretion rate with radius (see the review of Lasota et al. 2001).

This limit-cycle model can explain the alternating periods of outburst and quiescence seen in the lightcurves of the dwarf novae subclass of disc accreting, white dwarfs (cataclysmic variables) but the exponential decay seen in the lightcurves of BHXRBs (fig 2.2) requires modification to the model. The difference lies in the highly luminous inner disc which results in irradiation which keeps the disc hot at even large radii (van Paradijs 1996). This irradiation may keep the disc on the hot branch (see fig 2.1), preventing the Hydrogen from recombining. Thus the disc is eaten away as $\dot{M} > \dot{M}_{trans}$ which lowers the temperature, mass accretion rate and X-ray irradiation. If the whole disc is irradiated this can provide the exponential decay (King & Ritter 1998). However, eventually this irradiation weakens to the point that the outer disc temperature drops below that needed for Hydrogen ionisation and the system switches to the cool branch (fig 2.1). The viscous timescale no longer represents the time taken for the disc to cool, as the innermost radial extent is set by the radius of the irradiated region. This has the effect of modifying the decay to a linear profile (King & Ritter 1998; Lasota 2001). Given that we observe the

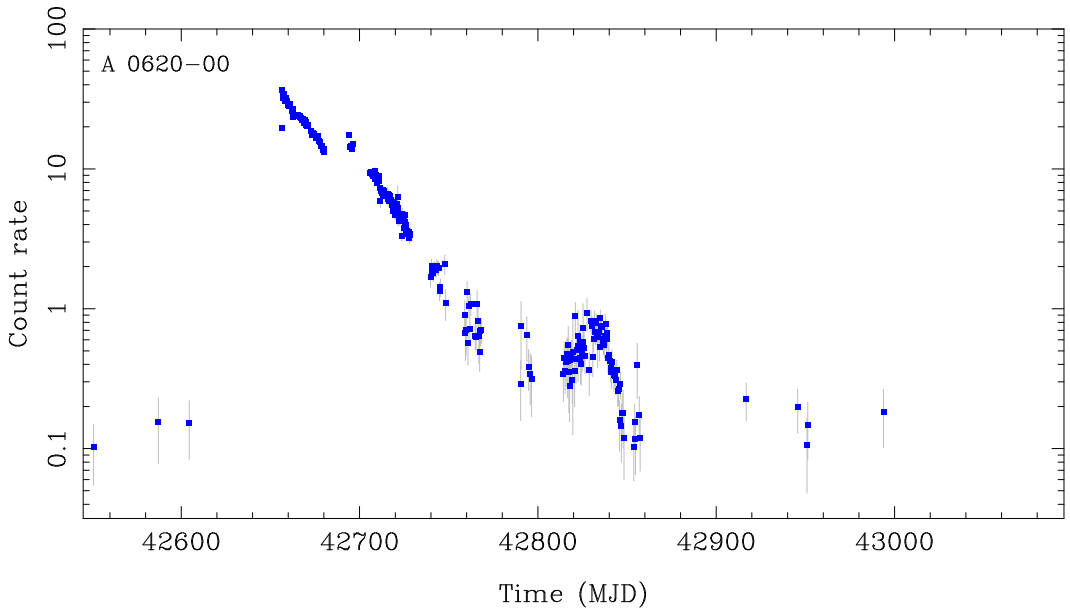

Figure 2.2: The lightcurve of BHXRB, A 0620–00 from the Ariel V all sky monitor. This clearly demonstrates a fast rise as expected from the Hydrogen ionisation instability. Irradiation from the inner disc prevents a return to quiescence, creating an exponential decay as the irradiation is strong enough to keep the temperature of the disc above that needed for the re-combination of Hydrogen. This is followed by linear decay as the size of the region decreases (King & Ritter 1998).

predicted decay profiles, this strongly supports these models of an irradiated disc, as do the optical spectra from these systems (van Paradijs & McClintock 1994). The many models of irradiated discs (e.g. Dubus et al. 1999, 2001; Lasota 2001) can also explain why the Roche lobe overflow HMXBs are seen to be 'persistent' sources, i.e. they show variability but not dramatic outbursts (e.g. Cyg X-1, LMC X-1 and X-3). As these have larger companion stars they typically have a higher $\dot{M}$ than a LMXB and as such have a higher outer disc temperature that more than compensates for the lower temperature expected from a larger disc due to the larger orbit. The outer edge of the disc therefore remains above the Hydrogen ionisation instability in HMXBs (van Paradijs 1996).

Whilst the match between disc theory and the observed lightcurves is highly suggestive of a Shakura-Sunyaev outer disc in these systems, many detailed features of the light curves remain unexplained. For example, the accretion rate through the disc can be variable even in the persistent systems while the outburst light curves of many transients can be much more complex than a simple linear or exponential decay. This variety of light curve behaviour may be explained by the interplay between the irradiation controlled Hydrogen ionisation instability and tidal instability and/or an enhanced mass accretion rate from the irradiated secondary (see the review by Lasota 2001).

Radiation instability

The Shakura-Sunyaev disc is also unstable at high mass accretion rates at small radii as there is a rapid increase in heating as the disc goes from being pressure dominated ($P_{gas} \propto T$) to radiation dominated ($P_{rad} \propto T^4$). It is easy to see that a small increase in temperature now results in a huge increase in radiation pressure and further heating as the stresses are assumed to be $\propto P_{tot}$. This increase is not balanced by a correspondingly large decrease in opacity that would allow increased

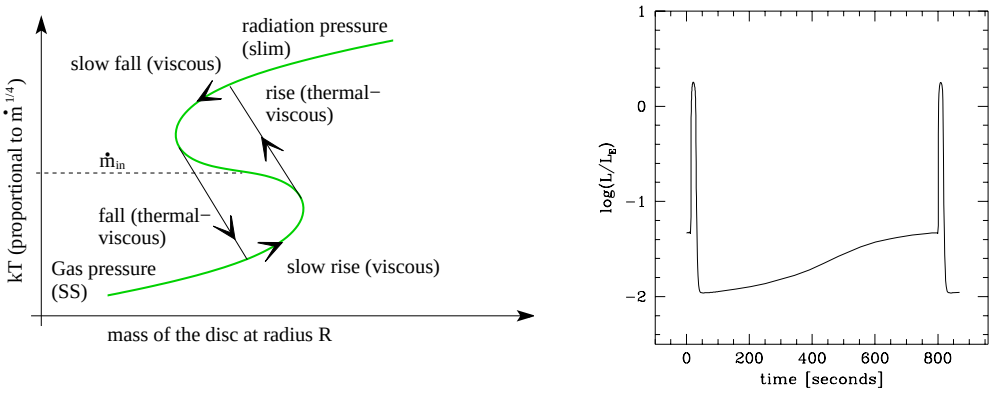

Figure 2.3: Left: The radiation pressure instability showing the mass accretion rate through the disc jumping discontinuously at a given radius. Right: The theoretical global result of this upon a Shakura-Sunyaev disc with $\alpha = 0.1$ and $L/L_{\rm Edd} = 0.06$. Note that no BHXRB has been observed to show behaviour that fits this shape at this luminosity (from Szuszkiewicz & Miller 2001)

cooling so there is runaway heating.

This high mass accretion rate, high temperature scenario would predict total disc collapse, however the inclusion of advection can lead to a stable solution. This allows some of the energy to be carried by the flow into the next annulus (Abramowicz et al. 1988). This creates a stable upper branch (fig 2.3) which can lead to a similar limit-cycle behaviour as for the Hydrogen ionisation instability. The radiation pressure instability should be present in a Shakura-Sunyaev disc at luminosities $\geq$0.06L$_{Edd}$ (Honma et al. 1991; Szuskiewicz & Miller 2001; Merloni & Nayakshin 2006) and the result should be dramatic changes visible in the lightcurve. However, BHXRBs are seen to be stable up to $\sim$0.7L$_{Edd}$ and so the Shakura-Sunyaev stress prescription must be wrong (Done & Davis 2008)! The famous source, GRS 1915+105, spends significant amounts of time at luminosities close to Eddington and *does* show some limit-cycle behaviour. It therefore seems likely that the stress scales somewhat

more slowly with temperature than predicted by radiation pressure but faster than predicted by gas pressure alone. Scaling the viscous stress to the geometric mean of gas and total pressure (Merloni 2003) gives a stable limit of $\sim 0.3 L_{Edd}$ with advection effects increasing this to $\sim 0.4 L_{Edd}$ (Honma et al. 1991; Merloni & Nayakshin 2006). A further small tweak in the prescription could probably produce a limit beyond $\sim 0.5 L_{Edd}$ as required (Done & Davis 2008), above which the onset of the radiation pressure instability can perhaps explain the unique limit-cycle variability seen in GRS 1915+105 (see the review of Fender & Belloni 2004).

2.2 Canonical spectral states

The Hydrogen ionisation instability can go some way to describing the long-term light curve behaviour in BHXRBs. The energy spectra of these systems however are not so easily explained. As described in section 1.1, the emission from the optically thick, geometrically thin disc has a robust, quasi-thermal shape and is subsequently Comptonised by a high-energy plasma possibly in the form of a corona, above and below the disc. This continuum can have reflection features imprinted onto it from down-scattering onto the cold disc with atomic features from Iron and a Compton hump above $\sim$10 keV.

Spectral states can be defined by the relative contributions of the disc and Compton components (not including reflection components) to the total emission and are shown in figure 2.4, plotted in $\nu f(\nu)$ so that the peak indicates the energy at which the source luminosity peaks. The high-soft state is dominated by the thermal disc emission with a non-thermal tail of hard emission extending to high energies. When the tail is extremely weak this state may be referred to as ultrasoft. Conversely, the low-hard state is dominated by the hard thermal-Comptonised component. Note that the nomenclature of 'low' and 'high' refers to the early analysis of these objects over a narrow bandpass where the flux was seen to change between states by

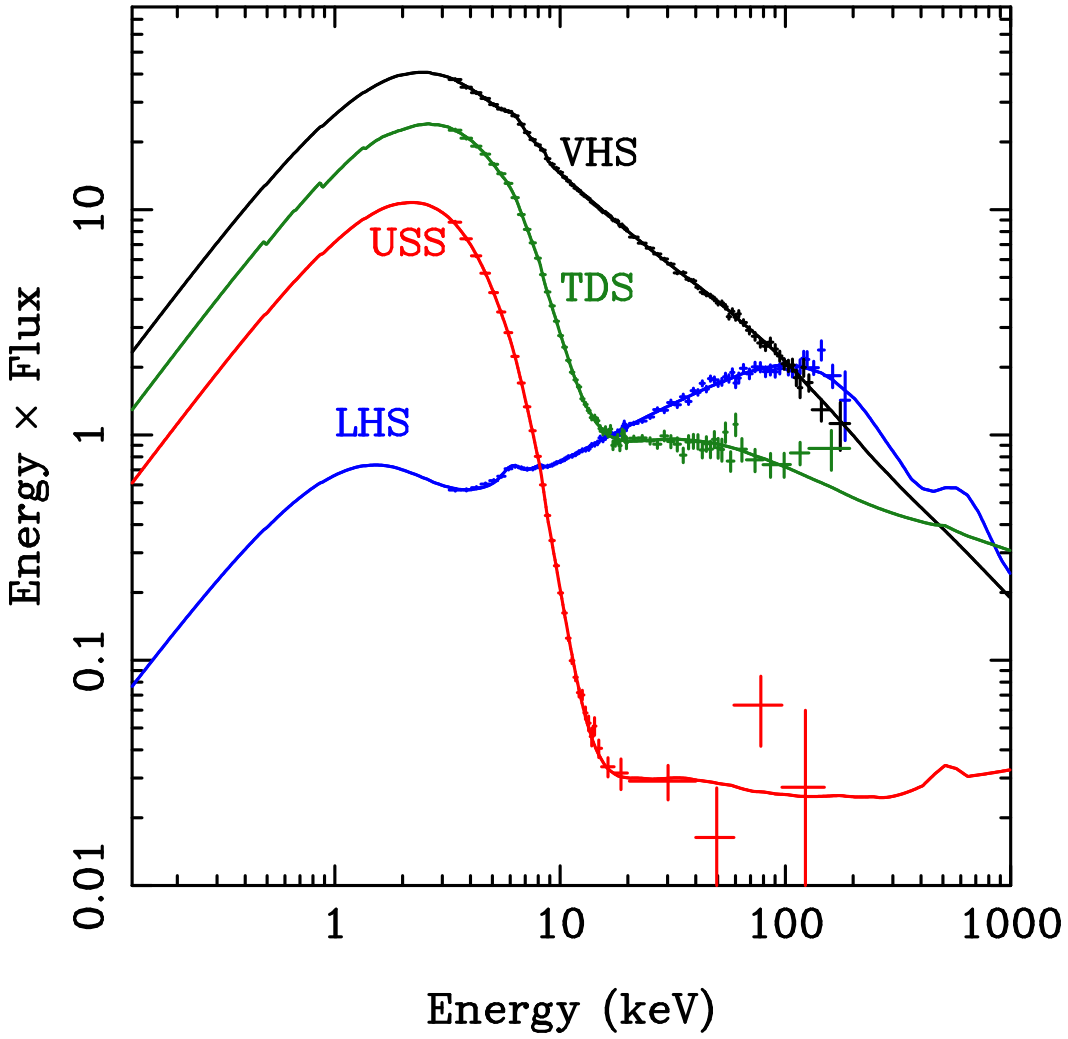

Figure 2.4: The various spectral states seen in the 2005 outburst of GRO J1655-40 which can be explained in terms of the truncated-disc, hot inner flow model. VHS: very high state, TDS: thermally dominant or high-soft state, USS: ultra-soft state and LHS: the low-hard state.

as much as a factor of ∼5, whereas the more accurate and descriptive 'soft' and 'hard' reflect the shape of the spectrum. An observation of a bright outburst of GX 339-4 (Miyamoto et al. 1991) identified spectra that appeared like the soft state, in that they peaked in $\nu f(\nu)$ at energies expected for the optically thick disc, but with very strong high-energy emission, and were subsequently termed the very-high state. Similar spectra but at lower luminosity, occurring during state transitions are referred to as intermediate-state.

Clearly the existence of multiple states requires a more complex model than a simple disc and corona. These can be understood if the accretion flow makes a transition to a hot, optically thin solution, such as an advection dominated accretion flow (ADAF: Narayan & Yi 1995). The accretion flow then emits by Comptonisation (along with Bremsstrahlung and cyclo-synchrotron) instead of a cool disc black-body.

Truncated disc model

Figure 2.5 demonstrates how the cool disc and hot inner flow can be put together to produce the different observed spectral states. To describe the balance between heating and cooling we use the ratio of energy density (parameterised by a compactness) between the electrons and soft, illuminating photons, l_h/l_s. In the low-hard state the inner, optically thick disc is replaced by a hot, optically thin flow, most probably via evaporation (Meyer & Meyer-Hoffmeister 1994; Różańska & Czerny 2000; Mayer & Pringle 2007). There are few seed photons illuminating the hot inner flow so Compton cooling of the electrons is not very strong and the electrons are hot. As a result, $l_h/l_s \gg 1$ which produces the hard thermal Comptonised spectra of the form $N(E) \propto E^{-\Gamma}$, with photon index $1.5 < \Gamma < 2$. As the mass accretion rate increases, this state becomes brighter, entering the hard intermediate state up to the point the flow becomes optically thick and collapses to a Shakura-Sunyaev disc (see the previous section). This marks the transition from the hard interme-

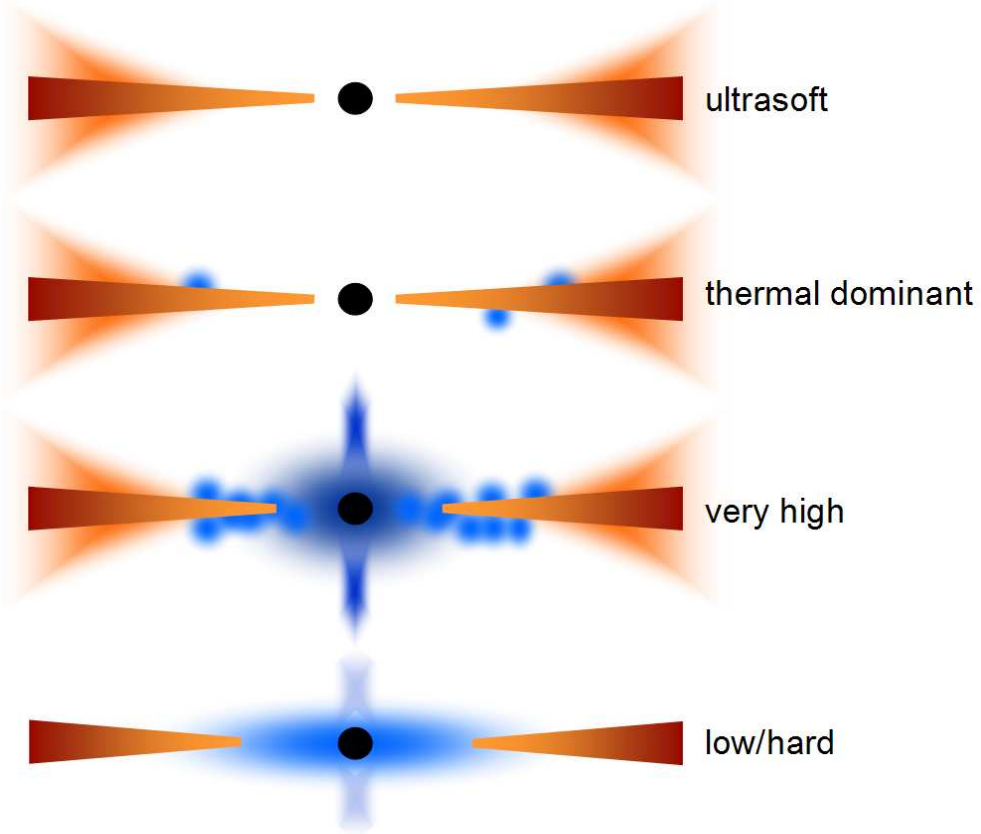

Figure 2.5: The proposed geometry of the truncated disc model which can, in turn, explain the various shapes of the energy and variability spectra. This includes the contributions by the disc, hot inner flow, jets, winds and active regions above and below the disc (Done, Gierliński & Kubota 2007).

diate state to the soft intermediate state (Esin et al. 1997; Poutanen et al. 1997). Any electrons which gain energy above this optically thick material (in some sort of corona, possibly formed by re-connection of magnetic flux tubes - Galeev, Rosner, & Vaiana 1979) have $l_h/l_s \leq 1$ and so the Comptonised spectra are much softer, roughly characterised by a power law of index $\Gamma \geq 2$ and are very bright (similar to the very-high state).

In the very high state the disc is predicted to extend further inwards but with a hot inner flow reprocessing the seed photons, together with electrons above the optically thick material. When the disc extends down to the spin-dependent LSO, with very little in the way of Comptonising electrons to reprocess this quasi-thermal emission, the system is in the ultrasoft state.

The accretion structure is understood at some level as the observed, disc dominated spectra are close to the expectations of an optically thick, geometrically thin disc. This allows the disc spectra to be used to probe the dramatically curved spacetime in the vicinity of the black hole as the LSO gives a clear inner edge to the disc and can provide an observational diagnostic of the spin from the observed temperature and luminosity of the disc spectrum (Ebisawa et al. 1991, 1993; Kubota et al. 2001; Kubota & Makashima 2004; Kubota & Done 2004; Gierliński & Done 2004; Middleton, Done & Gierliński 2007, Kolehmainen & Done 2009).

Spectral evolution

It is possible to observe the spectral evolution of multiple BHXRBs using a colour-colour diagram. This relies on obtaining the absorption corrected fluxes from physically motivated models which fit the data well, and determining the ratio between certain energy bands such that there is a soft colour and hard colour. Many BHXRBs can then be plotted together (e.g. Done & Gierliński 2003) with the paths on the diagram describing the spectral evolution of a particular source. Done & Gierliński

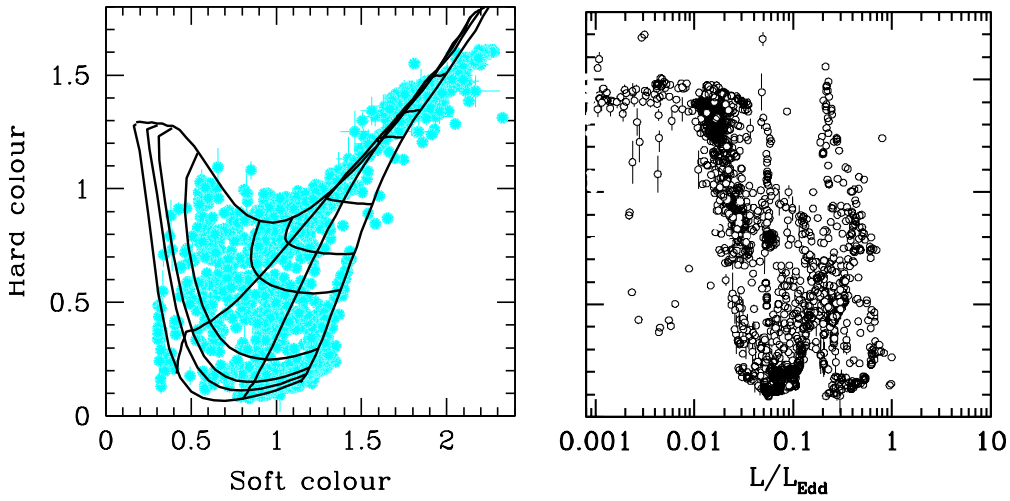

Figure 2.6: Left: The colour-colour diagram made from the ratios of model dependent fluxes in soft and hard energy bands. The black lines show the predicted bounds from the truncated disc model. Right: Hard colours versus L/L_{Edd} which shows that the spectral states are non-unique with luminosity (Done, Gierliński & Kubota 2007).

(2003) found that *all* black holes are consistent with the same track in the colour-colour diagrams which can be explained by the truncated disc model. However, figure 2.6 shows that this evolution does not uniquely correlate with mass accretion rate (hereafter L/L_{Edd}), as many different spectral states are observed at any particular L/L_{Edd}. As the same BHXRB can show this feature it is clearly not dependent upon mass or distance to the source. This is the hysteresis effect (see Nowak 1995) and occurs for all BHXRBs except for Cyg X-1 (see Maccarone & Coppi 2003). As this effect is only seen in transients it probably has its origins in a non-equilibrium effect (Gladstone et al. 2007).

2.3 Timing properties

Clearly the spectral states change with time, as such, variability analysis can allow us to infer the physical state of the system.

2.3.1 Power spectra

The power density spectrum (PDS) describes how the power of a time series, such as a light curve, varies in frequency. The method and complexities of extracting this are discussed in depth by Vaughan et al. (2003).

The PDS of BHXRBs are plotted in $\nu P(\nu)$ to show equal variability power-per-decade in frequency and are generally well described as band limited noise with a 'flat top' i.e. $P(\nu) \propto \nu^{-1}$. This extends between a low frequency break, ν_b, below which the PDS is $P(\nu) \propto \nu^0$, and a high frequency break, ν_l, above which the spectrum steepens to $P(\nu) \propto \nu^{-2}$.

With the launch of RXTE, excellent timing data became available for BHXRBs. The resulting power spectra showed 'elbows', forming an intrinsically bumpy shape which were well fit by multiple Lorentzians, where the peak frequency, width and normalisation are free to vary (Belloni, Psaltis & van der Klis 2002, Nowak 2000). Each Lorentzian is given by:

$$P(\nu) = \frac{r^2\Delta}{\pi}\frac{1}{\Delta^2 + (\nu - \nu_0)^2} \tag{2.2}$$

where r is the integrated (-$\infty \rightarrow +\infty$) fractional rms of each Lorentzian, Δ its HWHM and ν_0 its centroid frequency. The components are usually described by their 'characteristic' frequency, i.e. where the Lorentzian peaks in $\nu P(\nu)$:

$$\nu_{max} = \sqrt{\nu_0^2 + \Delta^2} = \nu_0\sqrt{1 + \frac{1}{4Q^2}} \tag{2.3}$$

where Q$\equiv \nu_0/2\Delta$ and is a measure of the coherence of the signal.

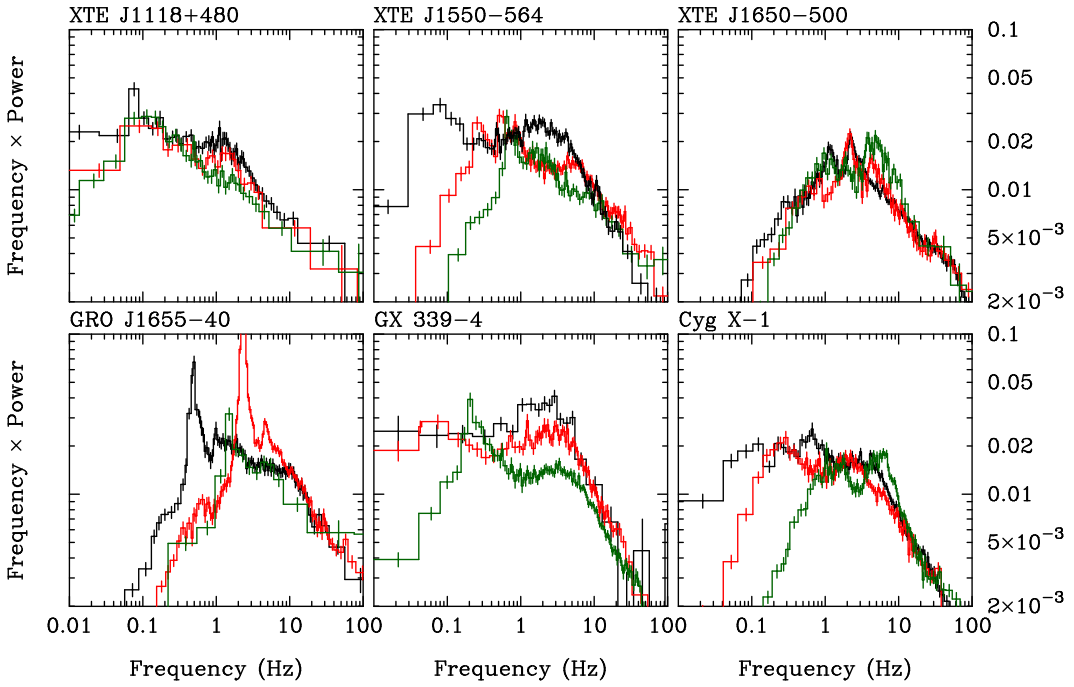

Figure 2.7: The power spectra of several BHXRBs in the low-hard state over different observations. Although the coherence and significance varies between sources, the LFQPO is seen throughout (from Gierliński et al. 2007).

Using this method of describing the broad-band shape, the 'flat-top' of the power spectrum is made from 2-3 Lorentzians of roughly equal power, producing the observed broad peak in $\nu P(\nu)$ between ν_b and ν_l. In addition to these broad Lorentzians, narrow components are needed to explain the presence of peaks in the power spectrum. These are a result of quasi-periodic oscillations (QPOs) in the lightcurve occurring across a large range in frequency. For example, fig 2.7 shows the low frequency QPO which is seen in all observations of the low-hard state at slightly different frequencies.

The truncated disc model can explain the broad-band power spectral shape as it naturally predicts certain characteristic frequencies. The lowest characteristic frequency should be the viscous timescale of the inner edge of the disc, which can

naturally act as a low-pass filter and suppress any faster fluctuations in the mass accretion rate through the disc (Psaltis & Norman 2000; Churazov et al. 2001). This predicts that $\nu_b \sim \nu_{visc}$, which, from equation 2.1 for a black hole of mass $m/M_\odot$ and $H/R \sim \alpha \sim 0.1$, gives:

$$\nu_b \sim 0.2(\frac{r}{6})^{-3/2}(\frac{m}{10})^{-1}Hz \tag{2.4}$$

This predicts that, as the state transits from hard to soft and r decreases from 20 to $6r_g$ that ν_b takes values from 0.03 to 0.2Hz as observed (Ingram & Done 2009).

The truncated disc model also implies that whatever fluctuations are produced at the truncation radius have to propagate down through the hot flow and, as such, the emission at small radii is modulated by variability produced at larger radii. In particular, the viscous timescale of the inner edge of the hot flow can act as a further low pass filter at ν_{max}. The *observed* power spectrum is then the power spectrum of the fluctuations multiplied by the spectrum of this low-pass filter which forms a high frequency barrier at ν_{max}. The prediction of these models is that, as the spectrum softens as the disc moves inwards, we should see all the characteristic frequencies increase but those faster than the viscous timescale at the inner radius of the hot flow are strongly damped. As each Lorentzian component approaches ν_{max} the high frequency edge is trimmed making it asymmetric and, as the peak moves through ν_{max}, the variability power is strongly suppressed. This explains how the power at high frequencies stays remarkably constant as can be seen for the BHXRBs in fig 2.7. The truncated disc model can therefore fully explain the evolution of the PDS as is shown in figure 2.8 for Cyg X-1 (see Done, Gierliński & Kubota 2007; Arévalo & Uttley 2006; Kotov et al. 2001 for a more detailed explanation of the fluctuations).

The shifting frequency of the observed low frequency QPO shown in figure 2.7, requires a more detailed understanding of what these complex signals represent.

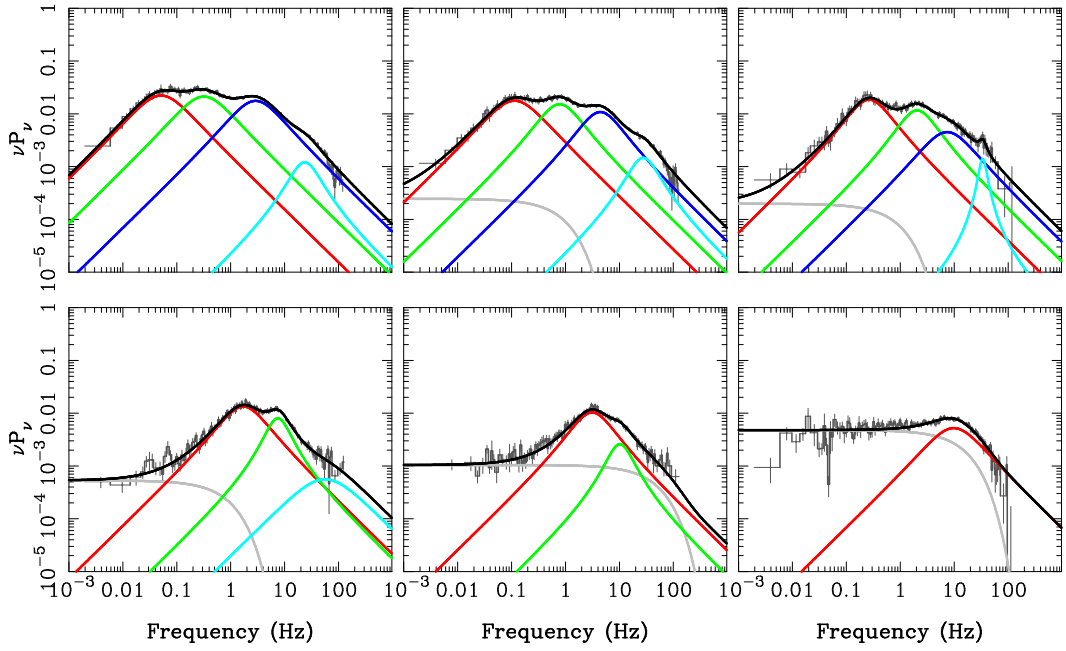

Figure 2.8: The evolution of the power spectrum of Cyg X-1 as it transits from the low-hard to high-soft state, fitted with multiple Lorentzians to describe the broad-band noise and respective breaks. As the characteristic frequencies increase (and do so together) the upper edge is suppressed by the low-pass filter of the inner edge of the hot flow. The additional component in grey is not seen in transient BHXRBs (from Done et al. 2007).

The low frequency QPOs

The low frequency QPOs (LFQPOs) can be subdivided into 3 separate classes dependent upon their coherence, fractional power and corresponding spectral state. These are called the type A, B and C LFQPOs respectively (not to be confused with a similar nomenclature used by Belloni et al. 1996 to describe the spectral states of GRS 1915+105) and are seen to appear in the sequence C, B, A, as the system progresses from the low-hard state through to the high-soft state.

The type C LFQPO, shown in the power spectra of a number of BHXRBs in figure 2.7, is almost always present in the low-hard state (Gierliński, Nikołajuk & Czerny 2008; Revnivtsev, Gilfanov, & Churazov 2000) and is thus known as the ubiquitous QPO (see also fig 2.9 although note that the type C LFQPO in this figure is made from co-added observations and is artificially broad). It has frequency which increases between $\sim$ 0.01-6 Hz as the spectrum softens from a dim, harder, low-hard state to a bright, softer low-hard state, through to the hard intermediate state (Belloni et al. 2005). There is a correlated increase in strength, coherence and harmonic structure of the QPO (van der Klis 2004; Remillard & McClintock 2006) together with a correlation to the shape of the underlying broad-band power spectrum. The latter is seen as the low frequency break, ν_b, increases together with the LFQPO frequency such that $\nu_{LFQPO} \sim 5\nu_b$ (Psaltis et al. 1999; Wijnands & van der Klis 1999).

The prevalent nature of this QPO has led to attempts to correlate characteristic frequencies with physical parameters (see Rodriguez et al. 2002). Current speculation favours either an origin through Lense-Thirring precession (Ingram, Done & Fragile 2009) or via the accretion-ejection instability (Tagger & Pellat 1999) which might form a rotating spiral structure in the disc driven by magnetic stresses. The latter could create a 'hot-spot' due to the gas being heated and compressed which results in the periodic signal. This model naturally predicts the harmonics to be a

result of the non-linear behaviour of the spiral (Rodriguez et al. 2002).

The truncated disc model provides an explanation for the *behaviour* of the type C LFQPO. As the source softens from the low-hard state, the moving inner radius means that the section of the hot flow which is unconstrained by the disc gets smaller so increasing all its characteristic variability frequencies, while the smaller radial extent means the QPO can become stronger and more coherent.

As the spectrum transits from the hard intermediate state, showing the strongest type C LFQPO, to the soft state, the broad-band power collapses and the QPO (and related harmonics) is seen with increased prominence, as shown in fig 2.9 for XTE J1550-564 (Belloni et al. 2005). This is termed the type B LFQPO and is seen over a much narrower frequency range ($\sim$5-6Hz).

As the spectrum continues to soften in the soft intermediate state, the QPO is now above much lower continuum noise (fig 2.9) and is termed type A. This is usually weaker ($Q \leq 3$) and much broader (so there is no harmonic structure discernible) than a type B LFQPO, but appears at similar frequencies. As the spectrum continues to soften into a completely disc dominated state the QPOs disappear altogether (Remillard & McClintock 2006; Casella et al. 2005).

The high frequency QPOs

Transient high-frequency QPOs (HFQPOs) are detected in several BHXRBs (see fig 2.10) and appear to be constant in frequency despite changes in luminosity by a factor of 3-8 and may therefore represent a stable signature of the accretion system. They are often seen in 3:2 ratio, implying that some sort of resonance sets the frequencies, but the exact nature of this resonance is yet to be clearly determined (Abramowicz & Kluzniak 2001; Kluzniak et al. 2004; Török et al. 2005; Kato et al. 2004; Rezzolla et al. 2003; Fragile et al. 2005).

When these QPOs appear together with LFQPOs the coherence appears to

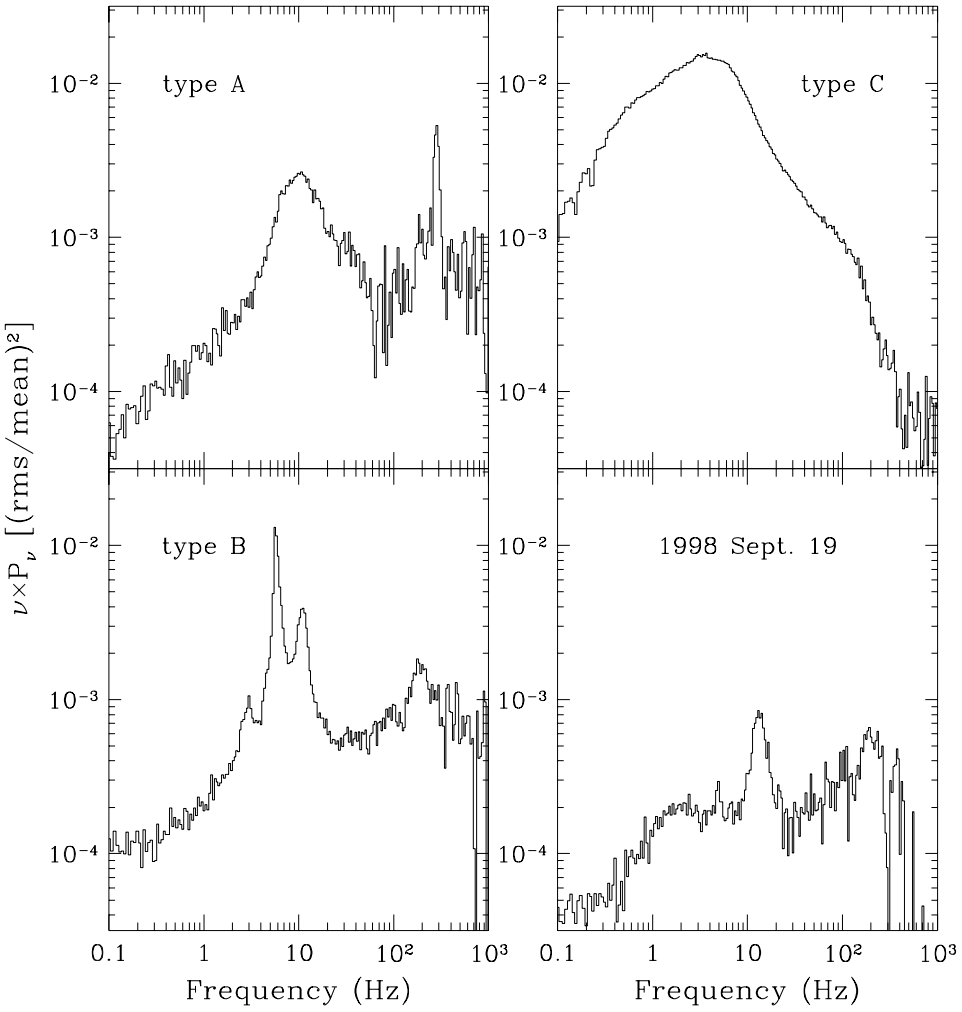

Figure 2.9: The power spectra of XTE J1550-564 in different spectral states (from Remillard et al. 2002) showing the evolution of the variability and associated LFQPOs; from type C (which appears artificially broad due to co-adding many characteristic frequencies) over a powerful noise spectrum to the state softening and the noise collapsing to show the QPO at higher significance (type A and B).

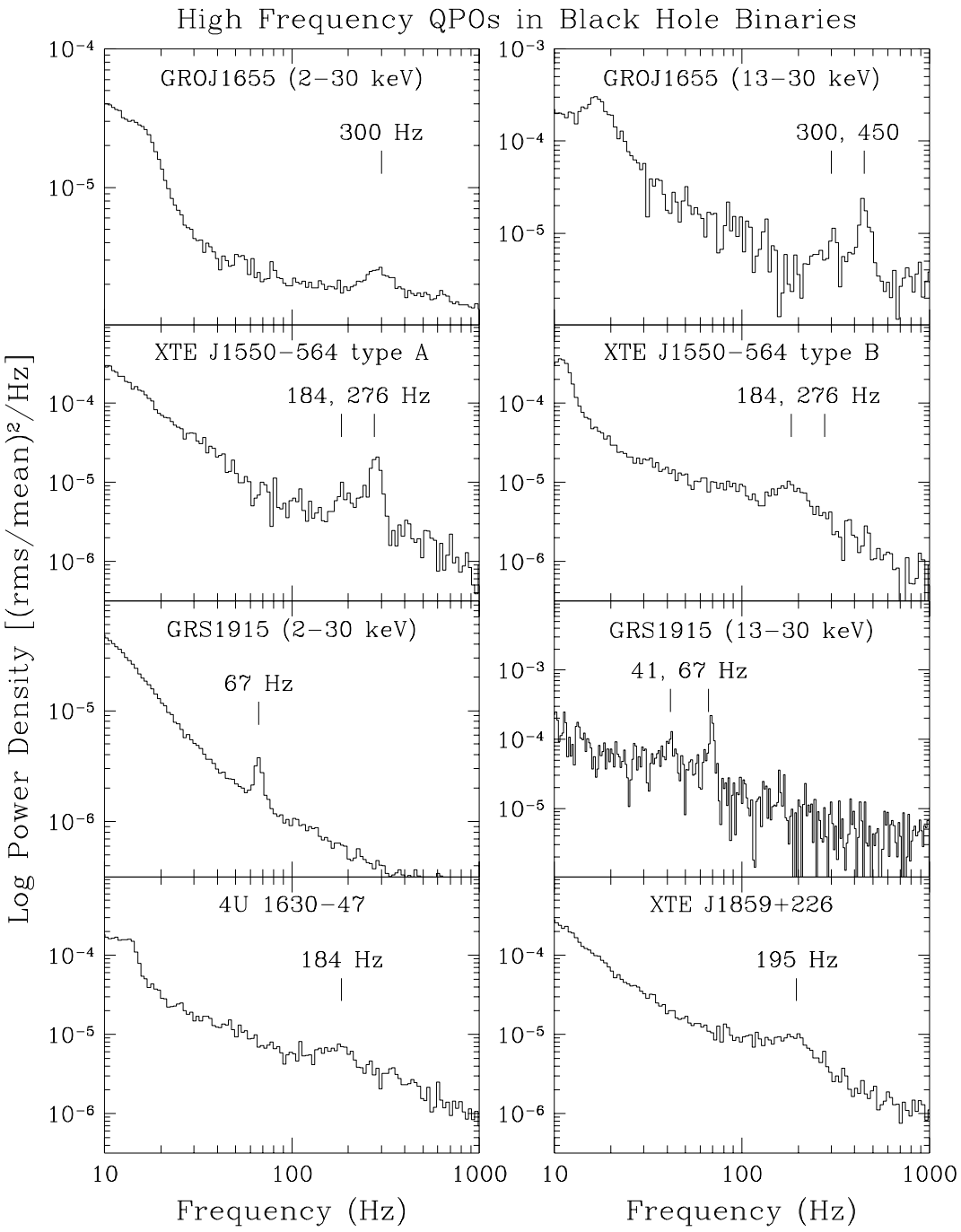

Figure 2.10: The power spectra of several sources showing a variety of HFQPOs. The spectra are created from lightcurves in the 6-30 keV energy band unless otherwise indicated (from Remillard et al. 2003).

change with the type of companion signal. In the low-hard state showing the type C LFQPO, the red noise is strong and steep (fig 2.9) and no HFQPOs appear, however, when the broad-band noise collapses as the energy spectrum softens (i.e. when the type A and B LFQPO are seen - fig 2.9) the HFQPOs are detected. These are seen above a much flatter spectrum, with those associated with the type A LFQPO having a greater coherence (Remillard et al. 2002), see fig 2.10.

RMS spectra

Another useful weapon in the timing analysis arsenal is the RMS spectrum which utilises the value of the fractional variability amplitude, F_{var} (e.g. Vaughan et al. 2003; Edelson et al. 2002; Markowitz, Edelson & Vaughan 2003). This quantifies the intrinsic variability amplitude relative to the mean count rate in excess of the measurement noise in the light curve:

$$F_{var} = \sqrt{\frac{S^2 - < \sigma_{err}^2 >}{< X >^2}} \tag{2.5}$$

where S^2 is the total variance of the lightcurve, $< \sigma_{err}^2 >$ is the mean square error and $< X >$ is the mean count rate of N total points.

By splitting the lightcurve into a number of energy bins it becomes possible, together with time-averaged spectrometry, to determine which component is varying, allowing important physical constraints to be placed. For example, it has been discovered that, in general, BHXRBs at high mass accretion rates, which are usually in the very high state or high-soft state, have stable discs. This suppresses/dilutes the variability of the hard Compton component at soft energies (Churazov, Gilfanov, Revnivtsev 2001), visible in the RMS spectrum. An example of this is given in figure 2.11 for the BHXRB XTE J1550-564.

A particular use of RMS spectra is the analysis of the QPO spectrum from which it becomes possible to determine an origin. For example, Morgan, Remillard

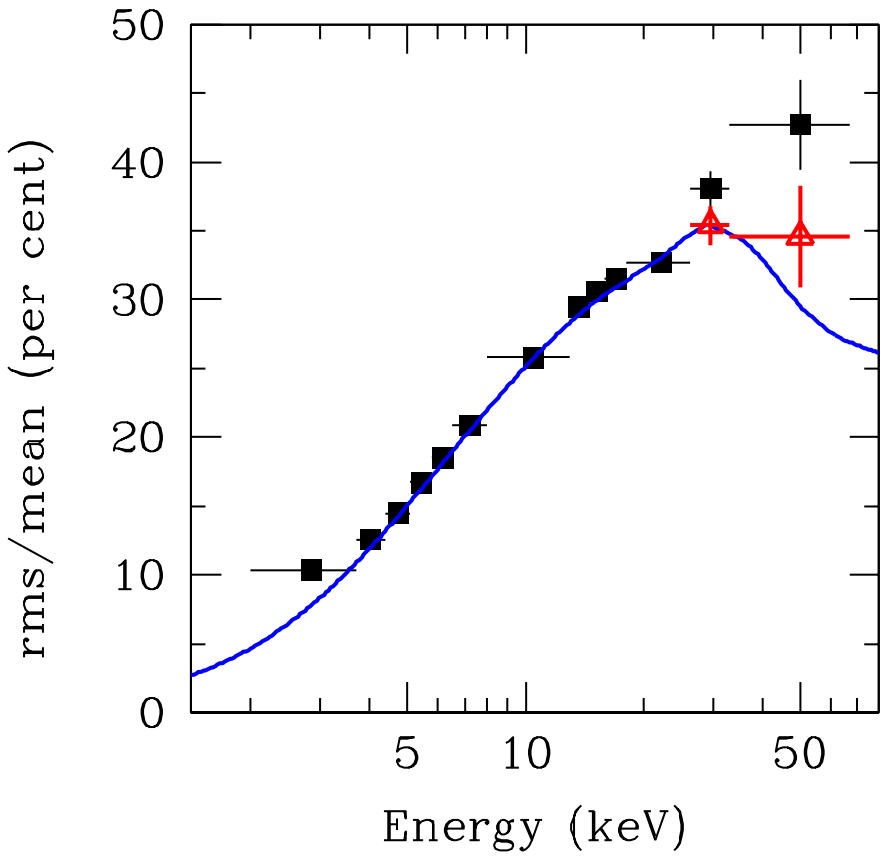

Figure 2.11: RMS spectrum of XTE J1550-564 from Gierliński & Zdziarski (2005), showing a shape consistent with a variable hard component and stable disc which dilutes the variability at soft energies.

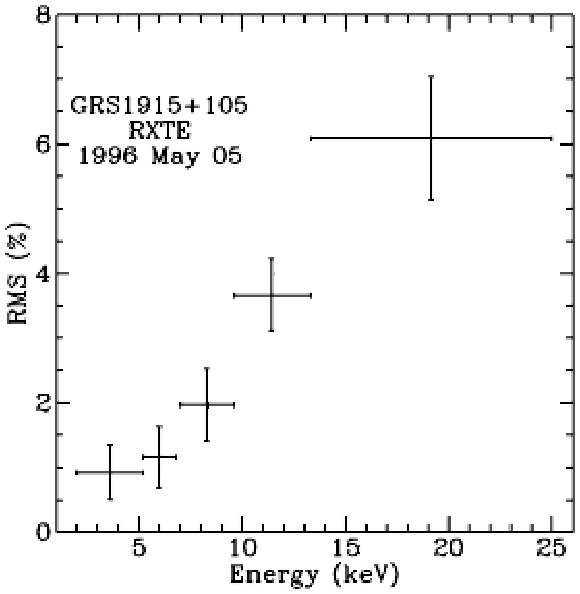

Figure 2.12: RMS spectrum of the 67Hz QPO in GRS 1915+105 from Morgan & Remillard (1997). The increase in RMS with energy suggests that the QPO has its origin in a hard spectral component.

& Greiner (1997) show the RMS spectrum of the 67Hz QPO in GRS 1915+105 (fig 2.12) which demonstrates an increase in fractional variability amplitude with energy. This indicates an origin in a hard spectral component such as thermal Comptonisation in the hot inner flow, consistent with the source energy spectra being in the very-high state.

2.4 Eddington and beyond

Whilst the previous sections can explain the spectral and timing properties in the context of a single model, we must take into account changes that occur to the disc

structure at higher mass accretion rates.

Certain BHXRBs with L/L_{Edd} >0.5 have been known to exhibit absorption lines for highly ionised elements, most often He- and H-like Fe, their energies often indicating that the ionised material is outflowing (e.g. Ueda et al. 2004; Miller et al. 2006). These lines are ubiquitously seen from high inclination objects in the high-soft state and their strength suggests that the absorbing material is in the form of a wind, driven from the accretion disc and then photo-ionised by emission from the innermost accretion flow. There are three ways that a wind can be driven and these are described below.

Radiation-driven winds

As the accretion rate approaches Eddington, the radiation pressure in electrons becomes dynamically important. This can become even more important if the line opacity increases the interaction cross-section between the matter and radiation. As there are multiple line transitions in the UV region of the spectrum, a UV disc can drive a powerful wind even well below Eddington. However the disc temperature is too high in BHXRBs and so UV line-driven winds are unlikely (Proga & Kallman 2002), so radiation driving only becomes important around L_{Edd}.

Thermally-driven winds

The central accreting region will illuminate and heat the upper layers of the disc (as described by Begelman et al. 1983). These layers will expand due to the pressure gradient and at large radii the thermal energy is greater than the binding energy and so an outflow is formed in the outer disc, though at smaller radii this instead forms a static corona. For an inclination angle of 70°, at even moderate luminosities (L/L_{Edd} ∼0.3), a wind with a column density of $\sim 3 \times 10^{23} cm^{-2}$ and outflow velocity of $720 kms^{-1}$ can be created by this mechanism and an even more powerful wind

can be formed at higher luminosities by the inclusion of radiation pressure (Proga & Kallman 2002).

Magnetically-driven winds

Simulations involving the complex and poorly understood MHD turbulence can also produce winds and jets (e.g. Balbus 2005). More specifically, Proga (2000; 2003) perform calculations involving a geometrically thin disc and determine that the mass loss rate depends on the external field geometry, although winds can be substantially enhanced and launched from any disc radius. Whilst we certainly expect the magnetic field of the flow to play an important part in accretion and mass outflow, we cannot as yet predict its properties. Thus magnetic driving is only required if all other wind formation mechanisms are ruled out. It is likely, however, that this is the explanation for the Chandra observation of GRO J1655-40 (Miller 2006) which suggests that the launching radius is smaller than can be produced by a thermal wind.

Super-Eddington flows

Although the theoretical limit for spherical accretion is Eddington, a disc may not need to obey this limit. Indeed, a number of BHXRB sources are seen to exhibit luminosities in excess of this, including V404 Cyg and V4641 Sgr near the peak of their outbursts together with GRS 1915+105 and the HMXB SS433 (seen to accrete at hyper-Eddington rates: Begelman et al. 2006; Poutanen et al. 2007). The disc instability model predicts that the peak luminosity is proportional to the size of the disc and so systems with long orbital periods and large enough discs can potentially reach $L/L_{Edd}>1$. If this is reached, high mass accretion rate outflows can be launched from closer to the black hole (as the effective gravity goes as $1\text{-}L/L_{Edd}$) and mass loss may become important for the structure of the discs, though obviously not to the

point of preventing the source from accreting above Eddington. Good examples of this in action are V404 Cyg and V4641 Sgr in outburst at $L/L_{Edd} \sim$ 2-3 where ejected material is seen to completely obscure the source (Tanaka & Lewin 1995; Życki et al. 1999; Revnivtsev et al. 2002). Conversely however, GRS 1915+105 shows quasi-steady super-Eddington accretion with a limit-cycle (see section 2.1) which suggests a stable branch for $L \geq L_{Edd}$ possibly through optically thick advection, winds or cooling by the jet. Whichever method provides a cooling channel, the outflows will certainly alter the disc structure which will no longer be well described by the standard disc equations (with or without advection).

Chapter 3

Introduction to: AGN I, Taxonomy

The previous chapter detailed the spectral and physical properties of the 'small' stellar mass black holes. Measurements of stellar and gas kinematics have demonstrated that most galaxies, including our own (see e.g Schodel et al. 2002), harbour a *supermassive* (10^5-$10^9 M_\odot$) black hole at their center (Kormendy & Richstone 1995; Magorrian et al. 1998; Ferrarese & Merrit 2000).

Whilst it is currently unclear as to quite how these supermassive black holes (SMBH) form, possible theories include the evolution from primordial black holes formed through early cosmic timescale perturbations, direct formation via the collapse of self-gravitating gas in dark matter halos (Begelman et al. 2006) or even core-collapse of dense stellar clusters (Spitzer 1987). Observations of SMBHs show that the mass scales with the properties of the galaxy's bulge, including its velocity dispersion (Gebhardt et al. 2000; Tremaine et al. 2002), luminosity (Marconi & Hunt 2003) and stellar density profile (Graham et al. 2001). This clearly suggests that the formation of the black hole and the galaxy are somehow intertwined.

Whilst the majority of galaxies in the local Universe are quiet, some are 'feeding' and have 'active galactic nuclei' (AGN). The massive luminosities observed at high energies from such objects is generally accepted to be due to accretion disc processes together with powerful jets from the core, which are easily observable by their radio emission (but also energies through to gamma-rays).

As the accretion disc properties scale with the mass then the peak of the emission

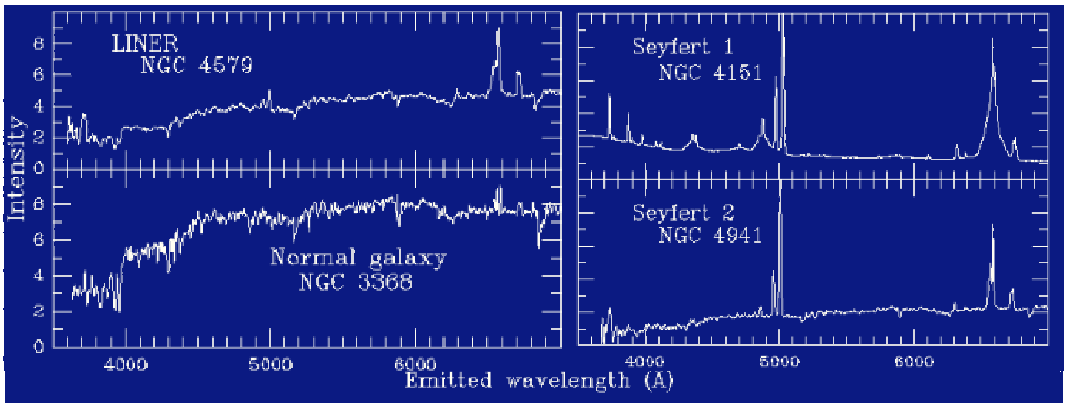

Figure 3.1: Example line spectra of LINER and Seyfert type 1 and 2s relative to a normal galaxy's optical spectrum. This highlights the presence and lack of broad lines respectively.

will be in the unobservable EUV which results in a huge amount of optical line emission which can be used to describe the AGN 'zoo'. In addition, whilst the BHXRBs accreted matter from a companion star, this is clearly not the case for AGN and so their disc size can potentially be unconstrained allowing them to have much larger mass accretion rates.

It is generally accepted that AGN may be split into 2 distinct groups, the radio-loud and radio-quiet (although see White et al. 2000; Cirasuolo et al. 2003), with a deficiency of sources at intermediate radio powers. The radio quiet are those where the jet luminosity is negligible (although the kinetic luminosity may be substantial) and these are further subdivided based on their emission properties. As the AGN studied in this thesis are all radio-quiet I will restrict the following to an explanation of their sub-types only.

LINERs

Low-ionisation nuclear emission region AGN or LINERs are low luminosity AGN that are characterised by optical spectra dominated by emission lines of moderate

intensities, arising from lower ionisation states than classical AGN (fig 3.1 and see Heckman 1980; González-Martín et al. 2000 and references therein for more detailed descriptions). There is still a question regarding whether these objects are all truly AGN as some/all of their emission may result from starburst activity rather than accretion onto a SMBH.

Seyfert AGN

The first distinct AGN type to be identified were the Seyfert galaxies which were first identified by Carl Seyfert in 1943 for whom the class is named. These are normally found within spiral or irregular host galaxies and show strong nuclear X-ray emission together with optical nuclear continuum emission, emission lines (both broad and narrow) and sometimes a weak small-scale radio jet. These can be further sub-divided by their emission line properties with Seyfert 1s showing broad emission lines whilst Seyfert 2s do not (fig 3.1). An extra class of Seyfert 1s were identified by Osterbrock & Progge (1985) by their strong FeII permitted lines and high Hβ/O[III]λ5007. These are of a similar nature to Seyfert 1s, but with narrower permitted optical lines (only just broader than their forbidden lines). These are termed narrow-line Seyfert 1s (NLS1) and an arbitrary Hβ line FWHM of 2000kms^{-1} is often used as a means of distinguishing them from their broader counterparts (Goodrich 1989, though for a full description of the optical spectra see Mullaney & Ward 2008). Quasars are essentially more luminous versions of Seyfert 1s, where the difference is usually expressed in terms of a limiting optical magnitude (M$\approx$-25.5: Rees 1984). These show all the original features associated with the term quasar: optical luminosities that are much greater than that of their host galaxy, X-ray continuum emission, and broad and narrow optical emission lines. In the context of the above, Quasar 2s are the more luminous analogies to Seyfert 2s.

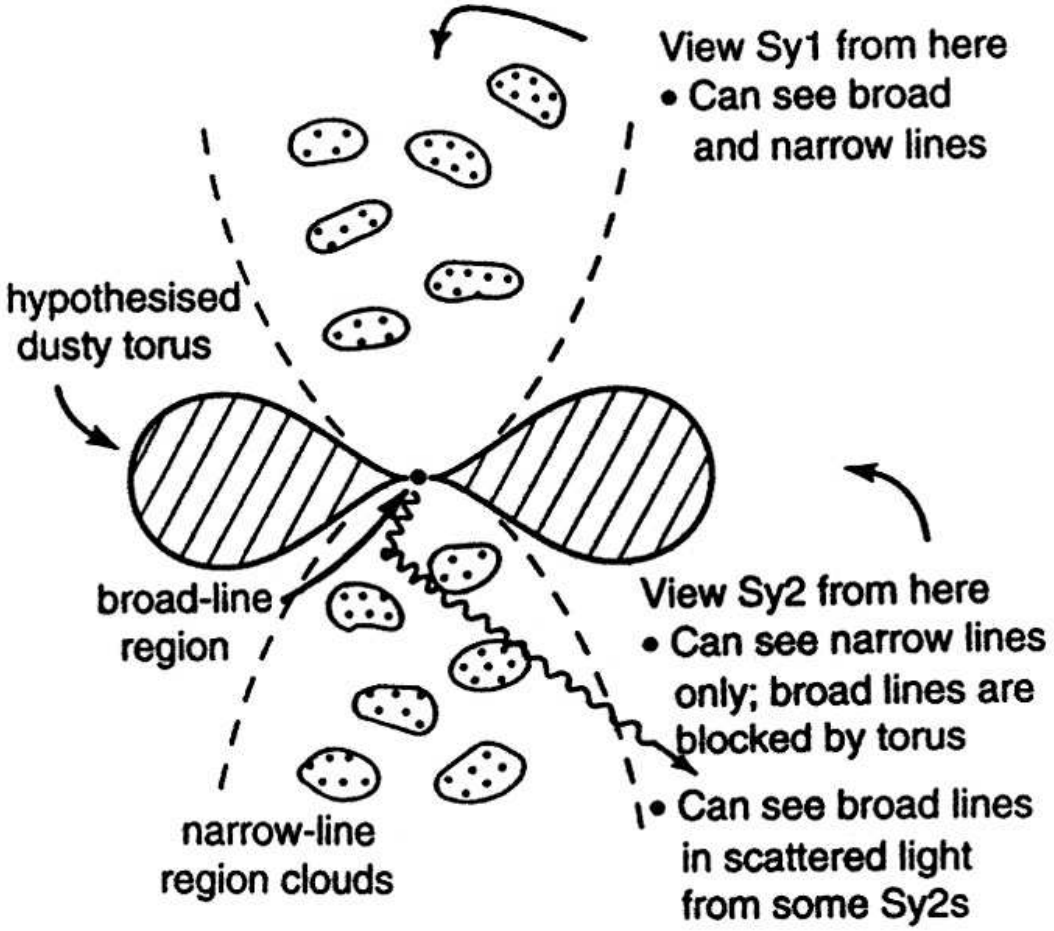

Figure 3.2: The Unified model of AGN as proposed by Antonucci & Miller (1985).

3.1 Unified model

The well known Unification model of AGN (see Antonucci & Miller 1985 and Antonucci 1993) shown in figure 3.2 provides a zeroth order model of the nuclear region of a galaxy and proposes that the different types of AGN are formed from the same intrinsic nuclear components viewed at different angles. Besides the central SMBH, the regions are: a narrow line region (NLR), broad line region (BLR) and dusty torus.

If the line-of-sight intersects the dusty torus, the central regions (SMBH, accretion disc and BLR) are all obscured. The only detectable nuclear emission seen directly is reprocessed IR emission from the dusty torus and emission lines from the NLR. As such the optical spectra are dominated by narrow lines. This can explain the spectral characteristics of Seyfert 2s. Seyfert 1 AGN can be explained if we are looking through the polar hole in the obscuring material and so can see both the BLR and NLR together with emission from the accretion disc. Reflection of nuclear emission by hot gas above and below the torus provides a ready explanation for the presence of polarised broad emission lines (most notably in NGC 1068) and the observations of hidden BLRs in some Seyfert 2s (e.g. Tran 1995, Heisler et al. 1997).

A more detailed description of the model components is given below.

Narrow line region

The narrow line region (NLR) extends out to at least several hundred parsecs from the nucleus (Schmitt et al. 2003a; 2003b) and is the smallest UV/optical resolved structure that is directly affected by the ionisation and dynamics of the inner, unresolved nucleus. It is composed of low density, ionised gas clouds that move with low velocity (thus narrow emission lines with widths of $\sim 500\text{kms}^{-1}$ FWHM) with the low density allowing observation of forbidden lines that would otherwise be

suppressed.

Ruiz et al. (2005) describe the respective morphology and properties of the NLR from Hubble space telescope (HST) observations of several Seyfert AGN. Observations have shown that the NLR is clumpy with resolved 'knots' of emission, typically of a few arcseconds in size (Evans et al. 1991, 1993; Schmitt et al. 2003a). The morphology is found to be extremely varied, with triangular, S-shaped, linear, arclike, circular and amorphous all common. In agreement with the predictions of the Unified model where, for a Seyfert 2, the torus blocks our view of the BLR, we see a more extended, triangular NLR. For a Seyfert 1 we are now looking at an angle allowing us to observe the BLR, and so the NLR looks more compact and circular (Schmitt et al. 2003b).

Broad line region

The relative strengths of optical/UV lines suggest that the broad profiles originate from a dense, cool gas, photo-ionised by the central source (Ferland & Peterson 1989; Ferland et al. 1992) in which case the velocity dispersion of the line emitting gas sets the width of the line profiles (Blandford & Rees 1992; Osterbrock 1993). To explain this it was proposed that a broad-line region (BLR) exists, composed of individual clouds, as the sum of contributions from these would naturally produce a similar total AGN spectrum to what is observed (Baldwin et al. 1995). This is supported by the small derived filling factor (Netzer 1990) and the analysis of line profiles of Seyferts (Capriotti et al. 1981; Atwood et al. 1982; Arav et al. 1997, 1998; Dietrich et al. 1999) which suggests that there could be between 10^4-10^7 of these clouds of mass 10^{-7}-$10^{-8}M_\odot$ (Peterson 1997). However, to explain the observed strength of the lines the covering fraction must be 50% (Gaskell, Klimek & Nazarova 2007) if the cloudlets are distributed uniformly about the central source. Lyman continuum absorption should then be common but has never been convincingly

detected (MacAlpine 2003). To account for this high covering fraction and lack of absorption, Gaskell (2009) suggests that the distribution of cloudlets in the BLR is flattened and that we observe it through a hole (as shown in fig 3.3).

The very small mass of the clouds suggests a confinement problem due to evaporation (Krolik 1999) and many attempts to provide a mechanism have been postulated including a hot intercloud medium (Krolik et al. 1981), magnetic fields (Rees 1987), magnetically driven winds (e.g. Emmering et al. 1992) or externally irradiated atmospheres of giant stars in the central star cluster (e.g. Norman & Scoville 1988).

BLR models that instead derive the emission from a continuous line emitting region embedded in a hydrodynamical flow can directly solve the confinement problem. These include accretion disc winds, hydrodynamical flows and the shock interaction between a disc wind and wind from the central source (Smith & Raine 1985, 1988; Pelletier & Pudritz 1992; Cassidy & Raine 1993; Murray & Chiang 1995, 1997; Murray et al. 1995).

Although much progress has been made in understanding the BLR, no single model can yet account for all of the features seen and many problems remain (see Gaskell 2009 for a review of these).

The dusty torus

A circumstellar dusty molecular torus is proposed to explain the obscuration of the BLR from view in the case of Seyfert 1 AGN. As such it must be optically thick from infrared to X-rays and geometrically thick enough to obscure a substantial solid angle around the central source. Its existence is supported by observations of the IR spectra from 60% of Seyferts which are dominated by a thermal hump due to re-emission of the nuclear emission by dust (Miley, Neugebauer & Soifer 1985; Edelson, Malkan & Rieke 1987). However, there are likely to be several

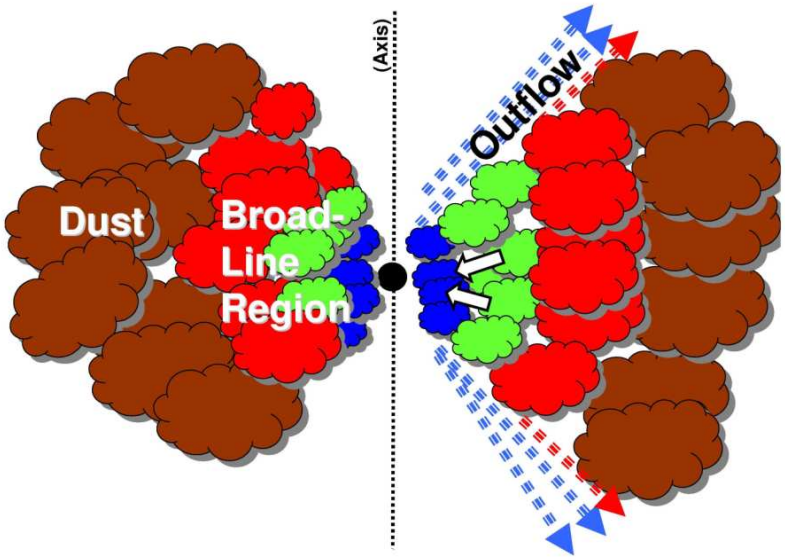

Figure 3.3: Cartoon from Gaskell (2009) depicting the BLR and outflows relative to the the dusty torus.

contaminating sources of IR emission that do not originate in the torus. For example, IR emission from nearby dust outside the torus (Mason et al. 2006) and starburst emission can create problems when comparing models of the torus to observations (see Nenkova et al. 2008b), although Spitzer can distinguish the latter as starburst emission contains multiple PAH (polycyclic aromatic hydrocarbon) features whist AGN show Si emission/absorption (Weedman & Houck 2009).

Supported by recent observations of clumpy, filamentary structure in Circinus (Tristram et al. 2007), the torus is thought to consist of a large number of very optically thick, discrete clouds (Krolik & Begelman 1988) whereas initial models of the torus assumed a smooth distribution. A fundamental difference between these models is that radiation can propagate freely between different regions of an optically thick medium when it is clumpy but not otherwise. New, realistic models

are beginning to incorporate this radiative transfer and can explain the emission from individual optically thick clouds (Mason et al. 2006; Nenkova et al. 2002, 2008a).

Problems with the Unified model

There is certainly a great deal of evidence in favour of the standard Unification model. It can explain the dichotomy between type 1 and 2 AGN, the larger absorbing columns in X-ray spectra of Seyfert 2s and correspondingly weaker luminosities (Mushotzky 1982; Pounds et al. 1990; Singh & Vahia 1992). It also explains the existence of Seyfert 2s which show hidden BLRs (e.g. NGC1068, Miller & Goodrich 1990).

However, there are features that the Unification model cannot explain which suggests that we need more than orientation effects to describe the morphological 'zoo' of AGN.

The most obvious problem is the difference between unobscured AGN which, according to the Unified model, should not show significant differences. For example, Seyfert 1s and Quasars have fundamentally very similar spectra but the latter are far more luminous. This could be explained by a difference in central mass. However, a more complex problem is that spectral softening at high energies occurs from LINERs to Seyfert 1s to NLS1s (for example Shemmer et al. 2006; Brandt, Mathur & Elvis 1997). This might be explained if we are observing objects which have intrinsically different mass accretion rates so that the spectra soften with increasing luminosity (Pounds, Done & Osborne 1995).

Chapter 4

Introduction to: AGNII, Radiative properties

4.1 The AGN spectrum

The spectra of BHXRBs can be well described by the relative contributions of a thermal disc and Comptonised tail of emission to high energies (chapter 2). As AGN are far more massive, the peak of the disc emission is in the unobservable EUV so the X-rays are dominated by the Comptonised tail. As with BHXRBs we expect to see a softening of the tail with mass accretion rate (e.g. Shemmer et al. 2006; Laor 2000; Remillard & McClintock 2006) and indeed unobscured AGN show an analogous softening from the low luminosity LINERs through to Seyfert 1s/Quasars and on to the extremely luminous NLS1s (in direct conflict with the predictions of the Unified model).

In this picture LINERs display X-ray spectra analogous to the low-hard state and are of low mass accretion rate. It is likely that the inner region of these sources becomes an advection dominated accretion flow (ADAF: see Narayan & Yi 1994) where the low density results in an electron-proton thermalisation time which is much longer than the in-fall time and so the ions carry energy into the black hole without it being radiated away.

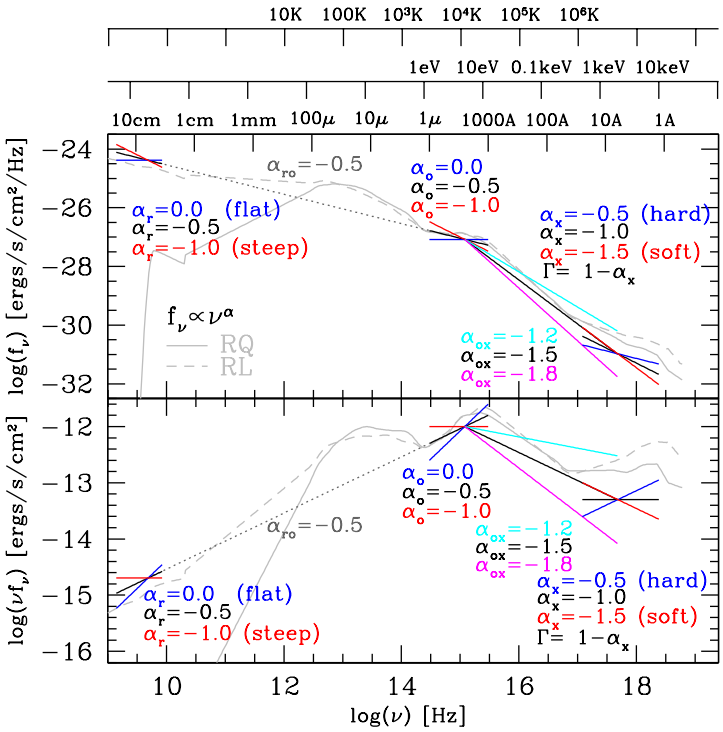

Figure 4.1: Average Quasar SED from Richards et al. (2006) showing the soft components in solid grey from Elvis et al. (1994), including the large UV disc below 1 eV in both $f(\nu)$ (top panel) and $\nu f(\nu)$ (bottom panel). The coloured lines represent typical spectral indices in the radio, optical and X-ray.

Bright Quasars and NLS1s then represent the highest mass accretion rates and are analogous to the high-soft and very-high states where the UV disc dominates the spectrum (fig 4.1). This is consistent with accretion via a geometrically thin, optically thick disc (as described by Shakura & Sunyaev 1973), the peak temperature of which is determined by the mass of the black hole and the spin (see chapter 1). However, in contrast with BHXRBs where the spin was a result of formation, the spin of a SMBH reflects the growth process via accretion and mergers (King 2008). Even with a maximally spinning SMBH, the result of the huge mass difference between stellar mass and SMBHs means the peak emission is still in the unobservable EUV rather than the X-ray band (fig 4.1).

In the case of BHXRBs the disc is very hot so any material irradiated by the emission tends to be completely ionised and cannot imprint atomic features onto the spectrum. AGN environments however are much cooler and so material is only partially ionised, which, together with the complex nature of the AGN environment means there are a wide variety of atomic features at varying ionisation states present in the spectrum.

4.2 Absorption

4.2.1 Compton-thin absorption

Photo-electric absorption imprints lines and edges onto the spectrum (as described in chapter 1). Indeed, soft (0.1-10 keV) excitation features of elements from C to Ni are commonly seen and many photo-ionisation models have been created to explain these, assuming complex geometrical models for the ionised gas with the ionisation structure determined by assuming the gas is in thermal equilibrium (e.g. the review of Turner & Miller 2009).

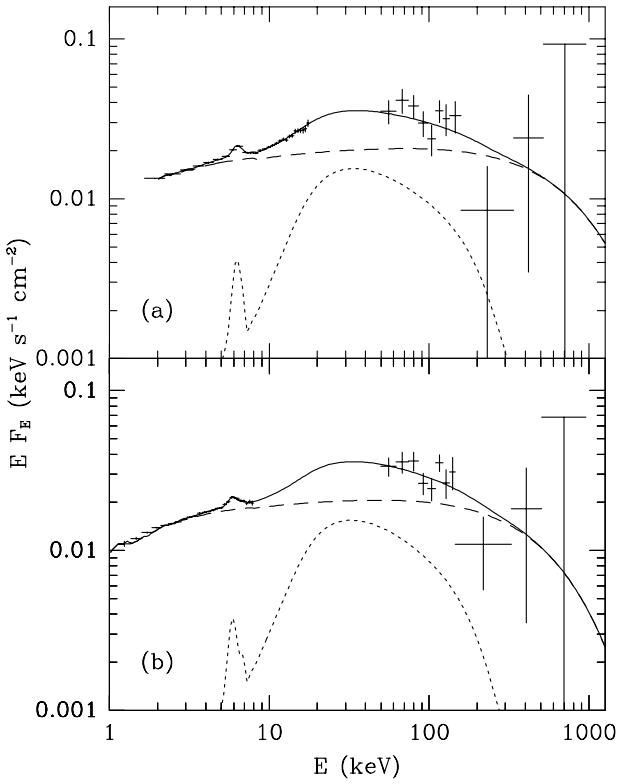

Figure 4.2: The average continuum spectrum of unobscured (type 1) AGN from Ginga/OSSE (top panel) and EXOSAT/OSSE (bottom panel) with 2σ upper limits. The roll-over at high energies is clearly present (from Gondek et al. 2006).

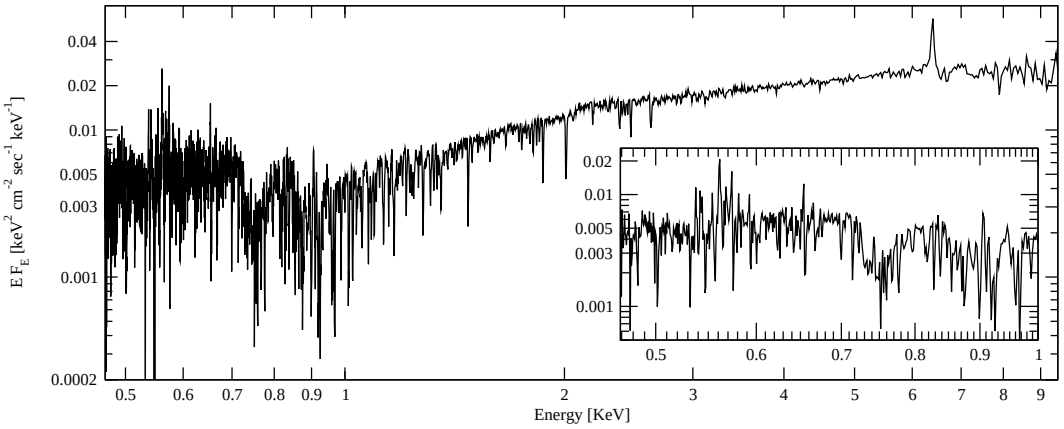

Figure 4.3: The warm absorber in NGC3783 as viewed by the High-Energy Transmission Grating Spectrometer on-board Chandra for a 900ks exposure (from Kaspi et al. 2002).

4.2.2 The warm absorber

The presence of narrow absorption lines in the soft X-ray spectrum indicates a 'warm absorber' in the system. This was first seen in the spectrum of a QSO (Halpern 1984) and has since been detected in ∼50% of Seyfert 1 AGN by ASCA (Reynolds 1997). The strongest features are generally for partially ionised populations of Oxygen (in particular OVII and OVIII) and provide evidence of partially ionised material in our line-of-sight to the nucleus.

XMM-Newton and Chandra have greatly improved our understanding of these features due to their high-resolution grating spectrometers. The observations have shown that the soft X-ray absorption is composed of lines from a range of elements at many ionisation states (Kaastra 2000; Kaspi et al. 2000a) from H- and He- like Fe to the Fe M-shell unresolved transition array (UTA). One of the best examples of the warm absorber is that of NGC3783 taken with the Chandra grating (fig 4.3 - Kaspi et al. 2002) which clearly shows the range of absorption lines present in the spectrum. These lines indicate the ionisation state and abundance of elements

but also that the gas is outflowing with a velocity of a few hundred kms^{-1} with calculations for a sample of nearby Seyferts (Blustin et al. 2005) suggesting that the base of the outflow must be beyond the BLR, suggesting an origin in the torus (Krolik & Kris 2001).

There are also indications of higher columns of highly ionised absorption in some objects. This is strongly seen as FeKα absorption and may have its origins in an accretion disc wind, separate from the slower multi-phase warm absorber already described (e.g. the compilation by Reeves et al. 2008).

4.2.3 Disc wind mechanisms

Whilst the presence of line-driven winds in BHXRBs is unlikely given the temperature of the disc (Proga & Kallman 2002), the AGN disc has a peak temperature in the UV and so would be expected to produce powerful line-driven winds (Arav et al. 1996; Chelouche & Netzer 2003; Everett 2005) for mass accretion rates even well below Eddington. Indeed, hydrodynamic simulations of accretion discs ubiquitously show mass outflows (e.g. Proga 2003). However, such line-driven winds probably require modifications (Königl 2006). In particular, for the gas to be accelerated efficiently, the outflow must be shielded from the hard X-rays to reduce the ionisation state of the gas. This may be accomplished by failed disc winds (Murray et al. 1995) whereby the inner outflowing regions become highly ionised by the illuminating X-rays and can no-longer be line-driven, stall and fall to the disc. This shields the outer outflowing regions as supported by numerical simulations (Proga et al. 2000; Proga & Kallman 2004). These simulations however cannot yet adequately describe the effects of ionisation and acceleration due to the disc and continuum, together with scattering and absorption in the shielding medium.

In addition to the line-driven winds, discs threaded by open magnetic field lines should produce centrifugally-driven outflows (Blandford & Payne 1982). However,

these depend strongly on the (unknown) magnetic field configuration and so are not considered further here.

4.3 Reflection

Besides Compton-thin material, possibly in the form of an outflow, it is likely that the X-ray continuum photons will also be incident upon high column density gas $\sim 10^{25}\mathrm{cm}^{-2}$ in which we would expect Compton reflection effects to be important (i.e. the gas is Compton-thick). Such optically thick gas is thought to exist in the disc where the material is sufficiently cold ($\mathrm{T}\leq 10^{6}\mathrm{K}$) and dense (Guilbert & Rees 1988; Ferland & Rees 1988). Where X-ray photons illuminate this optically thick material they penetrate to a mean optical depth of unity and are either Compton scattered or photo-electrically absorbed, forming the characteristic reflection spectrum (as described in chapter 1).

Reflection is particularly noticeable above 10 keV as the Compton 'hump' enhances the reflected spectrum (fig 4.4). However, the vast majority of X-ray missions have very poor effective areas at these high energies (Suzaku being the notable exception). Therefore, to see the signatures of reflection we must rely on fluorescence line emission from photo-electric absorption, dominated by the Kα lines of the most abundant metals.

4.4 The soft excess

In general, although the irradiated environment differs between AGN and BHXRBs, they show the same two-component spectra when sub-Eddington. However, AGN at the highest mass accretion rates (typically NLS1s) ubiquitously demonstrate an excess of flux above the extrapolated, well-fitting 2-10 keV power-law (fig 4.5). This 'soft excess' is defined as the ratio of data to power-law model at 0.5 keV. It should

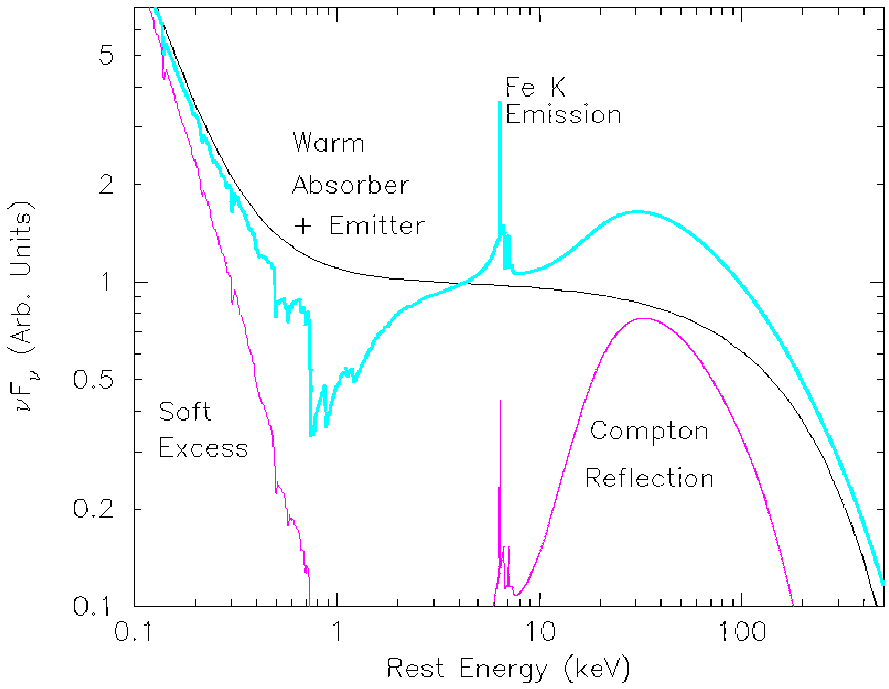

Figure 4.4: The average total spectrum of a type 1 AGN showing the reflection features, warm absorber and a soft excess made by reflection. The continuum is well fit by a power law (absorbed at soft energies) with a high-energy exponential cut-off at E $\sim$ 100-300 keV as expected from thermal Comptonisation.

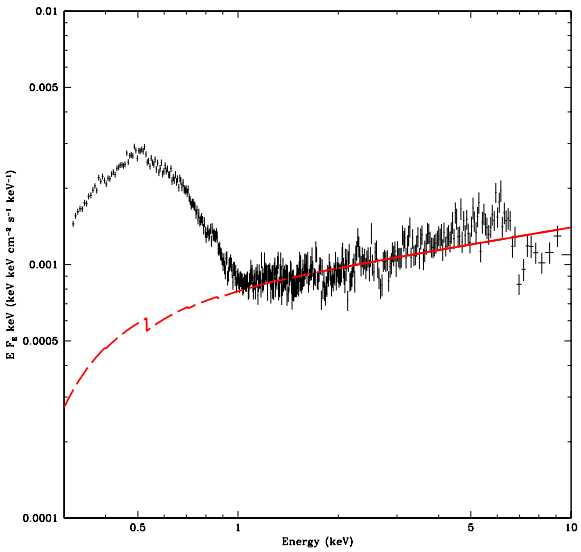

Figure 4.5: The 2-10 keV spectrum of PG1211+143 is well fit by a simple absorbed power-law as expected from Compton scattering by a thermal or non-thermal population of electrons (chapter 1), though it also has obvious emission and absorption features at FeKα. When this is extrapolated back to soft energies an excess of flux is clearly visible.

be noted that there will undoubtedly be some contribution from reflection at soft energies and so the value of the soft excess using the above definition is an upper limit.

Across a range of high L/L$_{Edd}$ AGN, this component has roughly the same temperature and appears smooth and featureless as shown in figures 4.6 and 4.7 for a sample of luminous PG QSOs and NLS1 AGN. Although the resulting temperature of the soft excess in these objects is apparently generic, the amount of soft excess can vary from very small, e.g. PG0050 which has almost no soft excess, to the current record holder of $\sim$ 10 from REJ1034+396 as shown in figure 4.8 (see chapters 7, 8 and 9 for detailed discussions on this source).

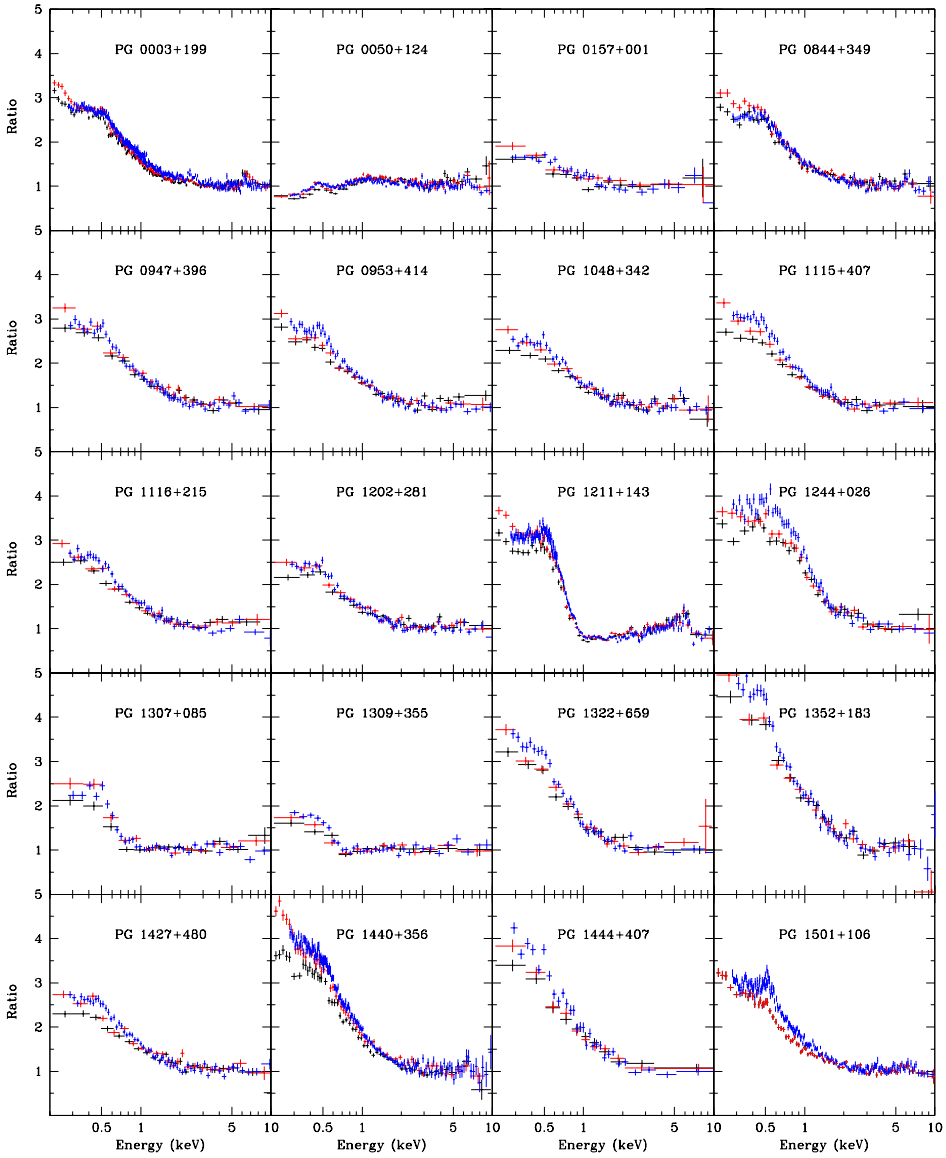

Figure 4.6: The soft excess (ratio of data to 2-10 keV power-law) of a sample of luminous PG QSOs.

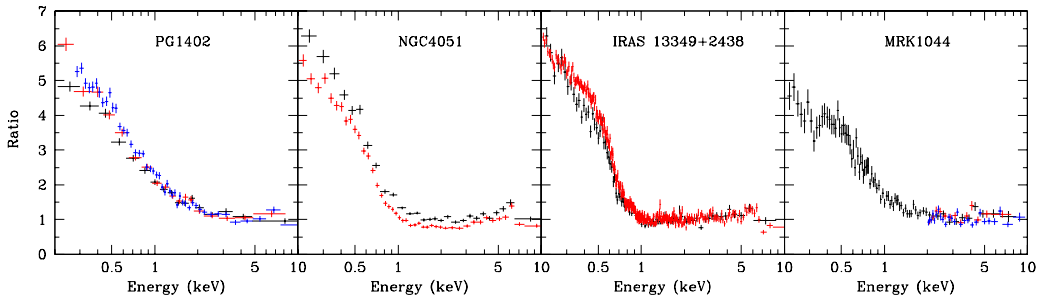

Figure 4.7: The soft excess (ratio of data to 2-10 keV power-law) of a number of Seyfert AGN.

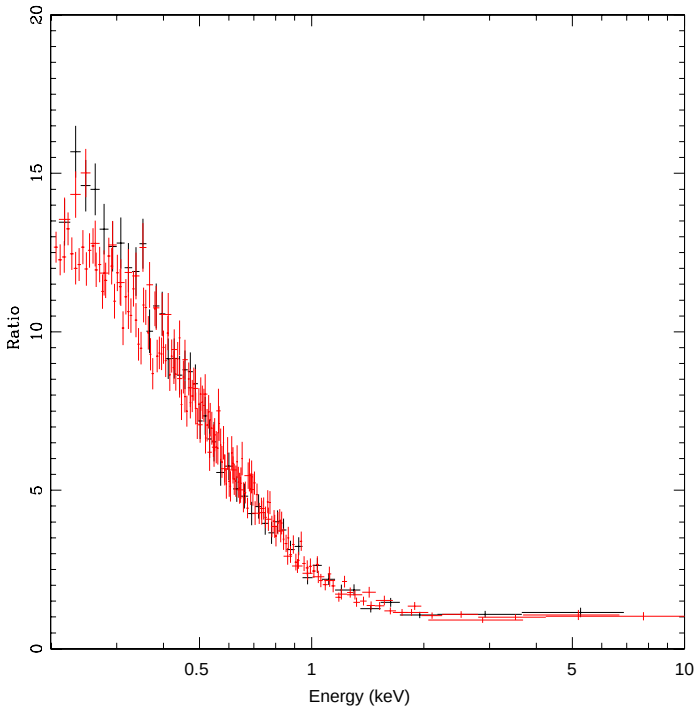

Figure 4.8: The soft excess (ratio of data to 2-10 keV power-law) of NLS1 REJ1034+396, the largest soft excess seen in any object.

In the past, explanations for the soft excess have included a separate soft component such as a disc black-body with temperatures in the range 0.1-0.2 keV (Walter & Fink 1993; Czerny et al. 2003). This is obviously too hot to be direct emission from an accretion disc around a SMBH (even if photon trapping is invoked: see Abramowicz et al. 1988; Mineshige et al. 2000) but could potentially be Compton scattered emission (e.g. Czerny & Elvis 1987; Wang & Netzer 2003). However, this requires an extremely narrow range of plasma temperatures for a large range (10^6-$10^8 M_\odot$) in mass (Gierliński & Done 2004), effectively ruling this out as the source of the soft excess in the majority of sources unless there is some (unknown) thermostat operating.

A more likely explanation for the characteristic energy of the soft excess is some origin in atomic processes which are undoubtedly present as they are needed to explain the observed absorption and emission features. In particular, the OVII/OVIII and Fe M shell UTA can provide a dramatic increase in opacity at ∼0.7 keV. However, in order for the atomic features to be smoothed out to match the observed shape of the soft excess, there must be a large velocity distribution to provide Doppler smearing. This atomic origin also explains why the soft excess is not seen in BHXRBs as, even if the same material is present in the smaller systems, the higher temperature accretion disc would result in the complete photo-ionisation of Oxygen and so there will not be the strong jump in opacity at ∼0.7 keV.

This partially ionised material could produce the soft excess either from optically thick reflection or optically thin absorption in a wind.

4.4.1 Reflection

Partially ionised reflection can fit the spectra of high L/L_{Edd} sources (e.g. Crummy et al. 2006) and can easily create the smaller soft excesses. However, it is limited if the source is isotropic. The maximum amount of reflected continuum below 0.7 keV

is, by definition, the illuminating continuum and, even with the inclusion of line emission, this results in fluxes only a factor of 2-3 above the 2-10 keV continuum (Sobolewska & Done 2007). In order to accommodate the larger soft excesses, the reflection geometry needs to be modified to suppress the intrinsic emission either by gravitational light bending or a corrugated disc surface, although light bending has the natural advantage in that it also requires the same very extreme smearing needed to remove the atomic features (Fabian et al. 2002a; Miniutti et al. 2003; Miniutti & Fabian 2004). However, a serious problem occurs if the reflecting material is in hydrostatic equilibrium, as the details of the pressure balance mean that the required partially ionised Oxygen is only present in a small optical depth of the disc. This can limit the size of the soft excess to even smaller values than for the case of a constant density, reflecting slab (Done & Nayakshin 2007).

4.4.2 Absorption

If the absorbing material completely covers the source then a large velocity shear is needed to remove the characteristic absorption features and produce the observed smooth soft excess. This can be produced if the material is outflowing in a wind, possibly via the line-driving already discussed. Models for such a wind of partially ionised material can fit the spectrum to an equivalent quality as reflection models (see chapter 7) but, in contrast, naturally predict the presence of partially ionised Oxygen and can directly reproduce the smallest to the largest soft-excesses (Sobolewska & Done 2007). The velocity needed to smear out the atomic features is prohibitively large ($> 0.2c$ - see chapter 7) which would require an origin linked with the jet.

The same spectra may also be well fit by a combination of one or more partial covering fractions of neutral or partially ionised material which may have their origins in a failed disc wind as invoked for line-driving. In this case the characteristic

atomic features are hidden by dilution of the spectrum rather than velocity smearing. However, the properties and numbers of these clouds are difficult to constrain unambiguously.

To distinguish between models for the soft excess, one would ideally try and look for distinguishing features such as absorption or emission lines, however the invoked Doppler smearing prevents such an approach. As such, the best that can be hoped for is a comparison of the current models' ability to adequately describe the generic features of the X-ray spectrum (see chapter 7) even though both models are still in their infancy and cannot encapsulate the true physical complexity in any unambiguous way (Turner & Miller 2009). For this reason one must be careful when comparing the overall goodness-of-fit from such models, e.g. a standard χ^2 test, and expect some ambiguity in the conclusions being drawn. However, with the latest generation of instruments, with improved resolution and sensitivities, this ambiguity should be addressed.

4.5 AGN variability

Much like BHXRBs there are multiple timing analysis techniques that can assist in breaking model degeneracy and tell us more about the physical system being investigated.

Although the timescale for spectral changes in AGN are much longer than for BHXRBs due to mass scaling, they are still expected to occur on timescales shorter than the duration of typical observations. As a result, the fitted spectra are usually time-averaged spectra that may lead to key information being missed. If the variations include certain physical properties such as opacity changes, then the model fitted, time-averaged spectra are likely to provide a poor representation of the physical state of the system. Analysing time selected spectra however, can allow us to break the ambiguity that exists between models such as absorption and reflection

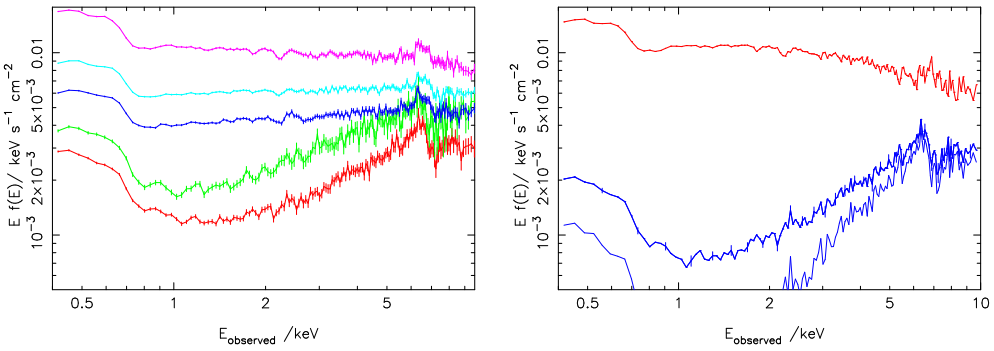

Figure 4.9: Left: data from MRK766 from XMM-Newton used for PCA. This has been averaged into 5 logarithmically spaced flux states based on the 1-2 keV flux and ratio-ed to a power law of $\Gamma = 2$ with unit normalisation. This illustrates how the source hardens to low fluxes (from Miller et al. 2007). Right: The result of PCA showing the variable principle component as the upper red line. The possible range of a non-variable zero-point spectrum is shown by the lower, blue spectra.

models, i.e. rather than fitting time-averaged spectra which may be misleading, time-binned spectra allow components to be disentangled by their different patterns of spectral variability.

Such time-resolved spectroscopy has been used to determine that the primary variable component in the marked spectral variability of MRK766 has the form of an absorbed power-law with accompanying ionised reflection, that varies with the continuum (Miller et al. 2006 and see Turner et al. 2007). A still more powerful tool to determine the origin of spectral variability is that of Principal Component Analysis (PCA). First used by Vaughan & Fabian (2004) in the analysis of MCG-6-30-15, this method correlates flux at different spectral energies such that the data can be broken down into variable constituent additive components (direct or re-processed emission) in a similar fashion to the RMS spectrum discussed in section 2.3. However, this method cannot separate multiplicative components that would

be caused by changing absorption. An example of this method is shown in figure 4.9 for MRK766 (Miller et al. 2007) from which it was found that the source can be well modelled by a variable power-law and ionised Fe emission line together with a stable, extremely smeared, reflection component.

4.5.1 Power spectra - the AGN-BHXRB connection

Given that black holes, irrespective of environment, may be described by only mass and spin, it seems likely that the underlying physics of accretion should not differ. This is supported by compelling evidence including the fundamental plane relations of Merloni, Heinz & di Matteo (2003); Falcke, Körding & Markoff (2004). From the sections covered in this chapter and those before, it is clear that, in spite of the differences between AGN and BHXRBs, they appear to show very similar spectral states in support of a simple scaling. This scaling should also produce similar timing properties which should be clear from a comparison of power spectra.

Irrespective of the limited statistics of AGN, their power spectra can generally be described by the same broad-band shape as BHXRBs only shifted in frequency going as inverse mass (see Markowicz et al. 2003). Thus the power spectral slope (in $\nu P(\nu)$) appears as $P(\nu) \propto \nu^{-1}$ between a low frequency break, ν_b, below which the PDS is $P(\nu) \propto \nu^0$, and a high frequency break, ν_h, above which the spectrum steepens to $P(\nu) \propto \nu^{-2}$. This is shown in figure 4.10 for 2 sources compared to the well studied BHXRB, Cygnus X-1 (McHardy et al. 2004).

These power spectra can provide powerful diagnostic tools and can test whether AGN demonstrate the scaled-up properties of BHXRBs. In particular, McHardy et al. (2006) show that the characteristic timescale of the high frequency break correlates with the FWHM of optical lines in AGN (fig 4.11) which in turn correlates with the mass of the black hole and mass accretion rate via scaling with the BLR. This provides strong evidence of a simple scaling between the two species.

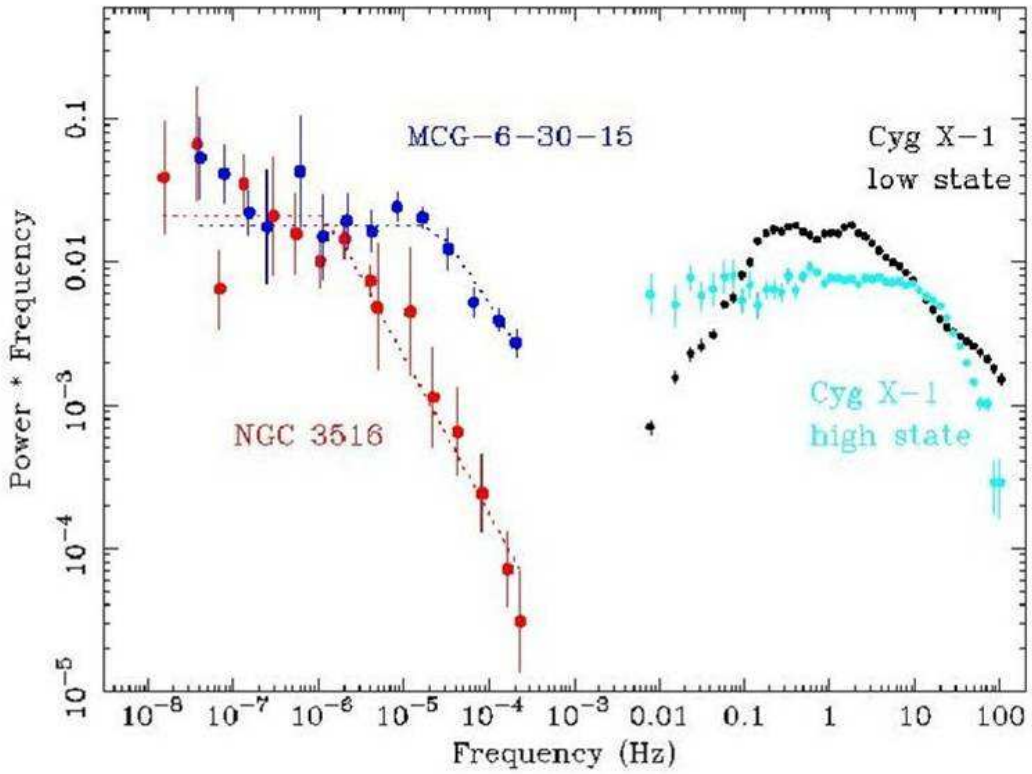

Figure 4.10: The power spectra (in $\nu P(\nu)$) of NGC3516 and MCG-6-30-15 next to the power spectrum of Cyg X-1 in the low-hard and high-soft states respectively (McHardy et al. 2004). The shape of the power spectra are very similar albeit shifted in frequency due to mass scaling. This lends credence to the idea that AGN are scaled-up BHXRBs.

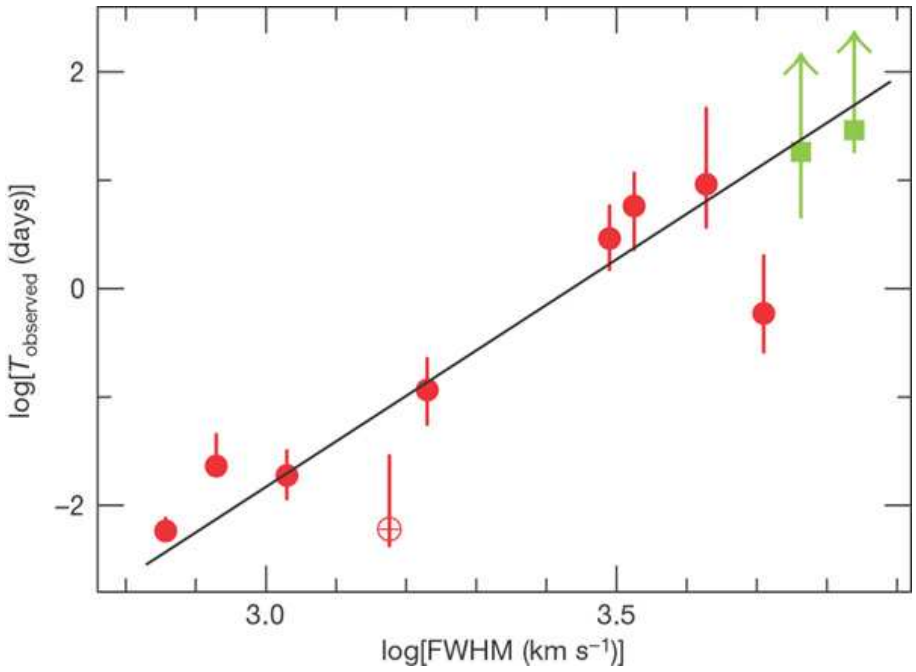

Figure 4.11: The correlation of the high-frequency break with the FWHM of optical emission lines in a sample of AGN with well constrained power spectra. This tight correlation suggests a simple scaling between AGN and BHXRBs. From McHardy et al. (2006).

In any variability analysis it is important to consider exactly what is being compared. For example, the BHXRB spectrum is dominated by a disc with a hard Compton tail, whereas in AGN, the spectral components are shifted to lower temperatures and, in X-rays, are dominated by the Comptonised tail. A result of this 'bandpass' effect is that AGN have much higher apparent RMS variability and any similarities between the spectra and variability are masked. Thus the AGN power spectra should only be compared to the high-energy power spectra of BHXRBs (Done & Gierliński 2005).

An important *difference* between the power spectra of AGN and BHXRBs is the lack of QPOs in the AGN power spectra that would be expected at frequencies

scaled with the mass. However, Vaughan & Uttley (2005) explain that we should not expect to see LFQPOs in AGN due to a lack of sensitivity available in current detectors. This has not prevented many claims for analogous QPOs in AGN being made, although all have been shown to not be formally significant at $>3\sigma$. The majority of these incorrectly modelled the aperiodic (red) broad-band noise below the QPO and subsequent correct modelling (Vaughan & Uttley 2006) reduced the significance of the putative detections below 3σ.

Although the lack of LFQPOs in the power spectra of AGN is expected, the discovery of a HFQPO in an AGN should be possible and important for a number of reasons. Firstly, if the analogy to a BHXRB QPO can be found then there lies the potential to unify the underlying physics of the accretion flow. Secondly, whilst BHXRB QPOs are many and varied, they mostly occur on timescales which are too short to fully diagnose the physical mechanism that is producing them. By contrast, an AGN QPO will have a much lower frequency allowing a full deconstruction and hopefully be tied to a physical origin that can be modelled in other AGN and BHXRBs (see chapters 8, 9 & 10).

Chapter 5 | *Paper Overview*

5.1 Introduction

The following chapters represent the body of my PhD work, taking the form of 5 papers, across which I try to address some of the fundamental problems preventing a unification of accretion processes in AGN and BHXRBs. Each paper introduces the reader to the particular physics necessary to understand the contained work, the basics of which have been covered in the first 4 chapters of this thesis.

The first of these papers probes the predictions of the Unified model (chapter 3) by analysing the high energy (20-200 keV) spectra of a sample of Seyfert AGN. The Unified model predicts that there should not be a difference between the spectra however we find that the spectral slope probably changes with accretion rate as seen in BHXRBs (see chapter 2).

Paper 2 extends this idea by looking at a large sample of luminous PG QSOs and NLS1 AGN and reproduces the trend of spectral index increasing with L/L_{Edd} as seen in paper 1. This paper also allowed us to test two of the competing models for the soft excess, partially-ionised reflection and partially ionised wind absorption (see chapter 4). We find that both of these can fit the data but both require conditions which are quite extreme.

Of particular interest are the sources which show the largest soft excesses as any generic model must be able to reproduce these. To this end we applied for, and received, $\sim$ 100ks of XMM-Newton time to observe the NLS1 REJ1034+396 which,

from paper 2, we knew demonstrates a very large soft excess.

This observation was intended to provide a high signal-to-noise spectrum so as to break the degeneracy between the soft excess models. What we discovered, however, would provide the basis for a further 3 papers. The lightcurve demonstrated a very obvious periodicity, even to the eye, which translated into a highly significant ($>5\sigma$) QPO, the first of its kind to be detected in an AGN. This discovery is presented in paper 3. As chapter 4 explains, this is of great importance as it may hold the key to unifying the accretion flow of AGN and BHXRBs. This relies on determining an origin and ideally a BHXRB counterpart. Paper 4 attempts to address the origin by comparing the rms fractional variability to that expected from varying spectral components. In doing so we evaluate the origin of the soft excess in *this* object and discover that it likely has its origin in a separate low temperature Compton component which looks very similar to that seen occasionally in the unique BHXRB, GRS 1915+105.

Paper 5 uses the likely counterpart of GRS 1915+105 to try to identify an analogous signal to the AGN QPO. This would be quite straight-forward if a reliable mass estimate for REJ1034+396 was available. Sadly this is not the case and so we approached the problem from a more indirect route. This involved rigorous examination of the shape of the power spectrum below the QPO by simulating lightcurves with the same statistical properties as the real data. By comparison with the range of QPOs in the power spectrum of GRS 1915+105 and taking into account the bandpass effects, we concluded that the likely counterpart is the rarely seen 67Hz QPO.

What follows is an index of the paper abstracts allowing the reader an easy access summary of the papers.

5.2 Abstract index

Paper 1: High Energy spectra of Seyferts and Unification schemes

The Unified Model of AGN predicts the sole difference between Seyfert 1 and Seyfert 2 nuclei is the viewing angle with respect to an obscuring structure around the nucleus. High energy photons above 20 keV are not affected by this absorption if the column is Compton thin, so their 30–100 keV spectra should be the same. However, the observed spectra at high energies appear to show a systematic difference, with Seyfert 1s having $\Gamma \sim$2.1 whereas Seyfert 2s are harder with $\Gamma \sim 1.9$. We estimate the mass and accretion rate of Seyferts detected in these high energy samples and show that they span a wide range in L/L_{Edd}. Both black hole binary systems and AGN show a correlation between spectral softness and Eddington fraction, so these samples are probably heterogeneous, spanning a range of intrinsic spectral indices which are hidden in individual objects by poor signal-to-noise. However, the mean Eddington fraction for the Seyfert 1s is higher than for the Seyfert 2s, so the samples are consistent with this being the origin of the softer spectra seen in Seyfert 1s. We stress that high energy spectra alone are not necessarily a clean test of Unification schemes, but that the intrinsic nuclear properties should also change with L/L_{Edd}.

Paper 2: An absorption origin for the soft excess in Seyfert 1 AGN

The soft excess (SX) seen in the X-ray spectra of many AGN can be well modelled by reflection from a partially ionised accretion disc. However, this often requires extreme parameters in both the underlying spacetime and the reflection geometry, and requires that the disc is far from hydrostatic equilibrium. An alternative model uses similarly partially ionised, velocity smeared material but from an accretion disc wind seen in absorption. We explicitly compare these two models for the origin of the SX using XMM-Newton data for PG QSOs and NLS1s. We find that, while reflection and absorption give comparably good fits to the data, the absorption model allows a clearer correspondence with the stellar mass black holes. All the objects are high mass accretion rate AGN, so should be analogous to the high-soft and very high states (VHS) in BHXRBs. The intrinsic spectral indices derived from the absorption model are all consistent with a one-to-one mapping between spectral state and AGN type, with the NLS1s corresponding to the VHS and broad line AGN corresponding to the high-soft state. While this supports an absorption interpretation of the SX, we note that the required Gaussian velocity dispersion of $\geq 0.2c$ (corresponding to an outflow velocity $\geq 0.4c$) is too fast for a radiatively driven accretion disc wind and instead requires that the material is entrained in a magnetic outflow (jet). We also use the simultaneous OM data to derive the ratio of disc to total accretion power which is another tracer of spectral state in BHXRBs. This does not always show that the disc in NLS1s contributes less than 80% of the total power, as expected for a VHS. We suggest that this is an artifact of the standard disc models used to determine the disc luminosity in our fits. The disc seen in the VHS of BHXRBs is often observed to be distorted from the standard shape, and a similar effect in NLS1s could recover the one-to-one mapping between black hole binary spectral state and AGN type.

Paper 3: A periodicity of $\sim$ 1 hour in X-ray emission from the active galaxy REJ1034+396

Active galactic nuclei and quasars are thought to be scaled-up versions of Galactic black hole binaries, powered by accretion onto supermassive black holes with masses of 10^6-$10^9 M_\odot$, as opposed to the $\sim 10 M_\odot$ in binaries (here $M_\odot$ is the solar mass). One example of the similarities between these two types of systems is the characteristic rapid X-ray variability seen from the accretion flow (McHardy et al. 2006). The power spectrum of this variability in black hole binaries consists of a broad noise with multiple quasi-periodic oscillations superimposed on it. Although the broad noise component has been observed in many active galactic nuclei (Edelson & Nandra 1999; Markowitz et al. 2003) there have hitherto been no significant detections of quasi-periodic oscillations (Benlloch et al. 2001; Vaughan & Uttley 2005; Vaughan & Uttley 2006). Here we report the discovery of an $\sim$1-hour X-ray periodicity in a bright active galaxy, REJ1034+396. The signal is highly statistically significant (at the 5.6σ level) and very coherent, with quality factor $Q > 16$. The X-ray modulation arises from the direct vicinity of the black hole.

Paper 4: RE J1034+396: The origin of the soft X-ray excess and QPO

The X-ray quasi-periodic oscillation (QPO) seen in RE J1034+396 is so far unique amongst AGN. Here we look at another unique feature of RE J1034+396, namely its huge soft X-ray excess, to see if this is related in any way to the detection of the QPO. We show that all potential models considered for the soft energy excess can fit the 0.3–10 keV X-ray spectrum, but that the energy dependence of the rapid variability (which is dominated by the QPO) strongly supports a spectral decomposition where the soft excess is from low temperature Comptonization of the disc emission and remains mostly constant, while the rapid variability is produced by the power law tail changing in normalization. The presence of the QPO in the tail rather than in the disc is a common feature in black hole binaries, but low temperature Comptonization of the disc spectrum is not generally seen in these systems. The main exception to this is GRS 1915+105, the only black hole binary which routinely shows super-Eddington luminosities. We speculate that super-Eddington accretion rates lead to a change in disc structure, and that this also triggers the X-ray QPO.

Paper 5: The X-ray Binary Analogy to the First AGN QPO

The discovery of a Quasi-periodic oscillation (QPO) in the power spectrum of the NLS1, REJ1034+396 provides important support for simple scaling of accretion flow models between supermassive and stellar mass black holes. However, there are multiple types of QPO seen in any given black hole binary (BHB) system, so we need to identify which BHB QPO corresponds to the one seen in the AGN. This is not straightforward as the mass of the AGN is not well determined. Instead, we use lightcurve simulations to constrain the shape of the underlying continuum power spectrum in REJ1034+396. We find that this is consistent with a broken power law, which steepens from ν^{-1} to ν^{-2}, as seen accompanying the low frequency QPO in BHB. Alternatively, the data are equally well described by a single power law with index $\nu^{-1.3}$. This is flatter than the ν^{-2} which might be expected for the high frequency continuum power, but the (poorly constrained) BHB data show that the high frequency QPO may lie on an additional, lower normalisation ν^{-1} noise component. While the continuum shape is then consistent with either type of QPO, its normalisation is a factor 10 too small for the low frequency QPO even with careful matching of the energy bands to ensure the same spectral components dominate the lightcurves. However, mass scaling to the high frequency QPO implies a sub Eddington flow, in conflict with the 'hot disc dominated' AGN spectrum, which most probably implies a super Eddington accretion flow. The only persistent super Eddington BHB is GRS1915+105, which occasionally shows an additional QPO at 67 Hz. Mass scaling from this frequency implies that the AGN is also mildly super Eddington. The 67 Hz QPO is seen in data where the energy spectra are similarly dominated by a 'hot disc' component and the continuum power spectrum has similar shape and normalisation to that seen in the AGN. Hence we suggest that the AGN QPO in REJ1034+396 is the counterpart of the 67 Hz QPO seen in GRS1915+105.

Chapter 6

Paper 1: High Energy spectra of Seyferts & Unification schemes

6.1 Introduction

The simplest version of the Unification model of Antonucci & Miller (1985) is that the central engine (black hole, its accretion disc and broad line region: BLR) are the same in all AGN, but that this is embedded in an obscuring torus. The nucleus is seen directly only for inclination angles which do not intersect this material, giving the classic Seyfert 1 AGN signature of a strong and variable UV/X-ray continuum and broad emission lines. Conversely, where the obscuration is in the line of sight, these features are hidden, and the presence of an AGN can only be inferred from the high excitation lines produced in the narrow line region on much larger scales (Seyfert 2s). A key piece of evidence for this scenario is the detection of polarized broad emission lines in classic Seyfert 2 galaxies (most notably in NGC 1068), showing that the BLR is present, but can only be seen via scattered light (e.g. Antonucci & Miller 1985; Tran 1995, Heisler et al. 1997). This scattering medium, filling the 'hole' in the torus, is also detected in transmission in Seyfert 1s through the partially ionised absorption signatures seen in soft X-rays (e.g. Blustin et al. 2005).

The intrinsic X-ray spectrum of a type 1 AGN can be well described by a power-

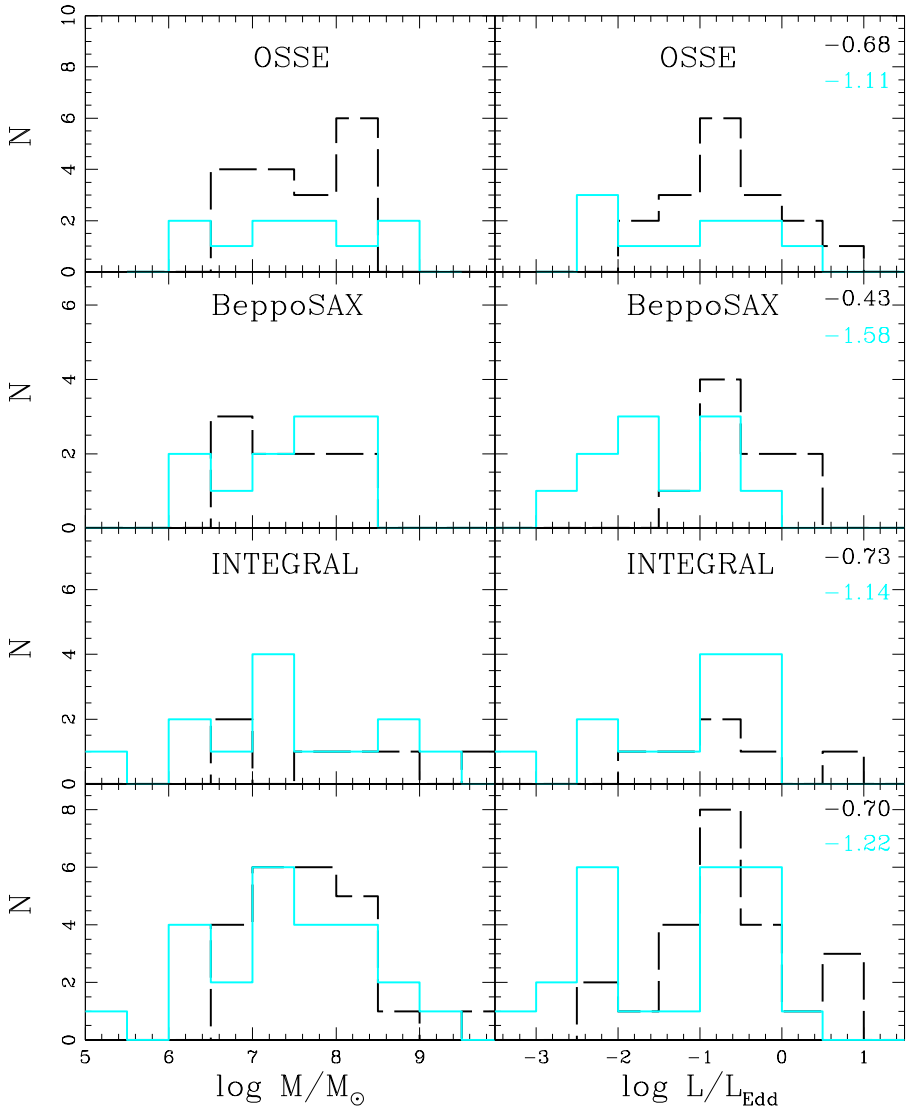

Figure 6.1: Plots showing the distribution of log mass and log accretion rate for individual instruments and the full sample (bottom panels) with Seyfert 1 sources shown by a black dashed line and Seyfert 2 sources by a solid cyan line. The log mean accretion rate for each type is given in the top right hand corner.

law (of photon spectrum $N(E) \propto E^{-\Gamma}$) together with its Compton reflection from the optically thick accretion disc and/or torus (e.g. Nandra & Pounds 1994). Again, the Unified models are supported by X-ray observations, which show that this intrinsic spectrum is substantially suppressed at low energies due to absorption in Seyfert 2s (Awaki et al. 1991; Smith & Done 1996; Turner et al. 1997; Bassani et al. 1999; Cappi et al. 2006). However, the strong energy dependence of photoelectric absorption means that this is unlikely to affect samples above 10 keV for columns which are not Compton thick, yet high energy experiments show that the intrinsic spectra of Seyfert 2 galaxies are systematically harder ($\Gamma \sim 1.9$ - 2) than for the Seyfert 1s, which have $\Gamma > 2$ (Zdiarski et al. 1995, Gondek et al. 1996, Perola et al. 2002, Malizia et al. 2003, Beckmann et al. 2006). This is not consistent with the idea that these nuclei are identical, unless the intrinsic emission is anisotropic, being harder in the equatorial plane.

However, all accreting black hole systems (both stellar and supermassive) generally show softer intrinsic spectra at higher accretion rates (hereafter parameterised as Eddington fraction, L/L_{Edd}), e.g. Laor (2000); Remillard & McClintock (2006). Thus inclination alone is not the sole determinant of the observed spectrum, and Seyferts at different L/L_{Edd} should not be expected to have the same intrinsic emission. Here we collate estimates of black hole mass and mass accretion rate for the Seyfert 1 and 2s detected out to > 50 keV from CGRO (OSSE), BeppoSAX (PDS) and INTEGRAL (IBIS) instruments. We show that these high energy samples of Seyferts span a large range in L/L_{Edd}, so should include a range of intrinsic spectral slopes. The mean L/L_{Edd} for the Seyfert 1s in the sample is higher than that for Seyfert 2s, consistent with the steeper spectral slope inferred for the Seyfert 1s being due to the intrinsic spectrum softening at higher L/L_{Edd}. We stress that samples of Seyfert 1 and 2 AGN need to be matched on intrinsic properties such as L/L_{Edd} in order to explore differences in orientation.

Source	Instrument	$\log M/M_\odot$	L/L_{Edd}	Reference
MCG–6-30-15	*OSSE* , *BeppoSAX*, *INTEGRAL*	$6.81\ ^{+0.54}_{-0.54}\ ^{\sigma}$	$0.25\ ^{x}$	6 (18) + 23
IC 4329A	*OSSE*	$6.70\ ^{+0.56}_{-peg}$ (mean) ^{r}	$0.79\ ^{f}$	20+ 20
		$6.85\ ^{+0.55}_{-peg}$ (rms) ^{r}		
MR 2251-178	*INTEGRAL*	$6.92\ ^{+0.22}_{-0.22}\ ^{m}$	$4.68\ ^{z}$	10 + 21
NGC3783	*OSSE* , *BeppoSAX*	$6.97\ ^{+0.30}_{-0.97}$ (mean) ^{r}	$0.23\ ^{f}$	2 + 20
		$7.04\ ^{+0.30}_{-0.96}$ (rms) ^{r}		
NGC7469	*OSSE* , *BeppoSAX*	$6.81\ ^{+0.30}_{-peg}$ (mean) ^{r}	$2.14\ ^{f}$	20 + 20
		$6.88\ ^{+0.29}_{-peg}$ (rms) ^{r}		
ESO 141-55	*OSSE* , *BeppoSAX*	$7.10\ ^{+0.57}_{-0.57}\ ^{m}$	$2.51\ ^{ox}$	1
MCG–2-58-22	*OSSE*	$7.14\ ^{+0.57}_{-0.57}\ ^{m}$	$3.47\ ^{ox}$	1
NGC6814	*OSSE*	$7.08\ ^{+0.57}_{-0.57}\ ^{r}$	$0.05\ ^{f}$	22 + 2
3C120	*BeppoSAX*	$7.36\ ^{+0.22}_{-0.28}$ (mean)^{r}	$0.65\ ^{f}$	20 + 20
		$7.48\ ^{+0.21}_{-0.27}$ (rms) ^{r}		
NGC3516	*OSSE*	$7.36\ ^{+0.59}_{-0.59}\ ^{r}$	$0.07\ ^{f}$	2
Mrk279	*OSSE*	$7.54\ ^{+0.10}_{-0.13}\ ^{r}$	$0.13\ ^{z}$	5
NGC3227	*OSSE*	$7.59\ ^{+0.19}_{-peg}$ (mean) ^{r}	$0.01\ ^{f}$	20 + 2
		$7.69\ ^{+0.18}_{-peg}$ (rms) ^{r}		
NGC5548	*OSSE* , *BeppoSAX*	$8.09\ ^{+0.09}_{-0.07}$ (mean) ^{r}	$0.05\ ^{f}$	20 + 20
		$7.97\ ^{+0.08}_{-0.07}$ (rms) ^{r}		
1H 1934-063	*INTEGRAL*	$7.86\ ^{+0.63}_{-0.63}\ ^{m}$	$0.07\ ^{ox}$	1
Fairall 9	*BeppoSAX*	$7.90\ ^{+0.11}_{-0.31}$ (mean) ^{r}	$0.16\ ^{s}$	20 + 20
		$7.91\ ^{+0.11}_{-0.32}$ (rms) ^{r}		

Table 6.1: Table A, see description in table B.

Source	Instrument	$\log M/M_{\odot}$	L/L_{Edd}	Reference
NGC7213	*OSSE*	$7.99\ ^{+0.64}_{-0.64}\ ^{\sigma}$	$0.02\ ^{f}$	2
MCG +8-11-11	*OSSE*	$8.06\ ^{+0.64}_{-0.64}\ ^{m}$	$0.35\ ^{ox}$	1
NGC526A	*OSSE* , *BeppoSAX*	$8.11\ ^{+0.65}_{-0.65}\ ^{\sigma}$	$0.17\ ^{ox}$	6 (18) + 1
Mrk841	*OSSE*	$8.49\ ^{+0.68}_{-0.68}\ ^{r}$	$0.17\ ^{f}$	22 + 2
Mrk509	*OSSE* , *BeppoSAX*, *INTEGRAL*	$8.16\ ^{+0.04}_{-0.04}\ ^{r}$	$0.45\ ^{ox}$	5 + 1
III Zw 2	*OSSE*	$8.42\ ^{+0.67}_{-0.67}\ ^{r}$	$0.13\ ^{z}$	3
PG 1416-129	*INTEGRAL*	$8.75\ ^{+0.70}_{-0.70}\ ^{r}$	$0.12\ ^{z}$	3
3C111	*INTEGRAL*	$9.56\ ^{+0.76}_{-0.76}\ ^{m}$	$0.01\ ^{z}$	9

Table 6.2: Table B: Seyfert 1 sub-sample. Name superscripts indicate the hard X-ray satellite that observed the source, o: *OSSE*, i: *INTEGRAL*, b: *BeppoSAX*. Mass superscripts refer to the measurement method, σ: stellar velocity dispersion, r: reverberation mapping, m: other. Accretion rate superscripts denote the method by which the bolometric luminosity was determined, x: correction from X-ray, f: integration of the SED flux, ox: correction from OIII, s: SED modelling, z: other. References, 1: Wang et al. (2007), 2: Woo & Urry (2002), 3: Hao et al. (2005), 4: McHardy (1988), 5: Vestergaard & Peterson. (2006), 6: Garcia-Rissmann et al. (2005), 7: Bian & Gu (2007), 8: Greenhill et al. (1997), 9: Grandi et al. (2006), 10: Morales & Fabian (2002), 11: Marconi et al. (2006), 12: Whysong & Antonucci (2004), 13: Awaki et al. (2005), 14: Czerny et al. (2001), 15: Tadhunter et al. (2003), 16: van Bemmel et al. (2003), 17: Gu et al. (2006), 18: Tremaine et al. (2002), 19: Risaliti et al. (2005), 20: Kaspi et al. (2000), 21: Monier et al. (2001), 22: Laor et al. (2001) 23: Dadina (2007). Where more than one reference is given, the first refers to the black hole mass and the second to the accretion rate. Where reference 18 is given in brackets, the relation from Tremaine et al. (2002) has been used to determine the black hole mass via stellar velocity dispersion.

Source	Instrument	$\log M/M_{\odot}$	L/L_{Edd}	Reference
NGC6300	*INTEGRAL*	$5.45^{+0.44\ m}_{-0.44}$	$0.91^{\ x}$	13
NGC7314	*BeppoSAX*	$6.03^{+0.48\ \sigma}_{-0.48}$	$0.41^{\ x}$	17 (+18)
NGC4945	*OSSE* , *INTEGRAL*	$6.15^{+0.49\ \sigma}_{-0.49}$	$0.17^{\ x}$	8
MCG–5-23-16	*OSSE* , *BeppoSAX*	$6.29^{+0.50\ m}_{-0.50}$	$0.09^{\ ox}$	1
Circinus	*INTEGRAL*	$6.42^{+0.51\ \sigma}_{-0.51}$	$0.32^{\ ox}$	7
NGC5506	*OSSE*	$6.65^{+0.53\ \sigma}_{-0.53}$	$2.51^{\ ox}$	7
NGC4593	*INTEGRAL*, *BeppoSAX*	$6.91^{+0.55\ r}_{-0.55}$	$0.12^{\ f}$	2
ESO 103-G35	*INTEGRAL*, *BeppoSAX*	$7.14^{+0.57\ m}_{-0.57}$	$0.01^{\ x}$	14
NGC4388	*OSSE* , *INTEGRAL*	$7.22^{+0.58\ \sigma}_{-0.58}$	$0.79^{\ ox}$	7
NGC1068	*INTEGRAL*	$7.23^{+0.58\ \sigma}_{-0.58}$	$0.44^{\ f}$	8 + 2
NGC7582	*OSSE*	$7.25^{+0.58\ \sigma}_{-0.58}$	$0.35^{\ ox}$	7
NGC5674	*BeppoSAX*	$7.36^{+0.59\ \sigma}_{-0.59}$	$0.17^{\ x}$	17 (+18)
ESO 323-G077	*INTEGRAL*	$7.39^{+0.59\ m}_{-0.59}$	$0.28^{\ ox}$	1
NGC4507	*OSSE* , *INTEGRAL*	$7.58^{+0.61\ \sigma}_{-0.61}$	$0.27^{\ ox}$	7
NGC4258	*BeppoSAX*	$7.62^{+0.61\ \sigma}_{-0.61}$	$0.01^{\ f}$	2
NGC7172	*OSSE* , *BeppoSAX*	$7.67^{+0.61\ \sigma}_{-0.61}$	$3\text{x}10^{-3\ ox}$	7
NGC2992	*BeppoSAX*	$7.72^{+0.62\ \sigma}_{-0.62}$	$0.01^{\ f}$	2
NGC5252	*BeppoSAX*	$8.04^{+0.64\ \sigma}_{-0.64}$	$0.17^{\ s}$	2
Centaurus A	*INTEGRAL*	$8.04^{+0.64\ \sigma}_{-0.64}$	$7\text{x}10^{-4\ s}$	11 + 12
NGC1365	*BeppoSAX*	$8.18^{+0.65\ m}_{-0.65}$	$2\text{x}10^{-3\ x}$	19
NGC2110	*OSSE* , *BeppoSAX*	$8.30^{+0.66\ \sigma}_{-0.66}$	$5\text{x}10^{-3\ f}$	2
NGC1275	*OSSE* , *INTEGRAL*	$8.51^{+0.68\ \sigma}_{-0.68}$	$0.03^{\ f}$	2
Mrk3	*OSSE* , *INTEGRAL*	$8.65^{+0.69\ \sigma}_{-0.69}$	$6\text{x}10^{-3\ f}$	2
Cyg A	*INTEGRAL*	$9.40^{+0.75\ \sigma}_{-0.75}$	$8\text{x}10^{-3\ x}$	15 + 16

Table 6.3: Seyfert 2 sub-sample. Superscripts and references as for Table 6.2.

6.2 Data

We construct a moderately sized sample of local, hard X-ray detected AGN. These data, shown in Table 1, 2 & 3, are taken from Malizia et al. (2003 - *BeppoSAX*), Zdziarski et al. (2000 - *OSSE*) and Beckmann et al. (2006 - *INTEGRAL*), resulting in a total sample of 47 AGN; 23 Seyfert 1s and 24 Seyfert 2s. There is always some ambiguity in assigning objects as type 1 or 2, firstly as there are optical intermediate types, and secondly as the absorption environment is complex. There is (Compton thin) molecular gas in the plane of the galaxy as well as the much smaller scale (and possibly Compton thick) molecular torus (Maiolino & Rieke 1995), and these two obscuring structures are not aligned (Nagar & Wilson 1999; Schmitt et al 2002). Thus a face on (type 1) nucleus can be obscured at both optical and X–ray wavelengths, leading to a type 2 classification (e.g. NGC 5506: Nagar et al 2002). Nonetheless, these classifications are those for which the difference in X-ray spectral index is claimed, so this is the only sample definition we can use to explore whether accretion rate can be the reason for this difference.

The black hole masses for the objects in the sample are derived primarily from stellar velocity dispersion (21 objects) and reverberation mapping (15 objects). For the remaining 11 sources the black hole masses are inferred from optical line widths and X-ray variability measurements. For those sources with reverberation mapping measurements, the black hole mass errors quoted are those stated in the referenced literature. For the remaining sources, the quoted black hole mass errors are calculated from the relation presented in Tremaine et al. (2002).

The bolometric luminosities for the majority of the sample (22 objects) have been calculated by converting the OIII and/or X-ray luminosity to bolometric luminosity, using the relations given in Wang & Zhang (2007) and Satyapal et al. (2005) respectively. For the remaining sources, 20 have bolometric luminosities measured from the AGN SED (17 from integration of the SED and 3 from modelling) and

the remaining 5 sources have bolometric luminosities stated in the literature. The mass accretion rate is parameterised by the ratio of the bolometric luminosity to the Eddington luminosity for the given black hole mass, i.e. $\dot{M}=L_{bol}/L_{Edd}$ where $L_{Edd} = 1.3 \times 10^{38}(M_{BH}/M_{\odot})$.

Figure 6.1 shows the distribution of black hole mass (left panel) and Eddington fraction (right panel) for each of the high energy samples of Seyfert 1s (black, dashed line) and Seyfert 2s (cyan, solid line). It is plain that the mass accretion rates span a wide range in $L/L_{Edd} \sim 10^{-3}$–1. This means that these AGN form a very heterogeneous sample, with the clear expectation that their high energy spectra are also heterogeneous.

The mean log mass accretion rate for each of the samples is given in the top right hand corner of the plot with Seyfert 1 in black and Seyfert 2 in red. All three instruments have higher mean L/L_{Edd} for Seyfert 1s than for the Seyfert 2s. For the complete sample we perform a series of 10,000 Monte Carlo Bootstrap simulations in order to determine rigorously the statistical significance of differences between the Seyfert 1 and Seyfert 2 distributions. The Monte Carlo Bootstrap simulations randomly select objects from the parent sample to construct paired random sub-samples (of the correct size). We then calculate the mean of the interesting parameters for each randomly generated sub-sample, and the difference between these means for the sub-samples in each pair. We then measure the frequency with which our random sub-samples show differences greater than, or equal to the differences measured between the Seyfert 1 and Seyfert 2 sub-samples.

The result of the bootstrap analysis shows that the difference is significant at only $\sim 1.7\sigma$ for the combined sample, though the mean L/L_{Edd} for the Seyfert 2s and Seyfert 1s are 0.06 and 0.20, respectively. We also try to assess the systematic uncertainties in this result due to the mass determination. Hβ FWHM values can give an alternative measure of black hole mass for the Seyfert 1s (e.g. Salviander

et al. 2006), and we find that these are within 0.3 dex for all but one source (MR 2251-178). Removing all sources where the mass and resulting accretion rate is not found from stellar velocity dispersion or reverberation mapping (which removes MR 2251-178) reduces the significance of the difference to $<1\sigma$ due to the smaller sample size. Nevertheless, the Seyfert 1 sample still has the higher mean accretion rate (0.15 compared to 0.06 for the Seyfert 2s).

6.3 Discussion

The X-ray spectra of stellar mass black hole binaries can be well described by a combination of emission from the accretion disc and a Comptonised tail (see e.g. the reviews by Remillard & McClintock 2006; Done, Gierliński & Kubota 2007). The relative importance of the disc and tail can change dramatically, as does the shape of the tail, giving rise to the well known 'spectral states' as a function of (average) L/L_{Edd}. In the low/hard state, generally seen at luminosities below a few percent of Eddington, the tail dominates the X-ray emission and its spectral index is fairly well correlated with (average) mass accretion rate, with $\Gamma \sim 1.5$ at the lowest luminosities softening to $\Gamma \sim 2.1$ just before the major transition to the soft, or disc dominated states. The tail in these states can be very weak, carrying less than 20 per cent of the total bolometric power, when it has $\Gamma \sim 2.1$ (disc dominant state). Conversely, the tail can also be much stronger and softer, with $\Gamma \sim 2.5$ (very high state or steep power-law state).

AGN spectra should show analogous spectral states if the properties of the accretion flow scale simply with black hole mass. There is evidence for this simple scaling, from the radio-X-ray 'fundamental plane' relations (Merloni, Heinz, & Di Matteo 2003; Falcke, Körding & Markoff 2004) and X-ray variability properties (McHardy et al. 2007; Gierliński et al. 2007). In this picture (see e.g. Boroson 2002), LINERS, with their hard X-ray spectra and weak UV disc, are the analogues

of the low/hard state (but see Maoz 2007), while Seyfert 1 and QSOs at higher L/L_{Edd} correspond to the disc dominated states, with the characteristic strong UV disc emission and consequent broad emission lines, and the Narrow line Seyfert 1s at the highest L/L_{Edd} may be the analogues of the very high state (Pounds, Done & Osborne 1995; Middleton, Done & Gierliński 2007).

Observations of type 1 AGN spectra in the 2–10 keV band are consistent with this predicted softening of the intrinsic spectrum with increasing L/L_{Edd} (e.g. Laor 2000), so it seems highly likely that the high energy X–ray spectra considered here should also change with L/L_{Edd}. We show that current samples of Seyferts detected at high energies are clearly highly heterogeneous in this parameter (see fig 6.1), so the mean spectral index will be determined by a signal–to–noise weighted average of L/L_{Edd}. The L/L_{Edd} distributions for the total Seyfert 1 and Seyfert 2 samples presented here are not significantly different (statistically) however the individual OSSE, BeppoSAX and INTEGRAL samples considered here are all consistent with having a higher mean L/L_{Edd} for the Seyfert 1s than for the Seyfert 2s. Thus, despite the limited sample size the apparently steeper spectra seen in the Seyfert 1s at high energy may be be due to an intrinsic softening with increasing L/L_{Edd}. Future studies with larger samples of high energy spectra of AGN should be able to test unambiguously whether L/L_{Edd} is the major parameter in determining the shape of the 20–100 keV spectrum in Compton thin Seyferts (see Winter et al. 2009).

Chapter 7

Paper 2: An absorption origin for the soft excess in S1 AGN

7.1 Introduction

X-ray spectra and variability provide important evidence to suggest that accretion systems of AGN are analogous to those of their smaller counterparts, the black hole binary (BHB) systems. Both show two major components in their high energy spectra, the accretion disc, together with a tail of emission extending to higher energies. The accretion disc temperature should scale with both mass ($m = M/M_{\odot}$) and mass accretion rate (hereafter parameterised as L/L_{Edd}) as $T \sim 10^7 (L/L_{Edd})^{1/4} m^{-1/4}$ K (Shakura & Sunyaev 1973). This component peaks in the soft X–ray range for bright BHB, but correspondingly large L/L_{Edd} AGN have discs which peak in the UV–optical region of the spectrum. This complicates a detailed comparison of the two systems. In BHB, the X–ray spectra contain contributions from both the disc and tail, whereas in AGN only the tail should contribute. This is particularly important as BHB show a complex range of *spectral states*, which can be roughly determined by the luminosity ratio between the disc and tail, together with the shape of the tail (see e.g. Remillard & McClintock 2006). In BHB these can all be (more or less) determined simply from a single X–ray spectrum, whereas to con-

strain the disc emission in AGN requires simultaneous UV–optical as well as X–ray data. This is now easily obtainable with the launch of the XMM-Newton satellite, which carries the Optical Monitor telescope with optical/UV filters, as well as the sensitive EPIC X–ray CCDs.

In BHB, the disc and high energy tail are well known to have different variability properties on short timescales, where the disc is rather constant while the high energy tail is not (e.g Churazov Gilfanov & Revnivtsev 2001). The effects of the stable accretion disc diluting the observed X–ray variability is important in BHB, and correcting for this effect results in AGN and BHB showing very similar variability power spectra (Done & Gierliński 2005), with characteristic frequencies simply scaling with mass for a given L/L_{Edd} (McHardy et al. 2006). This points to the same underlying physical mechanisms for forming the tail in both systems, strongly supporting models in which the accretion processes are the same.

However, despite this overall correspondence between the two systems, there are clear discrepancies which remain unexplained. Firstly there is the 'soft excess' seen ubiquitously in high L/L_{Edd} AGN. This is a smooth rise above the extrapolation of the higher energy continuum below ~ 1 keV. This energy is too high to be explained by the standard accretion disk model above, and alternative continuum models such as Comptonization of the disc (e.g. Czerny & Elvis 1987; Page et al. 2004) or a super-Eddington slim disk (e.g. Abramowicz et al. 1988; Tanaka, Boller & Gallo 2005) have problems in explaining why this component is always seen at the same energy in AGN spanning a large range in mass (Gierliński & Done 2004: hereafter GD04), and why this has no obvious counterpart in the BHB (GD04; Sobolewska & Done 2007). Secondly, some of these high L/L_{Edd} AGN have apparently flat 2–10 keV spectra. BHB at correspondingly high L/L_{Edd} normally have rather steep tails to high energies, with photon index $\Gamma > 2$ when characterised by a power-law (e.g. the review by Remillard & McClintock 2006).

Both of these problems can be addressed if there is substantial distortion of the AGN spectra by atomic processes. This rather naturally gives rise to a fixed energy for the soft excess from the dramatic increase in opacity in partially ionised material at ~ 0.7 keV provided by O VII/O VIII and the Fe M shell unresolved transition array (UTA). The observed smoothness of the soft excess then requires that this partially ionised material has strong velocity gradients to remove any lines or edges by Doppler smearing. This material can affect the spectrum in two rather different geometrical configurations, either in optically thick material seen in reflection (e.g. Crummy et al. 2006) or optically thin material seen in absorption (e.g. Gierliński & Done 2004, hereafter GD04; Chevallier et al. 2006), but in both models the enhanced opacity above 0.7 keV can lead to an apparently flat 2–10 keV spectrum even when the intrinsic emission is steep.

This all makes a compelling case for there to be substantial amounts of partially ionised, Doppler smeared material in AGN. Even if the same material is present in BHB it would not be easily seen as the higher temperature accretion disc will result in complete photoionization of Oxygen, so will not produce the strong opacity jump at 0.7 keV. In which case the question becomes whether this material is seen in reflection or absorption. This has additional importance as the difference between absorption and reflection mechanisms implies not only differing physical geometries but also a difference in the inferred properties of the spacetime (Gierliński & Done 2006).

In the reflection models, the strength of the soft excess is limited if the source is isotropic. The maximum reflected continuum below 0.7 keV equals the incident continuum and, even including line emission, results in a soft excess of no more than a factor of 2-3 above the extrapolated 2–10 keV continuum (Sobolewska & Done 2007). This is exceeded by many high L/L_{Edd} AGN, dramatically so by a few objects. Thus the reflection geometry also requires anisotropic illumination from

either gravitational light bending or a corrugated disc surface which acts to hide a large proportion of the incident flux from the line of sight (Fabian et al. 2002a; Miniutti et al. 2003; Miniutti & Fabian 2004). The problem becomes even more marked if the reflecting disc material is in hydrostatic equilibrium, as the details of the pressure balance means that there is only a small optical depth in the disc photosphere where Oxygen can be partially ionised. Thus these models give a much smaller soft excess than a constant density reflecting slab (Done & Nayakshin 2007).

Instead, the absorption model sets no such restrictive limits on the size of the soft excess, so does not require any geometry change to produce the strongest observed soft excesses (Sobolewska & Done 2007). Additionally, and in stark contrast to the reflection models, any pressure balance condition rather naturally produces the required (now much smaller) optical depth of partially ionised Oxygen (Chevallier et al. 2006).

While this all supports the absorption model, these arguments are indirect, relying on physical plausibility. A clear observational test between the two models would be more convincing. However, detailed studies of individual objects have shown that even good quality XMM-Newton data in the 0.3–10 keV bandpass cannot distinguish between reflection and absorption models for the origin of the spectral features (Chevallier et al. 2006; Sobolewska & Done 2007). Similarly, the 0.3–10 keV variability rms spectra of individual objects can also be equally well matched by both models (Ponti et al. 2006; Gierliński & Done 2006). This is the case even for the canonical reflection dominated, broad line source, MCG-6-30-15, for which the 0.3-10 keV spectrum and rms variability can be well fit by both reflection and absorption models (Done 2007; Gierliński & Done 2006). Even extending the bandpass to 40 keV (such as with the Suzaku HXD: Miniutti et al. 2007) does not break the model degeneracy of the spectra for this object (Done 2007), though the fact that the variable component can be well fit by a simple absorbed power-law is plainly

consistent with the reflection modelling (Miniutti et al. 2007).

Here instead we analyse the spectra of a large sample of PG quasars and Narrow Line Seyfert 1 galaxies fitted with the absorption models. This sample has previously been studied by Crummy et al. (2006), who fit the smeared reflection model so allowing a direct comparison of fit quality over a larger number of objects, with a large spread in spectral shape. We use XMM-Newton data so we can directly constrain the disc simultaneously with the high energy tail, and so directly test whether these do indeed correspond to the BHB high L/L_{Edd} spectral states, and identify where the anomalous soft excess and hard 2–10 keV spectra arise.

7.2 Data

We use the same source sample of high mass accretion rate AGN (PG Quasars and NLS1s) as Crummy et al. (2006). Those which overlapped the sample of GD04 had spectra extracted from the XMM-*Newton* database using SAS 5.4 software, selecting only X-ray events corresponding to patterns 0-12 (MOS) and 0-4 (PN), while those not included in the GD04 sample were extracted using SAS 7.0 with appropriate checks for consistency in extraction method and output performed. Source and background spectra were extracted from circular regions of 45 arcsec in radius around the object and in an offset position clear of other sources respectively. XMM-*Newton* Optical Monitor (OM) data was extracted using *omichain*, and the extracted instrumental magnitudes converted to flux points, calibrated with respect to Vega in each filter, with calibration values and corresponding fluxes provided by the XMM-*Newton* Science Operations Centre.[1]

[1]http://xmm.vilspa.esa.es/sas/documentation/watchout/uvflux.shtml

Source	z	logM/M$_\odot$	L/L$_{Edd}$	Galactic column (x10^{20}cm^{-}2)	$\Gamma_{2-10keV}$	Soft Excess at 0.5keV	Obs. Date
PG 0003+199	0.025	7.07	0.62	3.99	$2.216\ ^{+0.016}_{-0.016}$	2.680	2000-12-25
PG 0050+124	0.061	7.13	1.81	4.99	$2.284\ ^{+0.025}_{-0.024}$	1.008	2002-06-22
PG 0157+001	0.163	8.00	0.54	2.59	$2.117\ ^{+0.145}_{-0.139}$	1.712	2000-07-29
PG 0844+349	0.064	7.66	0.41	2.98	$2.126\ ^{+0.034}_{-0.034}$	2.621	2000-11-04
PG 0947+396	0.206	8.46	0.14	1.57	$1.843\ ^{+0.058}_{-0.057}$	2.682	2001-11-03
PG 0953+414	0.239	8.52	0.58	1.14	$1.974\ ^{+0.053}_{-0.053}$	2.512	2001-11-22
PG 1048+342	0.167	8.14	0.25	1.83	$1.804\ ^{+0.056}_{-0.055}$	2.367	2002-05-13
PG 1115+407	0.154	7.44	0.82	1.91	$2.133\ ^{+0.074}_{-0.073}$	2.800	2002-05-17
PG 1116+215	0.177	8.41	0.74	1.28	$2.076\ ^{+0.070}_{-0.069}$	2.356	2001-12-02
PG 1202+281	0.165	8.37	0.11	1.67	$1.657\ ^{+0.045}_{-0.044}$	2.543	2002-05-30

Table 7.1: Table A, see description of table B.

Source	z	logM/M$_\odot$	L/L$_{Edd}$	Galactic column (x10^{20}cm^{-}2)	$\Gamma_{2-10keV}$	Soft Excess at 0.5keV	Obs. Date
PG 1211+143	0.080	7.81	1.14	2.75	$1.765\ ^{+0.024}_{-0.024}$	2.961	2001-06-15
PG 1244+026	0.048	6.24	3.97	1.75	$2.486\ ^{+0.086}_{-0.084}$	3.609	2001-06-17
PG 1307+085	0.155	8.50	0.24	2.11	$1.494\ ^{+0.072}_{-0.071}$	2.454	2002-06-13
PG 1309+355	0.184	8.20	0.33	1.03	$1.755\ ^{+0.085}_{-0.084}$	1.614	2002-06-10
PG 1322+659	0.168	7.74	0.81	2.01	$2.156\ ^{+0.099}_{-0.096}$	2.925	2002-05-11
PG 1352+183	0.158	8.20	0.29	2.05	$1.926\ ^{+0.089}_{-0.087}$	4.075	2002-07-20
PG 1402+261	0.164	7.76	1.24	1.47	$2.069\ ^{+0.080}_{-0.079}$	4.227	2002-01-27
PG 1404+226	0.098	6.65	1.90	2.14	$1.002\ ^{+0.548}_{-0.455}$	77.61	2001-06-18
PG 1427+480	0.221	7.86	0.57	1.88	$1.922\ ^{+0.055}_{-0.054}$	2.363	2002-05-31
PG 1440+356	0.077	7.28	1.07	1.03	$2.276\ ^{+0.051}_{-0.050}$	3.391	2001-12-23
PG 1444+407	0.267	8.17	0.71	1.25	$2.107\ ^{+0.139}_{-0.126}$	3.752	2002-08-11
PG 1501+106	0.036	8.23	0.12	2.34	$1.940\ ^{+0.025}_{-0.025}$	2.769	2001-01-14

Table 7.2: Table B: Source properties of the PG quasars analysed here. Mass and luminosity are taken from Gierliński & Done (2004), based on Boroson (2002). The soft excess strength is the ratio of the source data to the extrapolated 2–10 keV power-law at 0.5keV.

Source	z	logM/M$_\odot$	L/L$_{Edd}$	Galactic column (x10^{20}cm^{-}2)	$\Gamma_{2-10keV}$	Soft Excess at 0.5keV	Obs. Date
NGC 4051	0.002	6.13 [f]	0.31 [a]	1.32	$1.245^{+0.048}_{-0.048}$	3.601	2001-05-16
IRAS 13349+2438	0.108	8.90 [d]	0.24[i]	1.16	$1.966^{+0.044}_{-0.043}$	3.634	2000-06-20
ARK 564	0.025	6.46 [e]	2.75 [a]	6.40	$2.501^{+0.027}_{-0.027}$	2.257	2000-06-17
MRK 1044	0.016	6.23 [e]	1.25 [a]	3.55	$1.937^{+0.062}_{-0.061}$	3.472	2002-07-23
E 1346+266	0.915	8.30 [b]	1.40 [b]	1.18	$2.299^{+0.290}_{-0.239}$	2.612	2003-01-13
MRK 0359	0.017	6.23 [e]	1.79 [a]	4.80	$1.765^{+0.063}_{-0.062}$	2.312	2000-07-09
PHL 1092	0.396	8.20 [b]	$\sim$1.00 [b]	4.07	$1.979^{+0.355}_{-0.443}$	18.621	2003-01-18
RE J1034+396	0.042	6.45 [a]	0.28 [a]	1.47	$2.290^{+0.256}_{-0.246}$	7.325	2002-05-01
PKS 0558-504	0.137	7.65 [c]	1.72 [g]	4.38	$2.255^{+0.053}_{-0.052}$	2.344	2000-05-24
MRK 0766	0.013	6.63 [e]	0.47 [a]	1.71	$1.917^{+0.028}_{-0.028}$	1.624	2000-05-20
MRK 0586	0.155	7.86 [f]	3.37 [h]	3.51	$2.245^{+0.083}_{-0.082}$	2.659	2002-07-23
TON S180	0.062	7.06 [f]	2.98 [a]	1.55	$2.286^{+0.034}_{-0.033}$	2.461	2000-12-14

Table 7.3: As for Table 7.2 but for the non-PG QSOs used in the extended AGN sample of Crummy et al. (2006). References are to: [a] Hao et al. (2005), [b] Dasgupta et al. (2004), [c] Brinkmann et al. (2004), [d] Blustin et al. (2005), [e] Wang & Lu (2001), [f] Woo & Urry (2002), [g] O'Brien et al. (2001), [h] Bian & Zhao (2003), [i] Beichman et al. (1986).

7.2.1 Sample properties

The Crummy et al. (2006) sample contains 21 NLS1 and 13 broad line AGN. The distribution of luminosities (from tables 1 & 2) are shown as a histogram in Fig. 7.1 and clearly show that the NLS1 AGN are the major contributors at the high luminosity end. A χ^2 test shows that the two luminosity distributions are different at 92 per cent confidence ($\chi^2/\nu = 14.2/8$), with the NLS1s having systematically higher inferred L/L_{Edd} than the non-NLS1 AGN, as noted by e.g. Boroson (2002).

We follow Sobolewska & Done (2007) and parameterise the strength of the soft excess in each source by fitting a power-law with galactic absorption to the 2-10 keV spectrum and then taking the ratio of this to the data at 0.5 keV. Fig. 7.2 shows the histogram of these values. Whilst the NLS1s show the highest soft excess values, the distribution is not significantly different to that of the broad line AGN. More than 70 per cent of the sample have soft excesses greater than the maximum value from isotropic reflection of ~ 2 (see fig. 7.4), and three sources (PG1404+226, PHL 1092 and REJ1034+396) have soft excesses ≥ 5.

Fig. 7.3 shows the distribution of apparent 2–10 keV power-law index. For this, and for all other histograms of fit parameters where the uncertainties are well defined, we use a bootstrap Monte Carlo method to assess the impact of these on each bin of the histogram. The uncertainties (shown as an error bar on each bin) are not independent as they have to sum to the given number of objects, but it is clear that the NLS1s show a different distribution to the broad line AGN. However, this is not a simple difference in mean spectral index as seen in previous studies where NLS1s were significantly steeper than broad line AGN over 2–10 keV (Brandt, Mathur & Elvis 1997). Fig. 7.3 shows that there are some NLS1s which are extremely flat, as well as some being very steep. The two sets of objects have similar mean indices in these samples, but the NLS1s have larger dispersion. As pointed out by Gierliński & Done (2004), intrinsic power-laws with $\Gamma < 2$ are not compatible with the *steep*

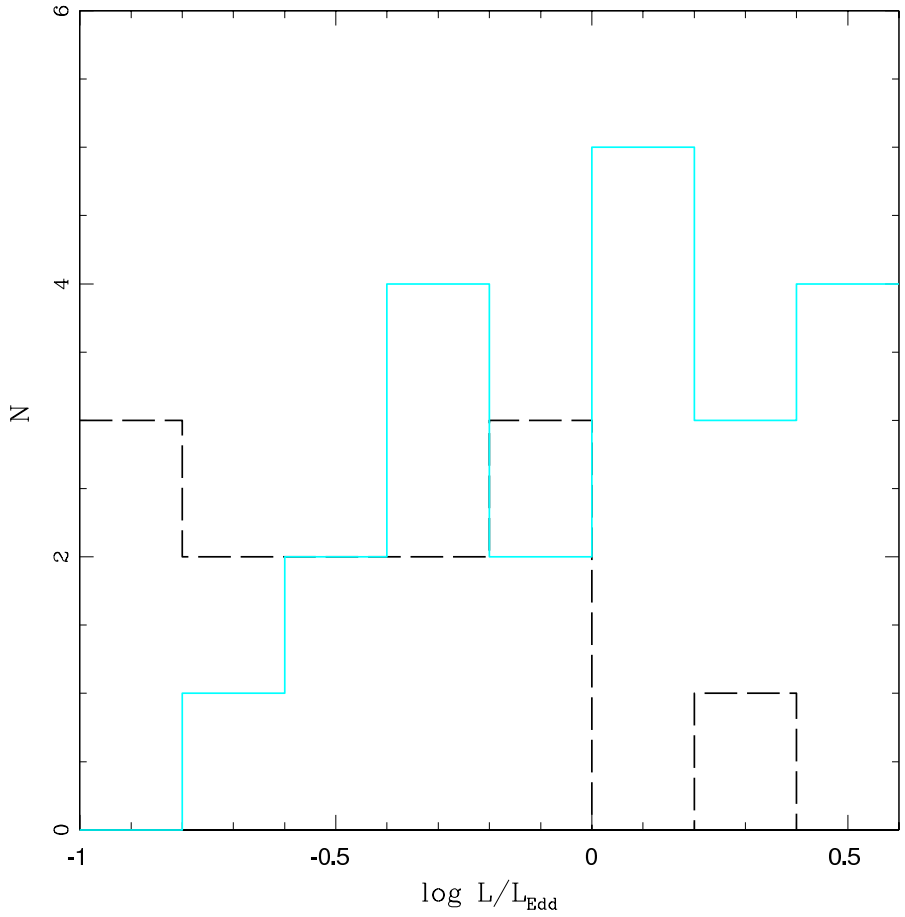

Figure 7.1: Histogram showing the distribution of luminosities across the sample. The NLS1s (cyan) clearly dominate the high luminosity end, with broad line AGN (black) having generally lower L/L_{bol}.

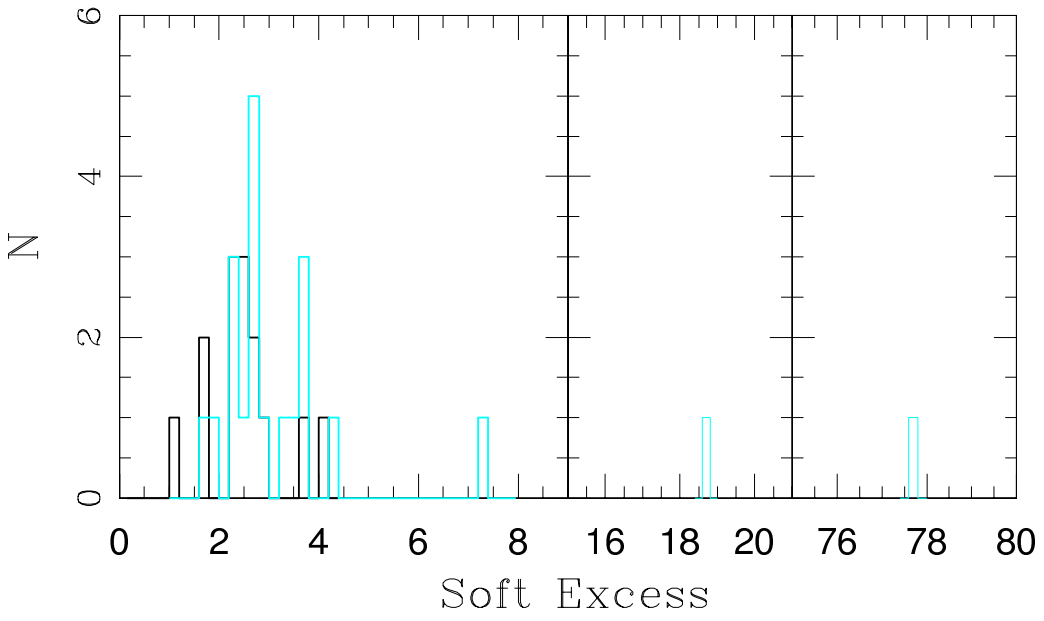

Figure 7.2: Histogram showing the distribution of soft excess (SX) at 0.5keV across the sample. The largest values of SX are found in the NLS1s (cyan) but there is also substantial overlap with the broad line AGN (black) at lower SXs.

tail seen in similarly high mass accretion rate BHB. Either the underlying emission mechanisms are substantially different between the stellar and supermassive black holes, or these spectra are highly distorted.

Fig. 7.4 shows the soft excess strength versus the 2–10 keV power-law spectral slope. This shows that there is no overall correlation between these two. This is somewhat surprising, as both reflection and absorption models would be expected to show such a correlation in their simplest versions where the ionization state of the material remains constant. However, observations show that the variability is more complex. Detailed variability studies of individual objects show that the spectra are steep at high flux levels, with iron features in emission and a moderate soft excess, while at minimum flux the 2–10 keV spectrum is very flat, with an extremely strong soft excess and complex Iron features (e.g. Miller et al. 2007).

7.3 Spectral fitting and results

We now fit the full smeared absorption model, SWIND1 as described by Gierliński & Done (2006) to the full 0.3–10 keV spectral data. This is parameterised by the velocity dispersion (σ, with upper limit of 0.5c as the terminal velocity in an outflow is at least twice the Gaussian dispersion), which controls the amount of smearing, as well as column density, N_H, and ionization state ξ. This smeared absorption is applied to an intrinsic power-law, and its reflected emission using the XION hydrostatic disc models, with inner and outer radii set to 30 and $1000R_g$ respectively, leaving the solid angle and ratio of X–ray to intrinsic disc illumination as free parameters. The limit of $30R_g$ is simply a result of not being able to constrain reflection when the soft excess has been made by absorption. This total spectrum is further modified by galactic absorption (WABS, with minimum value set to the Galactic column along the line of sight but with upper limit free to allow for host galaxy absorption) and one or more warm absorbers (XSTAR table models 19 and 25, publicly available from the XSTAR web site[2]), parameterised by column density, $N_{H,XSTAR}$, and ionization state ξ_{XSTAR}. We fix the redshift of both the narrow and smeared ionized absorbers to the rest-frame of the AGN. Our model then allows enough free-parameters to describe the data consistently across a broad sample and be well constrained even in the case of poor signal-to-noise.

[2]ftp://legacy.gsfc.nasa.gov/software/plasma_codes/xstar/xspectables

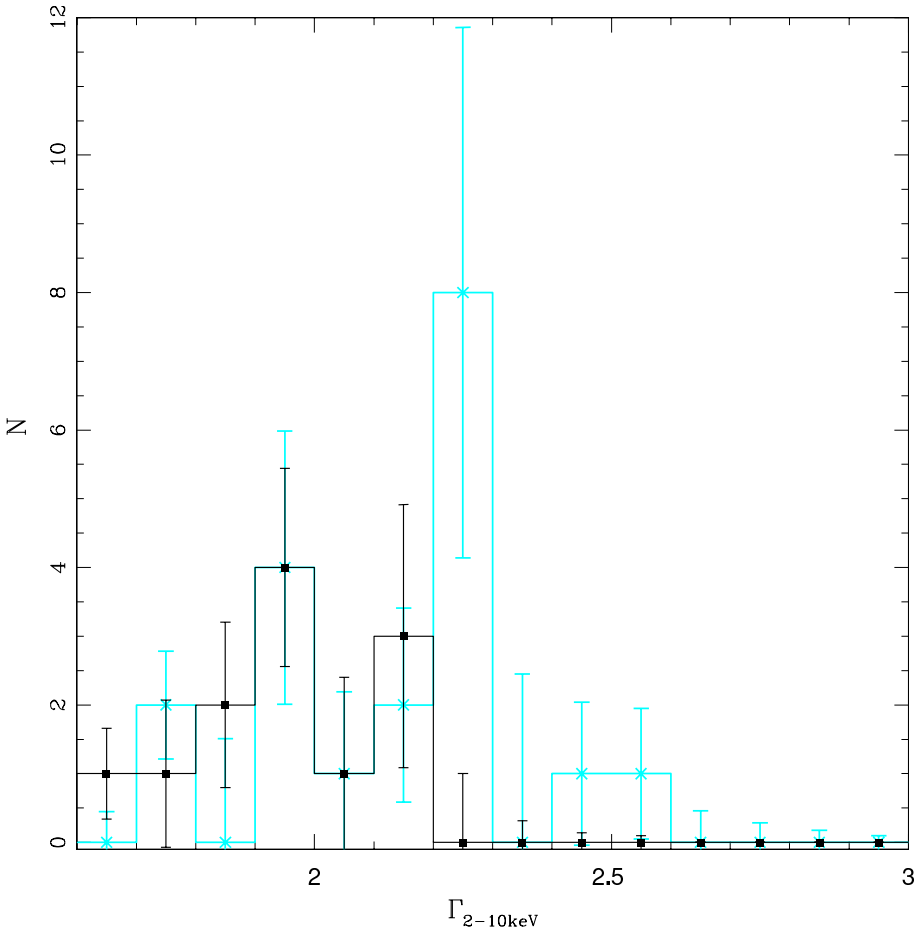

Figure 7.3: Histogram of the 2–10 keV power-law spectral index for the NLS1s (cyan) and broad line AGN (black). Error bars on the distribution are derived from a bootstrap Monte–Carlo method from the observed uncertainties on $\Gamma_{2-10\ keV}$. Although the steepest spectral indices are associated with the NLS1s, there is substantial overlap between the two AGN types, and both show spectra significantly flatter than $\Gamma_{2-10\ keV} = 2$, which is very unusual in high mass accretion rate BHBs.

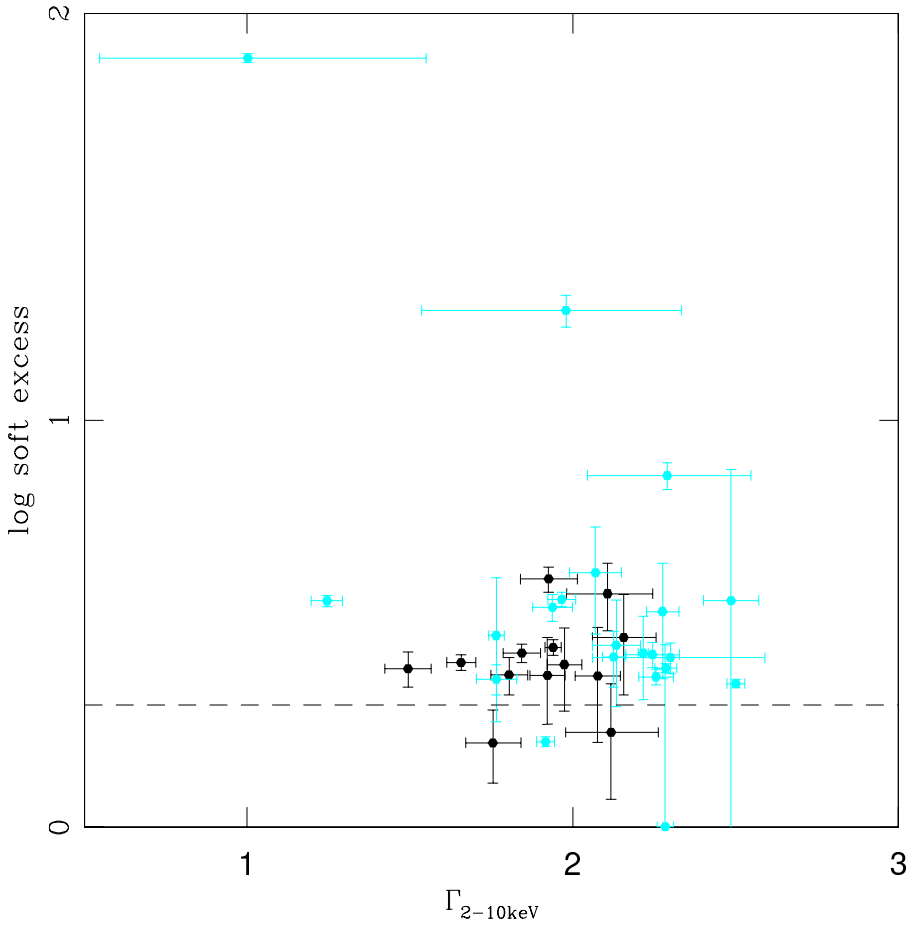

Figure 7.4: Soft excess strength (measured at 0.5keV) versus apparent 2–10 keV power-law spectral index for NLS1s (cyan) and broad line AGN (black). The object with the largest soft excess also has a flat spectrum, but in general there is no clear correlation, nor dependence on AGN type. The dashed horizontal line shows the limit of soft excess that can be produced by a reflection model.

Source	χ^2_ν (d.o.f) Reflection	χ^2_ν (d.o.f) Absorption	SWIND1 ξ	SWIND1 N_H	SWIND1 σ	Intrinsic Γ	L_{disc}/L_{bol}
PG 0003+199*	0.939 (968)	1.214 (2112)	$2.879\ ^{+0.043}_{-0.035}$	$11.1\ ^{+1.0}_{-1.2}$	$0.500\ ^{+peg}_{-0.005}$	$2.559\ ^{+0.014}_{-0.015}$	0.409
PG 0050+124*	1.117 (924)	1.183 (1616)	$3.608\ ^{+0.022}_{-0.047}$	$50.0\ ^{+peg}_{-5.0}$	$0.500\ ^{+peg}_{-0.033}$	$2.457\ ^{+0.013}_{-0.015}$	0.518
PG 0157+001	0.861 (234)	1.030 (511)	$3.229\ ^{+0.460}_{-0.496}$	$19.4\ ^{+30.6}_{-11.8}$	$0.500\ ^{+peg}_{-0.159}$	$2.379\ ^{+0.133}_{-0.114}$	0.850
PG 0844+349*	0.987 (627)	1.039 (1361)	$3.075\ ^{+0.061}_{-0.070}$	$17.5\ ^{+3.1}_{-2.8}$	$0.333\ ^{+0.052}_{-0.026}$	$2.513\ ^{+0.035}_{-0.021}$	0.521
PG 0947+396	0.893 (477)	0.944 (874)	$3.552\ ^{+0.087}_{-0.201}$	$50.0\ ^{+peg}_{-22.2}$	$0.500\ ^{+peg}_{-0.141}$	$2.176\ ^{+0.044}_{-0.030}$	0.865^{OM}
PG 0953+414	1.055 (512)	1.065 (899)	$3.318\ ^{+0.158}_{-0.098}$	$34.9\ ^{+15.1}_{-8.1}$	$0.500\ ^{+peg}_{-0.068}$	$2.349\ ^{+0.065}_{-0.045}$	0.878^{OM}
PG 1048+342	1.043 (534)	1.075 (907)	$3.103\ ^{+0.082}_{-0.087}$	$20.0\ ^{+12.8}_{-3.5}$	$0.500\ ^{+peg}_{-0.197}$	$2.190\ ^{+0.032}_{-0.042}$	0.914^{OM}
PG 1115+407*	0.913 (413)	0.912 (746)	$3.597\ ^{+0.202}_{-0.137}$	$34.4\ ^{+15.6}_{-9.3}$	$0.482\ ^{+peg}_{-0.110}$	$2.535\ ^{+0.059}_{-0.055}$	0.945^{OM}
PG 1116+215	1.007 (397)	0.900 (845)	$3.280\ ^{+0.240}_{-0.189}$	$25.4\ ^{+20.9}_{-8.0}$	$0.500\ ^{+peg}_{-0.131}$	$2.406\ ^{+0.064}_{-0.045}$	0.935^{OM}
PG 1202+281	1.009 (553)	1.038 (992)	$3.174\ ^{+0.116}_{-0.093}$	$28.7\ ^{+4.1}_{-5.0}$	$0.445\ ^{+peg}_{-0.081}$	$2.111\ ^{+0.046}_{-0.061}$	0.810^{OM}
PG 1211+143*	1.274 (936)	1.400 (1608)	$2.547\ ^{+0.006}_{-0.006}$	$9.5\ ^{+0.2}_{-0.3}$	$0.114\ ^{+0.005}_{-0.004}$	$2.556\ ^{+0.015}_{-0.010}$	0.964^{OM}
PG 1244+026*	1.102 (292)	1.070 (745)	$3.364\ ^{+0.022}_{-0.053}$	$50.0\ ^{+peg}_{-7.0}$	$0.500\ ^{+peg}_{-0.016}$	$2.733\ ^{+0.031}_{-0.028}$	0.306
PG 1307+085	0.871 (265)	0.972 (608)	$3.007\ ^{+0.069}_{-0.131}$	$21.0\ ^{+5.8}_{-6.7}$	$0.358\ ^{+peg}_{-0.072}$	$2.115\ ^{+0.094}_{-0.083}$	0.971^{OM}
PG 1309+355	0.927 (293)	0.972 (580)	$3.741\ ^{+0.173}_{-0.762}$	$34.8\ ^{+peg}_{-30.8}$	$0.153\ ^{+0.150}_{-0.105}$	$2.030\ ^{+0.078}_{-0.038}$	0.974^{OM}
PG 1322+659	1.009 (331)	0.890 (614)	$3.050\ ^{+0.151}_{-0.189}$	$20.1\ ^{+9.0}_{-6.7}$	$0.413\ ^{+peg}_{-0.118}$	$2.635\ ^{+0.081}_{-0.073}$	0.901^{OM}
PG 1352+183	1.002 (370)	1.070 (855)	$3.358\ ^{+0.066}_{-0.121}$	$49.8\ ^{+0.2}_{-12.9}$	$0.500\ ^{+peg}_{-0.143}$	$2.347\ ^{+0.078}_{-0.034}$	0.734^{OM}
PG 1402+261*	1.129 (384)	0.901 (788)	$3.385\ ^{+0.064}_{-0.121}$	$45.4\ ^{+4.6}_{-13.1}$	$0.500\ ^{+peg}_{-0.063}$	$2.441\ ^{+0.029}_{-0.034}$	0.953^{OM}

Table 7.4: Table A, see description of table C.

Source	χ^2_ν (d.o.f) Reflection	χ^2_ν (d.o.f) Absorption	SWIND1 ξ	SWIND1 N_H	SWIND1 σ	Intrinsic Γ	L_{disc}/L_{bol}
PG 1404+226*	0.893 (190)	1.070 (364)	$2.953\ ^{+0.032}_{-0.061}$	$45.8\ ^{+3.4}_{-4.6}$	$0.346\ ^{+0.040}_{-0.045}$	$2.880\ ^{+0.078}_{-0.067}$	0.755
PG 1427+480	0.985 (524)	1.127 (915)	$3.301\ ^{+0.225}_{-0.129}$	$27.6\ ^{+8.6}_{-5.9}$	$0.500\ ^{+peg}_{-0.118}$	$2.245\ ^{+0.045}_{-0.081}$	0.925^{OM}
PG 1440+356*	0.989 (289)	1.064 (1321)	$3.145\ ^{+0.088}_{-0.064}$	$26.4\ ^{+4.8}_{-4.9}$	$0.500\ ^{+peg}_{-0.069}$	$2.701\ ^{+0.025}_{-0.028}$	0.941^{OM}
PG 1444+407	1.297 (289)	1.156 (470)	$3.444\ ^{+0.264}_{-0.185}$	$49.9\ ^{+peg}_{-22.1}$	$0.500\ ^{+peg}_{-0.210}$	$2.541\ ^{+0.064}_{-0.052}$	0.937^{OM}
PG 1501+106	0.981 (931)	1.250 (1655)	$3.086\ ^{+0.061}_{-0.021}$	$18.5\ ^{+3.9}_{-1.3}$	$0.332\ ^{+0.027}_{-0.026}$	$2.381\ ^{+0.019}_{-0.029}$	0.697
NGC 4051*	1.240 (1040)	0.982 (597)	$2.817\ ^{+0.060}_{-0.060}$	$18.2\ ^{+2.8}_{-3.1}$	$0.375\ ^{+peg}_{-0.083}$	$2.030\ ^{+0.037}_{-0.028}$	0.729^{BF}
IRAS 13349+2438*	1.198 (664)	1.372 (772)	$2.549\ ^{+0.026}_{-0.024}$	$10.9\ ^{+0.8}_{-0.8}$	$0.290\ ^{+0.025}_{-0.022}$	$2.779\ ^{+0.032}_{-0.031}$	0.917
ARK 564*	1.197 (666)	1.436 (1342)	$3.406\ ^{+0.074}_{-0.041}$	$36.2\ ^{+12.1}_{-2.8}$	$0.500\ ^{+peg}_{-0.006}$	$2.715\ ^{+0.011}_{-0.012}$	0.877^{OM}
MRK 1044*	1.081 (530)	1.144 (717)	$2.826\ ^{+0.075}_{-0.102}$	$12.6\ ^{+2.3}_{-2.1}$	$0.314\ ^{+0.170}_{-0.048}$	$2.492\ ^{+0.039}_{-0.043}$	0.593
E 1346+266*	1.068 (229)	1.071 (343)	$3.372\ ^{+0.079}_{-0.171}$	$45.6\ ^{+peg}_{-26.2}$	$0.500\ ^{+peg}_{-0.066}$	$2.900\ ^{+0.122}_{-0.050}$	0.525^{OM}
MRK 0359*	1.117 (527)	0.983 (673)	$3.295\ ^{+0.128}_{-0.117}$	$9.3\ ^{+10.9}_{-0.4}$	$0.500\ ^{+peg}_{-0.103}$	$2.083\ ^{+0.046}_{-0.036}$	0.941

Table 7.5: Table B, see description of table C.

Source	χ^2_ν (d.o.f) Reflection	χ^2_ν (d.o.f) Absorption	SWIND1 ξ	SWIND1 N_H	SWIND1 σ	Intrinsic Γ	L_{disc}/L_{bol}
PHL 1092*	1.237 (180)	1.279 (222)	$2.990\ ^{+0.025}_{-0.033}$	$50.0\ ^{+peg}_{-2.8}$	$0.500\ ^{+peg}_{-0.024}$	$3.388\ ^{+0.066}_{-0.062}$	0.741
RE J1034+396*	1.081 (282)	1.105 (370)	$2.650\ ^{+0.046}_{-0.015}$	$16.7\ ^{+2.9}_{-1.5}$	$0.500\ ^{+peg}_{-0.045}$	$3.357\ ^{+0.033}_{-0.054}$	0.629^{OM}
PKS 0558-504*	1.063 (371)	0.877 (949)	$2.751\ ^{+0.081}_{-0.071}$	$9.4\ ^{+1.8}_{-0.9}$	$0.500\ ^{+peg}_{-0.017}$	$2.547\ ^{+0.017}_{-0.017}$	0.932^{OM}
MRK 0766 *	1.119 (952)	1.163 (760)	$2.661\ ^{+0.119}_{-0.042}$	$4.6\ ^{+0.8}_{-0.4}$	$0.277\ ^{+0.029}_{-0.025}$	$2.222\ ^{+0.011}_{-0.010}$	0.914^{BF}
MRK 0586*	1.007 (523)	1.156 (524)	$2.861\ ^{+0.132}_{-0.167}$	$14.9\ ^{+2.1}_{-4.1}$	$0.351\ ^{+peg}_{-0.076}$	$2.698\ ^{+0.051}_{-0.041}$	0.952^{OM}
TON S180*	1.396 (778)	1.207 (990)	$3.168\ ^{+0.024}_{-0.010}$	$24.1\ ^{+2.2}_{-1.3}$	$0.500\ ^{+peg}_{-0.024}$	$2.632\ ^{+0.006}_{-0.009}$	0.465

Table 7.6: Table C: Comparison of fit quality obtained through photoionized reflection by Crummy et al. (2006) and the fits obtained here through photoionized absorption. * corresponds to the source being a NLS1. ^{peg} denotes that the upper or lower limit is outside of the tabulated parameter range. Both models can adequately describe the range of spectra seen in this heterogeneous sample of objects. The major parameters of the smeared wind model (ionization parameter and column density) are also tabulated (see figs 7.5 and 7.6). L_{disc}/L_{bol} is derived from simultaneous OM data where present (marked with ^{OM}), otherwise from disc fits to the archival optical data in table 7.1.

The results of the fits to our absorption model are shown in table 7.6. The reduced χ^2 are statistically indistinguishable from those obtained in the reflection fits of Crummy et al. (2006) over the large sample of objects. Both reflection and absorption models have enough freedom to produce an acceptable fit to the data over the 0.3–10 keV bandpass over a wide range of different spectral shapes, especially when including the presence of the narrow, warm absorber systems.

Figs. 7.5 and 7.6 shows the derived ξ and N_H for the wind. Plainly they are strongly peaked at $\sim 10^3$ and 3×10^{23} cm^{-2}, respectively. This apparent 'fine–tuning' can be explained as a consequence of the rapid change in ionization which is produced self–consistently in X–ray illuminated systems with some pressure balance condition (Krolik, McKee & Tarter 1981; Chevallier et al. 2006). The X–ray illuminated face of the cloud is heated to the Compton temperature, so expands and has low density. This means its ionization parameter, $\xi = L/nr^2$, is high, and the material is fully ionised and hence invisible. Further into the cloud, the X-ray heating is less effective due to scattering in the upper layers, so the density increases in order to maintain pressure. This increases the importance of Bremsstrahlung cooling, pulling the temperature down further, and increasing the density. Eventually ξ drops below $\sim 10^{3.5}$ where not all species are ionised resulting in bound–free and bound–bound transitions dramatically increasing the cooling. The density drops very rapidly, which further decreases the ionization, leading to the possibility of yet more line transitions. This runaway cooling only stops when the material is nearly neutral, so a further decrease in ionization does not lead to an increase in the available line transitions. The corresponding rapid contraction of the cloud (required to enhance the density) may lead to fragmentation of this low ionization part of the cloud into clumps. A line-of-sight through the cloud goes through the highly ionized layer (small opacity) and the transition layer (mean $\log\xi \sim 3$ and column of $\sim 10^{22-23}$ cm^{-2}) but is not likely to intercept any of the opaque cool clumps as these have low

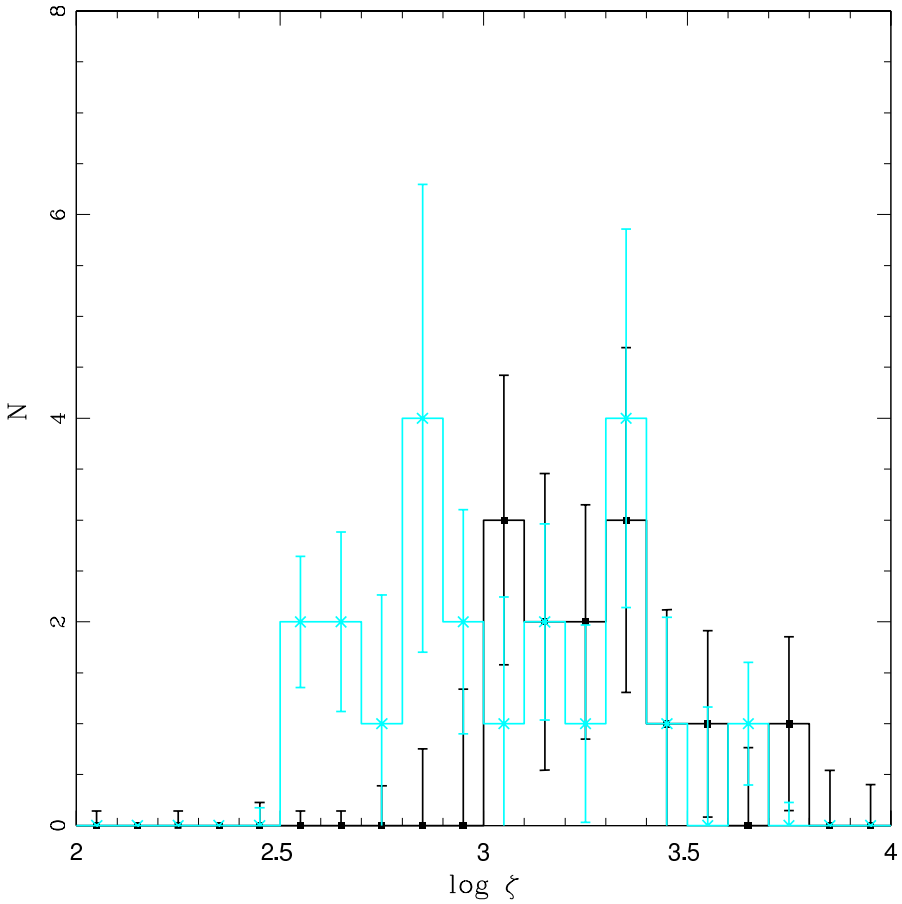

Figure 7.5: Histogram showing the distribution of best-fit wind ionization parameter with NLS1s shown in cyan and broad line AGN in black. Clearly these are strongly peaked around $\log \xi \sim 3$, as required to produce the soft excess from the strong opacity jump from OVII/VIII. This fine tuning is rather naturally produced if the absorbing clouds are at approximately constant pressure.

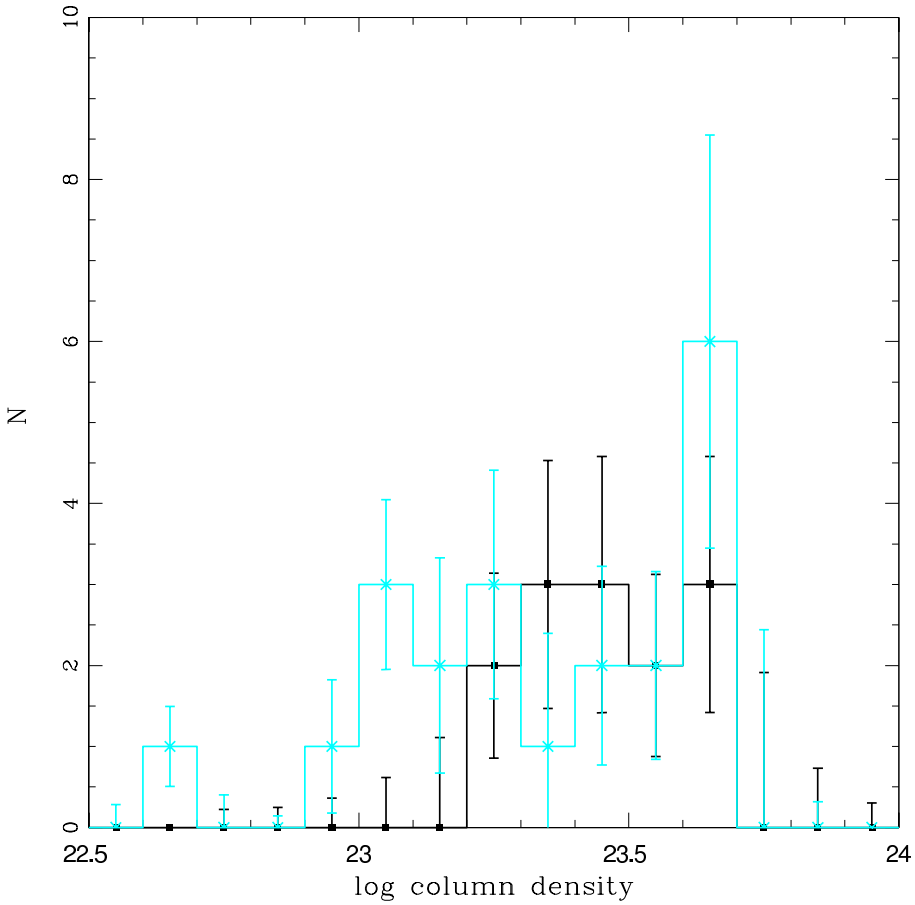

Figure 7.6: Histogram showing the distribution of best-fit wind column density for the NLS1s (cyan) and broad line AGN (black). This is strongly peaked, showing again that a 'fine-tuning' mechanism is required.

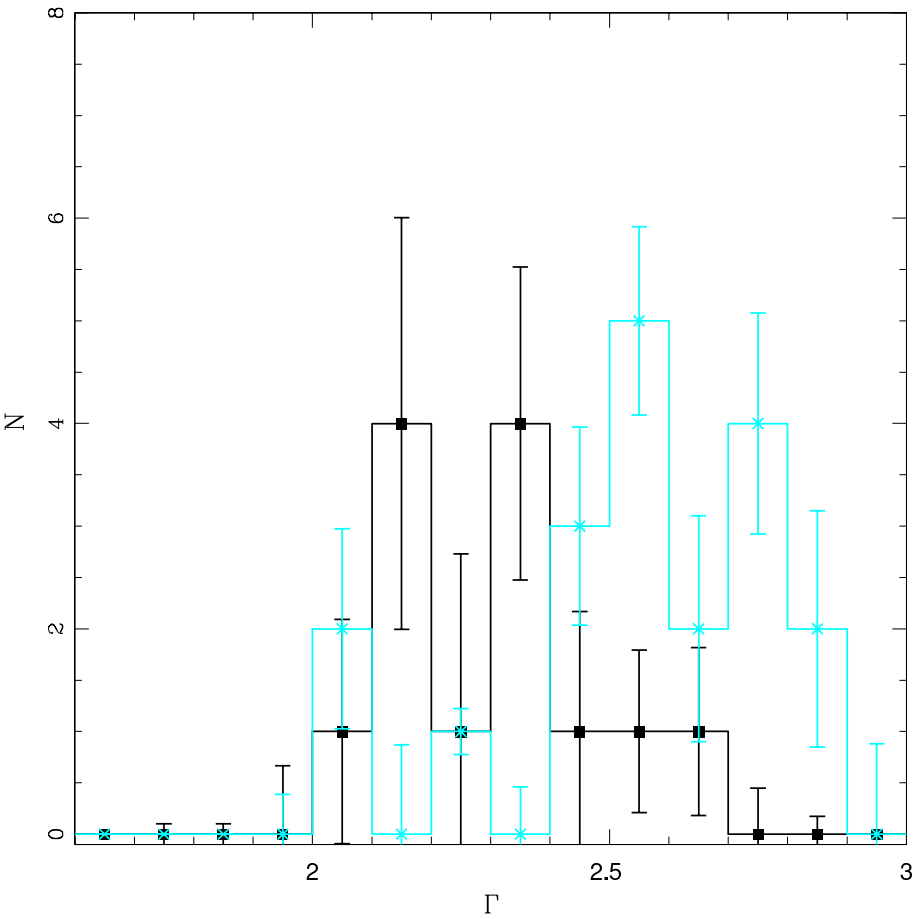

Figure 7.7: Histogram showing the distribution of best-fit intrinsic power-law spectral index for the NLS1s (cyan) and broad line AGN (black). Unlike the apparent 2–10 keV spectral index shown in fig. 7.3, here there is a clear distinction between the steeper NLS1s and flatter broad line AGN, and none of these have $\Gamma < 2$ as expected by analogy with the high mass accretion rate black hole binaries.

covering factor (Chevallier et al. 2006).

Table 7.3 shows the individual, best-fit wind velocity dispersions from our model. The values are large, with many pegged at the upper limit of 0.5c. Most of these can be somewhat reduced allowing the smeared absorber to be blue (or red) shifted.

This has no effect on the intrinsic spectral index but tends to decrease the derived column and ionisation parameter by a factor 2 (fairly negligible on a log plot such as figs 7.6 and 7.7). Nonetheless, even with this extra degree of freedom, the velocity dispersion rarely drops below 0.2c due to the requirement that the soft excess is a single smooth component, while atomic processes give *two* strong features, associated with OVII/VIII at 0.7-0.8 keV and Fe L at 1.5-2 keV, respectively. This is still too large to be associated with the UV line-driven disc wind which *must* be present in such high L/L_{Edd} AGN. Proga (2004) show that such winds have terminal velocities of ~ 0.2c, corresponding to a Gaussian dispersion of at least a factor 2 smaller (more precisely, $\sqrt{12}$ for constant acceleration: Schurch & Done 2007). Thus this requires that the outflow is magnetically driven (associated with the jet?) if the soft excess really is due to smeared absorption.

Fig. 7.7 shows the inferred intrinsic power-law index. Unlike the apparent 2–10 keV index shown in fig 7.3, there are now *no* objects with spectra significantly harder than $\Gamma = 2$. This is not the case for the reflection models of Crummy et al. (2006), where PG 1048+342, PG 1211+143, PG 1307+085 and (especially) Mkn 359 are all inferred to have hard spectra. This is an important difference, arguing in favour of the absorption modelling, as high mass accretion rate BHB almost always show soft spectra, so by analogy we expect the high mass accretion rate AGN to do likewise. This histogram also shows that the NLS1s have somewhat softer spectra than the broad line AGN, with $< \Gamma > \sim 2.6$ as opposed to ~ 2.3 (see also Brandt et al. 1997). By analogy with the BHB, this might indicate that the NLS1s correspond to the very high state, characterised by a soft tail, with $\Gamma \sim 2.5$, while the broad line AGN correspond to the high-soft (or thermal dominant) state, where the tail has $\Gamma \sim 2 - 2.2$ (Remillard & McClintock 2006).

Given that the NLS1s also have significantly higher L/L_{Edd} than the broad line AGN (Fig. 7.1) then it is also clear that in our sample the intrinsic spectral index

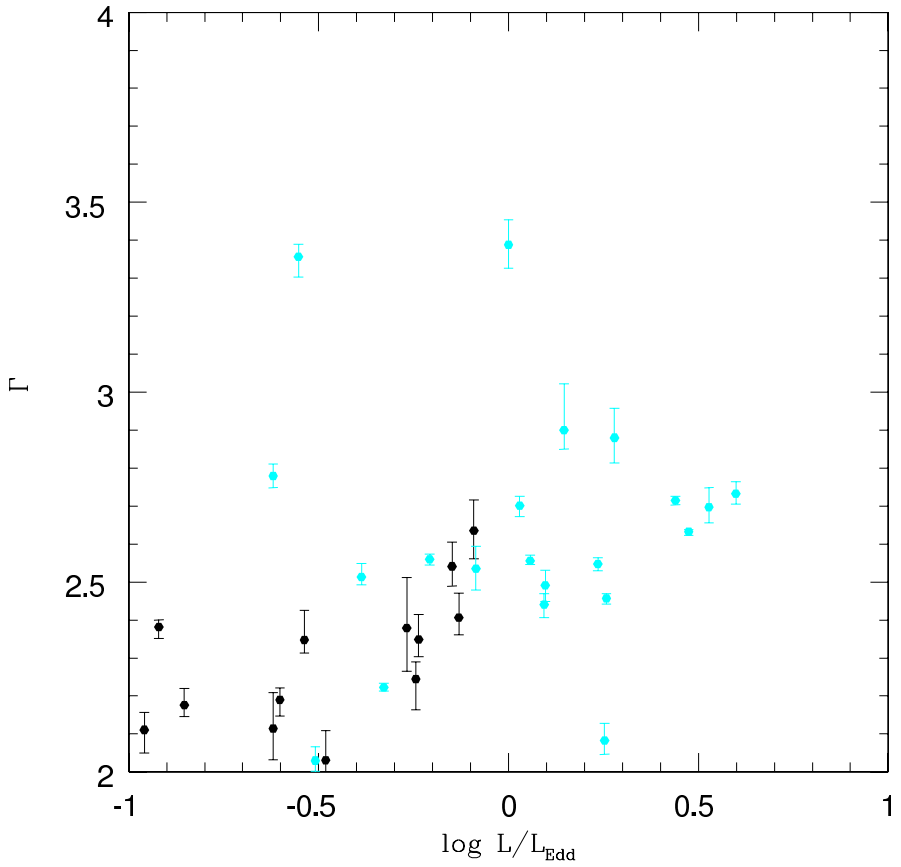

Figure 7.8: Intrinsic power-law index for the NLS1s (cyan) and broad line AGN (black), as derived from the absorption model, versus L/L_{Edd}. There is a clear correlation, especially given the uncertainties in mass determination.

will correlate with L/L_{Edd}. This is shown in Fig. 7.8, and is remarkably well defined, especially considering the uncertainties in determining mass for these AGN. There is no such clear correlation in the galactic binaries but this is probably due to hysteresis complicating their observed behaviour (e.g. Remillard & McClintock 2006). It is now clear that hysteresis in black hole binaries is connected to the dramatic disc instability (Gladstone, Done & Gierliński 2007), which probably does not occur in AGN (Done & Gierliński 2005). Thus it may be that AGN show the intrinsic (steady state) accretion flow properties more clearly than black hole binaries, and have spectral index correlated with L/L_{Edd} (Shemmer et al. 2006).

7.4 Simultaneous SEDs

The full observational criteria for BHB spectral state involves the fraction of the disc to total luminosity as well as the shape of the tail. For those observations for which there are at least two XMM-*Newton* OM data points we can construct the νf_ν SED spanning the optical-UV-X–ray range, i.e. covering both the disc and Comptonized tail. This means we can characterise the full accretion power of the system, and derive the disc to total power ratio, and hence determine spectral state.

We use the parameters of the best fitting model derived in section 7.3 to deconvolve the data from the instrument response, and to correct for neutral absorption (both from our galaxy and the AGN host galaxy) and narrow XSTAR ionised absorption. On top of these absorption corrected, deconvolved data, we also plot the best estimate for the intrinsic Comptonized spectrum (cyan, with seed photons assumed to be at the same temperature of the disc, see below) and the effect of smeared absorption on this (magenta). The inferred intrinsic reflection component is also included on the plot (green) and the total (intrinsic plus reflection, both absorbed by the smeared wind) fit to the data (blue).

We use the upper and lower limits on the (galactic and host galaxy) neutral

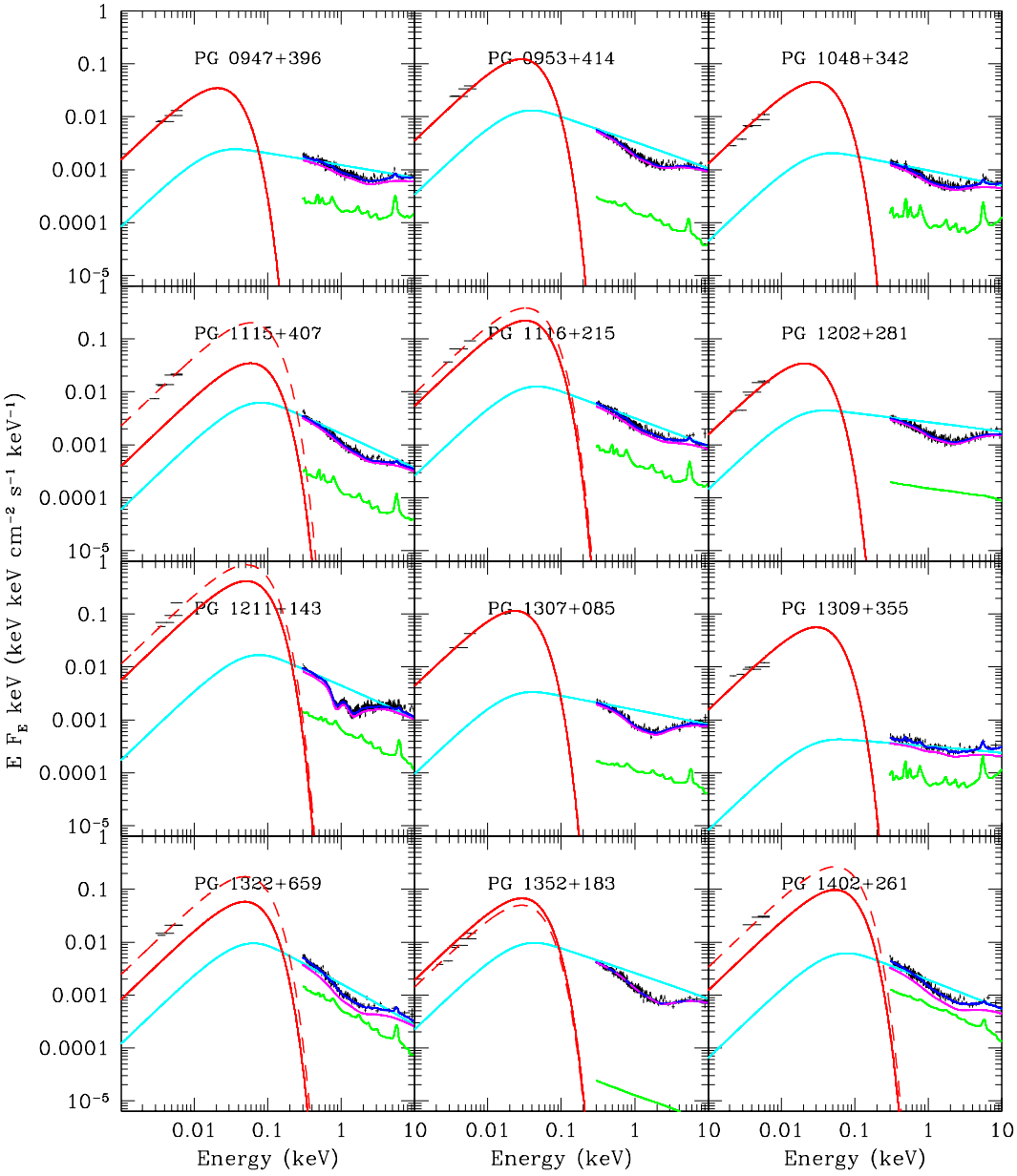

Figure 7.9: Broad-band νf_ν spectra of those sources with at least 2 XMM-*Newton* OM points. The data is absorption corrected, and decomposed into disc (red), intrinsic Comptonized continuum (cyan), its reflection (green) and the effect of the smeared wind on the continuum (magenta). The total spectrum is given by the Compton continuum plus reflection and absorption by the smeared wind (blue). The disc flux was originally calculated from the archival tabulated luminosity in table 7.1 (red solid line). Since AGN vary, this can differ substantially from the observed OM points, so the disc luminosity is recalculated from the best fit to the OM points (red dashed line).

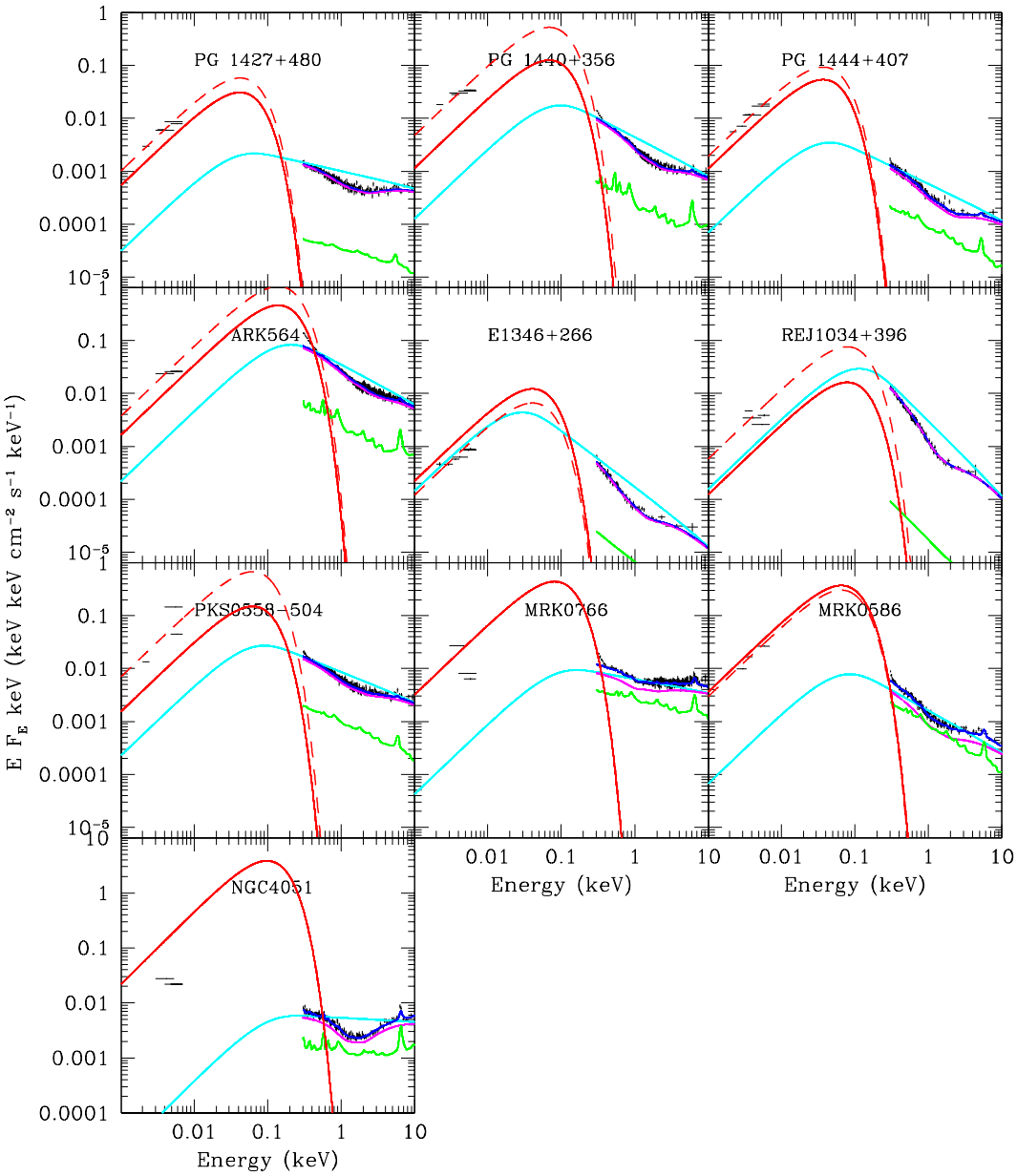

Figure 7.10: As for figure 7.9.

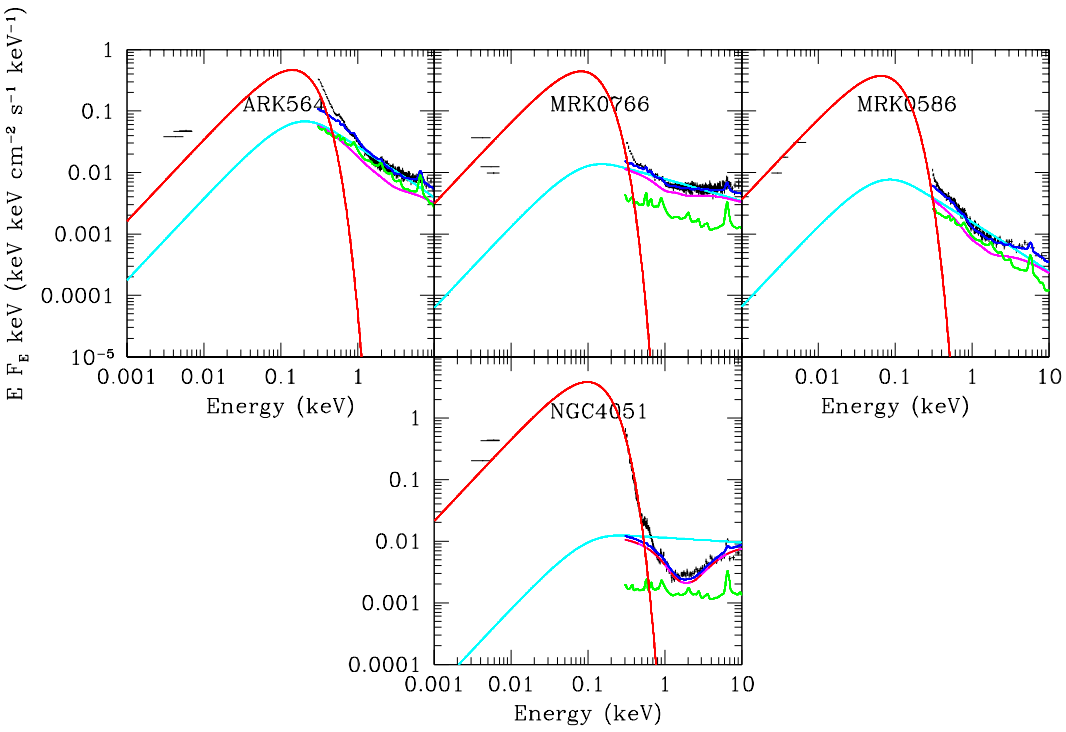

Figure 7.11: The standard X-ray spectral model did not include the disc component, but fig 7.9 shows that there are some sources for which the disc temperature is high enough to contribute to the soft X–ray flux. These sources also often have OM points which are significantly redder than expected for a disc. Refitting the X–ray data including the disc emission requires a much higher neutral absorption column, so giving a bigger correction for reddening, which can recover a disc–like optical–UV spectrum.

N_H to get upper and lower limits on the optical/UV reddening (Predehl & Schmidt 1995). These are used to get uncertainties on the dereddened optical/UV flux from the OM data. We include an additional standard DISKBB model with normalization and temperature determined from the tabulated M_{BH} and L/L_{Edd} for each AGN (red). This should generally overestimate the optical/UV flux, since this assumes that the entire bolometric luminosity is produced in the disc. The fact that this generally matches to the data shows immediately that this is a fairly good approximation for most of these AGN, and that the high energy tail (cyan) is not energetically dominant, though there are a few exceptions to this (E1346+266 and RE J1034+396). Since the luminosity is taken simply from the tabulated values then time variability is also an issue, hence we also show a disc spectrum which gives a better match to the OM points (dotted red line).

There are a few objects where the optical/UV spectra have a very different slope than that predicted by disc models, the NLS1s MRK 766 and NGC 4051. These are also objects where the black hole mass is low enough and L/L_{Edd} high enough for the predicted disc spectra to extend into the soft X–ray band. Since the disc was not included in the X–ray spectral model then its presence would lead to an underestimate of the X–ray column density. This would underestimate the internal host galaxy reddening which could lead to the observed downturn in optical/UV flux. Hence we refit the X–ray data of these objects including the disc component. The increased reddening in NGC 4051 is sufficient to reverse the optical/UV slope, making it much more compatible with the expected accretion disc spectrum. However, this is not the case for MRK 766, where the optical data clearly appear absorbed even with a larger host galaxy column. We suggest that these data are indeed strongly reddened, perhaps from dust entrained in the narrow warm absorber systems in a similar manner to MCG–6–30–15 (Reynolds 1997; Kraemer et al. 2000; Ballantyne, Weingartner & Murray 2003).

We use these best estimates of the unabsorbed disc spectrum (dotted red line) to quantify the ratio of luminosity in the tail to the total luminosity or L_{tail}/L_{tot}. In BHB the high-soft (thermal dominant) state is defined as $L_{disc}/L_{tot} \geq 0.75$, while the intermediate/very high state (steep power-law state) is defined to have $L_{disc}/L_{tot} < 0.8$ and $\Gamma > 2.4$. By contrast the low-hard state has $L_{disc}/L_{tot} \leq 0.2$ and $1.4 < \Gamma < 2.1$. The values of these ratios and the inferred, analogous BHB states are given in table 7.4 onwards, and the histogram of this for the entire sample is shown in fig. 7.12.

This shows a less clear cut distinction between the NLS1 and broad line AGN than in fig. 7.7. While the NLS1 spectral indices are indeed steep, as expected for the very high state in BHB, they do *not* in general have $L_{disc}/L_{tot} < 0.8$. Also, they do not in general have a significantly smaller L_{disc}/L_{tot} than the broad line AGN (though the objects with the weakest discs are NLS1s), as expected if the NLS1s correspond to the very high state, while the broad line AGN correspond to the high-soft state. This lack of correspondence with the BHB could be due to lack of data in the extreme UV where the disc spectra peak. The disc luminosities are inferred assuming that their spectra follow the expected standard form, yet there is clear evidence in BHB that this is not the case in the very high state, where discs in BHB can show much lower maximum temperature than expected for their luminosity (Kubota & Done 2004; Done & Kubota 2006). If the NLS1s are indeed analogous to the very high state and have similarly distorted disc spectra then our estimate of total disc luminosity from the optical/UV flux is too high. There is some evidence to support this in NGC 4051, as the high temperature, luminous disc component shown in fig. 7.11 is strongly ruled out by the XMM-*Newton* data.

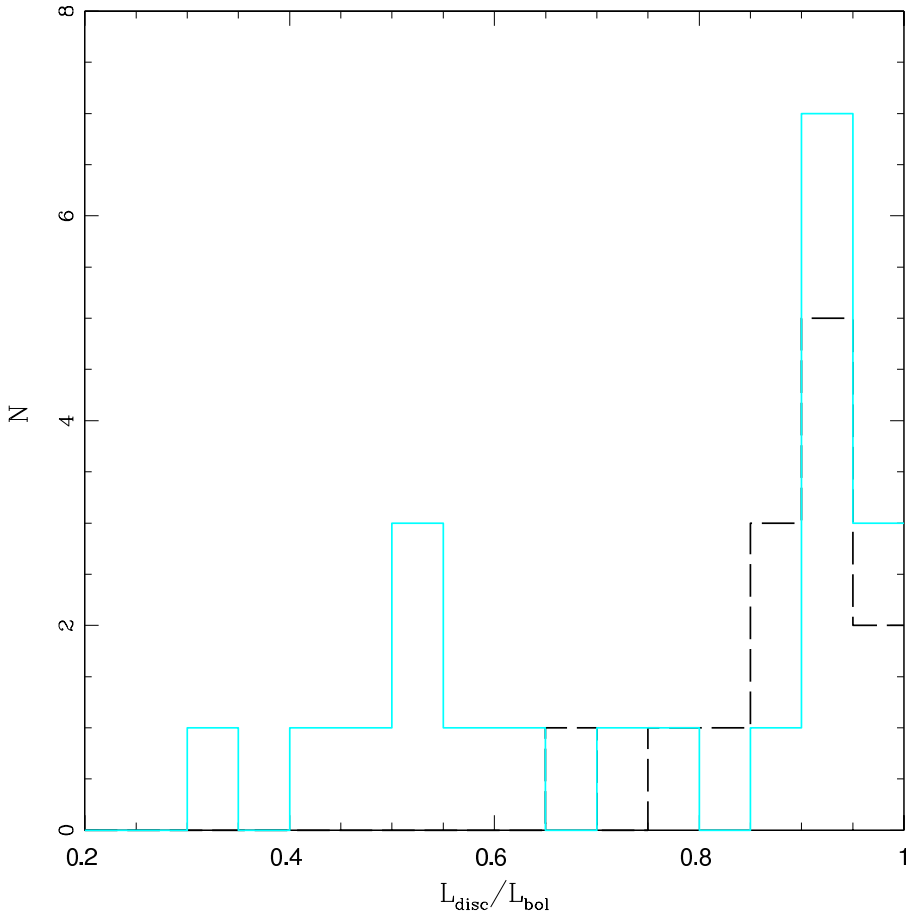

Figure 7.12: Histogram showing the distribution of L_{disc}/L_{bol}. While the spectral indices shown in fig 7.7 support an analogy between NLS1s (cyan) with the very high (steep power-law) state in BHB and broad line AGN (black) with the high-soft (thermal dominant) state, this is *not* carried over into the ratio of disc to total luminosity. The very high state is characterised by less than 80 per cent of power in the disc, yet many NLS1s have estimated disc spectra which are more dominant than this.

7.5 Conclusions

We show that the X–ray spectra of a heterogeneous sample of QSOs and NLS1s can be equally well fit by partially ionised, Doppler smeared material seen in absorption as by the alternative geometry where this material is optically thick and seen in reflection (Crummy et al. 2006). Thus the 0.3–10 keV spectral data alone cannot distinguish the underlying geometry of this partially ionised material, nor in fact can it unambiguously show that it does indeed exist, as the Doppler smearing is so extreme as to merge the characteristic atomic features into a quasi–continuum. Thus we have only indirect evidence for its existence, namely the peak in rms variability spectra between 0.7–3 keV (e.g. Ponti et al. 2006; Gierliński & Done 2006), the constant 'temperature' of the soft excess component, together with the fact that this material can also distort the higher energy spectra, producing occasional apparently anomalously hard (by comparison with high L/L_{Edd} BHB) 2–10 keV spectra. Similarly, indirect arguments from physical plausibility support a geometry in which this material is optically thin and seen in absorption (Chevallier et al. 2006; Sobolewska & Done 2007; Done & Nayakshin 2007). Such absorption is likely to be very complex, clumpy, and time dependent, with multiple velocity structures.

Nonetheless, despite the difficulties in producing realistic models to compare with the data, even the simple models used here can begin to reconstruct the intrinsic X–ray emission. These reinforce the links between supermassive and stellar mass black holes, as the inferred intrinsic X–ray spectra are all soft, as expected by analogy with the high mass accretion rate (high-soft and very high) states in the binary systems. All objects with the apparently hard 2–10 keV spectral indices can be explained as being intrinsically soft, but strongly distorted by the smeared absorption. Furthermore, there is a clear correlation between the intrinsic X–ray index and the type of AGN, with NLS1s having softer X–ray spectra than broad line AGN, consistent with them being the analogues of the very high state while the

broad line AGN are identified with the high-soft state respectively. However, this analogy does *not* appear to hold in terms of the ratio of disc to total luminosity. The very high state in BHB has the disc with less than 80 per cent of the total accretion power, while the NLS1s show a range of values, with many having the disc more dominant than expected. This could point to subtle differences in how spectral states are seen between stellar mass and supermassive black holes, but we stress that this could also result from a lack of data in the EUV region where the disc luminosity peaks. Disc spectra in the very high state in BHB are often somewhat distorted. Similar distortions in the NLS1s would result in an overestimate of the total disc flux inferred from the observed optical/UV points. This could recover a straightforward correspondence between the spectral states as seen in BHB and AGN type.

Chapter 8

Paper 3: A periodic signal from the active galaxy REJ1034+396

REJ1034+396 (also known as KUG 1031+398) is a nearby (redshift z = 0.042) active galaxy, spectroscopically classified as a narrow-line Seyfert 1 (NLS1). These objects have strong emission lines produced by high-density gas ionized by the ultraviolet and X-ray radiation from the accretion flow. These lines are rather narrow compared to the velocity widths seen in more typical broad-line active galactic nuclei (AGN). This fact, together with other evidence, has led to the suggestion that they host supermassive black holes that are less massive than those inferred in a typical AGN of similar luminosity (Boller, Brandt & Fink 1996).

From a long (91 ks) observation using the X-ray satellite XMM-Newton, we extracted a light curve for RE J1034+396 (fig. 8.1) over the energy band 0.3-10 keV. Even by eye it shows an evident periodic oscillation. To test more rigorously for the presence of a periodic signal, we folded the light curve with various trial periods and analysed the root-mean-square (rms) amplitude of the resulting pulse profile as a function of the period. We found a strong peak at 3,730±130 s (full-width at half-maximum). We used the best-fitting period to plot the expected times of minima in fig. 8.1 (dotted vertical lines). This shows that the periodicity changes its character at around t_0 = 25 ks. After that time, the troughs in the light curve follow the predicted minima very well, for almost 16 cycles, indicating a

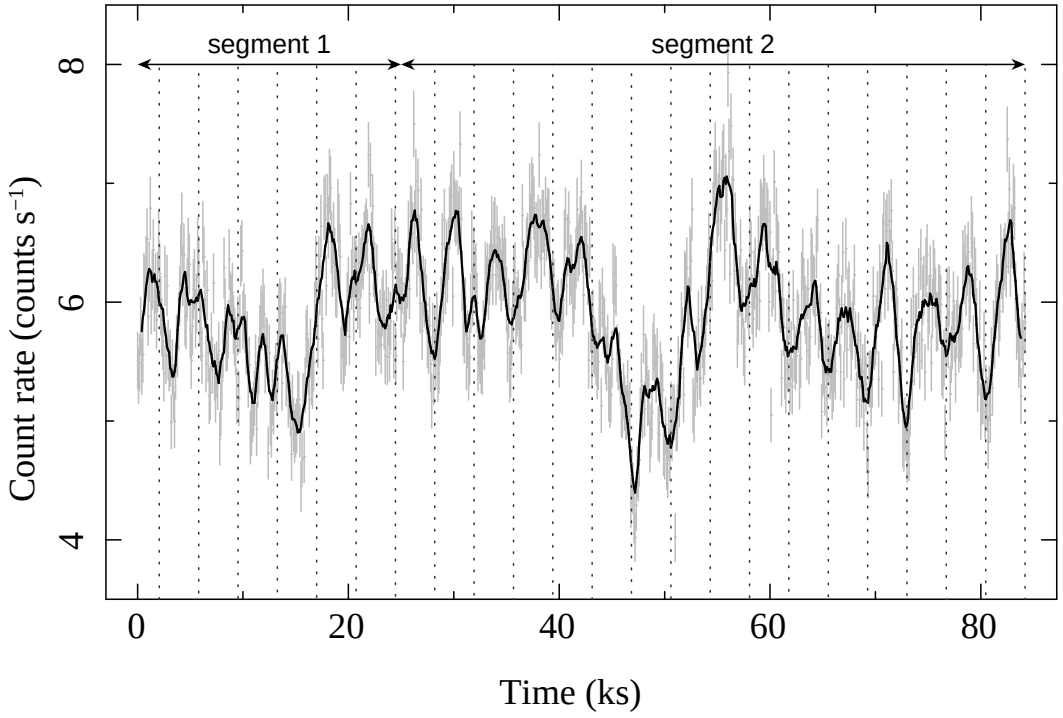

Figure 8.1: The start time of this observation was 2007 May 31, 20:10:12 utc. We extracted source and background light curves from the PN, MOS1 and MOS2 cameras in the 0.3-10 keV energy band, using 45-arcsec circular selection regions and rejecting the final ∼7 ks owing to background flares. We then combined the data from all cameras. This gave a mean count rate of 5.9 ± 0.6 and 0.04 ± 0.08 (s.d.) counts s^{-1} for the net and background light curves, respectively. The data points, binned in 100-s intervals, are plotted in grey; error bars, ±1 s.d. The thick black curve represents the running average over 9 bins around a given bin and shows clear periodicity. The dotted vertical lines show the expected times of minima obtained from folding segment 2 with the period of 3,733 s. In this paper we mainly analyse segment 2, which shows a periodicity with high coherence. It contains 593 contiguous 100 s bins, and almost 16 full cycles of the periodic signal. The fractional rms variability (in terms of excess variance: Vaughan et al. 2003) in this segment is 9.2 ± 0.2%.

highly coherent signal, but before t_0 the troughs are shifted in phase and there are occasional, additional minima. This shows that the feature is not a true periodicity, but that it wanders in phase, amplitude and/or frequency, as seen in the quasi-periodic oscillations (QPOs) in black hole binaries (BHBs)(Remillard & McClintock 2006). Hence, we will refer to this signal as a QPO.

We concentrate first on the coherent part of the light curve (segment 2 in fig. 8.1). Figure 8.2 shows this light curve segment folded with the best-fitting period, and fig. 8.3 shows its periodogram with a strong peak at $\sim 2.7 \times 10^{-4}$ Hz. In order to quantify the statistical significance of the peak, we adopt the method proposed to test the significance of periodicities against an underlying continuum (Vaughan 2005). This method involves dividing the periodogram by the best-fitting power-law and using the known distribution of the periodogram ordinates to estimate the likelihood of observing a given peak. The confidence limits (3σ and 99.99%) shown in fig. 8.3 are calculated including the uncertainties in the power-law model. The QPO is well above these limits, with a chance probability of a spurious signal of 2×10^{-8} (corresponding to the $\sim 5.6\sigma$ significance level). Even in the total light curve, (including segment 1 which has less obvious periodicity), the signal is still significant at the $\sim 3.4\sigma$ level.

This method assumes that the underlying continuum has a power-law shape, but there can be breaks in this continuum, changing the derived significance of the QPO. We tested this with Monte Carlo simulations, generating a series of light curves following a given power spectral distribution (Timmer & Koenig 1995). The simulated light curves had the same number of bins, mean count rate and variance as the observed light curve. We then calculated periodograms for each of them, and found the power corresponding to the upper 3σ limit in each frequency channel (the maximum significance in this method is 3.8σ owing to the limited number of simulated light curves). The results for a single power-law distribution with

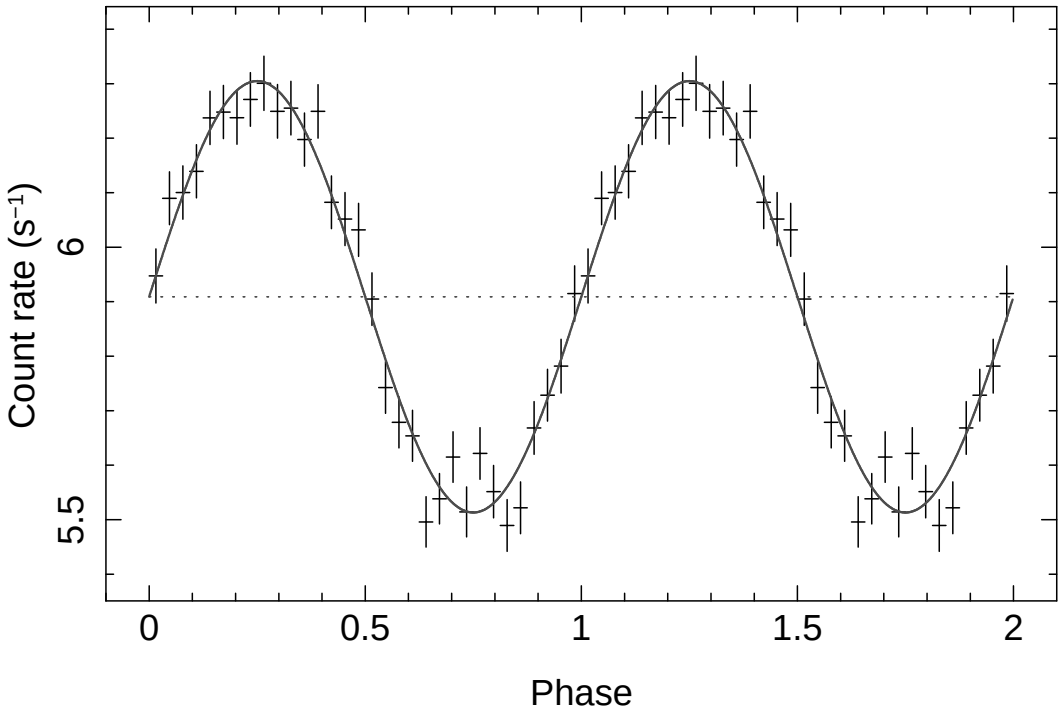

Figure 8.2: We folded the part of the light curve with significant periodicity (segment 2 in fig. 8.1) with the period of 3,733 s. Errors are propagated from the unfolded light curve, and represent 1 s.d. Two cycles are plotted for clarity. The solid line represents the best-fitting sinusoid, the dotted line, the mean count rate. The amplitude of the sinusoid is ∼6.7% of the mean, which corresponds to ∼4.7% of the fractional rms variability in the pulse profile.

the index taken from the best fit to our data (with index uncertainties taken into account) are comparable to the analytical limits shown in fig. 8.3, as expected. A broken power-law with indices -1 and -2 below and above the break frequency of 2.7 $\times$ 10^{-4} Hz, respectively, decreases the confidence limits around the break, but the QPO remains highly significant ($> 3.8\sigma$). Therefore, we conclude that the observed signal at $\sim$2.7 $\times$ 10^{-4} Hz in REJ1034+396 is significant at a very high statistical level, irrespective of the assumed model for the continuum power. The QPO lies within just one frequency bin of the periodogram, which makes it highly coherent, with a quality factor $Q = f/\Delta f > 16$, where f and Δf are the bin frequency and width, respectively. The rms fractional variability in the QPO is $\sim$4.7% in the 0.3-10 keV energy band, which constitutes about half of the rms variability in the light curve. The strength of the QPO depends significantly on energy, increasing from $\sim$2% in the 0.2-0.3 keV band to $\sim$10% above 1 keV. There is also a time lag of $\sim$260s in the QPO phase between the 2-10 and 0.3-0.4 keV energy bands (softer X-rays lagging behind harder X-rays) as seen in fig 8.4.

This is the first time that such a strong QPO has been convincingly found in the X-ray light curve of any AGN. Earlier claims all failed a more stringent statistical analysis (Benllock et al. 2001; Vaughan & Uttley 2005, 2006), such as that used here. The only exception was that claimed for NGC 6814, which turned out to be from a galactic cataclysmic variable along the line-of-sight (Madejski et al. 2003). However, XMM-Newton is an imaging instrument and has a positional accuracy of $\sim$2-3 arcsec, so considering that the number of X-ray-detected cataclysmic variables is $\sim$100 (Verbunt et al. 1997), the probability of a chance superposition with the AGN is vanishingly small ($<10^{-8}$). We therefore conclude that the X-ray source is associated with the galaxy. Furthermore, its X-ray luminosity (4×10^{43} erg s^{-1} in the 0.3-10 keV band) is then too bright for an ultra-luminous binary X-ray source, which have luminosities below $\sim 10^{41}$ erg s^{-1}. Therefore it must originate from the

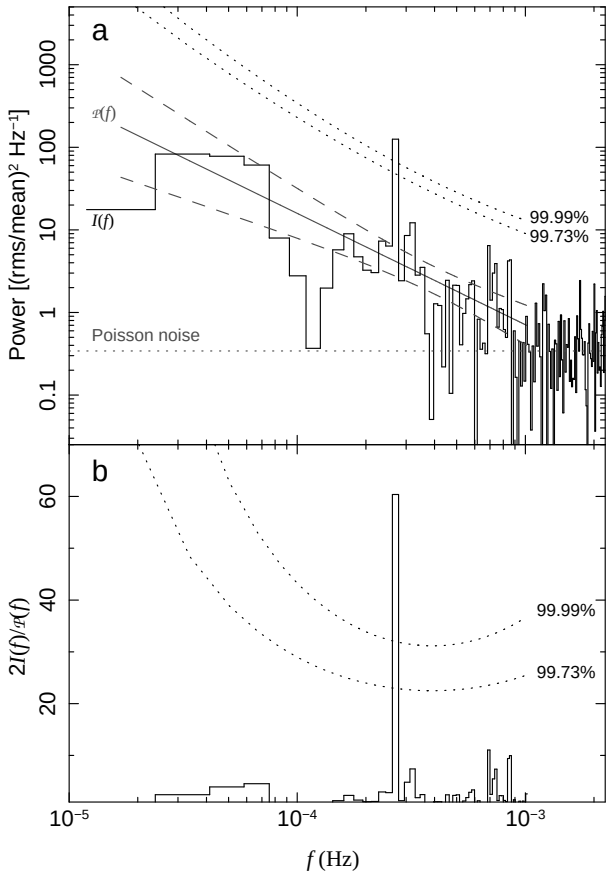

Figure 8.3: a, Power spectrum calculated from segment 2 of the light curve (fig. 8.1). The solid line is the de-biased (Vaughan 2005), best-fitting (least squares method) power-law, P(f), with index -1.35± 0.18. The fit excluded the white noise dominated data above 10^{-3} Hz. We checked that a particular choice of the cut-off did not affect the significance of the peak. The dashed curves represent the uncertainty in the power-law model. The dotted horizontal line shows the expected level of the Poissonian noise. The K-S test returned the P value of ∼84%, so the null hypothesis is not rejected at the significance level of, for example, 5%. This shows that a single power-law is a good description of the underlying noise process. We also confirm this by Monte Carlo simulations, which allow us to estimate 1 s.d. errors in each frequency channel and calculate $\chi^2 = 68.4$ at 58 degrees of freedom. We use the χ^2 distribution of 2I(f)/P(f) to calculate the confidence limits on the suspected periodic signal. b, Plot of 2I(f)/P(f) together with 3σ (99.73%) and 99.99% confidence limits. The same confidence limits are also plotted in a. We see that the periodic signal at $\sim 2.7 \times 10^{-4}$ Hz is very strong, significant at a level in excess of 99.99%. The periodic signal is also highly significant in the individual light curves extracted from each separate X-ray camera.

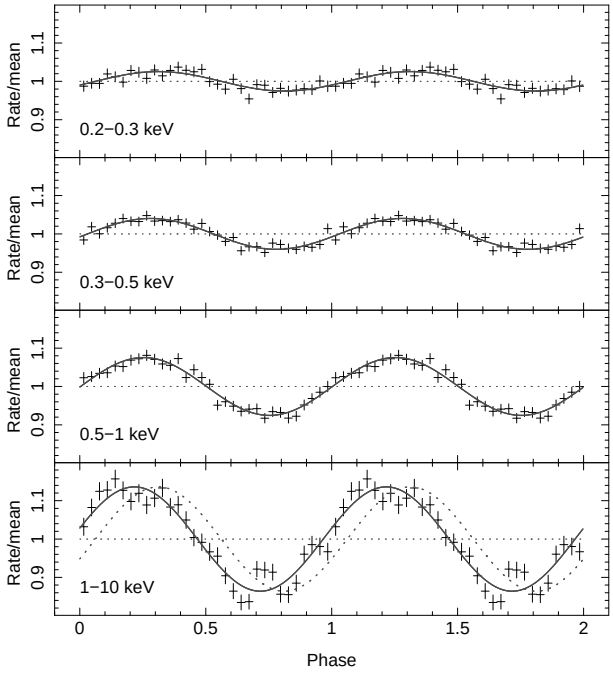

Figure 8.4: Folded light-curves at different energies. The dotted sinusoid in the bottom panel shows the position of the pulse were it in-phase with the softest energy band in the top panel, thus clearly demonstrating the phase lag between hard and soft energies.

AGN.

The black hole mass in REJ1034+396 is not well determined, and different methods of measurement give conflicting results (Bian & Zhao 2004). The virial mass derived from the Hβ emission line velocity dispersion in the broad-line region (Kaspi et al. 2000) is $6.3 \times 10^5 M_\odot$, and differs significantly from an estimate of 3.6×10^7 $M_\odot$ obtained using OIII as a proxy for the stellar velocity dispersion in the bulge (Tremaine et al. 2002). On the other hand, if the mass-velocity dispersion relation in NLS1s (Grupe & Mathur 2004) differs from that in broad-line galaxies (Kaspi et al. 2000), then the latter mass measurement may be overestimated. Our observed periodicity, if it is related to the Keplerian period of the innermost circular stable

orbit, would correspond to a central mass of between 8×10^6 and $9 \times 10^7 M_\odot$, for a non-rotating and maximally rotating black hole, respectively.

Galactic BHBs show a huge variety of QPOs, differing in frequency, power and coherence (Klein-Wolt & van der Klis 2008). Generally, they can be divided into the low- and high-frequency QPOs, with frequencies <50 and >100 Hz, respectively. The strongest and most coherent low-frequency QPOs are typically seen at frequencies <10 Hz, which, when scaled to the frequency of 2.7×10^{-4} Hz reported here, would imply a black hole mass of less than $\sim 4 \times 10^5$ $M_\odot$ in REJ1034+396. Given the observed bolometric luminosity (dominated by the soft X-ray/far ultraviolet component) of $\sim 5 \times 10^{44}$ erg s^{-1}, such a low mass requires that the system be radiating at about 10 times the Eddington limit (L_{Edd}).

High-frequency QPOs are occasionally seen in several BHBs with high coherence (Remillard & McClintock 2006), sometimes occurring in pairs, with a frequency ratio of 3:2. These frequencies appear to be stable, and are regarded as a signature of strong gravity in the vicinity of a rotating black hole (Abramowicz & Kluźniak 2001). A tentative frequency-mass relation, $f_0 = 931\ (M/M_\odot)^{-1}$ Hz, can be derived from three objects (Remillard & McClintock 2006). Here f_0 is the fundamental frequency of the pair; that is, the observed frequencies are $2f_0$ and $3f_0$ (the fundamental is not seen). This relation yields the black hole mass in REJ1034+396 of 6.9×10^6 or 1.0×10^7 $M_\odot$, depending on whether the observed periodicity corresponds to $2f_0$ or $3f_0$ respectively. This would imply a luminosity of 0.5 or 0.3 L_{Edd} respectively. All this clearly shows that better mass estimates (using, for example, reverberation mapping or accurate stellar velocity dispersion) are required for REJ1034+396 before the QPO type can be uniquely identified.

Finally we should ask why REJ1034+396 is unique in showing the first convincing evidence for a QPO, given that many AGN have comparable quality X-ray data and have been monitored for similar or longer timescales. Perhaps we have been

exceptionally lucky in detecting a QPO with a small duty cycle (the high-frequency QPO in BHBs is seen only occasionally). Alternatively, it may be connected to the fact that REJ1034+396 is extreme even among NLS1 galaxies, with an unusual spectral energy distribution peaking in the far ultraviolet (Pounds, Done & Osbourne 1995, Casebeer, Leighly & Baron 2006). This component extends into the soft X-ray band pass, but not to the harder X-rays where the QPO is seen. Thus the far ultraviolet/soft X-ray component cannot be directly responsible for the QPO signal, but it may indicate that REJ1034+396 has an extreme mass accretion rate and that this drives both the unusual spectrum and the QPO.

QPOs remain enigmatic, but they clearly contain information about the dynamics of the infalling material. The larger mass of an AGN means that we see fewer cycles of a QPO, but with much higher time resolution compared to BHBs. Therefore, future studies of such phenomena in AGN will shed new light on the origin of QPOs, and in turn, on the behaviour of accretion flows around black holes.

Chapter 9

Paper 4: REJ1034+396: The origin of the soft excess & QPO

9.1 Introduction

The discovery of a significant quasi-periodic oscillation in the X-ray light curve of a Narrow Line Seyfert 1 AGN, RE J1034+396 (Gierliński et al. 2008) strengthens arguments stressing the similarities in the physics of the accretion flow between supermassive and stellar mass black holes. Previous evidence for a simple correspondence between AGN and the black hole binaries (BHB) included similarities in the broad-band shape of the X-ray variability power spectra, with characteristic break timescales scaling with mass (e.g. M^{c}Hardy et al. 2006), but the characteristic QPOs often seen in BHB light curves remained undetected until now (Vaughan & Uttley 2005; Leighly 2005).

The QPOs in BHB can be split into two main groups, at high and low frequencies, respectively. While there is as yet no clear mechanism for producing either set of QPOs (or the correlated broad-band variability) there are many pointers to their origin from the observations. Most clearly, their amplitude increases with increasing

energy. The BHB spectra typically contain two components, a disc and tail, and this increasing amplitude is consistent with the QPO (and all the rest of the rapid variability) being associated with a variable tail while the disc remains constant (e.g. Churazov, Gilfanov & Revnivtsev 2001; Sobolewska & Życki 2006; Gilfanov, Revnivtsev & Molkov 2003). This suggests that QPOs are produced by some mode of the hot coronal flow rather than a mode of the thin disc. (see e.g. the reviews by Van der Klis 2004; McClintock & Remillard 2006; Done, Gierliński & Kubota 2007).

The rest of the QPO properties are more complex. The high frequency (HF) QPO may have a constant fundamental frequency (though it is seen at 3:2 harmonic ratios of this), which may relate to the mass of the black hole. By contrast, the frequency (and other properties) of the low frequency (LF) QPO change dramatically with mass accretion rate, correlating with the equally dramatic changes in the source spectra. Typically these show that, at low mass accretion rates compared to Eddington, $L/L_{\rm Edd} \ll 1$, the LFQPO is at low frequencies, but is weak and rather broad. The corresponding energy spectra are dominated by a hard power-law (photon index $\Gamma < 2$) which rolls over at around 100 keV (low-hard spectral state). As the mass accretion rate increases, the LFQPO increases in strength and coherence as well as frequency, while the power-law spectrum softens and the disc increases in strength relative to the power-law. The QPO is at its highest frequencies, is strongest and most coherent where the spectrum has both a strong disc component and a strong soft tail of emission to higher energies ($\Gamma > 2.5$). After this, the LFQPO frequency remains more or less constant as the tail declines and hardens to $\Gamma \sim 2.2$, leaving the spectra dominated by the disc component (high-soft state), though it becomes harder to follow the QPO as increasing contribution from the stable disc (thermal dominant state) swamps the signal from the variable tail (e.g. McClintock & Remillard 2006 and references therein).

The only major difference expected in scaling these models up to the supermassive black holes in AGN is the decrease in disc temperature down to the UV band. The X-ray spectra of AGN should then always be dominated by the tail, irrespective of spectral state (e.g. Done & Gierliński 2005). The predicted change in shape of the tail with spectral state/mass accretion rate gives an explanation for the variety of spectral properties seen in *unobscured* subtypes of AGN such as broad line AGN, Narrow Line Seyfert 1s (NLS1) and LINERs (e.g. Middleton et al. 2008). The generally hard X-ray spectra seen in LINERS could be explained as a low $L/L_{\rm Edd}$ flow (e.g. Yuan et al. 2008 but see Maoz 2007), while broad line AGN with a strong UV disc component and weak ($\Gamma \sim 2$) X-ray tail would be analogous to the high-soft state in BHB. The NLS1s probably have the highest mass accretion rates, so have lower mass for a given luminosity (Boroson 2002), and their steeper X-ray spectra (Brandt, Mathur & Elvis 1997; Leighly 1999; Shemmer et al. 2006) make them natural counterparts for the very high state (Pounds, Done & Osborne 1995; Murashima et al. 2005; Middleton et al. 2007, M$^{\rm c}$Hardy et al. 2007) where all QPOs (both high and low frequencies) are strongest. Intriguingly, RE J1034+396 is a NLS1, so its QPO detection is consistent with these scaling models.

All this supports models where the underlying physics of the accretion flow is very similar between BHB and AGN. However, the scaling clearly breaks down under more detailed study of the X-ray spectra from high mass accretion rate objects. These should have spectra dominated by the steep tail which is typical of the high and very high states, with no disc emission in the X-ray band. Yet *all* the high mass accretion rate AGN show an excess below 1 keV (Gierliński & Done 2004; Brocksopp et al. 2006). This 'soft X-ray excess' is completely inconsistent with the expected disc component, both as its temperature is higher than predicted from the mass and mass accretion rate of these AGN (e.g. Bechtold et al. 1987), and as its shape is much smoother than a sharply peaked disc spectrum (Czerny et al. 2003;

Gierliński & Done 2004). Either the soft X-ray excess is an additional component which breaks the scaling between AGN and BHB, or it is produced by some external distortion of the intrinsic emission. Obviously it is very important to distinguish between these alternatives and the objects with the strongest soft excesses offer the most stringent constraints.

RE J1034+396 has one of the largest soft excesses known, which appears to connect smoothly onto the enormous EUV peak of its spectral energy distribution (Middleton et al. 2007). The size and temperature of this peak is extreme even amongst NLS1s (Puchnarewicz et al. 2002, Casebeer et al. 2006; Middleton et al. 2007), and an obvious question is whether this extreme soft excess is somehow linked to the detection of the QPO. Here we use *XMM-Newton* data on RE J1034+396 to test the various models for the soft X-ray excess, and speculate on its connection to the QPO.

9.2 The origin of the soft excess in high mass accretion rate AGN

There are multiple models for the origin of the soft X-ray excess seen ubiquitously in high mass accretion rate AGN. The most obvious possibility is that it is related somehow to the disc. One way to do this is if the mass accretion rate is super Eddington, so the disc spectrum is distorted by advection of radiation in the very optically thick flow. Such slim discs (Abramowicz et al. 1988) have spectra which are less peaked than a standard disc (Waterai et al. 2000) so give a better fit to the shape of the soft excess (Mineshige et al. 2000; Wang & Netzer 2003; Haba et al. 2008). Another way to modify the shape of the (standard or slim) disc emission is if it is Comptonized by low temperature electrons (Czerny & Elvis 1987; Kawaguchi 2003), perhaps produced by a hotter skin forming over the cooler disc (Czerny et

al. 2003). However, the derived temperature for this skin is remarkably similar for all objects at 0.1–0.2 keV despite a large range in black hole mass (and hence disc temperature: Czerny et al. 2003; Gierliński & Done 2004, hereafter GD04; Crummy et al. 2006). This argues against it being related to the disc, so it is unlikely to be a true continuum component.

Instead, a constant energy is most easily explained through atomic processes, in particular the abrupt increase in opacity in partially ionized material between $\sim$0.7–2 keV due to OVII/OVIII and Fe transitions. This results in an increase in transmitted flux below 0.7 keV, which could produce the soft excess either from absorption in optically thin material in the line of sight, or from reflection by optically thick material out of the line of sight. In both models the observed smoothness of the soft excess requires large velocity smearing (velocity dispersion $\gtrsim$0.3c) in order to hide the characteristic *sharp* atomic features, but with this addition both reflection and absorption models fit the shape of the soft excess equally well (Fabian et al. 2002, 2004; GD04; Crummy et al. 2006; Chevallier et al. 2006; Schurch & Done 2006; Middleton et al. 2007; Dewangan et al. 2007, D'Ammando et al. 2008). Such high velocities are naturally produced only close to the black hole, so both absorption and reflection models predict that the soft excess arises in regions of strong gravity. However, both models also require some extreme, and probably unphysical, parameters. In the reflection model, the inferred smearing can be so large that the required emissivity must be more strongly centrally peaked than expected from purely gravitational energy release, perhaps pointing to extraction of the spin energy itself (Wilms et al. 2001). The amount of reflection required to produce the soft excess can also be extreme. Quasi-isotropic emission sets a limit to the size of the soft excess of no more than a factor of 2–3 above the harder continuum emission (Sobolewska & Done 2007), yet the strongest observed soft excesses are a factor 4 larger than this (a factor $8-10$ above the extrapolated continuum), requiring that

the intrinsic illuminating spectrum is strongly suppressed (e.g. Fabian et al. 2002). This issue becomes even more problematic when incorporating any pressure balance condition (such as hydrostatic equilibrium) as this strongly limits the section of the disc in which partially ionized material can exist, hence making a much smaller soft excess (Done & Nayakshin 2007; Malzac, Dumont & Mouchet 2005).

Conversely, in the smeared absorption model, pressure balance rather naturally produces the required partially ionized zone (Chevallier et al. 2006). However, these models also imply extreme velocities, with a peak outflow velocity of ~ 0.8c required in order to smooth away the characteristic absorption features from a smooth wind which covers the source (Schurch & Done 2007; 2008). This is much larger than the maximum velocity of $\sim$ 0.2-0.4c produced by models of a radiation driven disc wind (Fukue 1996), so the absorber must instead be associated with faster material in this description. The obvious physical component would be a jet/magnetic wind, yet the amount of material is probably far too large to be associated with either of these (Schurch & Done 2007; 2008).

Thus there are physical problems with all of these models: the Comptonized disc cannot explain the narrow range in inferred temperatures, smeared reflection cannot produce the strongest soft excesses seen if the disc is in hydrostatic equilibrium, and smeared absorption requires a fast wind/jet which is not readily associated with the properties of any known component.

An alternative possibility for the absorption model is that the characteristic absorption features are masked by dilution instead of smearing, perhaps due to the wind becoming clumpy so that it partially covers the source (Boller et al. 1996; Tanaka et al. 2004; Miller et al. 2007; 2008). These models lack diagnostic power as the potential complexity of the wind means that any number of partial absorbers can be added until the model fits the observed spectra. Nonetheless, this may correspond to the more messy reality of high Eddington fraction winds from UV luminous discs

(Proga & Kallman 2004). Some of the clumps could even have high enough column to produce significant reflected emission as well (Malzac et al. 2005; Chevallier et al. 2006), giving a complex mix of reflection and partial absorption from a range of different columns, velocities and ionization states of the material.

It is important to distinguish between these very different potential origins of the soft excess as they make very different predictions about the environment and geometry of the accreting material close to the black hole. The extreme broad iron lines required in the pure reflection models are not required in the absorption models (either smeared: Sobolewska & Done 2007; Done 2007 or partial covering: Miller et al. 2008) as the broad feature redwards of the iron line is fit instead by continuum curvature (see also Sim et al. 2008). All the absorption models require the presence of material above the inner disc, probably in the form of a wind, whereas the reflection models instead suggest a clean line of sight to the inner disc. The large velocity shear in the smeared wind model requires that the material is strongly accelerated, so it potentially carries an enormous amount of kinetic energy (Chevallier et al. 2006; Schurch & Done 2006) with a corresponding impact on AGN feedback/galaxy formation.

Spectral fitting alone cannot distinguish between these very different spectral models in the 0.3–10 keV bandpass (Crummy et al. 2006; Sobolewska & Done 2007; Middleton et al. 2007; Miller et al. 2007; 2008). Variability gives additional information, but the smeared reflection and smeared absorption models are known to be able to predict similar variability patterns (Ponti et al. 2005; Gierliński & Done 2006). Here for the first time we fit *all* of these models to the data and calculate their predicted variability to see which description of the soft excess best matches the *simultaneous* constraints from both spectral and variability data.

9.3 Data Extraction

XMM-Newton observed RE J1034+396 on 2007-05-31 and 2007-06-01 for about 93 ks (observation id. 0506440101, revolution no. 1369). We extracted source and background light curves and noticed background flares and data gaps in the final 7 ks. Therefore, we excluded this data segment from analysis and used 84.3 ks of clean data starting on 2007-05-31 20:10:12 UTC for further analysis.

9.3.1 Spectra

We selected data from the PN (patterns 0–4) and MOS (patterns 0–12) in a region of radius 45 arcsec. The data are very similar in shape to a previous 16 ks *XMM-Newton* observation, but are much higher quality due to the longer exposure. Because of the extreme softness of this particular source both MOS and PN are significantly piled up. We excised the central regions of the image until the observed single and double pattern fractions were within 1 σ of the predicted values as shown in the SAS task, epatplot. This required centroids of 7.5 arcsec and 32 arcsec for the MOS and PN respectively. Background was taken from 6 source free regions of the same size.

The known discrepancies at soft energies between the PN and MOS spectra makes simultaneous fitting of these two instruments very difficult for high signal-to-noise spectra. We choose to use the MOS data in the 0.3–10 keV range for spectral fitting as the spectral resolution of the MOS camera is greater than that of the PN at low energies, allowing the possibility of constraining soft features (Pounds & Page 2006).

We use XSPEC version 11.3.2, and fix the minimum galactic absorption at $1.31 \times 10^{20}\mathrm{cm}^{-2}$ in all fits, but also allow a separate neutral absorption column to account for additional absorption in the host galaxy.

9.3.2 Energy dependence of the variability: rms spectra

A successful model must be able to describe *both* the spectrum *and* the variability. Fig. 9.1a shows the full light curve for these data, with the clear QPO which is remarkably coherent in the latter part of the observation (25–85 ks: Gierliński et al. 2008). There is also a large scale drop in flux at 40–55 ks. This looks very similar to an occultation event such as those recently recognised in other AGN (McKernan & Yaqoob 1998; Gallo et al. 2004; Risaliti et al. 2007; Turner et al. 2008). Fig. 9.1b shows the light curve in the high energy bandpass, where this dip is *not* present. This shows that there is clearly energy dependent variability in this event which is not present in the rest of the light curve. Thus the variability is *complex* and made from more than one component.

We explore this further by calculating the root mean square fractional variability amplitude (hereafter we will use the term 'rms' for simplicity) as a function of energy (see Edelson et al. 2002; Markowitz, Edelson & Vaughan 2003 and Vaughan et al. 2003). We first calculate this for the total light curve with 100s binning. Fig. 9.2a shows this rms spectrum rising smoothly with energy. This behaviour is quite unlike the rms spectra seen from other NLS1s although these can show a variety of shapes, including flat (e.g. Gallo et al. 2007; O'Neill et al. 2007), flat with a peak at 2 keV (Vaughan & Fabian 2004; Gallo et al. 2004; Gallo et al. 2007), and falling but with a peak at 2 keV (Ponti et al. 2006; Gallo et al. 2007; Larsson et al. 2008).

The rms is dominated by noise above ~ 4 keV as the count rate at high energies is very low due to the steep spectrum. In order to extend the rms to higher energies we extract light curves from the full source region, without excising the core to correct for pileup (red points in fig. 9.2b). This means that some fraction of the hard photons originate from much lower energies, but the steeply rising rms spectrum means that the variability of these pileup photons is rather small. Thus pileup adds an approximately constant offset to the hard spectrum, and so should dilute the

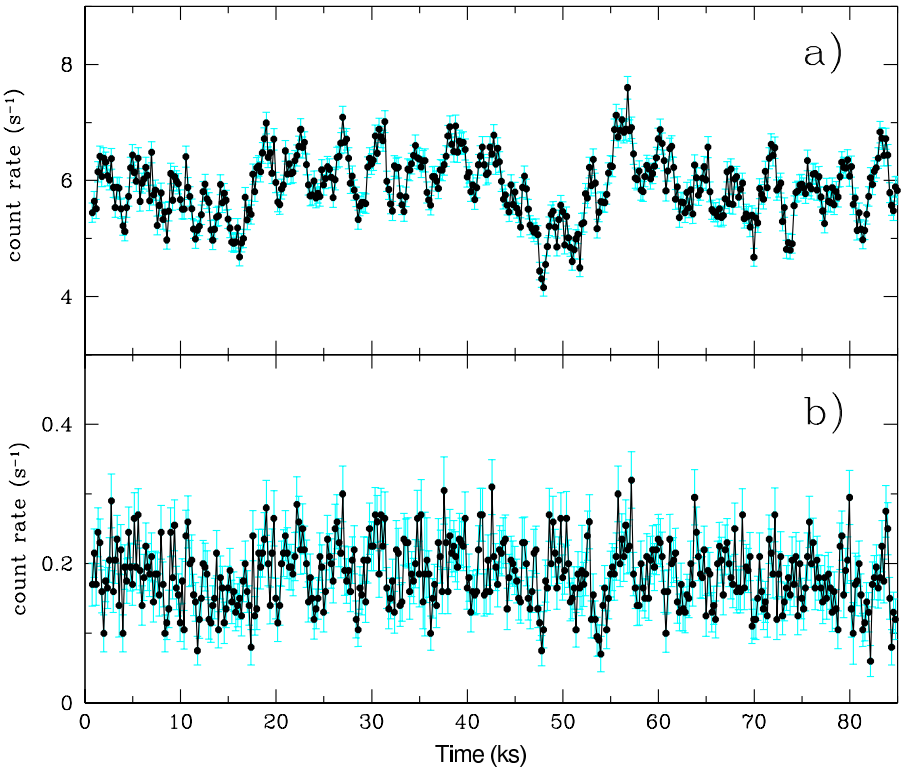

Figure 9.1: Light curve of the *XMM-Newton* (all detectors added together) observation of RE J1034+396 in (a) 0.3–10 and (b) 1–10 keV band. Clearly the 'dip' occurring ∼50 ks into the observation has little effect upon the light curve at high energies. The starting time of this observation was 2007-05-31 20:10:12 UTC.

Figure 9.2: Rms spectra. Panel (a) shows the rms from the data with the PSF core excised (black triangles). The rms rises linearly with energy but the uncertainties at high energies are large due to the low number of counts. Better statistics at high energy can be obtained by including all the data (red crosses). Pileup transfers photons from low energy to high energy, but the lack of variability in the data at low energy means that this effect dilutes the high energy rms. Thus these data give a lower limit on the variability at high energies. Panel (b) shows the different rms patterns produced from different timescale variability using all the data. The red crosses show the total variability as in (a), while the black squares show the long timescale variability (11.2–5000 μHz), the blue circles show the rms of the QPO alone (frequency of 270 μHz) and the green triangles show the rms of the rapid variability, including the QPO (135–5000 μHz).

variability seen at high energies. Instead, the rms spectrum continues to rise in a rather smooth fashion at high energies (red points in fig. 9.2b), showing that this is a good lower limit to the total variability at high energies.

The smooth increase of the rms as a function of energy seems initially most likely to be from a single component. However, there is clear evidence of different processes contributing to the variability from the different energy dependence seen in the dip event (fig. 9.1). We explore this by re-calculating the rms on a range of timescales by changing the bin time, ΔT, of the light curves. The rms is the square root of the integrated power in the light curve from frequencies of $1/T$ to $1/(2\Delta T)$ Hz, where T = 84300 s is the length of the light curve. Thus the original binning of 100 s means that the rms at each energy is the integral of the power spectrum from 11.2 to 5000 μHz. We compare this to the rms of the long timescale variability by increasing the binning to 3700 s (the QPO period), i.e. corresponding to the frequency range 11.2–135 μHz. This is shown by the black data in fig. 9.2b, and has a very different shape to the total rms (red points), with a similar amount of variability at low energies, but a sharp break around 0.7 keV so that the variability at higher energies is much lower. The variability may increase again above 2keV but we caution that these high energy points may be affected by pile-up. Subtracting this long timescale rms from the total rms (in quadrature) gives the rms of the rapid variability (including the QPO at 270 μHz), i.e. the integral of the power spectrum from 135 to 5000 μHz (green points in fig. 9.2b). This has a sharp rise with increasing energy at low energies. We can compare this directly to the rms of the QPO by calculating this from the folded light curve (blue points). This is indeed very similar in shape to the rms of the rapid variability, as expected as the QPO forms a large fraction (more than half) of the variability power in this frequency range. However, the shape at high energies is marginally different, with the rapid variability appearing to continue rising with energy while the QPO saturates at an rms of $\sim$0.2. Given the potential

problems with pileup, and the size of the uncertainties, this difference is probably not significant.

9.4 Simultaneous constraints from spectra and variability

In the following sections we take each model for the soft excess and fit it to the 0.3–10 keV spectrum. The models are listed in table 9.1. The fit results are shown in table 9.3. Then we inspect this best-fitting model to see how varying these components might produce the observed energy dependence of the variability. We focus here on the rapid variability, which is dominated by the QPO, as it is clear that the longer timescale variability may contain contributions from multiple processes. We calculate the simulated rms spectra by randomly varying a spectral model parameter with the mean equal to the best-fitting value and a certain standard deviation (Gierliński & Zdziarski 2005). We calculate the rms spectrum at high energy resolution, but then bin this to the same resolution as the real rms for direct comparison.

9.4.1 Separate component for the soft excess: DISK, SLIM and COMP

We first test the models where the soft excess is a separate emission component. A standard accretion disc spectrum (DISKBB in XSPEC) is much more strongly peaked than the data, giving a very poor fit, $\chi^2_\nu = 517/211$, showing that this is an unacceptable description of the broad-band curvature. The mass estimate of $10^{6.45} M_\odot$ from the Hβ line-width and 5100$\mathring{A}$ continuum flux (Hao et al. 2005) gives a mass accretion rate of $\sim 0.3 \mathrm{L}_{Edd}$, not formally high enough to be advection dominated. Nonetheless, we test models of an advective (slim) disc as the mass estimate is not

well constrained. Theoretical calculations show that the spectrum of a slim disc can be approximated by a sum of blackbodies, similar to the standard disc models, but with $T \propto r^{-p}$, where $0.5 < p < 0.75$ (the higher limit is the standard disc profile, while the lower limit is a fully advection dominated disc: Waterai et al. 2000). Fig. 9.3a shows that such models (DISKPBB, available as an additional local model for XSPEC) are still not broad enough to match the shape of the soft excess ($\chi^2_\nu = 457/210$). Instead, a low temperature Comptonization component (COMPTT) gives a reasonable fit to the data (fig. 9.3b). The model allows us to constrain the temperature of the seed photons to be ∼0.03keV which is consistent with the expected accretion disc, given the mass and mass accretion rate estimates (see Middleton et al. 2007, fig 10). Thus this could physically be low-temperature Comptonization of the disc emission. Hereafter we refer to this model as COMP.

It is plain from the residuals to this fit (lower panel of fig 9.3b) that there are weak atomic features at low energies, especially at ∼0.6 keV. Adding a series of narrow Gaussians gives a reduction in χ^2 of ~ 30 for significant emission features at ~ 0.55, 0.74 and 0.87 keV. These are consistent with He–like O Lyα and He- and H-like O radiative recombination continua i.e. indicating photoionized material. However, there are no corresponding narrow lines in the RGS data, so these features must be intrinsically broad. Their equivalent width is ≤ 10 eV, so these have negligible impact on the derived continuum which is the subject of this paper.

In BHB the power-law tail is generically very variable, while the disc is remarkably constant (Churazov et al. 2001). If the soft excess is really related to the disc and is constant, then we expect the low energy variability to be suppressed, as observed, because of increasing dilution of the variable power-law by the constant soft excess at low energies.

We quantify this effect by taking the same Comptonization plus power-law model as fits the spectrum of the soft excess, and varying the normalisation of the power-

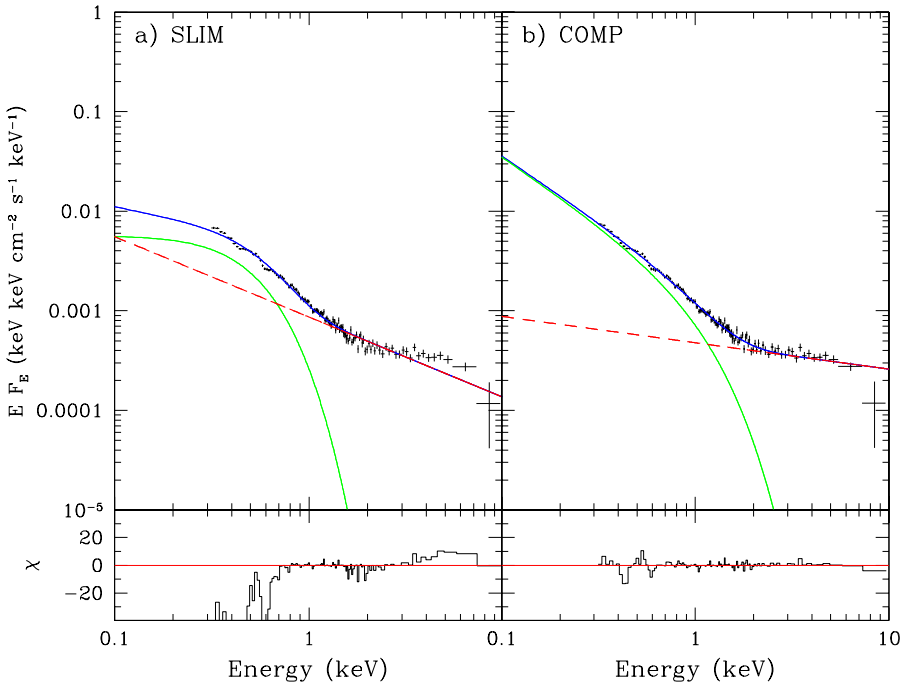

Figure 9.3: Spectral models for a separate component for the soft excess: The upper panel shows the deconvolved spectra, while the lower panel shows residuals to the fit. (a) uses an advective disc to describe the soft excess while (b) uses a Comptonized disc (green solid curve). Both models require a separate power-law to fit the spectrum above 2 keV (red dashed line) to produce the total spectrum (blue solid line). It is clear that the smooth curvature of the soft excess rules out the simple advective disc model, while it is well described by the Comptonized disc.

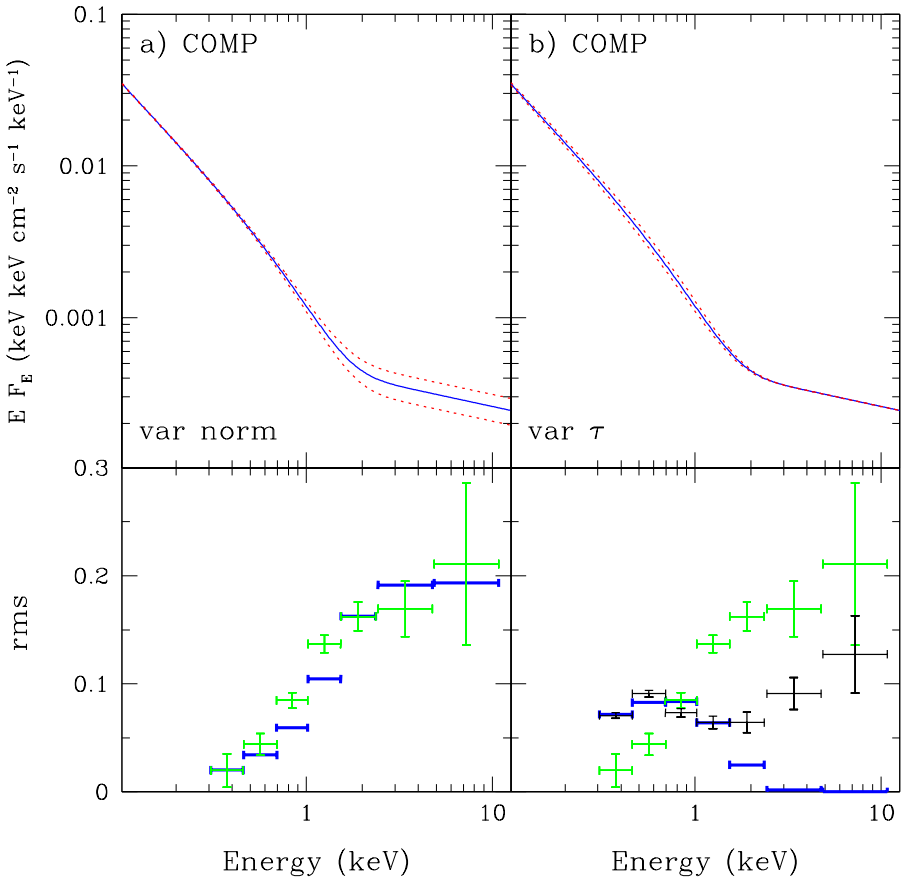

Figure 9.4: Variability of a Comptonized disc and power-law: The upper panel shows the mean spectrum (solid blue curve) and $\pm 1\sigma$ variability (dotted red curves). The lower panel shows the rms produced by this variability (dark thick blue horizontal lines) compared to that seen in the data on short timescales (light green crosses). Panel (a) shows the patterns produced by varying the power-law in normalisation while keeping the Comptonized disc constant. The rapid increase in dilution of the power-law variability below 1 keV exactly matches the rapid drop on short timescales. This is very strong evidence that this spectral decomposition is correct. (b) shows the pattern produced by changing the optical depth of the Comptonized disc by 1.5 per cent, whilst keeping the power-law constant. This gives a fairly good match to the observed long timescale variability (shown as black crosses in the lower panel).

law tail by 20 per cent. This gives a constant rms where the tail dominates (above 2 keV) and a dramatically increasing suppression of the variability below this, as the fractional contribution of the constant soft excess increases (fig. 9.4a). This looks very similar to the observed drop in rms at low energies in the rapid variability (and QPO). This provides very strong evidence that a two component model is the correct spectral decomposition as both the spectrum and spectral variability can be easily described in this model. The soft excess is a separate component above the power-law tail at low energies, and the rapid variability (including the QPO) is a modulation of the tail.

This spectral decomposition also gives a framework in which to explain the long-timescale variability as there is a separate soft component. However, simply varying the normalisation of the Comptonized disc results in a flat rms spectrum until the power-law significantly dilutes the variability at $\sim$ 1keV. This conflicts with the observed rise in rms to $\sim$0.7 keV, so requires a change in shape of the soft component. Physically, this could be due to a change in either the optical depth or temperature, and both of these would result in the Comptonisation spectrum pivoting about its low energy cutoff at $\sim 5kT_{\rm seed} \sim 0.15$ keV (see also the discussion in Gierliński & Zdziarski 2005). Fig. 9.4b shows how changing the optical depth by 1.5 per cent can produce this characteristic rise, which is then diluted by the constant power-law above $\sim$ 0.7 keV. While this does indeed match the broad shape of the long timescale rms, we caution that there should also be some contribution to this from partial covering if the dip in the light curve is indeed an occultation event.

9.4.2 Smeared Reflection models: REF1 and REF2

We next explore how the reflection model for the soft excess can fit both the spectrum and spectral variability. We use the constant density reflection models of Ballantyne, Iwasawa & Fabian (2001) (available as a table model in XSPEC). These

models (described in more detail in Ross & Fabian 2002) become very dependent on the assumed cooling processes for spectra steeper than $\Gamma > 2.5$ (Done & Nayakshin 2007). To circumvent this, we instead use the spectra tabulated for $\Gamma = 2.2$, and multiply the model by $E^{-(\Gamma-2.2)}$ in order to limit the effect of such model uncertainties. We also convert the normalisation of the reflected emission to that of the illuminating power-law so that the amount of reflection is parameterised by the solid angle of the illuminated material, $\Omega/2\pi$ and inclination (Done & Gierliński 2006), which we fix at 30° . We smear this using the convolution version of the LAOR code for the velocity structure of an extreme Kerr spacetime (Laor 1991).

Fig. 9.5a shows that this is a very poor fit to the data ($\chi^2_\nu = 612/210$), as a single ionization state reflector cannot simultaneously produce both the hard tail *and* the shape of the soft excess. This is a common feature in good signal-to-noise data: multiple reflectors are required, one to fit the soft excess, another to fit the iron line, dispelling a key attraction of the model (Crummy et al. 2006). Nonetheless, a double reflector can indeed fit the data well (fig. 9.5b), where the hard tail/iron line region requires a neutral reflector (modelled using the THCOMP code: Życki, Done & Smith 2000 as the REFLION code does not extend down to the very low ionization states required). We hereafter refer to this model as REF2.

This is a very different spectral deconvolution to the one where the soft excess is a separate Comptonized component (COMP). The entire spectrum is now formed from a single Comptonization component (producing a power-law spectrum in this band-pass), and its reflection which forms a 'hard excess' at high energies.

A linearly rising rms can be produced by pivoting the steep Comptonization about its peak in seed photons (around ∼0.15 keV, as before), assuming both reflectors respond to this changing illumination (though we fix the ionization of each component for simplicity: fig. 9.6a). While this would fit the overall rms shown in fig. 9.2b, it plainly cannot match the two very different shaped components which

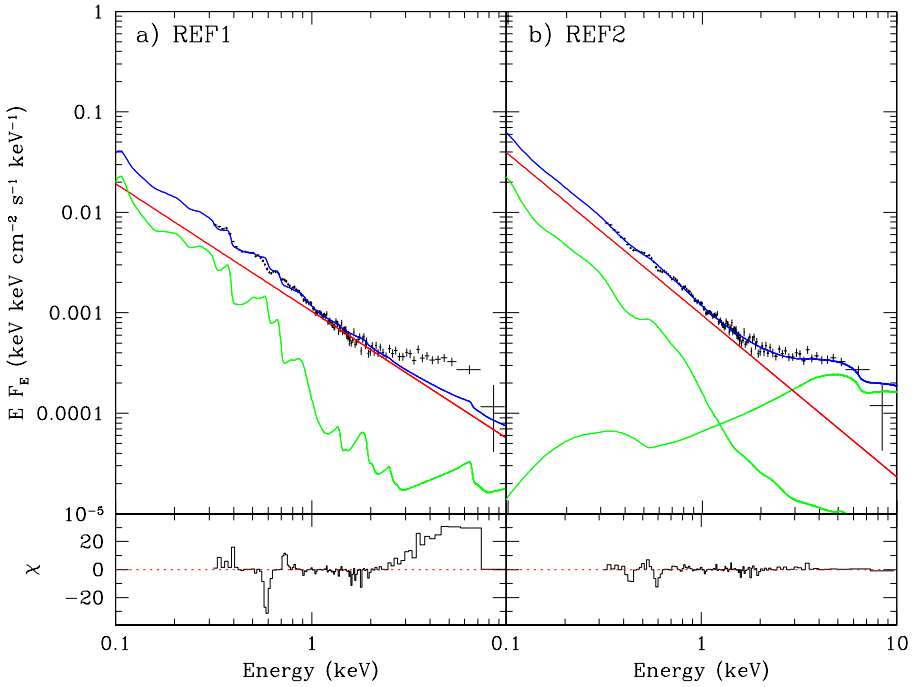

Figure 9.5: As for fig. 9.3 but for a reflection origin for the soft excess. (a) has a steep power-law (red dashed line) and its ionized, smeared reflection (light green curve) while (b) has the steep power-law illuminating two separate reflectors, one of which is similarly ionized to that in (a) and one which is predominantly neutral. The residuals clearly show that at least two reflectors are required to describe the spectrum in this model.

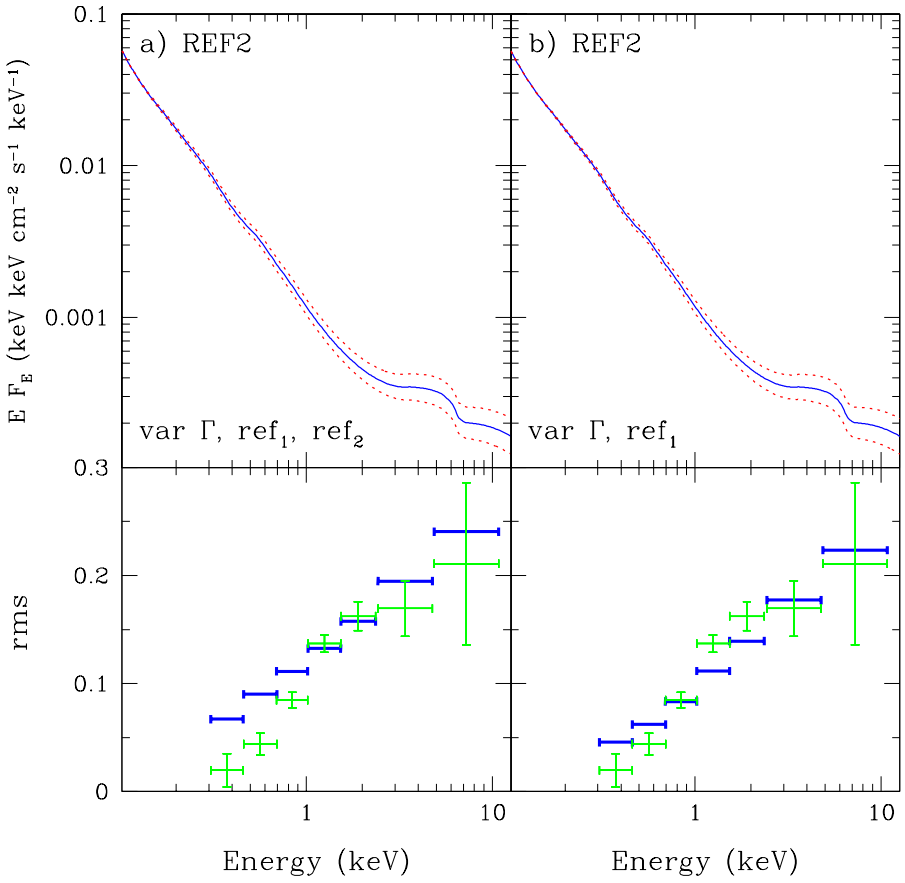

Figure 9.6: As for fig. 9.4 but for the double reflection model for the soft excess. (a) shows the rms produced by pivoting the steep spectrum about the peak in seed photon flux at $5kT_{\rm seed} \sim 0.15$ keV when both reflectors respond to this illumination. This gives a linear rise in rms as a function of energy, which does not match the sharper rise around 0.7 keV seen in the rapid variability. (b) shows that this can be roughly matched if the ionized reflector which contributes mainly at low energies remains constant while the more neutral reflector responds to the spectral pivoting.

underlie the variability. The rapid variability rms shape does *not* rise linearly with energy, there is a clear inflection point around ∼0.7 keV. This has an obvious origin in the separate Comptonized disc models discussed above, as this is the energy at which this component starts to dominate the spectrum and hence dilute the variability. However, it is possible to match this in the reflection model by assuming that the ionized reflector remains constant. Fig. 9.6b shows how this dilutes the variability towards lower energies, giving a fairly good fit to the rapid variability rms.

Constant reflection components are a feature of these models for the soft excess in other AGN, and may arise from strong light bending effects (Miniutti & Fabian 2004). This simultaneously explains the lack of variability together with enhanced amplitude and extreme smearing. However, our spectral deconvolution and variability require that the constant reflector is the one which is *not* enhanced relative to the illuminating power-law, making this model appear somewhat contrived in RE J1034+396.

9.4.3 Smeared Absorption Models: SWIND and XSCORT

We now fit the smeared absorption models. These assume the source is completely covered by a partially ionized wind from the disc, which has a large velocity shear to smear out the characteristic strong absorption lines. We first use the simple SWIND model (available on the local models page for XSPEC) of Done & Gierliński (2004; 2006), where the absorption from a partially ionized column of material is convolved with a Gaussian velocity field. This is an excellent fit to the data (fig. 9.7a), but the best-fit velocity dispersion goes to the upper limit of 0.5c allowed in the model. The Gaussian form of the velocity dispersion means that this corresponds to a velocity shear greater than the speed of light, which is obviously unphysical (see Middleton et al. 2007, Schurch & Done 2007a, b).

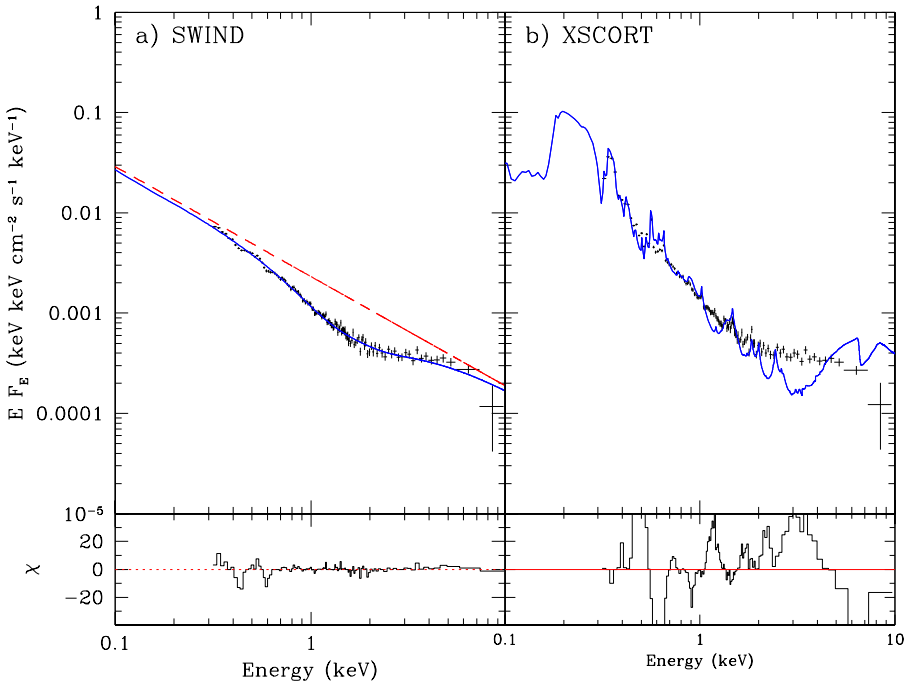

Figure 9.7: As for fig. 9.3 but for a smeared absorption origin for the soft excess. (a) has a steep power-law (dashed red line) which is distorted by a velocity smeared absorber which completely covers the source (solid blue curve). This produces a very good fit to the spectrum, but requires a large velocity dispersion in the material. (b) shows instead the results using the expected velocity dispersion from a line driven disc wind. The velocity spread of 0–0.3c is not sufficient to smear out the characteristic atomic features.

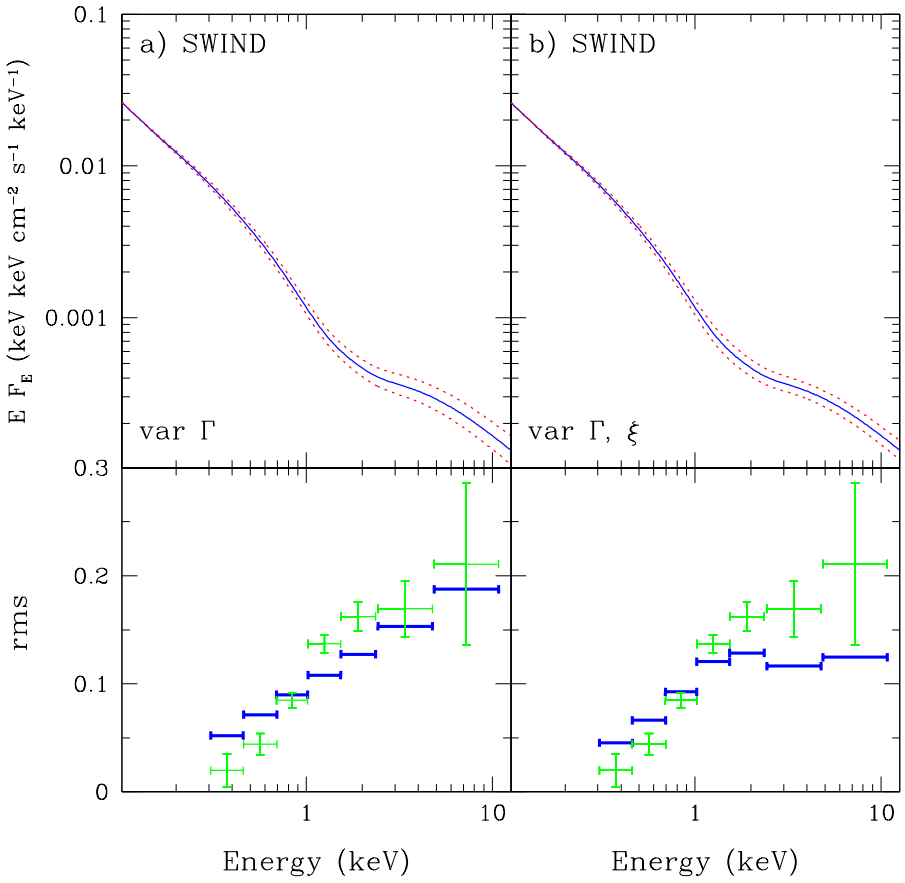

Figure 9.8: As for fig. 9.4 but for a smeared absorption model for the soft excess. (a) shows the rms produced by pivoting the steep spectrum about the peak in seed photon flux at $5kT_{\rm seed} \sim 0.15$ keV without changing the ionization of the absorber. Similarly to fig. 9.6, this linear rise in rms as a function of energy does not match the sharper rise around 0.7 keV seen in the rapid variability. (b) shows that this low energy rise can be matched if the ionization responds to the changes in illumination as this enhances the variability over 0.7–2 keV where the absorption dominates. However, this also predicts that the variability should drop above 2 keV, which is not seen in the data.

Instead we fit more physical wind absorption models, calculated from the XSCORT code, which accelerate the wind from 0 to 0.3c, and use this internal velocity field self-consistently in the photoionization code. These models have only been calculated for a small number of parameters (Schurch & Done 2007a), so cannot be properly fit to the data. However, we have taken the model with parameters closest to those required by the soft excess spectral shape, and then corrected for the different spectral index, as in section 9.4.2. Fig. 9.7b shows that, while this gives a strong soft excess, the velocity shear is insufficient to smooth the strong atomic features in the 0.7–3 keV band into the observed smooth rise, so this gives a very poor fit to the data ($\chi^2_\nu = 2153/212$). Thus the absorption does not arise in a line driven disc wind, but instead must be connected to much faster moving material in this model.

We explore the variability properties of the fast wind in fig. 9.7a, since the more physical wind (fig. 9.7b) does not fit the data. Because the whole spectrum is again made from the intrinsically steep spectrum, then simply pivoting this at the peak flux of the seed photons gives a linearly rising rms (fig. 9.8a), similar to that of fig. 9.6a. Instead, allowing the ionization of the fast wind to change in response to this changing illumination means that the variability is enhanced over the range where the partially ionized material has most effect on the spectrum i.e. 0.7–2 keV (Gierliński & Done 2006). Fig. 9.8b shows how this does not produce enough enhancement of the variability to follow the sharp rise in rms at ∼0.7 keV and it also predicts that this enhancement does not affect the spectrum above ∼2 keV so the rms at high energies is also too small.

Thus, while the smeared absorption model is a good fit to the spectrum, it cannot easily match the variability patterns seen, making it a less attractive solution.

9.4.4 Partial covering models: IONPCF1 and IONPCF2

If instead the absorption is clumpy then it can lead to clouds which partially cover the source. These can be ionized as they are illuminated by the central source, so we model this using partial covering by partially ionized material (ZXIPCF, available as an additional model for XSPEC). This fits the data fairly well (fig. 9.9a) for a column with very low ionization, covering 75 per cent of the source. We call this model IONPCF1. A second partially ionized, partial covering component is marginally significant ($\Delta\chi^2 = 12$ for 4 additional parameters), but this must be outflowing, with a blueshift of $0.12 \pm 0.01c$. This is similar to the velocities sometimes seen in highly ionized Kα absorption lines from iron in high mass accretion rate AGN (e.g. the compilation of Reeves et al. 2008), and also close to the theoretical expectations of the maximum velocity of a UV line driven disc wind (Proga et al. 2004). Hereafter we call this model IONPCF2.

Similarly to fig. 9.6a and fig. 9.8a, pivoting the steep illuminating spectrum about its peak flux at $\sim 5\mathrm{kT}_{seed}$ gives a linearly rising rms (fig. 9.10a) which does not match the sharper rise in rms seen in the data. Again, dilution by a constant component at low energies is required, so fig. 9.10b shows the variability pattern produced by assuming that the ionized absorption component at low energies remains constant while the rest of the spectrum varies as before. Physically this could arise from light travel time delays if this is scattered from ionized material at some distance from the source. This produces some suppression of variability at low energies, but not as much as required to fit the rms of the rapid variability.

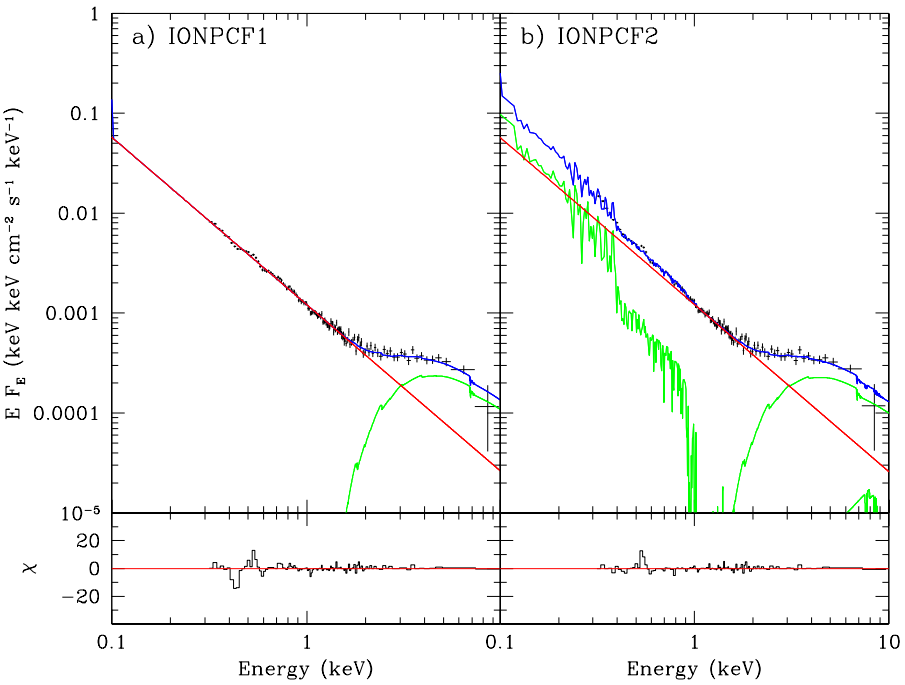

Figure 9.9: As for fig. 9.3 but for a partial covering model for the soft excess. (a) has an intrinsically steep power-law, part of which is strongly absorbed by nearly neutral material (light green curve) and part of which is unabsorbed (dashed red line). (b) shows a marginally better fit to the spectrum, where there is a second absorbed component from material which is ionized, so it also contributes at low energies.

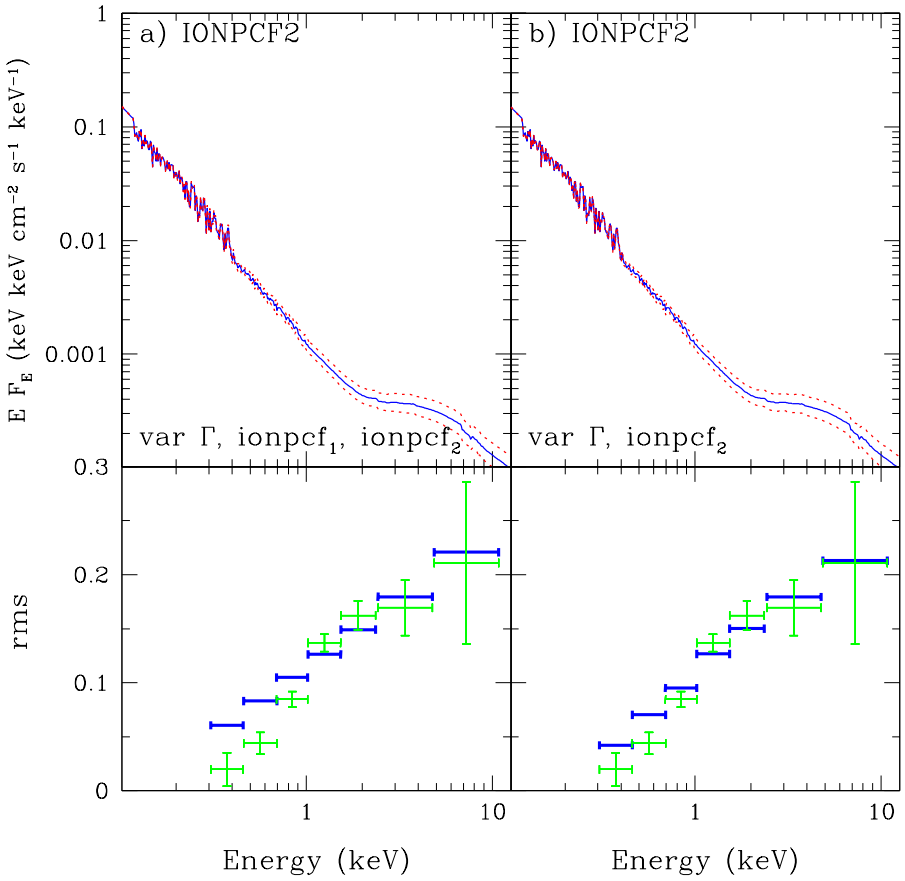

Figure 9.10: As for fig. 9.4 but for the partial covering model for the soft excess. (a) shows the rms produced by pivoting the steep spectrum about the peak in seed photon flux at $5kT_{\rm seed} \sim 0.15$ keV without changing the ionization of the absorber. Similarly to fig. 9.6a and fig. 9.8a, this linear rise in rms as a function of energy does not match the sharper rise around 0.7 keV seen in the rapid variability. (b) shows that this low energy rise is better fit if the ionized absorber, which contributes at low energies, is held constant while the spectrum pivots, but the model's predicted rise at ∼0.7 keV is still not as sharp as is observed.

Name	Description	XSPEC syntax
DISK	Standard disc	WABS(DISKBB+POWERLAW)
SLIM	Advective disc	WABS(DISKPBB+POWERLAW)
COMP	Comptonized component	WABS(COMPTT+POWERLAW)
SWIND	Smeared wind absorption	WABS*SWIND(POWERLAW)
XSCORT	Ionized absorption/emission	WABS(XSCORT)
REF1	Ionized reflection (single)	WABS(POWERLAW+CONLINE*REFLBAL(POWERLAW))
REF2	Ionized reflection (double)	WABS(POWERLAW+CONLINE(THCOMP) +CONLINE*REFLBAL(POWERLAW))
IONPCF1	Single ionized partial covering	ZXIPCF*WABS(POWERLAW)
IONPCF2	Double ionized partial covering	ZXIPCF*ZXIPCF*WABS(POWERLAW)

Table 9.1: Summary of the models used in the paper.

9.5 Constraints from spectra and variability

Any viable model for the soft excess must simultaneously fit both the spectrum and spectral variability with the same model parameters. The spectra alone can be fit with a variety of continua. There is clear curvature but this is degenerate. The spectra can either be fit with low energy spectral curvature, together with a ($\Gamma \sim 2.3$) power-law at high energies, or with a steep power-law at low energies ($\Gamma \sim 3.6$) together with curvature at high energies from emerging reflected (REF2) or absorbed components (IONPCF2), or by a somewhat less steep power-law ($\Gamma \sim 3.3$) with curvature around 0.7–2 keV from absorption in a rapidly accelerating wind (SWIND). However, the energy dependence of the rapid X-ray variability (which is dominated by the QPO in these data) breaks these degeneracies. The rms spectrum over the whole observation shows a smooth rise with energy, initially appearing to favour models where there is a single variable component which pivots about a point just below the low-energy band-pass of *XMM-Newton*. However, this total rms is made up from two quite dissimilar variability patterns for the short and long timescales. Both of these contain clear changes in the rms at ~ 0.7 keV, with the rapid variability amplitude strongly increasing with energy at this point while the longer timescale variability slightly decreases. These combine together in such a way as to produce an apparently featureless overall rms.

The rms of the rapid variability clearly supports the spectral decomposition where the soft excess is a separate, low temperature Comptonization component (COMP). The variability drops just where the low temperature Compton component starts to dominate, so the rms shape is easily produced from models where the soft excess remains constant and simply dilutes the variability of a high energy power-law tail. This is very similar to the sorts of spectral decompositions used in binary systems, where the QPO (and all other rapid variability) is associated with the tail, not with the disc.

Model	Parameter	Value	χ^2_ν/d.o.f
COMP	Γ	$2.28^{+0.13}_{-0.10}$	287/210
	$N_{\rm PL}$ ($\times 10^{-4}$)	$4.9^{+0.8}_{-0.3}$	
	T_{seed}	$0.03^{+0.01}_{-0.03}$	
	kT_e (keV)	0.26 ± 0.03	
	$N_{\rm comptt}$	$10.6^{+1.2}_{-0.8}$	
SWIND	Γ	$3.10^{+0.02}_{-0.05}$	306/210
	$N_{\rm PL}$ ($\times 10^{-4}$)	$23.1^{+0.9}_{-0.7}$	
	lg ξ	$2.82^{+0.09}_{-0.02}$	
	σ	$0.50^{+**}_{-0.05}$	
REF2	Γ	$3.61^{+0.08}_{-0.04}$	268/206
	$N_{\rm PL}$ ($\times 10^{-4}$)	$9.4^{+0.3}_{-2.4}$	
	$\Omega_1/2\pi$	$0.43^{+1.05}_{0.10}$	
	$R_{\rm in,1}$	$2.1^{+1.0}_{-0.8}$	
	lg ξ	$3.02^{+0.16}_{-0.07}$	
	$\Omega_2/2\pi$	56^{+15}_{-18}	
	$R_{\rm in,2}$	$3.2^{+0.4}_{-1}$	

Table 9.2: Table A, see description of table B.

Model	Parameter	Value	χ^2_ν/d.o.f
IONPCF1	Γ	3.69 ± 0.05	287/210
	$N_{\rm PL}$ ($\times 10^{-4}$)	74 ± 13	
	lg ξ	$0.8^{+0.3}_{-0.5}$	
	N_H (10^{22} cm^{-2})	14^{+2}_{-3}	
	f	$0.84^{+0.02}_{-0.04}$	
IONPCF2	Γ	$3.68^{+0.09}_{-0.13}$	233/206
	$N_{\rm PL}$ ($\times 10^{-4}$)	165^{+367}_{-69}	
	lg ξ_1	$0.7^{+0.4}_{-0.9}$	
	$N_{H,1}$ (10^{22} cm^{-2})	12^{+2}_{-5}	
	f_1	0.80 ± 0.06	
	lg ξ_2	$2.72^{+0.05}_{-0.5}$	
	$N_{H,2}$ (10^{22} cm^{-2})	153^{+13}_{-14}	
	f_2	$0.63^{+0.07}_{-0.09}$	
	v_2/c	0.12 ± 0.01	

Table 9.3: Table B: Best-fitting parameters of selected spectral models. Models described in the text that do not fit the spectrum are not shown here. Error bars are 90% confidence, and ** denotes a parameter that reached its limit. Γ is the photon spectral index, $N_{\rm PL}$ is the power-law normalization at 1 keV, ξ is the ionization parameter (in the units of erg cm s^{-1}), σ is the velocity dispersion in the units of c, Ω is the reflector solid angle, $R_{\rm in}$ is the inner disc radius (in the units of GM/c^2) and f is the covering factor.

By contrast, the alternative spectral models (where the soft excess is an artifact of some distortion on an intrinsic steep power-law spectrum) have much greater difficulty in matching the energy dependence of the rapid variability. Pivoting a steep intrinsic spectrum about its peak flux at $\sim 5kT_{seed}$ gives a linearly rising rms, so some additional assumptions are required to produce the observed faster drop in variability at low energies. Changing the ionization of the absorber in the smeared wind model (SWIND) gives enhanced variability in the 0.7–2 keV region which matches well to the shape of the rms at low energies. However, this then drops above 2 keV where ionization changes no longer affect the spectrum, which does not match the observed rms.

By contrast, both the double reflector (REF2) and double partial covering model (IONPCF2) have ionized components at low energies, so holding these constant dilutes the low energy variability. However, physically this seems somewhat contrived, and both these (but especially IONPCF2) have difficulties in suppressing enough variability at the lowest energies.

Thus the combined spectral and spectral variability constraints strongly favour the model where the soft excess is a true continuum component, described by a low temperature Comptonized disc component (COMP). The long timescale variability can also be explained in this spectral decomposition by changing the temperature and/or optical depth of the Comptonization to give a predicted rms which matches the data very well. However, the light curve shows that there can also be discrete energy dependent events (the dip), which seems more likely to be from an occultation. If so, then there should also be some contribution from absorption in the spectrum, and this might also shape the longer timescale variability.

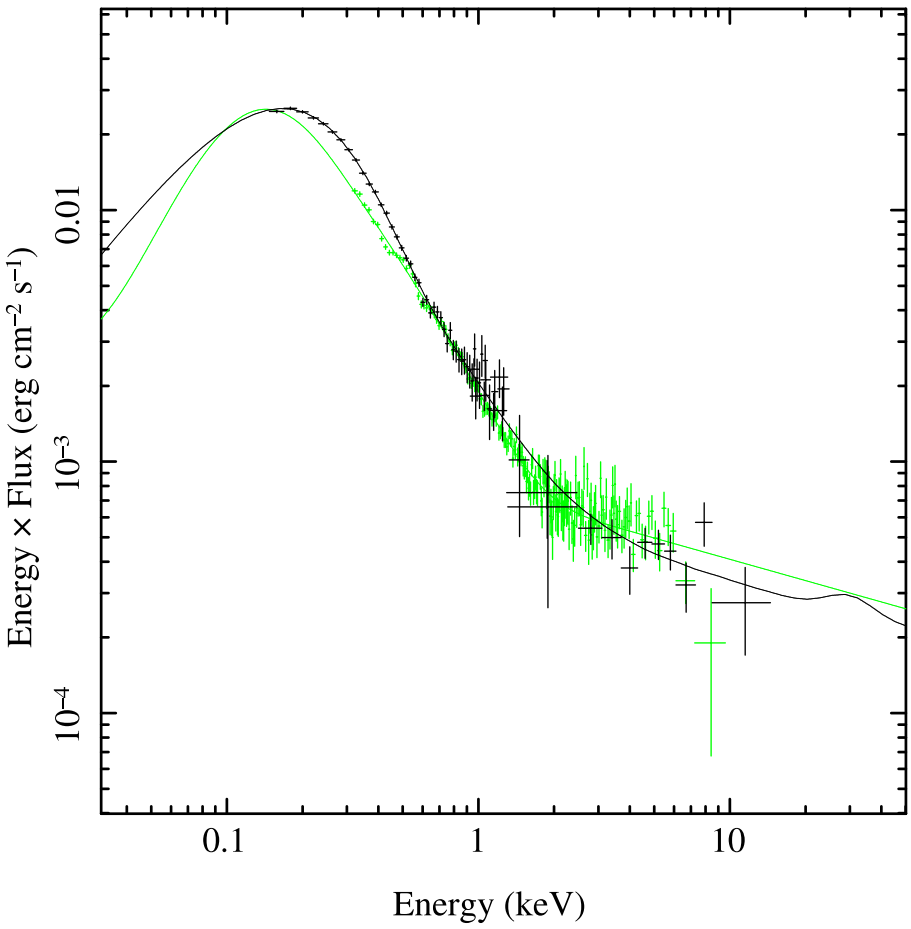

Figure 9.11: Comparison of RE J1034+396 (light green) and GRS 1915+105 (black) energy spectra. The GRS 1915+105 spectrum was shifted in energy by a factor of 20 and renormalized to match the RE J1034+396 spectrum.

9.6 Constraints from the broad-band spectral energy distribution

This decomposition of the X-ray spectrum into a Comptonized disc with separate tail to high energies (COMP) also looks sensible in light of the overall spectral energy distribution. Both the UV/EUV/soft X-ray shape and the rms variability of the X-ray emission show that this peaks at $\sim$ 0.15 keV (Puchnarewicz et al. 2000; Casebeer et al. 2006; fig. 9.2). Integrating the COMP model down to this energy gives a luminosity of $\sim 7\times10^{43}$ ergs s^{-1}. This is already more than 10 per cent of the bolometric luminosity of $\sim 5 \times 10^{44}$ ergs s^{-1}. However, in the reflection and partial covering models, REF2 and IONPCF2, the observed soft X-ray flux is only a small fraction of the total illuminating power-law. The hidden emission required by both of these models is a factor $\sim$ 10 larger. This luminosity must be reprocessed, yet is more than the total bolometric luminosity of the source! Thus these two models fail on energetics as well as requiring somewhat contrived assumptions in order to match the rms variability and requiring an uncomfortably steep ($\Gamma \sim 3.6$) intrinsic continuum.

This all strongly supports the conclusion that in RE J1034+396 the soft excess is a Comptonized disc component, connecting smoothly onto the EUV peak of the spectral energy distribution and extending out to $\sim$ 1 keV. This does not have an obvious counterpart in the typical black hole binary systems. These can show convincingly clean disc spectra (thermal dominant state, high-soft state, ultrasoft state), or higher temperature Comptonization (10–20 keV: very high state, intermediate state, steep power-law state), but generally they do not show low temperature Comptonization (see e.g. Done, Gierliński & Kubota 2007). However, most of these systems have $L/L_{\rm Edd} < 1$, so they may not be a good guide to the spectra of super-Eddington flows. The disc structure should change at such high mass

accretion rates, with strong winds potentially increasing the amount of material in the corona, leading to mass loading of the acceleration mechanism and decreasing energy per particle. Whatever the origin, a similar process of low temperature disc Comptonization probably happens in the unique galactic black hole binary GRS 1915+105. This is the only black hole binary in our galaxy which consistently shows super-Eddington luminosities (Done, Wardziński & Gierliński 2004), and it can show spectra which are dominated by a huge, low temperature Comptonized disc component, with a weak power-law tail to higher energies. Fig. 9.11 shows how one of these spectra from GRS 1915+105 (the low ω state in fig.7 of Zdziarski et al. 2005) fits almost exactly onto the *XMM-Newton* spectrum of RE J1034+396 with a shift in energy scale by a factor 20. This gives a mass estimate for RE J1034+396 of $\sim 2 \times 10^6 \mathrm{M}_\odot$ from scaling the disc temperature as $M^{-1/4}$, which seems quite reasonable (Puchnarewicz et al. 2002). Another more recent observation has confirmed the presence of the 67Hz QPO in a similar low-temperature Comptonised state of GRS 1915+105 (Ueda, Yamaoka & Remillard 2008). This is highly suggestive of an intrinsic similarity between the two objects.

Understanding the origin of the soft excess in RE J1034+396 may not necessarily solve the problem of the soft excess in general. The spectral energy distribution of this object is plainly rather different from that in most other high mass accretion rate AGN in that the soft excess contains a large fraction of the bolometric luminosity of the source (Middleton et al. 2007). Spectral distortion models (reflection or absorption) are clearly more likely to explain a feature carrying only a small fraction of the bolometric luminosity. Instead, the continuous EUV/soft X-ray excess in RE J1034+396 favours a common origin for the disc and soft excess, unlike that for most other quasars, where the UV and soft X–rays do not appear to smoothly connect to each other (Haro-Corzo et al. 2007).

9.7 Conclusions

The combined constraints from the spectrum and variability show the soft excess in RE J1034+396 is most likely a smooth extension of the accretion disc peak in the EUV probably arising from low temperature Comptonization of the disc. This remains more or less constant on short timescales, diluting the QPO and rapid variability seen in the power-law tail, at the low energies where the soft excess dominates. As in the black hole binary systems, the QPO is a feature of the tail *not* of the disc.

The conclusion that the soft excess is low temperature Comptonization of the disc emission may not necessarily be more widely applicable to other NLS1s. The spectrum of RE J1034+396 is unique, so extrapolating results from this object may not be justified. In particular, if this object has a very high (super-Eddington?) mass accretion rate then it could enter a new accretion state (perhaps analogous to the unique galactic binary GRS 1915+105 and the ultra luminous X-ray sources: Roberts 2007) which may also be the trigger for its, so far, unique QPO. A different origin for the soft excess in RE J1034+396 has the advantage that it would not require some unknown physical mechanism to restrict the temperature of the continuum in all objects to a narrow range (Gierliński & Done 2004), though does require a coincidence that this temperature in RE J1034+396 is so close to that ubiquitously seen for the soft excess. Nonetheless, it is clearly possible that, in selecting the most extreme soft excess object, we have also selected the one where the soft excess has a different origin.

Chapter 10

Paper 5: The X-ray Binary Analogy to the First AGN QPO

10.1 Introduction

Active galaxies (AGN) and accreting black hole binaries (BHB) are the most energetic and dynamic systems in the Universe, with intrinsic variability seen over a broad range of timescales. This variability is most often quantified via a power spectrum, showing the (squared) amplitude of variability as a function of frequency. For BHB this spectrum can be very approximately described as band limited noise, with a 'flat top' in $\nu P(\nu)$ (equal variability power per decade in frequency) i.e. $P(\nu) \propto \nu^{-1}$. This extends between a low and high frequency break, ν_b, below which the PDS is $P(\nu) \propto \nu^0$, and ν_h, above which the spectrum steepens to $P(\nu) \propto \nu^{-2}$. While this is adequate to describe the limited statistics of AGN power spectra (see the compilation of Markowicz et al. 2003), the excellent data from BHB show that band limited noise is intrinsically bumpy, and is better represented by a series (generally 4–5) of peaked noise components (Belloni & Hasinger 1990; Psaltis, Belloni & van der Klis 1999; Nowak 2000; Belloni, Psaltis & van der Klis 2002). Superimposed on this continuum are a series of narrower features, referred to as quasi-periodic oscillations (QPOs). These QPOs come in two distinct categories, termed low and

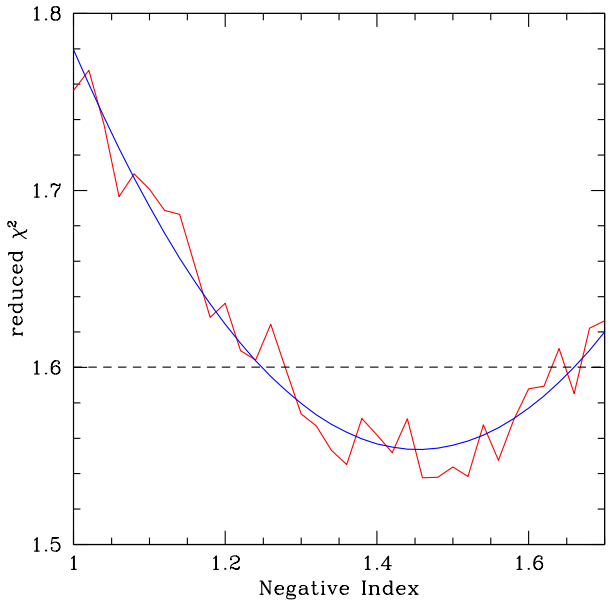

Figure 10.1: Reduced χ^2 (58 d.o.f.) plot for single power-law power spectrum simulations for the 'in-phase' lightcurve. We fit this to a quadratic function to smooth over the intrinsic stochastic effects. We use this to define the best-fit index and its uncertainty ($\Delta\chi^2 = 2.7$ i.e. 90 % confidence as shown by the dashed horizontal line) as -1.45$^{+0.20}_{-0.21}$. This is consistent with the analytical result of -1.35 ± 0.18 (Gierliński et al. 2008).

high frequency QPOs respectively, and their properties depend strongly on mass accretion rate (see e.g. the reviews by van der Klis 2004; Remillard & McClintock 2006; Done, Gierliński & Kubota 2007, hereafter DGK07).

There is now considerable evidence to suggest that AGN and BHB are mass-scaled analogies and share the same underlying physics of accretion, notably the Radio/X-ray fundamental plane relations (Merloni, Heinz & di Matteo 2003; Falcke, Körding & Markoff 2004), variability scaling (McHardy et al. 2006) and mass-accretion rate dependant spectral behaviour (Pounds, Done & Osborne 1995; Middleton, Done & Schurch 2008; Middleton et al. 2007). If this is the case then we

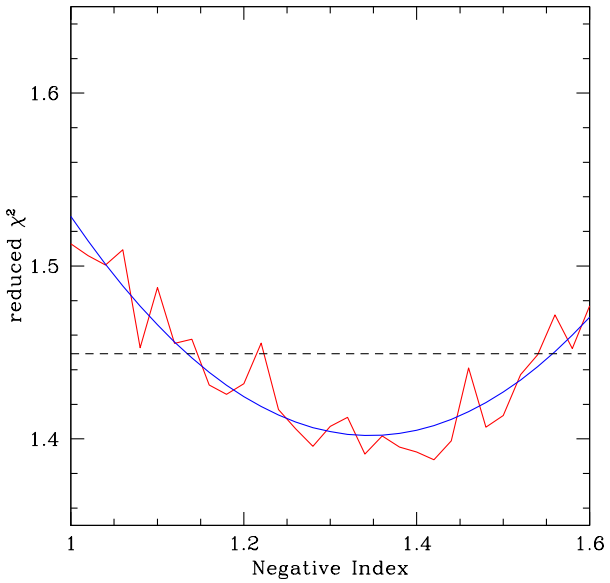

Figure 10.2: As for fig 10.1 but excluding the single frequency bin of the QPO in the 'in-phase' segment (57 d.o.f.). The result is consistent with that of simulations including the QPO over the same segment as expected, as the QPO is fairly central in the power spectrum so this power does not distort the index.

would naturally expect QPOs to be visible in the power spectra of AGN at frequencies inversely scaled with the mass. However, these much longer timescales make detecting such QPOs in AGN very challenging (Vaughan & Uttley 2006). Many claims for such periodic signals have been made, but these all failed to properly determine the significance of the QPO on top of the (uncertain determination) of the underlying red noise power spectrum (see the discussion in Vaughan 2005). By contrast, our discovery of a $\sim$ 1 hour periodic signal from a narrow line Seyfert 1 (NLS1), REJ1034+396 is highly significant (>99%) *with* correct modelling of the red noise spectrum (Gierliński et al. 2008).

Beyond simply detecting the QPO, we need to identify it with one of the multiple BHB QPOs. This is a problem as the mass of the AGN black hole is not well constrained, as different techniques (Hβ line width, stellar velocity dispersion) give

mass estimates which differ by a factor of 30-50 (Gierliński et al. 2008). Instead, we use the distinctive nature of the optical/UV/X-ray SED of REJ1034+396, where the bolometric luminosity is dominated by a very luminous component peaking in the EUV (Puchnarewicz et al. 2001; Middleton, Done & Gierliński. 2007) to argue for a super-Eddington mass accretion rate (Mineshige et al. 2000; Wang & Netzer 2003, Haba et al. 2008). Thus we need to study a super-Eddington BHB in order to find an analogue with the AGN QPO. GRS 1915+105 is the only BHB which spends significant time at (probably) super-Eddington accretion rates (Done, Wardziński & Gierliński 2004). This shows additional QPOs which appear distinct from the standard LFQPO and HFQPO seen in sub-Eddington flows. We outline the properties of all these QPOs below, and then use lightcurve simulations of the underlying power spectral shape to try to constrain which of these appears most like that seen in REJ1034+396.

10.2 QPO phenomenology in BHB

10.2.1 Low-frequency QPOs

These are subdivided into 3 classes, types A, B and C (see e.g. Casella et al. 2005), not to be confused with the spectral states in GRS 1915+105 which are given the same name (Belloni et al. 1997)!

The C class LFQPO is almost always present in the low-hard state of BHB. It has frequency which *increases* between $\sim$ 0.01-6 Hz as the spectrum softens from a dim, harder, low-hard state to a bright, softer low-hard state, through to the hard intermediate state (Belloni et al. 2005). There is a correlated increase in strength, coherence and harmonic structure of the QPO (van der Klis 2004; Remillard & McClintock 2006). Its spectrum closely follows that of the harder X-ray Comptonisation component rather than the soft disc emission (Rodriguez et al. 2002; Sobolewska &

Życki 2003; 2006), so it is produced by some fundamental mode of the corona, not of the disc. It is also correlated with the shape of the underlying broad-band noise power spectrum in the sense that the low frequency break, ν_b, where the underlying noise power breaks from ν^0 to ν^{-1} increases together with the LFQPO frequency (Psaltis et al. 1999). In observations of the type C LFQPO, the high frequency tail of the power spectrum is consistent with a steeper slope of $\sim \nu^{-2}$ (Gierliński, Nikołajuk & Czerny 2008; Revnivtsev, Gilfanov, & Churazov 2000; Remillard et al. 2002).

In the context of the truncated disc/hot inner flow models for the low-hard state, all these observations can be interpreted if the inner edge of the thin disc decreases as a function of mass accretion rate. The increasing overlap between the disc and hot flow means more seed photons from the disc intercept the hot flow, giving stronger Compton cooling and softer spectra. The moving inner radius means that the section of the hot flow which is unconstrained by the disc gets smaller, so increasing all its characteristic variability frequencies, while the smaller radial extent means the QPO can become stronger and more coherent (DKG07).

While this gives a qualitative match to the observations, there is still no generally accepted physical model for the QPO. Vertical (Lense-Thirring) precession (Stella & Vietri 1998; Psaltis & Norman 2000) of the hot flow can match the data (Ingram, Done & Fragile 2009). Alternatively, it could be produced by spiral structure in the hot flow driven by magnetic stresses (Tagger & Pellat 1999; Machida et al. 2008), or some other such mode of the hot flow which has yet to be identified.

The type B LFQPO is seen as the source continues to soften after the highest type C LFQPO from the hard intermediate state to the soft intermediate state. This is a rather subtle change in spectrum, but triggers an abrupt collapse of the underlying broad-band noise power spectrum, leaving the QPO (and its multiple harmonics) dramatically enhanced in prominence (Belloni et al. 2005).

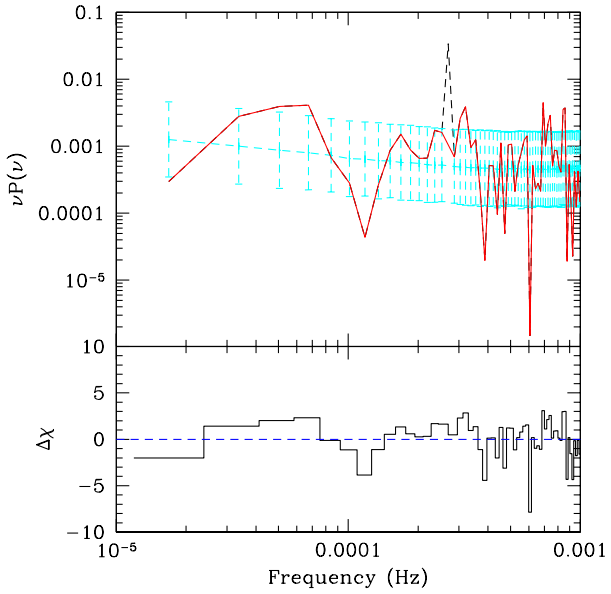

Figure 10.3: The upper panel shows the best-fit, average, simulated power spectrum (cyan) to that of the 'in-phase' data (red) without the QPO (shown as the dashed black line). This assumes a single power-law form for the intrinsic fluctuations, together with statistical (white) noise. The dispersion in the simulations is shown by the dashed error bars (cyan). The lower panel shows residuals to this best-fit.

As the spectrum continues to soften in the soft intermediate state, Class A LFQPOs can be seen. These are weaker and much broader (so there is no harmonic structure discernible) than the type B LFQPOs, but appear at similar frequencies, and again are seen against a very low continuum noise power. Then the QPOs disappear altogether as the spectrum continues to soften into a completely disc dominated state (Remillard & McClintock 2006; Casella et al. 2005).

While the type C LFQPO is ubiquitous in the low-hard and hard intermediate states, types B and A are much rarer, seen only in the soft intermediate state.

10.2.2 High-frequency QPOs

Transient high-frequency QPOs (HFQPOs) are detected in several BHB sources (GRO J1655-40, XTE J1550-564, GRS 1915+105, 4U 1630-47 and XTE J1859+226). These appear to be constant in frequency despite changes in luminosity by a factor of 3-8, so these may be a stable signature of the accretion system. The values are consistent with being directly proportional to the mass of the black hole (Remillard & McClintock 2006). They are often seen in 3:2 ratio, implying some sort of resonance sets the frequencies, but the exact nature of this resonance is yet to be clearly determined (Abramowicz & Kluzniak 2001; Kluzniak et al. 2004; Török et al. 2005; Kato 2004; Rezzolla et al. 2003; Fragile et al. 2005).

These seem to be detected only with the soft intermediate state, i.e. are seen simultaneously with type B and A LFQPOs and not with type C LFQPOs (Remillard et al. 2002). It is extremely difficult to accurately assess the underlying noise power spectral shape at such high frequencies as this is dominated by the statistical white noise, but the co-added spectra of Remillard et al. (2002) suggest that these high frequency QPOs sit on a broad band continuum which has a ν^{-1} shape (most likely another Lorentzian component). This has a normalisation which is over an order of magnitude below that seen for the lower frequency 'flat top' noise which accompanies the type C LFQPOs (Remillard et al. 2002). While the normalisation of the power spectrum strongly depends on the energy bandpass in BHB due to the different variability of disc and Comptonisation components (e.g. Churazov et al. 2001; Done & Gierliński 2005), the study of Remillard et al. (2002) used only data above 6 keV, where the disc makes little contribution. Hence this difference in normalisation is probably intrinsic rather than due to dilution of the variability by the constant disc.

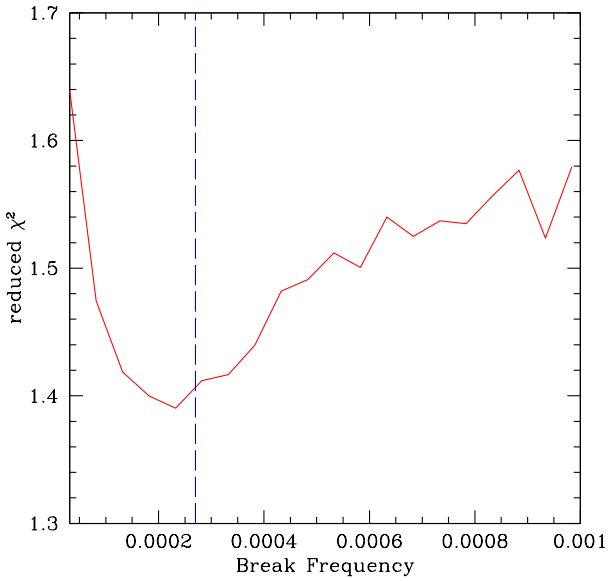

Figure 10.4: As in fig 10.1 but for an underlying broken power-law (indices from -1 to -2) spectral shape of the in-phase segment of the lightcurve without the QPO. The χ^2 of the best-fit of a break close to the QPO frequency (2.7×10^{-4} Hz: vertical dashed line) is similar to that for the single power-law fit in fig 10.2, so this is not a significantly better description of the spectral shape.

10.2.3 Additional QPOs seen only in GRS 1915+105

GRS 1915+105 is highly luminous, so never gets to the low-hard state. Instead it ranges between the hard intermediate state, soft intermediate state and disc dominated states. However, it also shows spectra which are unlike any of the standard states, being dominated by low temperature Comptonisation of the disc together with a very weak hard tail (Zdziarski et al. 2003). In this state it can show some particularly unique QPOs, including very strong, narrow QPOs with complex harmonic structure at tens of millihertz (Morgan, Remillard & Greiner 1997). These are startlingly similar to the QPO frequencies seen in the ultra-luminous X-ray sources M82 X-1 (Strohmayer & Mushotzky 2003) and NGC5408 X-1 (Strohmayer

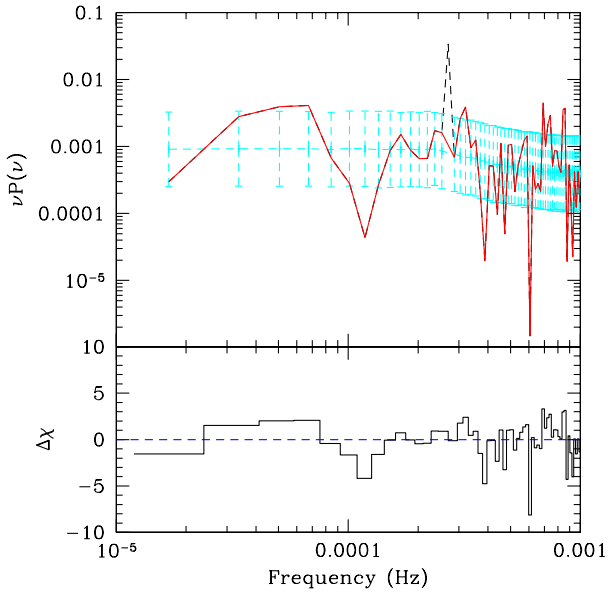

Figure 10.5: As in fig 10.3 but for a broken power-law (indices from -1 to -2) fit to the 'in-phase' power spectrum without the QPO.

at al. 2007). While these low frequencies clearly imply intermediate mass black holes if they are identified with the standard LFQPO, it is plain from the data of GRS 1915+105 that such low frequencies can also be formed from super-Eddington accretion onto a 14 $M_{\odot}$ black hole (Heil, Vaughan & Roberts 2009). Simultaneously with this very low frequency QPO, GRS 1915+105 can also show an occasional QPO at 67 Hz which is single peaked. This has only been strongly detected in a few datasets (Morgan, Remilllard & Greiner 1997) plus a few other weaker detections (Morgan, Remilllard & Greiner 1997; Ueda et al. 2009), in a possible 3:2 harmonic ratio with a feature at 41 Hz (McClintock & Remillard 2006). The statistical noise is not so dominant as for the HFQPOs as these are at lower frequencies. Nonetheless, it is far enough into the white noise to make it very difficult to determine the shape of the broad-band continuum power underneath this QPO.

10.2.4 AGN QPO identification

The frequencies of the LFQPO (A, B and C) range from $\sim$ 0.1-10 Hz in the BHB whose mass is $\sim 10M_{\odot}$. Scaling this to the 2.7×10^{-4} Hz signal of REJ1034+396 then implies a mass of $< 3.7 \times 10^{5}M_{\odot}$. This gives $L/L_{Edd} > 10$ as the bolometric luminosity of REJ1034+396 is $\sim 5 \times 10^{44}$ergs s^{-1}. This is inconsistent with the observation that the LFQPO in BHB occurs in sub-Eddington states.

The HFQPO instead gives a mass of 7×10^{6} or $10^{7}M_{\odot}$, depending on whether the observed periodicity corresponds to the 2nd or 3rd harmonic (Gierliński et al. 2008). This gives $L/L_{Edd} = 0.5 - 0.3$, consistent with the range in luminosity over which the HFQPO is seen in BHB. However, there are many active galaxies and Quasars seen at this mass and mass accretion rate (e.g. Boroson 1992) and none have the distinctive 'hot disc' dominated spectrum of REJ1034+396 (Middleton et al. 2008). The markedly different spectrum of REJ1034+396 to that of a 'composite' AGN spectrum (e.g Casebeer et al. 2006) makes a strong argument for it being a super-Eddington source, in which case its mass must be $\leq 4 \times 10^{6}M_{\odot}$.

Since REJ1034+396 is most probably super-Eddington, then it is likely that its QPO is none of the standard sub-Eddington QPOs. The closest analogy seems to be the 41/67 Hz QPO seen in the super-Eddington states of GRS 1915+105 which implies a mass of 2 and $3{\times}10^{6}M_{\odot}$ respectively. We explore this potential identification further by using the properties of the broad-band noise power. The type C LFQPO in BHB sits on the 'flat top', ν^{-1}, section of the continuum noise, just before it breaks at ν_h to ν^{-2} (van der Klis 2004; Remillard et al. 2002), while the type B and A LFQPOs should have very little underlying continuum noise. The HFQPO and 67 Hz QPO should also have very little underlying continuum noise, though the shape of this is poorly constrained by the BHB data.

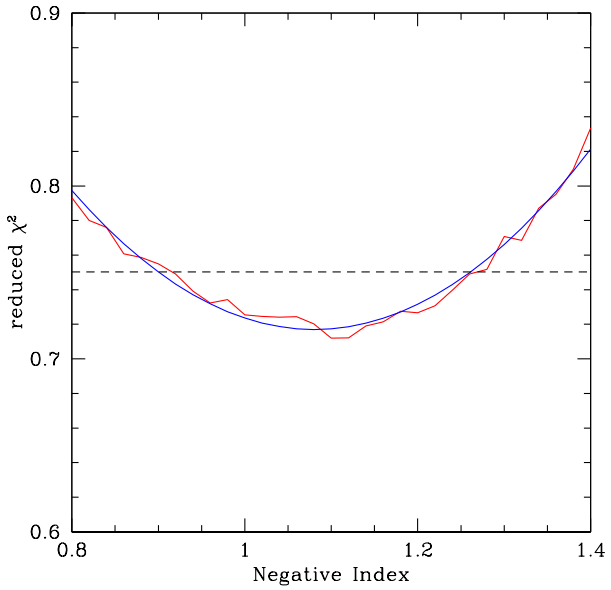

Figure 10.6: As in fig 10.1 for a single power-law description of the power spectrum without the QPO from the full lightcurve (81 d.o.f.)

10.3 Lightcurve Simulations

The analytical method of fitting the broad-band shape of the power spectrum of Vaughan (2005) is only applicable to a single power-law continuum noise shape, so does not include intrinsic breaks or the effects of statistics (white noise at high frequencies). Instead we simulate an ensemble of lightcurves with given power spectral properties using the method of Done et al. (1992), using the corrected power spectral statistics (Timmer & Koenig 1995), as developed by Uttley et al. (2002).

The real data are evenly sampled and binned on timescale Δt and span a total time of T_{data}. This has mean, I, total variance, $\sigma^2_{data} = \sigma^2_{int} + \sigma^2_{err}$, where σ^2_{int} is due to the intrinsic variability of the source and σ^2_{err} is the additional variance added by statistical uncertainties. We generate a lightcurve using the fast Fourier transform method of Timmer & Koenig (1995), spanning a timescale NT_{data} (where N$\gg$1) with some intrinsic power spectral shape, $P(f)sin^2(2\pi f\Delta t)/2\pi f\Delta t$, where the sin^2

term accounts for the suppression of high frequency power due to binning (Done et al. 1992). We snip this up into N separate lightcurves of length T_{data}. For each lightcurve we measure $\sigma^2_{i,int}$ and I_i, and then scale so that the average mean and variance of the ensemble is the same as that in the real data. We then add white noise with the same properties as in the real data, take the power spectra of the simulated lightcurves and use these to define the statistics of the power spectral distribution.

One key problem with this method is that it is *linear* while the real data are known to be non-linear. The physical process which generates the noise keeps σ_{int}/I constant as the source varies (Uttley & McHardy 2001). This is quite unlike the simulated lightcurve properties, e.g. for $P(f) \propto \nu^{-\alpha}$ with $\alpha > 1$ (red noise) then there is no well defined mean, so no well defined $\sigma_{i,int}/I_i$. Thus the snipped lightcurves made from this power spectrum have large dispersion in σ_{int}/I, so a large range in power spectral normalisation, defined as $\int P(f)df = (\sigma_{int}/I)^2$. This wide dispersion is unlike that of the real data, where the noise process is self-similar. An exponential transform of the simulated linear lightcurve can recover approximately the required statistical properties (Uttley, McHardy, & Vaughan 2005) but instead we simply choose to put a break in the input power spectrum at $0.5/T_{data}$. At frequencies below the break the spectrum is flat (α=0), and above the break the spectrum follows the desired input power spectral shape. The result is a set of snipped lightcurves of the same length and statistical properties as the real data, with a well defined mean and dispersion.

10.4 The underlying continuum power spectral shape of REJ1034+396

XMM-Newton observed REJ1034+396 on 2007-05-31 and 2007-06-01 for about 91

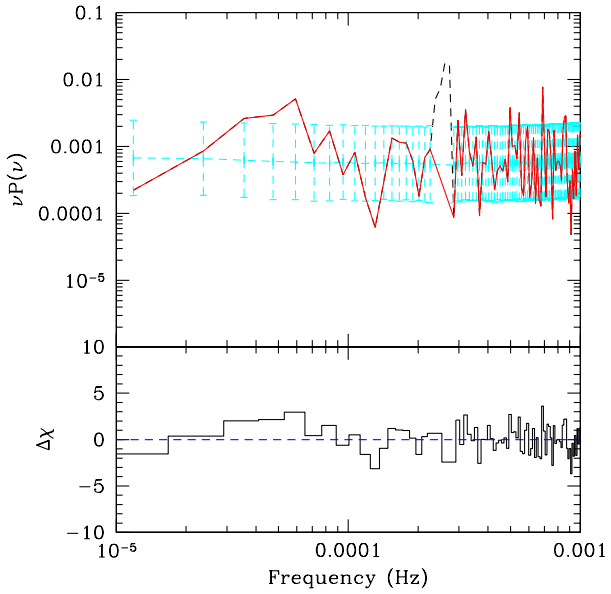

Figure 10.7: As in fig 10.3 for the best fit, single power-law fit to the power spectrum without the QPO from the full lightcurve.

ks (observation id. 0506440101, revolution no. 1369). Details of the data extraction are given in Middleton et al. (2009). This resulted in 84.3 ks of clean data starting on 2007-05-31 20:10:12 UTC. The QPO is highly coherent over 16 periods in a 59ks segment of this total lightcurve, hereafter called the 'in-phase' data. The resulting power spectrum of this 'in-phase' data is shown in figure 10.3, where the QPO is present at >99.9% significance above the red noise (Gierlińksi et al. 2008). The index of the total (i.e. including the QPO) power spectrum over the frequency range not dominated by statistical noise (i.e. above 10^{-3}Hz) was estimated using the analytical method of Vaughan (2005) to be 1.35 ± 0.18 (Gierliński et al. 2008).

10.4.1 Simulations of the in-phase segment

We first check that our simulations reproduce the analytical result. Fig 10.1 shows the χ^2 versus power spectral index for a single power-law fit to the entire power

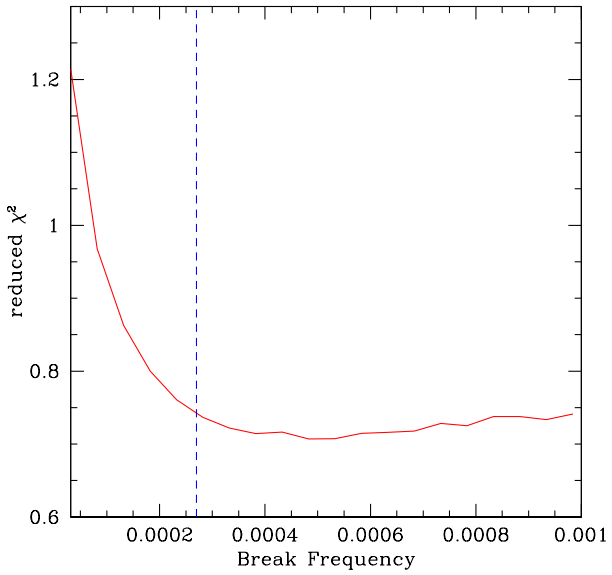

Figure 10.8: As in fig 10.1 for simulations of a broken power-law (indices -1 to -2) fit to the power spectrum without the QPO from the full lightcurve. Again, this is not a significantly better fit than the single power-law shown in fig 10.6.

spectrum below 10^{-3} Hz. The simulations are inherently stochastic so there are fluctuations. We smooth these by fitting a quadratic which gives a minimum at -1.45 $^{+0.20}_{-0.21}$, consistent with the analytical result.

However, here we are more interested in the shape of the power spectrum which underlies the QPO, so we remove the single point at the QPO frequency, replacing it with the fractional rms of the bin directly preceding it. We then redo the single power-law simulations with this reduced $(\sigma_{int}/I)^2$. We show the results from this in fig 10.2, again fit to a quadratic to smooth over the inherent stochasticity. This gives -1.35 $^{+0.22}_{-0.21}$, similar to the previous result as the QPO is fairly central in the fitted section of the power spectrum, so does not greatly distort the average power spectral slope. The fit is obviously better in terms of overall reduced χ^2, and is an acceptable description of the data at $\sim 97\%$ confidence. This best-fit, average power spectrum is shown together with residuals in fig 10.3.

We repeat the analysis using a broken power-law, fixing the slope below and above the break to -1 and -2 respectively, and then varying the break frequency. Fig 10.4 shows that there is a minimum in χ^2 for such a break at a frequency close to the QPO. However, the value of χ^2 is slightly (though not significantly) higher than that for a single power-law description of the underlying power spectrum, so this is not a better description of the power spectrum than a single power-law. The best-fit, average broken power-law together with errorbars from statistical uncertainties is shown in fig 10.5 together with the residuals to the real power spectrum (minus the QPO) in the panel below.

10.4.2 Full lightcurve

The longer timescale spanned by the 'full' lightcurve extends the power spectrum down to slightly lower frequencies so may give tighter constraints on any power spectral break. However, the QPO is now not so coherent, so is spread over more frequency bins. We simulate the underlying power spectrum by excluding 5 frequency bins around the QPO frequency, and replacing them with the preceding bins. Fig 10.6 shows the resulting χ^2 distribution for the single power-law, which has index $-1.08\pm^{+0.18}_{-0.18}$. The overall reduced $\chi^2 \approx 1$, showing that this is a good description of the data. Fig 10.7 shows the best-fit, average single power-law fit to the real power spectrum. Error bars come from statistical uncertainties and, as before, the residuals to the fit are shown in the panel below.

We again test for the presence of a break in the underlying red noise (excluding the QPO) by simulating a broken power-law with indices fixed at -1 and -2. The resulting χ^2 plot (fig 10.8) again shows that such a spectrum with a break frequency slightly above the QPO is consistent with the data, but is not required by it. As before, the best-fit, broken power-law is plotted in fig 10.9.

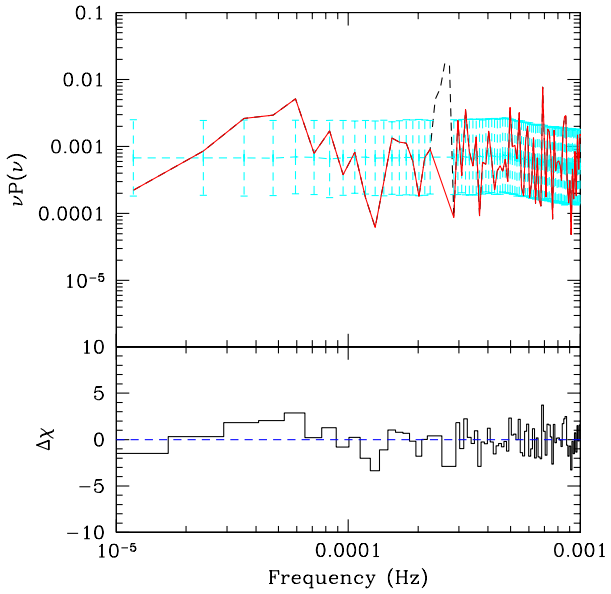

Figure 10.9: As in fig 10.3 for the best fit, broken power-law (indices -1 to -2) fit to the power spectrum without the QPO from the full lightcurve.

10.4.3 Summary of constraints from the power spectral shape

The underlying power spectral shape is consistent with a single power-law of index -1.3. This is inconsistent with the $\sim \nu^{-2}$ shape seen at high frequencies in the sub-Eddington states of Cyg X-1 (Revnivtsev et al. 2000), but may be consistent with the (very poorly constrained) noise power shape underlying the HFQPO or 67 Hz QPO. However, the power spectral shape is clearly consistent with that expected underneath the LFQPO, i.e. with a power spectrum which breaks from ν^{-1} to ν^{-2} at a frequency just above the LFQPO frequency.

While the power spectral shape cannot then easily distinguish between the type of QPO, its normalisation should break this degeneracy. The HFQPO and 67 Hz QPO in GRS 1915+105 lie on a much lower continuum noise power than the LFQPO. Our measured normalisation of $\nu P(\nu) \sim 10^{-3}$ is lower than the ~ 0.01 seen ubiquitously under the LFQPO, but higher than the $\sim 10^{-4}$ level underneath the 67 Hz QPO in

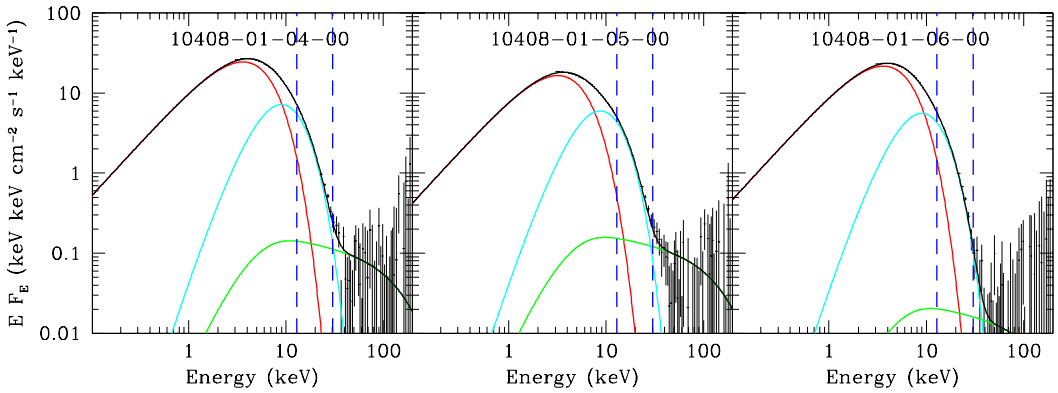

Figure 10.10: Unabsorbed PCA and HEXTE X-ray spectra of GRS 1915+105 in the three observations showing the 67Hz QPO at $\geq 3\sigma$. The total model (black) is made of components from a disc blackbody (red), low temperature, optically thick thermal Comptonisation (cyan), and thermal Comptonisation with a hotter plasma (green). The vertical dashed lines indicate the 13-30 keV energy band used to create the power spectrum shown in fig 10.12b.

GRS 1915+105 (Morgan et al. 1997). Instead it seems closest to the noise power seen underneath the HFQPO in Remillard et al. (2002). However, bandpass effects are very important as different components have different variability, and this can substantially affect the derived normalisation of the power (Churazov et al. 2001; Done & Gierliński 2005). Hence we now look in detail at the energy spectra for GRS 1915+105 at the time when it shows the 67 Hz QPO, our most likely candidate for the AGN QPO, and compare components and bandpass with REJ1034+396.

10.5 Energy spectra

The data from GRS 1915+105 which show the 67 Hz QPO are the RXTE observations on April the 20th (OBSID: 10408-01-04-00), April the 29th (OBSID: 10408-01-05-00) and May 5th (OBSID: 10408-01-06-00) 1996 (Morgan, Remillard & Greiner

1997). The energy spectra of these observations are shown in fig 10.10, fitted with a disc black-body component (DISKBB) and a low-temperature, optically thick thermal Compton component (COMPTT). This is accompanied by a tail to higher energies, which we model as high temperature thermal Comptonisation, with power-law index fixed at 2.2 and electron temperature at 100 keV. The tail is probably much more complex (see e.g Zdziarski et al. 2005), but this gives an adequate description of the RXTE data. We show the data with its corresponding best-fit model, corrected for absorption (fixed to the variable abundance model used in Done, Wardziński & Gierliński 2004), superimposed on the data in fig 10.10.

Fig 10.11 shows the spectrum of REJ1034+396 fitted with the same three component model. This has a ratio of inferred (bolometric) disc flux to Comptonised flux of 3.0, and a ratio of disc to power-law flux of 19, similar to that of GRS 1915+105 (4.3/38, 3.0/24 and 4.3/33 for the 04, 05 and 06 ObsIDs respectively). However, the ratio of electron temperature to disc temperature is rather higher for REJ1034+396 than for GRS 1915+105 (6.6 versus 1.6, 1.8 and 1.7), making the approximately power-law section of the 'soft excess' rather than Wien shape of this component. There are other energy spectra in GRS 1915+105 which match this aspect more closely (Middleton et al. 2009), but these data do not show a significant high frequency QPO.

We can now quantify the bandpass effects. In GRS 1915+105, Remillard et al. (2004) show the 41/67 Hz QPO computed from the lightcurve in the 13-30 keV bandpass range, rather than the 2–20 keV range in Morgan et al. (1997). We overlay this energy range on the spectra in fig 10.10 to show that this mostly samples the low temperature Comptonisation component, excluding most of the disc component which dilutes the variability, as well as most of the higher energy power-law. To be dominated by the corresponding spectral components in REJ1034+396 requires a bandpass of 0.3-1.5 keV.

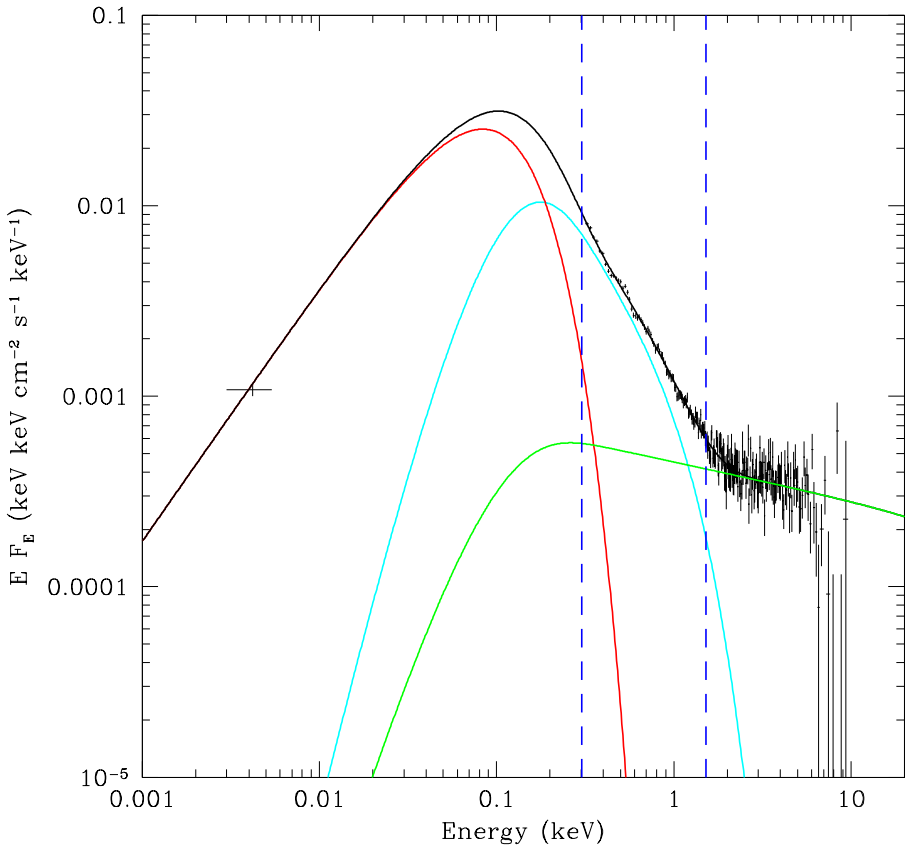

Figure 10.11: Unabsorbed optical/UV/X-ray SED of REJ1034+396 showing the deconvolved disc (red), low temperature Compton component (cyan) and Comptonisation from a higher temperature plasma (green). The vertical dashed lines indicate the energy band which contains a similar amount of the spectral components (dominated by the low temperature Comptonisation) as in the 13-30 keV energy band for GRS 1915+105 (fig 10.10).

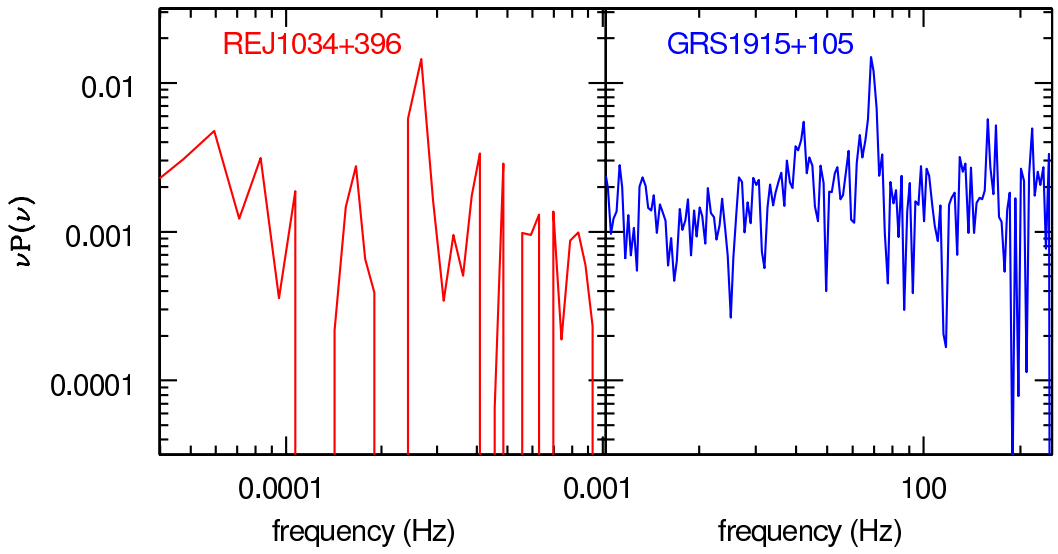

Figure 10.12: (a) shows the PDS of REJ1034+396 in the 0.3-1.5keV energy band, while (b) shows the corresponding PDS of GRS 1915+105 in the 13-30 keV energy band (Remillard et al. 2003). Unlike the other power spectra shown in this paper, the statistical noise has been subtracted from both, so that the PDS shows only the intrinsic power. Both cover 1.5 decades in frequency, and are on the same scale. Both normalisation and slope underlying the QPO are very similar, supporting the identification of the AGN QPO as analogous to the 67 Hz QPO in GRS 1915+105.

Fig 10.12a shows the resulting power spectrum from 0.3-1.5 keV. Unlike all the other power spectra, this one has statistical noise subtracted, so has less power at high frequencies. However, the intrinsic power is very similar to that of the total lightcurve in both shape and normalisation. Fig 10.12b shows the 13-30 keV power spectrum of GRS 1915+105 of Remillard et al. (2004), again with statistical noise subtracted. This is plotted using the same scale in $\nu P(\nu)$ over 1.5 decades in frequency (10-300Hz in GRS 1915+105, scaled by the putative mass difference of $3 \times 10^6/14$ corresponding to $4.66 \times 10^{-5} - 1.4 \times 10^{-3}$ Hz in REJ1034+396). These power spectra are startlingly similar in both shape and normalisation.

Conversely, this normalisation of the 'flat top' noise power at νP(ν)$\sim 10^{-3}$ is not consistent with the factor 10 higher noise power seen underlying the LFQPO in GRS 1915+105 (Zdziarski et al. 2005) and other BHB (Done & Gierliński 2005).

10.6 Conclusion

It is clearly important to identify the BHB analogue of the QPO seen in the power spectrum of REJ1034+396 as this has the potential to unify the physics of the accretion flow. However, we cannot simply mass scale the AGN QPO frequency to see which BHB QPO is closest in frequency as the mass of the AGN is poorly known. Instead we use more indirect arguments to constrain its nature.

The LFQPO is seen in BHB at sub-Eddington rates, but mass scaling the frequency to the AGN QPO implies strongly super–Eddington rates, making this unlikely to be the correct identification. Instead, the HFQPO is seen in the BHB around $\sim 0.3L/L_{Edd}$, similar to the accretion rate inferred for the AGN from mass scaling the QPO frequency. However, while this gives a consistent explanation for the observed frequency, it does not explain why the 'hot disc dominated' spectrum is so different from other AGN of this mass and mass accretion rate. Instead, the spectrum strongly suggests that the source is mildly super–Eddington. In this case,

the correct QPO should be one seen in mildly super–Eddington BHB.

GRS 1915+105 is the only BHB to spend significant time accreting at super–Eddington rates, where it can occasionally show a new type of QPO at $\sim$ 67 Hz. Mass scaling the observed AGN QPO frequency to this, implies an AGN mass of 2-3$\times10^6$ $M_\odot$ and hence a mildly super–Eddington flow. The energy spectra of GRS 1915+105, where this QPO is detected, are dominated by low temperature Comptonisation of the accretion disc spectrum, similar to the spectral shape required to fit the 'hot disc' seen in REJ1034+396. This spectral shape may well be the new 'ultra-luminous state' proposed by Gladstone et al. (2009) for the broad curvature seen in the X-ray spectra of the ultra-luminous X-ray sources.

An identification with the 67 Hz QPO also matches the continuum power spectral shape. We use simulations to show that the underlying power spectrum can be described by a single power-law with index -1.3 or by a broken power-law with index steepening from -1 to -2 around the QPO frequency. The broken power-law matches the shape of the power spectrum underneath the LFQPO, while the single power-law can match the (poorly determined) continuum slope underneath the HFQPO and the 67 Hz QPO in GRS 1915+105. We use the normalisation of the continuum power spectrum to distinguish between these two possibilities. With careful matching of the energy bandpass to ensure that the BHB and AGN lightcurves cover the same spectral components, we show that the continuum noise power is a factor 10 too small to be associated with the LFQPO, but is consistent with that seen underneath the HFQPO and 67 Hz QPO.

Hence we propose that the 67 Hz QPO, seen in the BHB GRS 1915+105, is the counterpart of the $\sim$ 3700 s QPO in the AGN REJ1034+396. This gives a consistent match to both the power spectrum and energy spectrum for a 2-3$\times10^6 M_\odot$ black hole accreting at mildly super-Eddington rates.

Chapter 11 | *Concluding remarks*

The work in this thesis points towards some broad conclusions and some rather more specific.

Papers 1 and 2 provide yet more evidence that spectral state transitions vary with mass accretion rate much in the same way as BHXRBs (Pounds, Done & Osborne 1995). This, together with the fundamental plane relations (Merloni, Heinz & di Matteo 2003; Falcke, Körding & Markoff 2004) and similarities in the timing properties (Done & Gierliński 2005; McHardy et al. 2006) is highly suggestive of a simple scaling between AGN and BHXRBs. The only big piece of the puzzle missing was the lack of a QPO in an AGN power spectrum until our discovery of a $\sim$1 hour signal in REJ1034+396 (paper 3). RMS spectra suggest that the origin of this QPO is in a variable hard component as seen in the HFQPOs of BHXRBs and, in this case, is diluted by a stable, low temperature Compton component at soft energies (paper 4). To find an analogy in the BHXRBs we had to look for a similar source, one which demonstrated the same extreme properties. Perhaps the most obvious choice is GRS 1915+105 which shows sustained high mass accretion rates, often in excess of Eddington. REJ1034+396 would also appear to show such high mass accretion rates as evidenced by its SED (paper 2). From a comparison of the two sources with the restriction that the AGN must have $L/L_{Edd} \geq 1$, the 67Hz QPO of GRS 1915+105 appears to be the likely counterpart. This is somewhat confirmed by a comparison of red noise properties underlying the QPO, where a correction for

bandpass effects can reproduce the same normalisation and slope as is present under the 67Hz QPO (paper 5).

In this thesis I also tried to address the outstanding problem of the soft excess seen ubiquitously in high L/L_{Edd} Seyfert 1 AGN. In paper 2 we tried to find a generic origin by comparison with a sample of PG QSOs and NLS1s. This could not adequately distinguish between the photo-ionised models of smeared reflection or wind absorption. This was to be expected due to the lack of sophistication of the models (see chapter 4). It would appear however, that in the specific case of REJ1034+396, the soft excess is formed by low temperature Comptonisation of seed disc photons as this extends into soft X-ray energies. It should be stressed that this cannot conceivably provide a generic origin for the soft excess due to the extremely narrow plasma temperatures required across a wide range of sources of differing masses.

11.1 What lies ahead...

In order to solve the respective problems that remain in determining the dominant processes in AGN we need more accurate models that can fully reproduce the physical effects of an accretion disc wind (which should also account for velocity shear and MHD effects) and include the undoubtedly present reflection features which must take into account stratified ionisation structure. In addition, higher resolution spectroscopy might be able to discern the narrow signatures of atomic processes. If this is combined with a larger bandpass out to higher energies then the predicted shapes of reflection and absorption should diverge (although this has been shown not to work in certain cases, see Miniutti et al. 2007).

Although the results of paper 1 & 2, regarding the changing spectral state with mass accretion rate are compelling, the results from paper 1 could be far improved if the sample of Seyfert 1s and 2s were much larger such that the high energy spectra

could be more meaningfully compared. If the results of paper 1 are reproduced in this larger sample then the statistical evidence should be overwhelming (see Winter et al. 2009).

In order to fully identify the important QPO of REJ1034+396 we would ideally need a reliable mass estimate and a longer observation taken with *XMM-Newton* such that the QPO duty cycle can be observed. This observation would also allow constraints to be placed on the shape of the high energy RMS spectrum allowing a more definitive answer to the origin of the QPO and soft excess in this object. If it turns out that the unique SED and large soft excess is intrinsically linked to the presence of the QPO (as it would appear to be for the 67Hz QPO of GRS 1915+105) then it is quite possible that other sources showing similar SEDs with low-temperature Compton components could also show QPOs in their power spectra.

This work is just the first step on the road to unifying the physics of the accretion flow and the new generation of instruments will allow many of the remaining problems and ambiguities to be addressed, as Frank Sinatra would put it, "the best is yet to come".

Bibliography

[1] Abramowicz M. A., Czerny B., Lasota J. P., Szuszkiewicz E., 1988, ApJ, 332, 646

[2] Abramowicz M. A., Kluźniak W., 2001, A&A, 374, L19

[3] Antonucci R., 1993, ARA&A, 31, 473

[4] Antonucci R. R. J., Miller J. S., 1985, ApJ, 297, 621

[5] Arav N., Barlow T. A., Laor A., Blandford R. D., 1997, MNRAS, 288, 1015

[6] Arav N., 1996, ApJ, 465, 617

[7] Arav N., Barlow T. A., Laor A., Sargent W. L. W., Blandford R. D., 1998, MNRAS, 297, 990

[8] Arévalo P., Uttley P., 2006, MNRAS, 367, 801

[9] Atwood B., Baldwin J. A., Carswell R. F., 1982, ApJ, 257, 559

[10] Awaki H., Kunieda H., Tawara Y., Koyama K., 1991, PASJ, 43, L37

[11] Awaki H., Murakami H., Leighly K. M., Matsumoto C., Hayashida K., Grupe D., 2005, ApJ, 632, 793

[12] Balbus S. A., 2005, ASPC, 330, 185

[13] Balbus S. A., Hawley J. F., 1998, RvMP, 70, 1

[14] Baldwin J., Ferland G., Korista K., Verner D., 1995, ApJ, 455, L119

[15] Ballantyne D. R., Iwasawa K., Fabian A. C., 2001, MNRAS, 323, 506

[16] Ballantyne D. R., Ross R. R., Fabian A. C., 2001, MNRAS, 327, 10

[17] Ballantyne, D. R., Weingartner, J. C., & Murray, N. 2003, A& A, 409, 503

[18] Bassani L., Dadina M., Maiolino R., Salvati M., Risaliti G., della Ceca R., Matt G., Zamorani G., 1999, ApJS, 121, 473

[19] Bechtold J., Czerny B., Elvis M., Fabbiano G., Green R. F., 1987, ApJ, 314, 699

[20] Beckmann V., Gehrels N., Shrader C. R., Soldi S., 2006, ApJ, 638, 642

[21] Begelman M. C., McKee C. F., Shields G. A., 1983, ApJ, 271, 70

[22] Begelman M. C., King A. R., Pringle J. E., 2006, MNRAS, 370, 399

[23] Begelman M. C., Volonteri M., Rees M. J., 2006, MNRAS, 370, 289

[24] Beichman C. A., Soifer B. T., Helou G., Chester T. J., Neugebauer G., Gillett F. C., Low F. J., 1986, ApJ, 308, L1

[25] Belloni T., Hasinger G., 1990, A&A, 230, 103

[26] Belloni T., Mendez M., King A. R., van der Klis M., van Paradijs J., 1997, ApJ, 488, L109

[27] Belloni T., Psaltis D., van der Klis M., 2002, ApJ, 572, 392

[28] Belloni T., Méndez M., Homan J., 2005, A&A, 437, 209

[29] Belloni T., Méndez M., King A. R., van der Klis M., van Paradijs J., 1997, ApJ, 488, L109

[30] Benlloch S., Wilms J., Edelson R., Yaqoob T., Staubert R., 2001, ApJ, 562, L121

[31] Bian W., Gu Q., 2007, ApJ, 657, 159

[32] Bian W., Zhao Y., 2003, ApJ, 591, 733

[33] Bian W., Zhao Y., 2004, MNRAS, 352, 823

[34] Bianchi S., Matt G., Nicastro F., Porquet D., Dubau J., 2005, MNRAS, 357, 599

[35] Blandford R. D., Payne D. G., 1982, MNRAS, 199, 883

[36] Blumenthal G. R., Gould R. J., 1970, RvMP, 42, 237

[37] Blustin A. J., Page M. J., Fuerst S. V., Branduardi-Raymont G., Ashton C. E., 2005, A&A, 431, 111

[38] Boller T., Brandt W. N., Fink H., 1996, A&A, 305, 53

[39] Boroson T., 1992, BAAS, 24, 730

[40] Boroson T. A., 2002, ApJ, 565, 78

[41] Brandt W. N., Mathur S., Elvis M., 1997, MNRAS, 285, L25

[42] Brinkmann W., Arévalo P., Gliozzi M., Ferrero E., 2004, A&A, 415, 959

[43] Brocksopp C., Starling R. L. C., Schady P., Mason K. O., Romero-Colmenero E., Puchnarewicz E. M., 2006, MNRAS, 366, 953

[44] Cannizzo J. K., 1993, ApJ, 419, 318

[45] Cappi M., et al., 2006, A&A, 446, 459

[46] Capriotti E., Foltz C., Byard P., 1981, ApJ, 245, 396

[47] Casebeer D. A., Leighly K. M., Baron E., 2006, ApJ, 637, 157

[48] Casella P., Belloni T., Stella L., 2005, ApJ, 629, 403

[49] Cassidy I., Raine D. J., 1993, MNRAS, 260, 385

[50] Chelouche D., Netzer H., 2003, MNRAS, 344, 233

[51] Chevallier L., Collin S., Dumont A.-M., Czerny B., Mouchet M., Gonçalves A. C., Goosmann R., 2006, A&A, 449, 493

[52] Churazov E., Gilfanov M., Revnivtsev M., 2001, MNRAS, 321, 759

[53] Cirasuolo M., Celotti A., Magliocchetti M., Danese L., 2003, MNRAS, 346, 447

[54] Coppi P. S., 1999, ASPC, 161, 375

[55] Crummy J., Fabian A. C., Gallo L., Ross R. R., 2006, MNRAS, 365, 1067

[56] Cunningham C. T., 1975, ApJ, 202, 788

[57] Czerny B., Elvis M., 1987, ApJ, 321, 305

[58] Czerny B., Nikołajuk M., Piasecki M., Kuraszkiewicz J., 2001, MNRAS, 325, 865

[59] Czerny B., Nikołajuk M., Różańska A., Dumont A.-M., Loska Z., Życki P. T., 2003, A&A, 412, 317

[60] Dadina M., 2007, A&A, 461, 1209

[61] D'Ammando F., Bianchi S., Jiménez-Bailón E., Matt G., 2008, A&A, 482, 499

[62] Dasgupta S., Rao A. R., Dewangan G. C., 2004, ApJ, 614, 626

[63] Dewangan G. C., Griffiths R. E., Dasgupta S., Rao A. R., 2007, ApJ, 671, 1284

[64] Dietrich M., Wagner S. J., Courvoisier T. J.-L., Bock H., North P., 1999, A&A, 351, 31

[65] Done C., 2007, PThPS, 169, 248

[66] Done C., Davis S. W., 2008, ApJ, 683, 389

[67] Done C., Kubota A., 2006, MNRAS, 371, 1216

[68] Done C., Gierliński M., 2003, MNRAS, 342, 1041

[69] Done C., Gierliński M., 2005, MNRAS, 364, 208

[70] Done C., Gierliński M., 2006, MNRAS, 367, 659

[71] Done C., Gierliński M., Kubota A., 2007, A&ARv, 15, 1

[72] Done C., Madejski G. M., Mushotzky R. F., Turner T. J., Koyama K., Kunieda H., 1992, ApJ, 400, 138

[73] Done C., Nayakshin S., 2007, MNRAS, 377, L59

[74] Done C., Osborne J. P., 1997, MNRAS, 288, 649

[75] Done C., Sobolewska M. A., Gierliński M., Schurch N. J., 2007, MNRAS, 374, L15

[76] Done C., Wardziński G., Gierliński M., 2004, MNRAS, 349, 393

[77] Dubus G., Lasota J.-P., Hameury J.-M., Charles P., 1999, MNRAS, 303, 139

[78] Edelson R., Nandra K., 1999, ApJ, 514, 682

[79] Edelson R., Turner T. J., Pounds K., Vaughan S., Markowitz A., Marshall H., Dobbie P., Warwick R., 2002, ApJ, 568, 610

[80] Ebisawa K., Mitsuda K., Hanawa T., 1991, ApJ, 367, 213

[81] Edelson R. A., Malkan M. A., Rieke G. H., 1987, ApJ, 321, 233

[82] Elvis M., et al., 1994, ApJS, 95, 1

[83] Emmering R. T., Blandford R. D., Shlosman I., 1992, ApJ, 385, 460

[84] Esin A. A., McClintock J. E., Narayan R., 1997, ApJ, 489, 865

[85] Fabian A. C., Ballantyne D. R., Merloni A., Vaughan S., Iwasawa K., Boller T., 2002, MNRAS, 331, L35

[86] Evans I. N., Tsvetanov Z., Kriss G. A., Ford H. C., Caganoff S., Koratkar A. P., 1993, ApJ, 417, 82

[87] Evans N. J., II, Lacy J. H., Carr J. S., 1991, ApJ, 383, 674

[88] Everett J. E., 2005, ApJ, 631, 689

[89] Fabian A. C., Crawford C. S., Iwasawa K., 2002, MNRAS, 331, L57

[90] Fabian A. C., Iwasawa K., Reynolds C. S., Young A. J., 2000, PASP, 112, 1145

[91] Fabian A. C., Miniutti G., Gallo L., Boller T., Tanaka Y., Vaughan S., Ross R. R., 2004, MNRAS, 353, 1071

[92] Falcke H., Körding E., Markoff S., 2004, A&A, 414, 895

[93] Fender R. P., Belloni T. M., Gallo E., 2004, MNRAS, 355, 1105

[94] Ferland G. J., Persson S. E., 1989, ApJ, 347, 656

[95] Ferland G. J., Peterson B. M., Horne K., Welsh W. F., Nahar S. N., 1992, ApJ, 387, 95

[96] Ferland G. J., Rees M. J., 1988, ApJ, 332, 141

[97] Ferrarese L., Merritt D., 2000, ApJ, 539, L9

[98] Fragile P. C., Miller W. A., Vandernoot E., 2005, ApJ, 635, 157

[99] Frank J., King A. R., Raine D. J., 1995, AN, 316, 414

[100] Fukue J., 1996, PASJ, 48, 631

[101] Galeev A. A., Rosner R., Vaiana G. S., 1979, ApJ, 229, 318

[102] Gallo L. C., Boller T., Tanaka Y., Fabian A. C., Brandt W. N., Welsh W. F., Anabuki N., Haba Y., 2004, MNRAS, 347, 269

[103] Gallo L. C., Brandt W. N., Costantini E., Fabian A. C., 2007, MNRAS, 377, 1375

[104] Garcia-Rissmann A., Vega L. R., Asari N. V., Cid Fernandes R., Schmitt H., González Delgado R. M., Storchi-Bergmann T., 2005, MNRAS, 359, 765

[105] Gaskell C. M., 2009, arXiv, arXiv:0908.0386

[106] Gaskell C. M., Klimek E. S., Nazarova L. S., 2007, arXiv, arXiv:0711.1025

[107] Gebhardt K., et al., 2000, ApJ, 539, L13

[108] Ghisellini G., 1987, MNRAS, 224, 1

[109] George I. M., Fabian A. C., 1991, MNRAS, 249, 352

[110] Ghisellini G., Haardt F., Matt G., 1994, MNRAS, 267, 743

[111] Gierliński M., Done C., 2004, MNRAS, 349, L7

[112] Gierliński M., Done C., 2004, MNRAS, 347, 885

[113] Gierliński M., Done C., 2006, MNRAS, 371, L16

[114] Gierliński M., Done C., 2006, MNRAS, L64

[115] Gierliński M., Middleton M., Ward M., Done C., 2008, Natur, 455, 369

[116] Gierliński M., Nikołajuk M., Czerny B., 2008, MNRAS, 383, 741

[117] Gierliński M., Zdziarski A. A., 2005, MNRAS, 363, 1349

[118] Gilfanov M., Revnivtsev M., Molkov S., 2003, A&A, 410, 217

[119] Gladstone J., Done C., Gierliński M., 2007, MNRAS, 378, 13

[120] Gladstone J. C., Roberts T. P., Done C., 2009, MNRAS, 948

[121] Goodrich R. W., 1989, ApJ, 342, 224

[122] Gondek D., Zdziarski A. A., Johnson W. N., George I. M., McNaron-Brown K., Magdziarz P., Smith D., Gruber D. E., 1996, MNRAS, 282, 646

[123] González-Martín O., Masegosa J., Márquez I., Jiménez-Bailón E., 2007, IAUS, 238, 373

[124] Graham A. W., Erwin P., Caon N., Trujillo I., 2001, ApJ, 563, L11

[125] Grandi P., Malaguti G., Fiocchi M., 2006, ApJ, 642, 113

[126] Greenhill L. J., Moran J. M., Herrnstein J. R., 1997, ApJ, 481, L23

[127] Grupe D., Mathur S., 2004, ApJ, 606, L41

[128] Gu Q., Melnick J., Fernandes R. C., Kunth D., Terlevich E., Terlevich R., 2006, MNRAS, 366, 480

[129] Guilbert P. W., Rees M. J., 1988, MNRAS, 233, 475

[130] Haba Y., Terashima Y., Kunieda H., Ohsuga K., 2008, PASJ, 60, 487

[131] Hao C. N., Xia X. Y., Mao S., Wu H., Deng Z. G., 2005, ApJ, 625, 78

[132] Heckman T. M., 1980, A&A, 87, 152

[133] Heil L. M., Vaughan S., Roberts T. P., 2009, MNRAS, 397, 1061

[134] Heisler C. A., Lumsden S. L., Bailey J. A., 1997, Natur, 385, 700

[135] Haro-Corzo S. A. R., Binette L., Krongold Y., Benitez E., Humphrey A., Nicastro F., Rodríguez-Martínez M., 2007, ApJ, 662, 145

[136] Ho L. C., Filippenko A. V., Sargent W. L. W., 1997, ApJ, 487, 568

[137] Honma F., Kato S., Matsumoto R., 1991, PASJ, 43, 147

[138] Ichimaru S., 1977, ApJ, 214, 840

[139] Ingram A., Done C., 2009, arXiv, arXiv:0907.5485

[140] Ingram A., Done C., Fragile P. C., 2009, MNRAS, 397, L101

[141] Kaspi S., et al., 2002, ApJ, 574, 643

[142] Kato Y., 2004, PASJ, 56, 931

[143] Kaspi S., Smith P. S., Netzer H., Maoz D., Jannuzi B. T., Giveon U., 2000, ApJ, 533, 631

[144] Kato Y., 2004, PASJ, 56, 931

[145] Kato S., Fukue J., Mineshige S., 1998, bhad.conf,

[146] Kawaguchi T., 2003, ApJ, 593, 69

[147] King A., 2008, MmSAI, 79, 1066

[148] King A. R., Ritter H., 1998, MNRAS, 293, L42

[149] Klein-Wolt M., van der Klis M., 2008, ApJ, 675, 1407

[150] Kluźniak W., Abramowicz M. A., Lee W. H., 2004, AIPC, 714, 379

[151] Kolehmainen, M., & Done, C. 2009, arXiv:0911.3281

[152] Kompaneets, A. S., 1957, Soviet Phys.Ž014JETP Lett., 4, 730

[153] Königl A., 2006, MmSAI, 77, 598

[154] Kormendy J., Richstone D., 1995, ARA&A, 33, 581

[155] Kotov O., Churazov E., Gilfanov M., 2001, MNRAS, 327, 799

[156] Kraemer, S. B., George, I. M., Turner, T. J., & Crenshaw, D. M. 2000, ApJ, 535, 53

[157] Krolik J. H., 1999, agnc.book,

[158] Krolik J. H., Begelman M. C., 1988, ApJ, 329, 702

[159] Krolik J. H., McKee C. F., Tarter C. B., 1981, ApJ, 249, 422

[160] Kubota A., Done C., 2004, MNRAS, 353, 980

[161] Kubota A., Makishima K., 2004, ApJ, 601, 428

[162] Kubota A., Makishima K., Ebisawa K., 2001, ApJ, 560, L147

[163] Laor A., 1991, ApJ, 376, 90

[164] Laor A., 2000, NewAR, 44, 503

[165] Laor A., 2001, ApJ, 553, 677

[166] Larsson J., Miniutti G., Fabian A. C., Miller J. M., Reynolds C. S., Ponti G., 2008, MNRAS, 384, 1316

[167] Lasota J.-P., 2001, NewAR, 45, 449

[168] Leighly K. M., 1999, ApJS, 125, 317

[169] Leighly K. M., 2005, Ap&SS, 300, 137

[170] MacAlpine G. M., 2003, RMxAC, 18, 63

[171] Maccarone T. J., Coppi P. S., 2003, MNRAS, 338, 189

[172] Madejski G. M., Done C., Turner T. J., Mushotzky R. F., Serlemitsos P., Fiore F., Sikora M., Begelman M. C., 1993, Natur, 365, 626

[173] Maiolino, R., & Rieke, G. H. 1995, ApJ, 454, 95

[174] Malizia A., Bassani L., Stephen J. B., Di Cocco G., Fiore F., Dean A. J., 2003, ApJ, 589, L17

[175] Malzac J., Dumont A. M., Mouchet M., 2005, A&A, 430, 761

[176] Maoz D., 2007, MNRAS, 377, 1696

[177] Machida M., Matsumoto R., 2008, PASJ, 60, 613

[178] Marconi A., Hunt L. K., 2003, ApJ, 589, L21

[179] Marconi A., Pastorini G., Pacini F., Axon D. J., Capetti A., Macchetto D., Koekemoer A. M., Schreier E. J., 2006, A&A, 448, 921

[180] Magorrian J., et al., 1998, AJ, 115, 2285

[181] Markowitz A., Edelson R., Vaughan S., 2003, ApJ, 598, 935

[182] Markowitz A., et al., 2003, ApJ, 593, 96

[183] Mason R. E., Geballe T. R., Packham C., Levenson N. A., Elitzur M., Fisher R. S., Perlman E., 2006, ApJ, 640, 612

[184] Matt G., Perola G. C., Piro L., 1991, A&A, 247, 25

[185] Matt G., Fabian A. C., Reynolds C. S., 1997, MNRAS, 289, 175

[186] Mayer M., Pringle J. E., 2007, MNRAS, 376, 435

[187] McClintock J. E., Remillard R. A., 2006, in: Compact stellar X-ray sources. W. Lewin, M. van der Klis (Eds.). Cambridge Astrophysics Series, No. 39, Cambridge University Press, 157

[188] McHardy I., 1988, MmSAI, 59, 239

[189] M^{c}Hardy I. M., Koerding E., Knigge C., Uttley P., Fender R. P., 2006, Natur, 444, 730

[190] McHardy I. M., Papadakis I. E., Uttley P., Page M. J., Mason K. O., 2004, MNRAS, 348, 783

[191] McHardy I., Uttley P., Taylor R., Papadakis I., 2007, ASPC, 360, 85

[192] McKernan B., Yaqoob T., 1998, ApJ, 501, L29

[193] Merloni A., 2003, MNRAS, 341, 1051

[194] Merloni A., Heinz S., di Matteo T., 2003, MNRAS, 345, 1057

[195] Merloni A., Nayakshin S., 2006, MNRAS, 372, 728

[196] Meyer F., Meyer-Hofmeister E., 1994, A&A, 288, 175

[197] Middleton M., Done C., Gierliński M., 2007, MNRAS, 381, 1426

[198] Middleton M., Done C., Schurch N., 2008, MNRAS, 383, 1501

[199] Middleton M., Done C., Ward M., Gierliński M., Schurch N., 2009, MNRAS, 394, 250

[200] Miley G. K., Neugebauer G., Soifer B. T., 1985, ApJ, 293, L11

[201] Miller L., Turner T. J., Reeves J. N., George I. M., Kraemer S. B., Wingert B., 2007, A&A, 463, 131

[202] Miller J. M., Raymond J., Fabian A., Steeghs D., Homan J., Reynolds C., van der Klis M., Wijnands R., 2006, Natur, 441, 953

[203] Miller L., Turner T. J., Reeves J. N., 2008, A&A, 483, 437

[204] Miller L., Turner T. J., Reeves J. N., George I. M., Porquet D., Nandra K., Dovciak M., 2006, A&A, 453, L13

[205] Mineshige S., Kawaguchi T., Takeuchi M., Hayashida K., 2000, PASJ, 52, 499

[206] Miniutti G., Fabian A. C., Goyder R., Lasenby A. N., 2003, MNRAS, 344, L22

[207] Miniutti G., Fabian A. C., 2004, MNRAS, 349, 1435

[208] Miniutti G., et al., 2007, PASJ, 59, 315

[209] Miyamoto S., Kimura K., Kitamoto S., Dotani T., Ebisawa K., 1991, ApJ, 383, 784

[210] Monier E. M., Mathur S., Wilkes B., Elvis M., 2001, ApJ, 559, 675

[211] Morales R., Fabian A. C., 2002, MNRAS, 329, 209

[212] Morgan E. H., Remillard R. A., Greiner J., 1997, ApJ, 482, 993

[213] Mullaney J. R., Ward M. J., 2008, MNRAS, 385, 53

[214] Murashima M., Kubota A., Makishima K., Kokubun M., Hong S., Negoro H., 2005, PASJ, 57, 279

[215] Murray N., Chiang J., 1995, ApJ, 454, L105

[216] Murray N., Chiang J., 1997, ApJ, 474, 91

[217] Murray N., Chiang J., Grossman S. A., Voit G. M., 1995, ApJ, 451, 498

[218] Nagar N. M., Wilson A. S., 1999, ApJ, 516, 97

[219] Nagar N. M., Oliva E., Marconi A., Maiolino R., 2002, A&A, 391, L21

[220] Nandra K., Pounds K. A., 1994, MNRAS, 268, 405

[221] Narayan R., Yi I., 1994, ApJ, 428, L13

[222] Nenkova M., Ivezić Ž., Elitzur M., 2002, ApJ, 570, L9

[223] Nenkova M., Sirocky M. M., Ivezić Ž., Elitzur M., 2008, ApJ, 685, 147

[224] Nenkova M., Sirocky M. M., Nikutta R., Ivezić Ž., Elitzur M., 2008, ApJ, 685, 160

[225] Netzer H., 1990, agn..conf, 57

[226] Novikov I. D., Thorne K. S., 1973, blho.conf, 343

[227] Norman C., Scoville N., 1988, ApJ, 332, 124

[228] Nowak M. A., 1995, PASP, 107, 1207

[229] Nowak M. A., 2000, MNRAS, 318, 361

[230] O'Brien, P. T., et al. 2001, A& A, 365, L122

[231] O'Neill P. M., Nandra K., Cappi M., Longinotti A. L., Sim S. A., 2007, MNRAS, 381, L94

[232] Osterbrock D. E., 1993, ApJ, 404, 551

[233] Osterbrock D. E., Pogge R. W., 1985, ApJ, 297, 166

[234] Page K. L., Reeves J. N., O'Brien P. T., Turner M. J. L., Worrall D. M., 2004, MNRAS, 353, 133

[235] Papadakis I. E., Lawrence A., 1993, MNRAS, 261, 612

[236] Pelletier G., Pudritz R. E., 1992, ApJ, 394, 117

[237] Perola G. C., Matt G., Cappi M., Fiore F., Guainazzi M., Maraschi L., Petrucci P. O., Piro L., 2002, A&A, 389, 802

[238] Peterson B. M., 1997, iagn.book,

[239] Ponti G., Miniutti G., Cappi M., Maraschi L., Fabian A. C., Iwasawa K., 2006, MNRAS, 368, 903

[240] Porquet D., Reeves J. N., O'Brien P., Brinkmann W., 2004, A&A, 422, 85

[241] Pounds K. A., Page K. L., 2006, MNRAS, 372, 1275

[242] Pounds K. A., Done C., Osborne J. P., 1995, MNRAS, 277, L5

[243] Poutanen J., Krolik J. H., Ryde F., 1997, MNRAS, 292, L21

[244] Poutanen J., Lipunova G., Fabrika S., Butkevich A. G., Abolmasov P., 2007, MNRAS, 377, 1187

[245] Pozdniakov L. A., Sobol I. M., Siuniaev R. A., 1976, SvAL, 2, 55

[246] Predehl P., Schmitt J. H. M. M., 1995, A&A, 293, 889

[247] Press W. H., Teukolsky S. A., Vetterling W. T., Flannery B. P., 1996, *Numerical Recipes*, Cambridge Univ. Press. (Cambridge)

[248] Proga D., 2000, ApJ, 538, 684

[249] Proga D., 2003, ApJ, 585, 406

[250] Proga D., Kallman T. R., 2002, ApJ, 565, 455

[251] Proga D., Kallman T. R., 2004, ApJ, 616, 688

[252] Proga D., Stone J. M., Kallman T. R., 2000, ApJ, 543, 686

[253] Psaltis D., Belloni T., van der Klis M., 1999, ApJ, 520, 262

[254] Psaltis D., Norman C., 2000, astro, arXiv:astro-ph/0001391

[255] Puchnarewicz E. M., Mason K. O., Siemiginowska A., Fruscione A., Comastri A., Fiore F., Cagnoni I., 2001, ApJ, 550, 644

[256] Rees M. J., 1984, ARA&A, 22, 471

[257] Rees M. J., 1987, MNRAS, 228, 47P

[258] Reeves J., Done C., Pounds K., Terashima Y., Hayashida K., Anabuki N., Uchino M., Turner M., 2008, MNRAS, 385, L108

[259] Remillard R. A., Gazak J. Z., Lin D., Morgan E. H., Pooley G. G., 2004, AAS, 36, 1516

[260] Remillard R. A., McClintock J. E., 2006, ARA&A, 44, 49

[261] Remillard R. A., Muno M. P., McClintock J. E., Orosz J. A., 2002, ApJ, 580, 1030

[262] Remillard R., Muno M., McClintock J. E., Orosz J., 2003, nvm..conf, 57

[263] Reynolds, C. S. 1997, MNRAS, 286, 513

[264] Reynolds, C. S. 1996, PhD thesis, University of Cambridge

[265] Reynolds C. S., 1999, ASPC, 161, 178

[266] Reynolds C. S., Fabian A. C., 1997, MNRAS, 290, L1

[267] Revnivtsev M., Gilfanov M., Churazov E., 2000, A&A, 363, 1013

[268] Revnivtsev M., Gilfanov M., Churazov E., Sunyaev R., 2002, A&A, 391, 1013

[269] Rezzolla L., Yoshida S., Maccarone T. J., Zanotti O., 2003, MNRAS, 344, L37

[270] Richards G. T., et al., 2006, ApJS, 166, 470

[271] Risaliti G., Elvis M., 2004, ASSL, 308, 187

[272] Risaliti G., Elvis M., Nicastro F., 2002, ApJ, 571, 234

[273] Risaliti G., Elvis M., Fabbiano G., Baldi A., Zezas A., 2005, ApJ, 623, L93

[274] Risaliti G., Elvis M., Fabbiano G., Baldi A., Zezas A., Salvati M., 2007, ApJ, 659, L111

[275] Roberts T. P., 2007, Ap&SS, 311, 203

[276] Rodriguez J., Durouchoux P., Mirabel I. F., Ueda Y., Tagger M., Yamaoka K., 2002, A&A, 386, 271

[277] Ross R. R., Fabian A. C., 1993, MNRAS, 261, 74

[278] Ross R. R., Fabian A. C., 2005, MNRAS, 358, 211

[279] Ross R. R., Fabian A. C., Ballantyne D. R., 2002, MNRAS, 336, 315

[280] Różańska A., Czerny B., 2000, MNRAS, 316, 473

[281] Ruiz J. R., Crenshaw D. M., Kraemer S. B., Bower G. A., Gull T. R., Hutchings J. B., Kaiser M. E., Weistrop D., 2005, AJ, 129, 73

[282] Rybicki G. B., Lightman A. P., 1986, rpa..book,

[283] Salviander S., Shields G. A., Gebhardt K., Bonning E. W., 2006, NewAR, 50, 803

[284] Satyapal S., Dudik R. P., O'Halloran B., Gliozzi M., 2005, ApJ, 633, 86

[285] Schmitt H. R., Donley J. L., Antonucci R. R. J., Hutchings J. B., Kinney A. L., Pringle J. E., 2003, ApJ, 597, 768

[286] Schmitt H. R., Donley J. L., Antonucci R. R. J., Hutchings J. B., Kinney A. L., 2003, ApJS, 148, 327

[287] Schmitt H. R., Pringle J. E., Clarke C. J., Kinney A. L., 2002, ApJ, 575, 150

[288] Schödel R., et al., 2002, Natur, 419, 694

[289] Schurch N. J., Done C., 2006, MNRAS, 371, 81

[290] Schurch N. J., Done C., 2007, MNRAS, 381, 1413

[291] Schurch N. J., Done C., 2008, MNRAS, 386, L1

[292] Shakura N. I., Sunyaev R. A., 1973, A&A, 24, 337

[293] Shapiro S. L., Lightman A. P., Eardley D. M., 1976, ApJ, 204, 187

[294] Shemmer O., Brandt W. N., Netzer H., Maiolino R., Kaspi S., 2006, ApJ, 646, L29

[295] Sim S. A., Long K. S., Miller L., Turner T. J., 2008, MNRAS, 388, 611

[296] Smith D. A., Done C., 1996, MNRAS, 280, 355

[297] Smith M. D., Raine D. J., 1985, MNRAS, 212, 425

[298] Smith M. D., Raine D. J., 1988, MNRAS, 234, 297

[299] Sobolewska M. A., Życki P. T., 2003, A&A, 400, 553

[300] Sobolewska M. A., Done C., 2007, MNRAS, 374, 150

[301] Sobolewska M. A., Życki P. T., 2006, MNRAS, 370, 405

[302] Spitzer L., 1987, degc.book,

[303] Stella L., Vietri M., 1998, ApJ, 492, L59

[304] Strohmayer T. E., Mushotzky R. F., 2003, ApJ, 586, L61

[305] Strohmayer T. E., Mushotzky R. F., Winter L., Soria R., Uttley P., Cropper M., 2007, ApJ, 660, 580

[306] Sunyaev R. A., Titarchuk L. G., 1980, A&A, 86, 121

[307] Szuszkiewicz E., Miller J. C., 2001, MNRAS, 328, 36

[308] Tadhunter C., Marconi A., Axon D., Wills K., Robinson T. G., Jackson N., 2003, MNRAS, 342, 861

[309] Tagger M., Pellat R., 1999, A&A, 349, 1003

[310] Tanaka Y., Boller T., Gallo L., 2005, gbha.conf, 290

[311] Tanaka Y., Boller T., Gallo L., Keil R., Ueda Y., 2004, PASJ, 56, L9

[312] Tanaka Y., Lewin W. H. G., 1995, xrbi.nasa, 126

[313] Tarter C. B., Tucker W. H., Salpeter E. E., 1969, ApJ, 156, 943

[314] Timmer J., Koenig M., 1995, A&A, 300, 707

[315] Török G., Abramowicz M. A., Kluźniak W., Stuchlík Z., 2005, A&A, 436, 1

[316] Tran H. D., 1995, ApJ, 440, 565

[317] Tremaine S., et al. , 2002, ApJ, 574, 740

[318] Tristram K. R. W., et al., 2007, A&A, 474, 837

[319] Turner T. J., George I. M., Nandra K., Mushotzky R. F., 1997, ApJS, 113, 23

[320] Turner T. J., Miller L., 2009, A&ARv, 17, 47

[321] Turner T. J., Miller L., Reeves J. N., Kraemer S. B., 2007, A&A, 475, 121

[322] Turner T. J., Reeves J. N., Kraemer S. B., Miller L., 2008, A&A, 483, 161

[323] Ueda Y., Murakami H., Yamaoka K., Dotani T., Ebisawa K., 2004, ApJ, 609, 325

[324] Ueda Y., Yamaoka K., Remillard R., 2009, ApJ, 695, 888

[325] Uttley P., McHardy I. M., 2001, MNRAS, 323, L26

[326] Uttley P., McHardy I. M., Papadakis I. E., 2002, MNRAS, 332, 231

[327] Uttley P., McHardy I. M., Vaughan S., 2005, MNRAS, 359, 345

[328] van Bemmel I. M., Vernet J., Fosbury R. A. E., Lamers H. J. G. L. M., 2003, MNRAS, 345, L13

[329] van der Klis M., 1989, tns..conf, 27

[330] van der Klis M., 2004, astro, arXiv:astro-ph/0410551

[331] van der Klis M., 2005, AN, 326, 798

[332] van Paradijs J., 1996, ApJ, 464, L139

[333] van Paradijs J., McClintock J. E., 1994, A&A, 290, 133

[334] Vaughan S., 2005, A&A, 431, 391

[335] Vaughan S., Edelson R., Warwick R. S., Uttley P., 2003, MNRAS, 345, 1271

[336] Vaughan S., Fabian A. C., 2004, MNRAS, 348, 1415

[337] Vaughan S., Uttley P., 2005, MNRAS, 362, 235

[338] Vaughan S., Uttley P., 2006, AdSpR, 38, 1405

[339] Verbunt F., Bunk W. H., Ritter H., Pfeffermann E., 1997, A&A, 327, 602

[340] Vestergaard M., Peterson B. M., 2006, ApJ, 641, 689

[341] Walter R., Fink H. H., 1993, A&A, 274, 105

[342] Wang T., Lu Y., 2001, A&A, 377, 52

[343] Wang J.-M., Netzer H., 2003, A&A, 398, 927

[344] Wang J.-M., Zhang E.-P., 2007, ApJ, 660, 1072

[345] Watanabe S., et al., 2003, ApJ, 597, L37

[346] Watarai K.-y., Fukue J., Takeuchi M., Mineshige S., 2000, PASJ, 52, 133

[347] Weedman D. W., Houck J. R., 2009, ApJ, 693, 370

[348] White R. L., et al., 2000, ApJS, 126, 133

[349] Whysong D., Antonucci R., 2004, ApJ, 602, 116

[350] Wijnands R., van der Klis M., 1999, ApJ, 514, 939

[351] Wilms J., Dove J. B., Nowak M. A., Begelman M. C., 1999, hxra.conf, 94

[352] Wilms J., Reynolds C. S., Begelman M. C., Reeves J., Molendi S., Staubert R., Kendziorra E., 2001, MNRAS, 328, L27

[353] Winter, L. M., Mushotzky, R. F., Reynolds, C. S., & Tueller, J. 2009, ApJ, 690, 1322

[354] Woo J.-H., Urry C. M., 2002, ApJ, 579, 530

[355] Woo J.-H., Urry C. M., 2002, ApJ, 581, L5

[356] Yuan W., Zhou H. Y., Komossa S., Dong X. B., Wang T. G., Lu H. L., & Bai J. M. 2008, ApJ, 685, 801

[357] Zdziarski A. A., 1986, ApJ, 303, 94

[358] Zdziarski A. A., Johnson W. N., Done C., Smith D., McNaron-Brown K., 1995, ApJ, 438, L63

[359] Zdziarski A. A., Lubiński P., Gilfanov M., Revnivtsev M., 2003, MNRAS, 342, 355

[360] Zdziarski A. A., Gierliński M., Rao A. R., Vadawale S. V., Mikołajewska J., 2005, MNRAS, 360, 825

[361] Zdziarski A. A., Poutanen J., Johnson W. N., 2000, ApJ, 542, 703

[362] Zhang S. N., Cui W., Chen W., 1997, ApJ, 482, L155

[363] *Ż*ycki P. T., Done C., Smith D. A., 2001, MNRAS, 326, 1367

[364] *Ż*ycki P. T., Done C., Smith D. A., 1999, MNRAS, 305, 231